Chaotic mixing by rod-stirring devices in open and closed flows

Emmanuelle Gouillart

THÈSE de DOCTORAT de l'UNIVERSITÉ PARIS 6 - PIERRE ET MARIE CURIE

Spécialité : Physique

présentée par
Emmanuelle GOUILLART

pour obtenir le grade de
DOCTEUR DE L'UNIVERSITÉ PARIS 6 - PIERRE ET MARIE CURIE

Ecole Doctorale ED 389 :
La Physique de la particule au solide, modèles et expériences

---

Etude de l'advection chaotique dans des mélangeurs à tiges, en écoulements ouverts et fermés

---

Directeur de recherche : Olivier DAUCHOT

Soutenue le 25 octobre 2007
devant le jury composé de :

M.	Armand Ajdari	Examinateur
M.	Philippe Carrière	Rapporteur
M.	Olivier Dauchot	Directeur de thèse
M.	Jean-Pierre Hulin	Rapporteur
M.	Franck Pigeonneau	Membre invité
M.	Stéphane Roux	Examinateur
M.	Jean-Luc Thiffeault	Directeur de thèse
M.	Stéphane Zaleski	Président

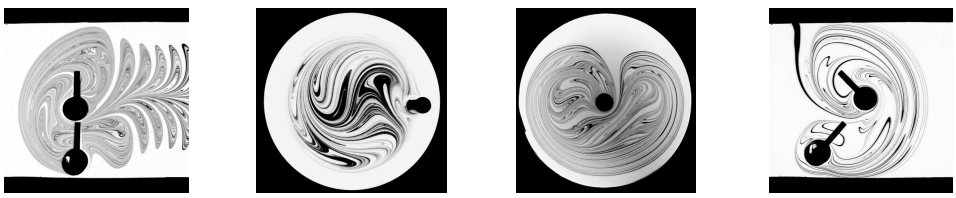

**Service de Physique de l'Etat Condensé, CEA Saclay -
Department of Mathematics, Imperial College London -
Saint-Gobain Recherche**

Résumé

Nous avons étudié le mélange de fluides visqueux dans des écoulements 2-D ouverts et fermés où des agitateurs créent de l'advection chaotique, i.e. des trajectoires lagrangiennes complexes. Notre étude, expérimentale, numérique et théorique, s'appuie sur deux types d'expériences de mélange chaotique, en domaine fermé et dans un canal ouvert. En système fermé, nous avons d'abord proposé une caractérisation topologique du mélange reposant sur l'enchevêtrement des trajectoires de points périodiques – les "tiges fantômes". D'autre part, l'étude expérimentale du champ de concentration d'un colorant nous a permis de décrire le rôle des murs du domaine où se fait le mélange, pour les écoulements fermés comme ouverts. En fermé, la nature chaotique ou régulière des trajectoires initialisées près des bords détermine l'évolution du champ de concentration, même loin des bords. Nous avons ainsi observé une dynamique lente (algébrique) de l'homogénéisation quand la région chaotique s'étend jusqu'à des murs non-glissants. En ouvert, nous avons décrit l'évolution du champ de concentration dans, et en aval de la région de mélange, résultant de l'injection d'un blob de colorant. Nous avons décrit les éléments mal mélangés qui s'échappent aux temps courts, et l'apparition d'un motif permanent (auto-similaire) aux temps longs, déterminé par les orbites périodiques de la région de mélange. Des modifications de ce scénario apparaissent quand la région de mélange va jusqu'aux murs. Enfin, une modélisation à base de transformation du boulanger généralisée nous a permis de comprendre l'essentiel des mécanismes rencontrés.

Mots-clés : mélange chaotique, mélangeur industriel, fluides visqueux, strange eigenmode, systèmes ouverts, selle chaotique, transformation du boulanger, mélange topologique, orbites périodiques.

Abstract

We have studied the mixing of viscous fluids in 2-D closed and open flows, where stirring rods create chaotic advection, i.e. complex Lagrangian trajectories. Our study, experimental, numerical and theoretical, is based on two types of chaotic mixing experiments, in a closed vat and in an open channel. For closed flows, we have first proposed a topological description of mixing by the entanglement of periodic orbits that we called "ghost rods". The experimental study of the concentration field of a dye has then revealed the role of the walls of the domain where mixing takes place, in closed and open flows as well. For closed flows, the chaotic or regular nature of trajectories initialized close to the wall determines the evolution of the concentration field, even far from the walls. In particular, we have observed slow (algebraic) dynamics of homogenization when the chaotic region extends to no-slip walls. In open flows, we have reported on the evolution of the concentration field in the mixing and downstream regions, resulting from the injection of a dye blob. We have described the poorly mixed elements that escape quickly, as well as the asymptotic onset of a permanent (self-similar) pattern determined by the periodic orbits inside the mixing region. Finally, various models derived from the baker's map have allowed us to understand most observed mechanisms.

Keywords : chaotic mixing, industrial mixers, viscous fluids, strange eigenmode, open flows, chaotic saddle, baker's map, topological mixing, periodic orbits.

Remerciements

Les travaux présentés dans ce manuscrit ont été réalisés d'abord au département de mathématiques appliquées de l'Imperial College à Londres, puis au Service de Physique de l'Etat Condensé du CEA Saclay. Cette thèse CIFRE a été financée par l'entreprise Saint-Gobain Recherche, que je souhaite remercier pour m'avoir donné cette belle opportunité d'être formée à la recherche, et ce dans d'excellentes conditions.

Je souhaiterais tout d'abord exprimer ma profonde gratitude à mes deux directeurs de thèse, Olivier Dauchot et Jean-Luc Thiffeault. Olivier et Jean-Luc ont été pour moi des encadrants exceptionnels, mais aussi des amis. Ils ont su me faire profiter de leur expérience et m'apprendre la recherche, tout en me laissant toujours la liberté dont j'avais besoin. Ils sont donc pour beaucoup dans le plaisir et l'épanouissement que j'ai pu trouver dans cette thèse. Jean-Luc a fait preuve de beaucoup de pédagogie pour me transmettre sa vision très complète du mélange chaotique. Son expérience de la programmation m'a également beaucoup appris, et nos nombreuses conversations « geek » ont été un plaisir. Si l'anglais de ce manuscrit est à peu près lisible, c'est en grande partie grâce à lui, qui a su gentiment ignorer mes sarcasmes sur l'accent québécois pour plutôt apprendre à sa thésarde *frenchie* à parler et écrire un peu mieux anglais. Olivier a relevé le défi d'apprendre à faire des manips à une thésarde – alors – théoricienne, venue tout droit de la topologie et des tresses. J'ai aussi beaucoup bénéficié de sa grande culture scientifique, et de son expérience dans le traitement et l'analyse des données. L'ambiance détendue et légèrement euphorique qu'il transporte avec lui a largement contribué au plaisir que j'ai eu à travailler sous sa direction.

Je voudrais également remercier très chaleureusement Stéphane Roux. Ma thèse doit beaucoup à ses interventions lumineuses ; je lui suis notamment redevable des « petits modèles » dérivés de l'application du boulanger, et je le remercie pour ses patientes tentatives pour m'insuffler un peu de sa rigueur et de sa logique impressionnantes. Cette collaboration passionnante a également été très agréable grâce à sa gentillesse et sa disponibilité.

J'ai aussi beaucoup bénéficié de l'expertise et de l'encadrement des chercheurs du GIT (l'inénarrable Groupe Instabilités et Turbulence, du Service de Physique de l'Etat Condensé du CEA Saclay). Merci à Bérengère Dubrulle, dont j'ai partagé le bureau pendant mon séjour au CEA : sa verve romanesque contribue grandement à l'ambiance du groupe, et si je n'ai su exploiter qu'une partie de sa myriade d'idées, nos discussions ont été très enrichissantes. Je remercie aussi vivement François Daviaud pour m'avoir accueillie dans son groupe (lourde charge que d'être responsable du GIT !) mais aussi pour m'avoir fait profiter de son savoir-faire d'expérimentateur et de ses connaissances en physique non-linéaire. Son aide lors des premiers mois de mon séjour au CEA a été précieuse, et je lui en suis très reconnaissante. Merci également à Arnaud Chiffaudel pour ses coups de pouce expérimentaux, son esprit critique et son enthousiasme scientifique. Merci à Eric Vincent pour m'avoir accueillie au Service de Physique de l'Etat Condensé, s'être intéressé à mon travail et avoir signé sans sourciller les commandes de centaines de litres de Canadou, et de divers colorants exotiques. Je voudrais également remercier nos incomparables techniciens Cécile Gasquet et Vincent Padilla, grâce à qui monter et faire fonctionner une manip devient une tâche agréable en plus d'être instructive. Merci à Vincent le mécanicien poète pour la qualité de son travail et pour son amitié. Merci à Cécile pour son efficacité infatigable et pour ne pas avoir hésité à mettre ses mains dans le Canadou avec moi lors des phases les plus ingrates des manips.

A Imperial College, j'ai eu beaucoup de plaisir à travailler avec Matt Finn : derrière son flegme si britannique et sa modestie, Matt cache une rigueur et une créativité admirables. Nombre de résultats présentés dans cette thèse ont été obtenus à partir des codes d'advection lagrangienne conçus et développés par lui.

A Saint-Gobain Recherche, au service Elaboration des Verres puis à l'Unité mixte Saint-Gobain/CNRS, Franck Pigeonneau a été un collaborateur précieux : j'ai pu bénéficier à de nombreuses reprises de ses connaissances en hydrodynamique, et les résultats de ses simulations numériques sont à la base de certaines orientations dans mon travail. Je remercie également Laurent Pierrot, chef du groupe Physique de la Fusion, pour l'intérêt qu'il a porté à mon travail tout au long de ma thèse, et pour ses nombreuses questions, toujours judicieuses. Jacques-Olivier Moussafir nous a procuré quelques excursions mémorables dans le monde merveilleux de la topologie où il se promène avec un naturel déconcertant, et un grand sourire. Je le remercie également pour son code de calcul d'entropie topologique des tresses. Jean-Marc Flesselles a identifié ce beau sujet qu'est le mélange chaotique dans les écoulements ouverts, et est à l'origine de la collaboration entre les différentes équipes qui ont encadré ma thèse : je ne saurais assez

l'en remercier. Mes remerciements vont également à Hervé Arribart pour avoir sélectionné ce projet sur le mélange parmi les thèses financées par Saint-Gobain, et pour l'intérêt qu'il a porté à mon travail.

Philippe Carière et Jean-Pierre Hulin ont accepté la lourde tâche d'être rapporteurs : je les remercie pour la précision de leur lecture et la pertinence de leurs questions, qui ont certainement amélioré ce manuscrit. Je remercie également Armand Ajdari et Stéphane Zaleski de m'avoir fait le plaisir et l'honneur de participer à mon jury.

Cette thèse n'aurait pas été aussi agréable sans l'ambiance très sympathique des différentes équipes où j'ai travaillé. A Londres, les soirées DVD chez Jean-Luc avec sa « dream team », Matt, Khalid Kamhawi, et Lennon O'Naraigh, ou les fins d'après-midi au pub avec le groupe de dynamique des fluides sont autant d'excellents souvenirs. A Saclay, le GIT tout entier est un microcosme extraordinaire, qu'il est difficile de quitter : outre les personnes déjà citées, je remercie ses membres permanents Marco Bonetti, Sébastien Aumaitre et Patrick Méninger, mes camarades thésards Raphaël Candelier, Frédéric Léchenault, Guillaume Marty, Romain Monchaux et Florent Ravelet, et ses « membres d'élection » Daniel Bonamy et Elisabeth Bouchaud. Je remercie aussi ma stagiaire Natalia Kuncio pour son excellent travail sur le mélangeur en huit. Après l'effort, le réconfort : les soirées à l'Olisphère, et les bières au « bar des sciences » du sous-sol – qui deviendra vite une institution, j'en suis sûre – me laissent de très beaux souvenirs. A Saint-Gobain Recherche, l'aventure continue puisque j'ai la chance de rejoindre pendant quelques mois le sympathique groupe Physique de la Fusion, où j'ai toujours été chaleureusement accueillie pendant ma thèse.

Je souhaiterais également exprimer ma reconnaissance à l'ensemble de la communauté des développeurs de logiciels libres. Il ne m'aurait sans doute pas été possible d'explorer autant de pistes ou de tester rapidement de nombreuses idées plus ou moins farfelues sans la puissance et la souplesse du système d'exploitation Linux, et la multitude de logiciels scientifiques libres et de grande qualité qui existent grâce à cette communauté.

Merci à ma famille pour son soutien et son affection. Ma famille et mes amis ont accepté avec le sourire de ne pas me voir beaucoup pendant ces trois ans, et je les en remercie. Merci à notre coloc Jonas pour son amitié et nos discussions, notamment sur les ondelettes. Merci à mon cher Gaël, dont la présence est la source de tant de joies ; ces années de thèse ont été illuminées par son soutien quotidien et l'enthousiasme avec lequel il s'est intéressé à mes travaux.

Contents

Chapter 1

Mixing viscous fluids: a general introduction

The work presented in this thesis is an attempt to describe and classify some generic features of mixing mechanisms leading to homogenization of fluids. We will mostly consider homogenization realized by two-dimensional laminar (non-turbulent) closed and open flows. Despite the apparent variety of industrial mixing processes, we wish to draw here universal characteristics that may help the engineer in designing new mixers and assessing their efficiency.

1.1 Industrial motivation for studying fluid mixing

Many industrial applications would benefit greatly from further insight into the mixing mechanisms of viscous fluids. Fields as diverse as chemical engineering, polymer processing , the pharmaceutical and cosmetics industry, pulp and paper industry, or food processing rely on processes where initially heterogeneous fluids are stirred together to obtain a product with a sufficient degree of "mixedness", a generic property that might stand for chemical and/or thermal homogeneity, mechanical properties (e.g. stiffness) spatial homogeneity, etc., depending on the desired qualities of the final product.

Depending on processes, mixing operations are realized in closed vats or open-flow continuous mixers (see Fig. 1.1). Most devices rely on moving stirrers (e.g. whisks in eggbeater-like devices) and mobile boundaries, or constrained mixer geometries (e.g. food processing screw extruders). There is a vast engineering literature dealing with the extensive study of mixing

(a) (b) (c)

Figure 1.1: Some examples of fluid mixers, from everyday life to industrial applications. (a) Egg beater. (b) Batch planetary mixer used in food processing. (c) Throughflow SMX mixer.

devices; for a review see e.g. the handbook [84]. However, what we aim to do here is in a sense the opposite approach to a handbook: instead of characterizing the difference and uses of a variety of devices, we wish to find general characteristics of fluid mixers.

For the engineer as for the physicist, two main issues arise immediately when considering mixing.

- First, it is of crucial importance to gain sufficient insight into physical mixing mechanisms to *predict the rate of mixing* that can be achieved by mixers. Common wisdom suggests that "the harder and faster you stir, the more you mix". Yet, precise knowledge of homogenization is necessary to achieve mixing at lowest cost, or while designing mixing installations. Also, the same mixing device may be used successively in various situations where different mixing qualities are required. A priori knowledge of generic mixing characteristics spares the time and money consuming process of repeated trial and error for tuning parameters such as flow rate, stirrer size and velocity, process duration, etc. Another requirement is to find laws that are valid for different initial conditions.

  Consider for example the simple mixer shown in Fig. 1.2. A cylindrical rod stirs repeatedly viscous sugar syrup on a figure-eight path – which is basically how you would stir chocolate with other cake ingredients in a cooking bowl. No chocolate is used here, instead we initially mark a small patch of fluid with ink. The filamentary pattern created by the rod movement evolves with time and progressively fills a large domain (see different stages of this evolution in Fig. 1.2). At each

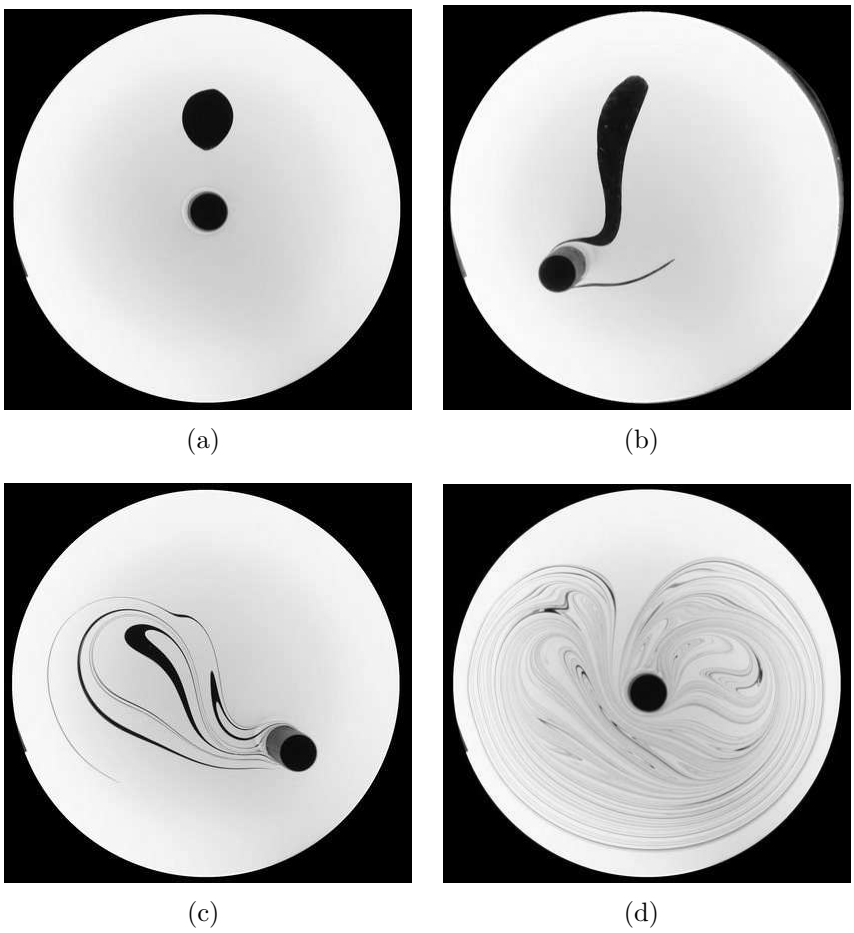

(a) (b) (c) (d)

Figure 1.2: Homogenization of a viscous flow with a simple stirring device (experiments described later in the thesis). A cylindrical rod stirs viscous sugar syrup by moving periodically on a figure-eight (∞) path. We visualize the mixing of an initial blob of dye after 2 (b), 4 (c) and 8 (d) periods of the stirring protocol. To characterize our mixer, we need to understand "how fast it mixes", that is how the mixing pattern develops and what is the degree of homogeneity of such a pattern.

instant, this pattern is fully characterized by the dye concentration field $C(\mathbf{x}, t)$, which evolves towards homogeneity as time progresses. One of the first tasks is therefore to describe this mixing pattern, e.g. by studying the concentration field statistical properties, in order to give a first answer to the question: How fast does it mix ? As we will see in Chapter 4, the answer is far from obvious.

- On the other hand, if one stirs the fluid with a different protocol than the figure-eight, we expect to see a different dye pattern. Another challenge in mixing processes is therefore to have at hand a collection of *criteria for evaluating the mixing quality* achieved by various mixers. One could naively conclude that evaluating mixing efficiency amounts to comparing mixed products qualities. Such an approach is in practice not sustainable. For example, an open-flow mixer might be composed of successive stirring parts that have to be compared independently, regardless of the final product. Also, complete information about the partly mixed state (that is $C(\mathbf{x}, t)$) is not always available, and mixers must be evaluated from partial information, such as pictures of the mixing pattern (Fig. 1.2). Also, nonintrusive mixing measures might be required in situations where one wishes to follow the mixing evolution without disturbing the system.

These two problems are of course intimately linked, and deciding which one to study first is quite a chicken and egg dilemma. The study of mixing mechanisms may reveal features of the partly mixed system – such as the spatial structure of the mixed pattern, or the amplitude of worst heterogeneities – from which extensive information about the mixedness of the system can be gained. If easily measurable, these quantities will be relevant candidates for characterizing mixing. On the other hand, describing the speed of mixing supposes a proper evaluation of the mixing state achieved at each time.

1.2 Basic mixing mechanisms in viscous fluid flows

We briefly present here a few common-wisdom elements aiming at answering the first question we suggested: how fast does it mix ? This paragraph was partly inspired by the introductory chapter of Ottino's reference textbook on mixing [82].

1.2.1 A simple picture

Although we have defined the aim of fluid mixing, that is homogenization, we have not yet characterized *how* mixing takes place. The successive pictures of Fig. 1.2 can help us to draw some building blocks of fluid mixing. Let us consider viscous fluid inside a mixer, initially seeded with some inhomogeneity, e.g. a blob of dye.

- Mobile parts of the device – such as the stirring rod in Fig. 1.2 (a) –, or geometry changes for continuous mixers, create a flow that is *spatially heterogeneous*. Velocity gradients, that is *shears*, deform locally fluid elements along preferred directions. The stirring rod in Fig. 1.2 (b) stretches for example the dye blob in its wake.

- Stretching of fluid elements causes the blob frontier to grow and the blob to be dispersed in a larger domain than it occupied at first – although its area remains constant in incompressible flows. This shuffling of fluid elements is the first ingredient of mixing: fluid elements initially close do not stay together but are instead dispersed over the fluid domain.

- However, this purely geometric rearrangement does not account for the whole mixing process. The mixing pattern on Fig. 1.2 (d) is not just a zebra-like juxtaposition of black and white fluid elements; intermediate gray levels are visible instead. This is due to *molecular diffusion* that blurs material contours and allows initially separated regions to interpenetrate each other. The action of diffusion is more spectacular on thin filaments, as it is then faster for the unmarked fluid particles to contaminate the dye filament to its core through random walking – a process responsible for the fading of black and white contrast. The *stirring* of fluid elements in thin filaments – a purely kinematics mechanism – facilitates intimate *mixing* realized by diffusion at the molecular scale. Also note that different gray levels along the elongated blob result from different stretching histories experienced by the particles.

One of the requirements for an efficient stirring velocity field is therefore to create small scales at which diffusion can act within a reasonable timescale. This might seem a challenge for laminar flows: unlike turbulent ones, low-Reynolds-number velocity fields have significant energy only at the integral scale of the flow (such as the scale of the flow domain, or the stirrer's size). They do not benefit from the short-correlated velocity fluctuations – and hence stretching – that act at various scales and lead to efficient

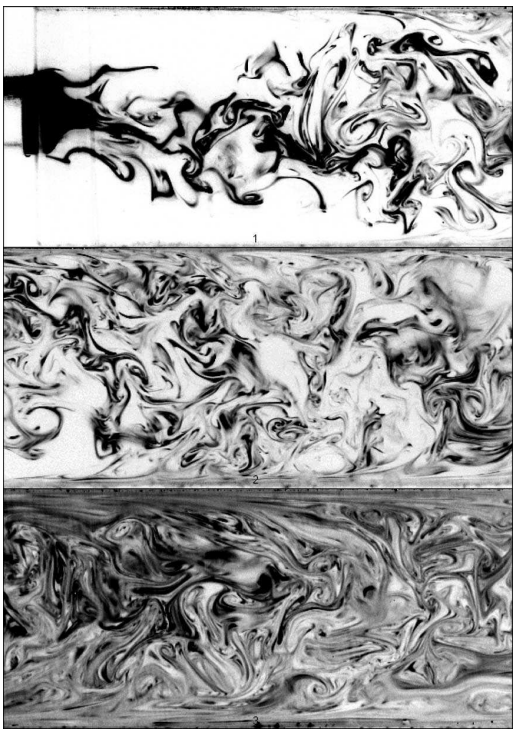

Figure 1.3: Turbulent mixing, experiments by Villermaux and Duplat [125]. In this turbulent flow, small-scale velocity fluctuations create random shears that stretch fluid in random directions and homogenize fluid uniformly across the domain. Note that the dye pattern is very different from the pattern in viscous fluid (Fig. 1.2).

mixing in turbulent flows, as can be observed in Fig. 1.3. On the contrary, we consider from now on smooth large-scale stirring flows with simple time dependence (stationary or time-periodic). Flow Reynolds numbers, defined by $Re = U\ell/\nu$, where U is a typical flow velocity, ℓ the typical flow scale and ν the fluid kinematical viscosity, will be small, typically $Re \sim 1$. The mixing pattern created in very viscous sugar syrup by the rod in Fig. 1.2 is very different from the turbulent one in Fig. 1.3; filaments are nicely packed in parallel structures, and not randomly pointing in rapidly varying directions, as in the turbulent case. One can also note that some parts of the domain are not contaminated by the dye expansion. One of the mechanisms we wish to describe is how a large-scale flow can create these thin filamentary structures.

1.2.2 Open flows: a transient stretching

We also aim at understanding and characterizing mixing in *open flows*. By open-flow mixers, we mean devices where a main flow crosses a mixing region where fluid particles are stretched as in the closed flow case. An example is shown on Fig. 1.4: viscous sugar syrup flows through a long shallow channel; constant flow rate imposes a stationary flow in the far upstream and downstream of the "mixing region", where two rods stir fluid in an egg-beater-like fashion. Another class of open-flow mixers, that will not be studied here, consists of the space-periodic juxtaposition of successive passive mixing elements such as bends or bas-relief structures along the main flow direction (these mixers are e.g. frequently used in microfluidics).

Mixing in open flows also relies on stretching and diffusion , with a crucial difference: the main flow that forces fluid particles to be carried away downstream. As a blob of inhomogeneity flows from upstream, a fraction is caught by the rods, stretched and folded in a complicated pattern (Fig. 1.4 (b) and (c)) as in closed flows. Note that the filamentary pattern around the rods in Fig. 1.4 (c) has some similarities with the one in Fig. 1.2 (d); the same combination of stretching and diffusion create intermediate grey levels with fading contrast. Nevertheless, contrary to closed flows, some dye particles are never caught inside the mixing region, but escape downstream without having experienced much stretching (the black lobes on top of Fig. 1.4 (b)). Also, because of the main flow that pushes fluid downstream, fluid leaks continuously from the mixing region, resulting in the "flower" pattern with partly mixed lobes shown in Fig. 1.4 (c)). This is due to the main flow: fluid particles that come from upstream must eventually escape downstream. However, fluid particles initially in the same small blob of dye (Fig. 1.4 (c)) can experience very different stretching and mixing history, depending on the time they spend in the mixing region. In closed flows, all particles spend the same time in the mixer; this is not the case in open flows where the chance to be stretched depends strongly on the initial condition. The escape process is irreversible: once a fluid particle leaves the mixing region, it cannot experience much more stretching – of course, diffusion continues to homogenize the filaments, and some additional stretching might be caused by a spatially nonuniform downstream flow, such as a Poiseuille flow, but for the cases we consider, the latter effect is weaker compared to the stretching realized by our rods. Thus, the fate of a fluid particle depends strongly on the particle residence time inside the mixing region. This explains the success of residence time distribution analyses used in the chemical engineering field since Danckwerts [30] to characterize mixing in open flows.

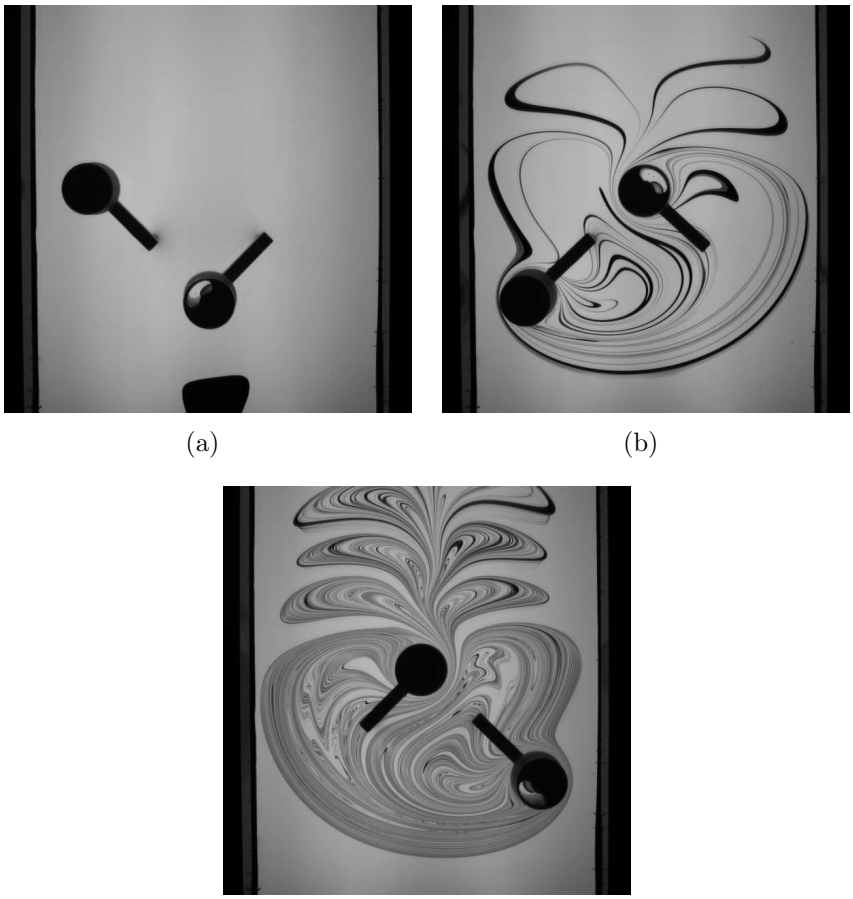

(a) (b)

(c)

Figure 1.4: **Mixing in open flows: a transient process.** (experiments described later in the thesis) (a) Viscous fluid (sugar syrup) flows in a long shallow channel at a constant flow rate. Two rods stir the passing fluid in an egg-beater-like fashion (the two rods move on intersecting circles in opposite senses). A blob of incoming fluid is marked with dye. (b) A fraction of the blob is caught by the rods inside the mixing region where it is stretched and folded in many filaments. However, other parts of the blob escape from the mixing region barely stretched. These are the thick black structures on top of the snapshot: they are very poorly-mixed and will not get any other chance to experience more mixing. (c) As time goes on, dyed fluid keeps leaking from the mixing region. The longer marked particles stay in the mixing region, the more stretching they experience: escaping lobes in the near downstream region look therefore more and more mixed – in a sense that has yet to be specified.

A necessary condition for good mixing in open flows is therefore to keep fluid particles inside the mixing region as long as possible so that they experience enough stretching. One could naively conclude that the right solution is then to increase the stirrers velocity, or equivalently to decrease the average flow rate, so that a particle spends on average more stirring periods inside the mixing region. However, flowrate directly controls the productivity in continuous open-flow mixing systems and decreasing it too much is usually undesirable. Conversely, the energetic cost of moving the stirrers faster might be prohibitive; fragile polymers might also forbid the use of hight stirring velocities . Besides, this tuning only changes the *average* residence time of particles inside the mixing region, and typical open-flow mixers create a broad residence-time distribution for fluid particles (cf. Fig. 1.4). Particles that escape faster than the mean residence time, like the thick black lines on Fig. 1.4 (b), are especially problematic. More insight into the range of histories of fluid particles in open flows is therefore necessary to characterize mixing.

1.2.3 The framework of chaotic advection: a study of Lagrangian dynamics

Now that we have introduced that homogenization results from the combination of stretching through stirring, and diffusion , we wish to relate quantitatively this process to an evaluation of the evolving mixing state of, say, a blob of dye. A first attempt in this direction may be to write directly the advection-diffusion equation

$$\frac{\partial C}{\partial t} + \mathbf{v} \cdot \nabla C = \kappa \Delta C, \tag{1.1}$$

which determines completely the evolution of the dye concentration field $C(\mathbf{x}, t)$, given suitable initial conditions. $\mathbf{v}$ is the stirring velocity field and κ the diffusion coefficient. However, this partial differential equation cannot be solved analytically in most cases. Only numerical integration of (1.1) can usually solve for C. Spectral methods allow to obtain the concentration field with a very good accuracy, yet other methods that suffer from numerical diffusion must somtimes be used for complicated geometries.

Generally, the Eulerian field $\mathbf{v}$ gives little information about the development of the mixing pattern. As we described in the previous paragraph, a natural description of mixing rather comes from following the stretching of elementary elements, or fluid particles – a *Lagrangian* description. Fortunately, such a description can be made in the rich framework of *dynamical*

systems, as we will describe throughout this paragraph. Indeed, if we consider the motion of a passive fluid element in a given velocity field $\mathbf{v}$, the trajectory of the fluid particle will be given by integrating the equation:

$$\dot{\mathbf{x}}(t) = \mathbf{v}_{\text{particle}}(\mathbf{x}, t) = \mathbf{v}_{\text{fluid}}(\mathbf{x}, t), \tag{1.2}$$

that is

$$\begin{aligned} \dot{x}(t) &= u(x, y, z, t) && (1.3)\\ \dot{y}(t) &= v(x, y, z, t) && (1.4)\\ \dot{z}(t) &= w(x, y, z, t) && (1.5) \end{aligned}$$

in 3-D flows, or

$$\begin{aligned} \dot{x}(t) &= u(x, y, t) && (1.6)\\ \dot{y}(t) &= v(x, y, t) && (1.7) \end{aligned}$$

in 2-D flows, on which we will mostly focus throughout this thesis.

The particle therefore evolves in a phase space whose dimension is given by the dimension n of the flow ($n = 2$ or 3 for physical fluid flows), plus an optional additional degree of freedom if the velocity field is time-dependent. Even for simple regular flows, the components of $\mathbf{v}$ are generically nonlinear functions of the coordinates. A three-dimensional phase space is enough for a nonlinear dynamical system to exhibit chaotic trajectories, that is extreme sensitivity to initial conditions (for a general introduction to dynamical systems, chaos and its applications, see the textbooks [67] and [14], or the more technical monographs [79] and [3].). A famous example is the three-dimensional system proposed by Lorenz to model convection [66] (it is a dissipative system, however). Two-dimensional time-dependent flows or three-dimensional stationary flows can therefore create chaotic trajectories. This situation is most beneficial for mixing, as two fluid particles initially close to each other (e.g. two marked particles inside the initial blob of dye) separate very fast – in fact, exponentially with time as predicted by the *Lyapunov* exponent of the flow (see Fig. 1.5) – and won't stay segregated in the same small area. For finite systems, this is only true until the separation is on the order of the system size. Another way to understand the advantages of chaos for mixing is to realize that points on the blob frontier will separate exponentially, hence the frontier will grow exponentially with time. In incompressible flows, mass conservation imposes in return that the size of the blob in the direction transverse to stretching decreases exponentially, thus facilitating the action of diffusion as we saw. Unlike many other domains, fluid mixing hence benefits from chaos!

The alert reader may now ask which suitable velocity fields (in Eq. (1.2)) might create such chaotic trajectories. As a general rule of thumb, flows can create chaotic trajectories, or equivalently exponential stretching, if fluid particles experience successively shears in transverse directions. Fig. 1.6 illustrates this condition. Fig. 1.6 (a) shows the mixing of a blob by a vortex-flow realized by Meunier and Villermaux [70]. In this stationary radial-shear flow, fluid particles align with flow streamlines on a spiral and are always stretched along the same direction. No chaotic trajectories can be created by this flow, where adjoining particles separate linearly with time, as in a classical shear flow. On the other hand, we can see on Fig. 1.6 (b) the deformation of a blob by the figure-eight protocol. Because of the figure-eight ∞ shape, the rod can cross the origin in two transverse directions, $\swarrow$ and $\searrow$. On Fig. 1.6 (b), the passing rod has first stretched the blob and aligned some part of it along the $\swarrow$ direction. However, half a period later the rod will stretch the blob, yet in the $\searrow$ direction this time. One can easily check that such a succession of stretching in different directions causes the distance between two particles to grow exponentially with time – a distinctive feature of chaos. Such mechanisms have been successfully studied of the *linked twist map* framework [130, 106]

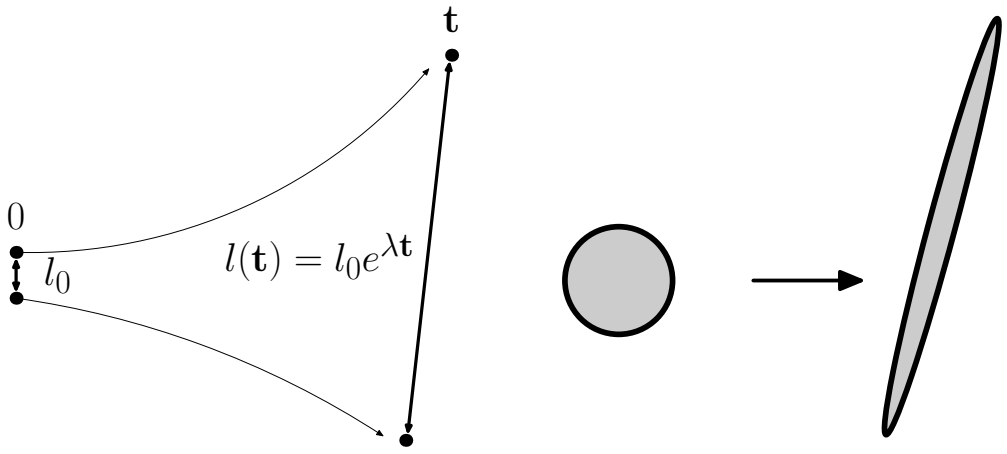

Figure 1.5: Sensitivity to initial conditions: in a chaotic flow, two neighboring particles separate exponentially with time and their distance grows as $l(t) = l_0 e^{\lambda t}$ during time t. λ is referred to as the stretching coefficient for the corresponding fluid particles, or finite-time Lyapunov exponent. As a consequence, material blobs are exponentially stretched along the separating direction. Note that particles at different locations may experience different finite-time stretching coefficients.

The ability for simple flows to create complicated – chaotic – trajectories was named *chaotic advection* by Aref in a seminal paper [8]. For the first time, Aref linked the familiar Lagrangian approach in fluids, and the then-recent discovery than dynamical systems could exhibit chaos. In this paper, Aref considered in particular the case of two-dimensional incompressible time-dependent flows, for which the equations of motion have a Hamiltonian form , due to the existence of the stream function Ψ:

$$\dot{x}(t) = u(x,y,t) = -\frac{\partial \Psi}{\partial y} \tag{1.8}$$

$$\dot{y}(t) = v(x,y,t) = \frac{\partial \Psi}{\partial x}. \tag{1.9}$$

The coordinates x and y are conjugated Hamiltonian variables, and the phase space is also the real physical space (x,y) of the experiment ! This property allows visualization of the beautifully elongated structures of chaos directly in dye spreading experiments as on Fig. 1.2, and explains partly all

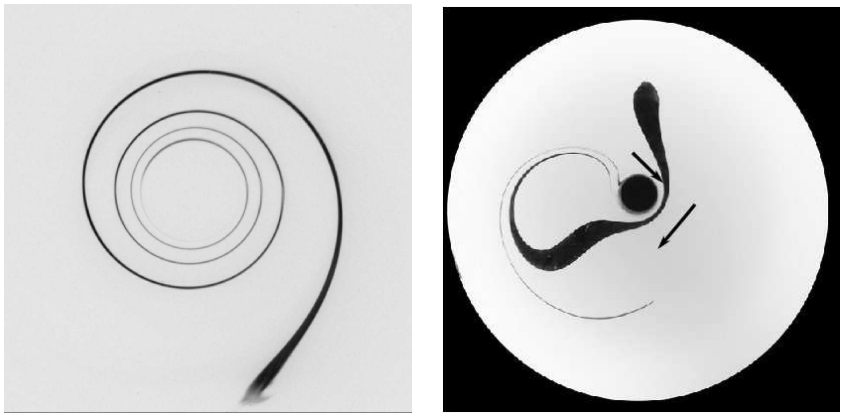

(a) (b)

Figure 1.6: Two possible stretching scenarios: simple-shear or chaotic flows. (a) Experiments by Meunier and Villermaux [70]. A vortex creates a radial shear flow that stretches a blob of dye linearly with time along a smooth spiral. No chaotic trajectories can be created by such a protocol, as in a stationary flow, particles trajectories coincide with streamlines. (b) In the figure-eight (∞) protocol, the self-crossing trajectory of the rod imposes that particles are successively stretched along transverse directions. This multiplicative stretching process imposes that neighboring particles separate exponentially with time on chaotic trajectories.

the enthusiasm generated by chaotic advection since 20 years (for a review see [82]).

However, a generic phase space is rarely entirely chaotic; usually, chaotic regions coexist with regular regions where stretching is not exponential, but at most algebraic with time. Fig. 1.7 (b) illustrates this coexistence. We have computed a so-called *Poincaré section* for two variants of our now-familiar figure-eight stirring-rod protocol. A Poincaré section consists in representing the regions that are visited by trajectories of single fluid particles, stroboscoped at each period of the stirring protocol. For obtaining Fig. 1.7 (b), we have integrated numerically the trajectory of a few initial conditions during a large number of periods of the protocol and we have represented the stroboscoped position of the particles at each period. The integration was realized using the Stokes flow described in [40] for the rod motion. For the protocol represented on Fig. 1.7 (a), a single particle trajectory fills the entire domain: we conclude that almost all trajectories are chaotic (there could be tiny islands not visible on the section). However, for a protocol with a smaller rod, Fig. 1.7 (b) reveals the presence of two small islands where the stroboscoped positions of particles (red points) are confined to elliptical paths . These two islands, and the large chaotic sea surrounding them, are an example of mixed phase space. In a caricatural way, the chaotic region is associated in the mixing literature to good mixing, because it causes exponential stretching, contrary to elliptical islands which have been stigmatized as regions with low stretching. Another disadvantage of elliptical islands is that they are invariant regions, hence particles from outside cannot cross their frontier. Islands are in this way barriers to transport, which can be seen on the dye spreading experiments shown in Fig. 1.7 (c) and (d). In Fig. 1.7 (c), an initial blob has spread over a large central part of the chaotic region. However, the blob in Fig. 1.7 (d) is initialized inside the chaotic region and cannot penetrate the elliptical islands, therefore visible as two big holes in the mixing pattern. Only diffusion can allow dye to cross the frontier between the chaotic region and an elliptical island – however, this is a quite inefficient mechanism.

Since the early work of Aref [8], many studies have therefore concentrated on determining the size of the chaotic regions in various 2-D time-dependent flows [22, 26, 61, 108, 50, 82], and characterizing how subtle changes in flow parameters modify the phase space portrait– the underlying goal being to design protocols with elliptical islands as small as possible, if any. This dualistic approach – chaotic is good, regular is bad – is still employed in many studies: a recent review article by Aref [9] focuses on this single aspect to characterize chaotic advection. However, we will see that even in the absence of elliptical islands, homogenization by chaotic

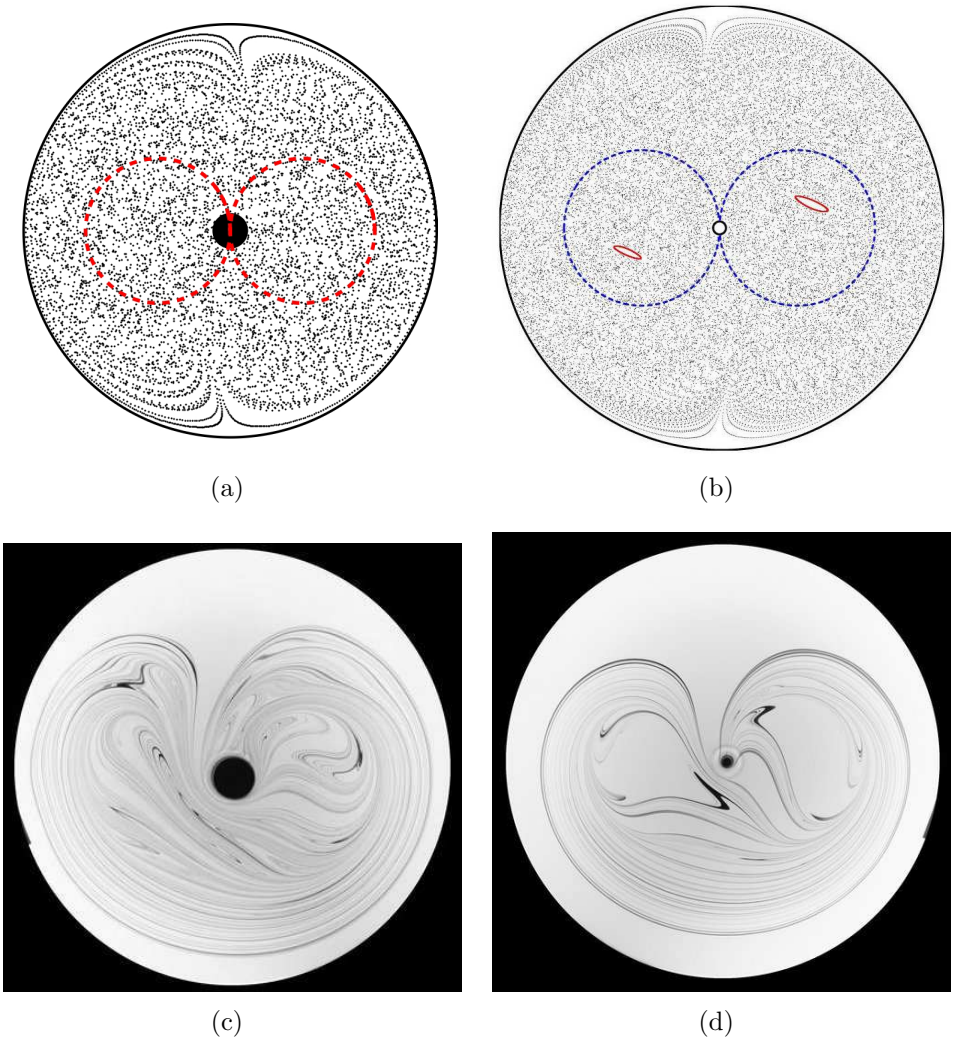

(a) (b)

(c) (d)

Figure 1.7: (a), (b): Poincaré sections for two versions of the figure-eight protocol. These sections are obtained by integrating numerically the trajectory of a few particles with a velocity field in the Stokes flow regime. The chaotic region spans the entire domain in (a), whereas two small small islands are visible for a protocol with a smaller rod (b). (c) and (d): Dye spreading experiments for protocols with the same geometry thean (resp.) (a) and (b). (b) and (d) A blob of dye initialized inside the chaotic region cannot cross the frontier of regular islands, which therefore act as transport barriers. Note that the holes in the dye filamentary pattern are bigger than the extent of the islands visible in the Poincaré section: this is due to the "stickiness" of the islands, that trap fluid around them for long times before their neighbourhood can be visited by new particles (the Poincarè section was obtained after 20000 periods.).

mixers can exhibit surprising dynamics, depending on hydrodynamics, and stretching inhomogeneities.

Several other features of dynamical systems have been studied in 2-D incompressible flows, such as periodic points and their manifolds, presence of homoclinic or heteroclinic points, of which the quantitative connection with mixing properties and efficiency is sometimes far from obvious. Many studies have focused on determining the spatial distribution of stretching, which was done numerically [75, 2, 4], or experimentally [128, 11], which is more of a challenge. In a nutshell, two particles initialized at different positions – e.g. one close to the rod, the other close to the tank wall – experience different instantaneous stretching. This non-uniform stretching accounts for the variable widths and contrasts of filaments on Fig. 1.2 (c): low-stretching histories will correspond to high-contrast filaments. This observation has motivated numerous studies based on stretching distributions [75], or related criteria such as interface growth [2, 73], or filaments widths distributions [4]. Another recent promising approach, called *topological mixing* [18] relies on using topological invariants of rod-stirring protocols to determine lower bounds of interface stretching – the basic idea being that rods stretch material lines at least as much as an elastic band pulled tight on the rods.

In open flows Lagrangian dynamics are slightly different. We may of course operate stirrers in the open-flow channel (Fig. 1.4) with a protocol known to create chaotic trajectories in a closed tank, and follow the motion of Lagrangian tracers. Inside the mixing region, the velocity field created by stirring rods is close to its closed flow version, with a perturbation responsible for the downstream leak: one therefore expects comparable stretching properties as in closed flows. However, particles can only experience "finite-time chaos": two adjoining particles that enter the mixing region separate fast – approximately exponentially with time – while they stay in the mixing region. Nevertheless, they always end up escaping downstream where their separation grows much more slowly, if at all. We already see one of the differences between closed and open flows: in open flows, most relevant quantities will be based on finite-time definitions, e.g. stretching rates experienced by particles while inside the mixing region. However, there exists also a fractal set of unstable periodic orbits , called the chaotic saddle [31, 87, 111], that stay forever inside the mixing region (e.g. points on the stirrers boundary). These orbits determine the structure of the mixing pattern and the stretching experienced by particles, as particles that enter the mixing region typically follow closely one or more of these orbits before escaping downstream. Most studies of chaotic advection in open flows [87, 104, 76, 53, 111] have therefore focused on studying the fractal proper-

ties of this set, which have been shown to be related to particles residence times and global stretching. However, a coherent vision of mixing in open flows is still lacking, as these purely kinematical studies do not describe quantitatively the response function of a mixer to an impurity, e.g. the blob of dye in Fig. 1.4. To our knowledge, no systematic study of stretching coefficients or filaments widths, or other parameters that might characterize the mixed state, has ever been carried out in open flows.

1.2.4 Homogenization dynamics

However, kinematical quantities based on Lagrangian point-like measures, such as stretching distributions, do not provide a completely satisfactory characterization of mixing, as they do not account directly for the homogenization of a scalar field such as dye concentration. It is of paramount importance for a more complete vision of mixing, as for applications, to understand how a scalar concentration field $C(\mathbf{x}, t)$ relaxes towards homogeneity under the action of chaotic stirring.

Passive scalar studies are classical in turbulence (for a review see [33]), where the effects of intermittency have been characterized by the statistical properties, or spatial structure, of passive scalar concentration fields [101, 102, 92, 99, 20]. Statistical methods are particularly adapted for turbulent flows, especially random flows (e.g. Kraichnan flows [57]) where ensemble averages over realizations can be performed.

Such an approach seems less suited for deterministic chaotic advection. Nevertheless, stretching distributions in chaotic mixing share some generic statistical properties, that have been used to characterize the power spectrum of a scalar field, where chaotic stretching creates smaller and smaller scales [80, 6, 7, 121, 122]. Homogenization dynamics are obtained by considering the fate a single dye filament under the combined action of stretching and diffusion. It is relatively easy to predict the evolution of the concentration field for a single blob subject to diffusion, and a constant stretching rate [115, 125], as the advection-diffusion equation (1.1) has then a simple form in a suitable comoving frame. Taking into account all different stretching histories, together with the fact that elementary filaments might overlap because of diffusion [125], is then more of a challenge. Several attempts have nevertheless been made in this direction [80, 6, 7, 121, 122, 115, 125], which all lead to an exponential relaxation of the concentration field – e.g. characterized by its variance – towards homogeneity.

Further insight into homogenization dynamics was gained when Pierrehumbert noticed in a 1994 paper [88] that under general assumptions, the concentration field converges asymptotically to an eigenvector of the

advection-diffusion operator. After a transient phase, the concentration field settles in a time-periodic pattern corresponding to this eigenvector, also called *strange eigenmode* by Pierrehumbert. Homogenization is controlled by the corresponding eigenvalue, and the decay of fluctuation is exponential. Experiments [95, 52] as well as numerical simulations [36, 48] have evidenced the onset of such persistent patterns. However, all these studies were conducted in model systems – e.g. in periodic domains without walls, or multi-cellular domains – far from the reality of industrial mixers that we wish to consider here. Moreover, the quantitative connection of the eigenmode decay rate with stretching properties of the underlying remains unclear for generic situations [48].

Finally, the problem of homogenization has hardly been addressed in open flows, where efforts have been preferentially devoted to determining fractal properties of chaotic orbits (for a review see [111]). This open problem will be one of our major concerns throughout this thesis.

1.3 Outline of the thesis

When I started the work presented in this thesis, the main goal for the three years to come was to adapt existing knowledge on mixing in closed flows, in order to characterize transient mixing in open flows. However, while revisiting the literature of mixing in closed flows, with its application to open flows in mind, several points remained unclear to us – such as the speed of homogenization in a basic mixing device like the one shown on Fig. 1.2. In parallel to our study of open flows, we carried complementary investigations in closed flows as a guide on the less-trodden path of open flows. As we have found, the two problems – homogenization in closed and open flows – are closely related, e.g as far as the importance of periodic orbits or the role of solid walls go. Throughout this manuscript, we will try to highlight analogies between the closed and open flows, rather than presenting them in an unrelated fashion. In the same way, we will present together results of numerical simulations, that yield Lagrangian trajectories of fluid particles, and dye experiments that give access to dye concentration fields. When possible, we will also use simple 1-D models derived from the classical baker's map, that allow us to test various situations and draw generic mechanisms.

This thesis is organized as follows. In Chapter 2, I present the various mixing devices we have studied experimentally and numerically. Detailed information about experimental set-ups in closed and open flows are given in this chapter. Chapter 3 focuses on the characterization of mixing by

tools from dynamical systems and topology, that is a purely kinematical approach to mixing (we do not consider diffusion in particular). Periodic points are shown to determine the structure of the mixing pattern, both in closed and open flows. In closed flows, a topological study of the entanglement of periodic points trajectories gives accurate information about interface stretching. Periodic orbits are of additional importance in open flows: transport phenomenon in open flows are accounted for by relating residence-time distributions to the set of periodic orbits inside the mixing regions – the *chaotic saddle*, and its manifolds. Chapters 4 and 5 address the experimental study of the concentration field resulting from the evolution of a blob of diffusive dye, in respectively closed and open flows. Chapter 4 takes on the study of homogenization speed in bounded stirring devices. For a first experiment with a fully chaotic Poincaré section, our results for homogenization dynamics are in contradiction with commonly accepted wisdom: we find an algebraic decay for the concentration variance, rather than the expected exponential decay. We relate this behavior to the role of no-slip hydrodynamics close to the fixed outer wall, on which a parabolic point controls the reinjection of poorly mixed fluid inside the bulk. In a second configuration, a regular region encircling the wall shields the chaotic region from the effect of the wall, and we recover exponential mixing dynamics. Insight gained in Chapter 4 is transposed to open systems in Chapter 5, where we study scalar homogenization by open flows achieved in a long shallow channel, where mixing is restricted to a limited region. Once again, no-slip walls are shown to be of paramount importance. In the case where the chaotic mixing region is shielded from the channel side walls, we observe the onset of a permanent concentration field which decays exponentially with time. Departure from this behavior is observed when the mixing region extends to the side walls. Chapter 6 is devoted to some possible measures of mixing in open flows. Finally, Chapter 7 offers some conclusions.

Chapter 2

The mixing systems

The choice of a model system is always difficult. It is an especially tricky problem for studying mixing, as there exists a huge variety of industrial mixing devices, as well as an extensive literature on mixing where different model systems have been proposed. In this chapter, we first discuss the reasons for choosing the different mixing systems studied in this work. A detailed description of the experimental set-up for a closed flow protocol and an open-flow protocol is then presented. Numerical simulations of Stokes flows allow us to explore a broader range of flow parameters and to access complementary measures: numerical protocols and methods are presented in Sec. 2.3.

2.1 Selection of the mixing protocols

2.1.1 Requirements for suitable mixing protocols

Our motivation is two-fold in selecting mixing protocols.

First, our systems must be close enough to feasible industrial devices. Mechanical stirring devices that can be operated with a reduced set of motors, gears and pulleys will be preferred. However, we wish to study simple systems from wish universal mechanisms of mixing can be derived, and we will limit ourselves to geometries as simple as possible, such as circular tanks, cylindrical stirrers or channels of constant rectangular section. Mixing mechanisms might be more difficult to understand in more refined systems, e.g. with sophisticated blades or impellers [12, 132].

Second, we want to study the impact of *chaotic advection* on fluid homogenization. We have seen in the previous chapter that chaotic trajectories could be created in flows with three or more degrees of freedom, that

is 2-D time-dependent flows or 3-D stationary flows. For the sake of simplicity, we will restrict our investigation to 2-D flows, where experimental flow visualization and numerical simulations are easier to perform than for full 3-D flows. For that matter, most previous studies of chaotic advection have been carried out in 2-D flows (see [82] for a review). We therefore need to use 2-D time-dependent protocols that create chaotic trajectories. The latter point is not such of a challenge: in fact most time-dependent 2-D flows will create chaotic trajectories in at least some part of the domain. We pointed out in the previous chapter some general tips which are useful – but not guaranteed – to cause chaos: break symmetries and shear fluid in successive transverse directions. This condition thus does not restrict too much the class of interesting protocols: stirrers moving on intersecting or self-intersecting paths will generically create chaotic advection. The interested reader is referred to the papers [41, 83] for a detailed discussion on conditions for a trajectory to be chaotic.

2.1.2 Historical 2-D stirring protocols

Many stirring protocols extensively studied in the literature actually meet the requirements defined in the previous paragraph. We describe below a few representative protocols and their specificities.

Blinking vortex flow

From a historical perspective, the *blinking vortex* flow is the first chaotic mixer ever studied. It was introduced by Aref in 1984 [8] and has received considerable attention since then [50, 69, 77]. Inside a circular domain, two point vortices are alternately switched on and off at each half-period of the stirring protocol (Fig. 2.3). The two vortices can be co- or counter- rotative. The flow time-dependency results from the alternation between the two stationary vortex flows. Trajectories during each half-period coincide with streamlines, which are simply circles enclosing the active vortex (see Fig. 2.1). However, trajectories jump from one streamline (corresponding to the former active vortex) to an intersecting streamline, this time corresponding to the new active vortex. This streamline-crossing is responsible for chaotic advection [106]. Consider for example two particles on the same streamline during one half-period: at the next blinking, they will jump to two different streamlines corresponding to different velocities, and hence separate.

Many reasons motivate the attention received by the blinking vortex flow. First, the piecewise-stationary nature of the flow provides insight into

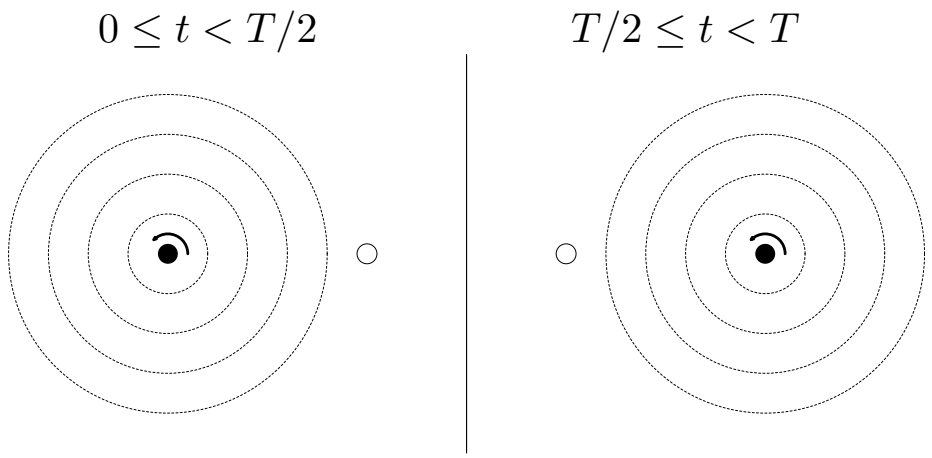

Figure 2.1: Blinking vortex flow: two point vortices are alternately switched on and off. This alternation between two different stationary flows enables particles to jump between intersecting streamlines, a mechanism responsible here for fast trajectories separation, i.e. chaotic advection.

mechanisms responsible for chaotic advection, using a very simple flow: the flow complexity results only from the switching between two otherwise simple stationary flows, and the consequent streamline jump. The circular nature of streamlines in the vortices' vicinity also allows instructive analytical calculation [8, 130]. Second, it is possible to derive an analytical expression for the flow created by a vortex inside a circle: this was first done by Aref [8] in a potential flow, using Milne-Thomson's [71] circle theorem, and extended to the Stokes flow case by Meleshko and Aref [69], who modeled the vortices by rotlets singularities. Such expressions have allowed extensive studies of particles advection in numerical simulations, such as Poincaré sections, analysis of streamlines patterns, computation of stretching coefficients, etc. Experimental realizations of the blinking vortex flow have also been carried out, using two fixed rotating rods as vortices [50] or magnet-driven vortices in a viscous conductive fluid [77]. The evolution of the area covered by dye has in particular been investigated in this flow [50].

However, there is a price to pay for the remarkable simplicity of the blinking vortex flow: particles initially close to one of the vortices will not much feel the effect of the other vortex, from which they are quite far (the velocity field amplitude decreases with the distance from the vortex): for a long time, these particles will effectively experience only the rotation due to one of the vortices, resulting in very poor stretching. On the other hand, particles initialized in a central region between the two vortices can easily switch between parts of the domain, because they feel the influence of

both vortices. As a result, stretching is very inhomogeneous in the blinking vortex flow.

Journal bearing flow

The *journal bearing flow* is also a piecewise-stationary flow. We consider the time-periodic viscous flow between two eccentric cylinders rotated alternately (Fig. 2.3 (d)). This flow has been much studied in the lubrication literature for the case of a thin gap between cylinders, but its first apparition in the chaotic advection literature goes back to 1986 [10, 22]. Once again, streamline crossing between the two streamline patterns created by the rotating cylinders is responsible for trajectories separation and chaotic advection. In the Stokes-flow regime, trajectories are uniquely determined by the boundary displacements: journal bearing flows are therefore characterized by a small number of parameters, that is, cylinders radii, (positive or negative) angular displacements, and eccentricity. Numerous studies have considered different variants of this protocol [10, 22, 108, 75, 74], both numerically and experimentally. The existence of an analytical expression for the corresponding Stokes flow is one of the reasons accounting for the popularity of the journal bearing flow, and abundant numerical simulations aiming at characterizing phase portraits or stretching distributions have been conducted in this flow.

However, this protocol suffers from the same limitation as the blinking vortex flow: trajectories initialized close to one of the boundaries will feel only the effect of the corresponding cylinder for a long time – they may escape from this region eventually – and experience simple shear due to rotation instead of immediate exponential stretching.

Cavity flows

Another class of interesting protocols concerns cavity flows, i.e. flows inside a rectangular cavity where the top and bottom boundary are alternately horizontally driven. This well-studied [26, 61, 74] protocol has the same advantages and limitations as the previously described boundary-driven protocols: simple experimental realizations and analytical expression available for Stokes flow simulations, but inhomogeneous stretching.

2.1.3 Mobile boundaries vs. rod-stirring protocols

The reader might have noticed that all protocols described so far – the historical stirring protocols – take place in a fixed geometry, where moving

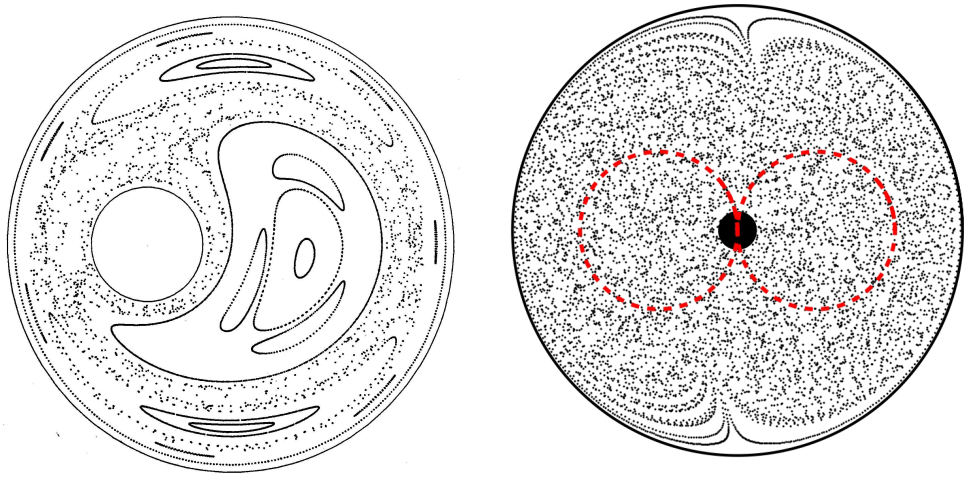

(a) (b)

Figure 2.2: Poincaré sections for a realization of the journal bearing flow (taken from the work of Chaiken et al. [22]) (a) and figure-eight protocol (b). Many regular regions are visible in (a), whereas the chaotic region spans the entire domain in (b). As the journal bearing flow is created only by the motion of the fixed boundaries, it is in practice difficult to avoid the presence of poor-stretch regions, among which regular islands.

boundaries drag along fluid, but stay at the same position. This would be a quite non-intuitive manner to stir cake ingredients in a bowl... Every kid knows instead how to stir a cake by moving a spoon in the mixture and visiting every part of the bowl for a faster result. Protocols with moving rods – hence with changing geometry – are therefore good candidates for studying mixing. Two reasons explain why boundary-driven protocols have been favored instead until recently. First, considering piecewise stationary protocols provides an elegant representation by streamline crossing for chaotic advection, and allows for simple calculations. Moreover, closed expressions for the stirring velocity field are highly desirable for numerical simulations of particle trajectories, but the Stokes flow velocity field for one or more moving stirring rods has only been derived recently [40, 38].

However, moving rods protocols are of high interest to us, as rods can explore a large part of the fluid domain on their path, hence create more uniform stretching. Fig. 2.2 illustrates this phenomenon: whereas a Poincaré section of the journal bearing flow (taken from [22]) reveals a complicated structures with many elliptical islands, the chaotic region spans the entire

domain for the figure-eight protocol. Recent studies [18, 40, 38, 39, 114], on the other hand, have shown that lower boundaries on stretching could be derived from topological invariants based on the various rods crossings. Finally, keeping in mind the comparison between closed and open flows, we advocate the use of stirring-rod protocols which can be performed in closed (e.g. circular) domains as well as in open-flow channels.

2.1.4 Selected protocols

In the spirit of the previously exposed argumentation, we have mostly considered rod-stirring protocols, but we have also studied historical stirring protocols such as the blinking vortex flow in numerical simulations, to better link our work to the existing literature. The two stirring rods protocols studied here are show in Fig. 2.3 (a) and (b). The first protocol is the figure-eight protocol, where a single rod is moving on a figure-eight path. We have already used this protocol many times to demonstrate useful concepts in mixing. We use this protocol in a closed flow. The second protocol, used in an open-flow channel, is the eggbeater flow, consisting of two rods moving in a contrarotative fashion on two intersecting circles. Note that both protocols share certain similarities, as can be seen in Fig. 2.3 (a) and (b): the movement of the rod(s) imposes in both cases that fluid is sucked into a central region from the upper part of the domain, while it is pushed downwards to the sides in the lower part. These similarities will allow us to find comparable effects in closed and open flows, although we do not use exactly the same protocol.

2.2 Experimental realizations of stirring protocols

We have built two experimental apparatus for studying mixing in closed and open flows. In both devices, we aim at measuring the concentration field resulting from the injection of a blob of dye, and its stirring and mixing by chaotic advection. Hence, we use comparable experimental methods for closed and open flows.

2.2.1 Set-up for a closed flow mixing experiment

I present here the setup of a closed-flow experiment designed to study homogenization by chaotic stirring. This experimental set-up has been devised

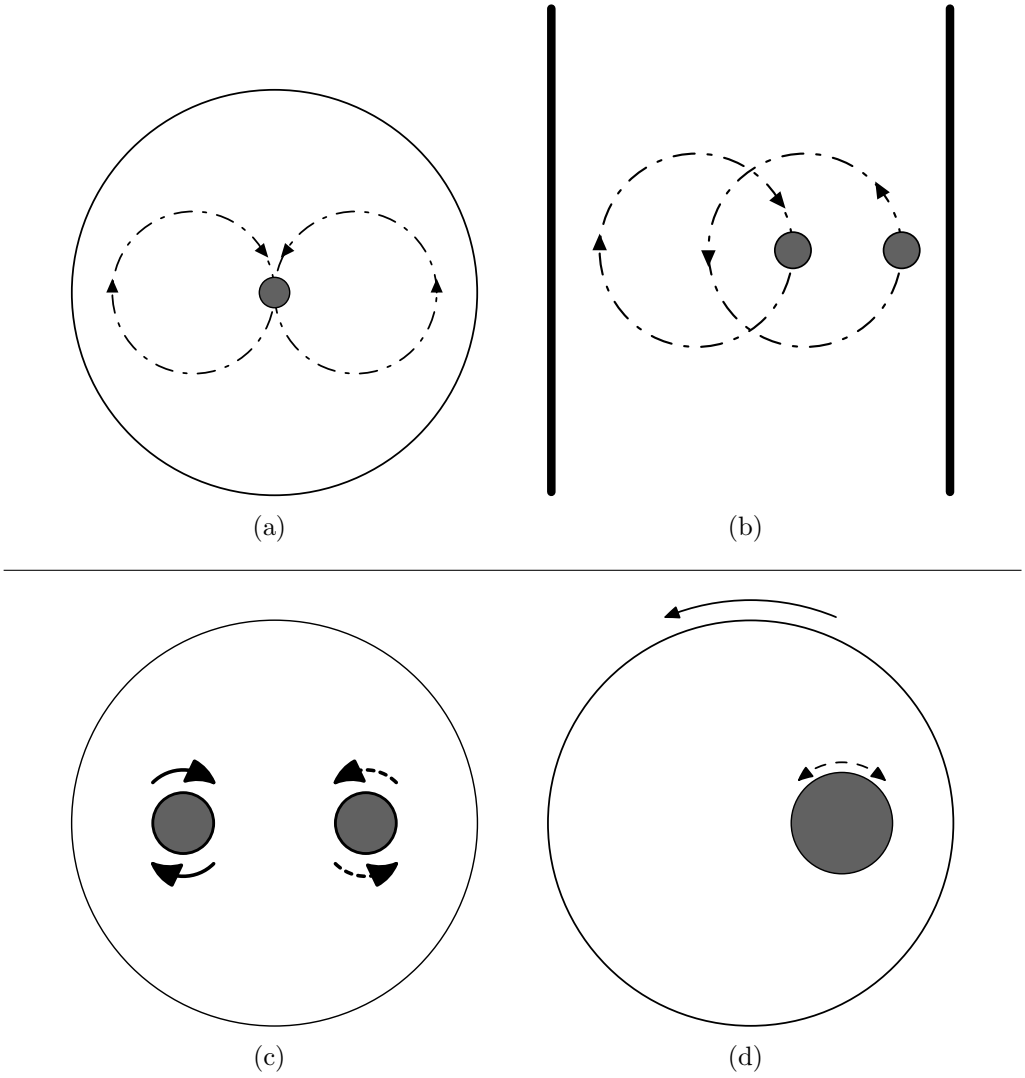

Figure 2.3: Selected protocols: the figure-eight protocol (a) and the eggbeater protocol (b) are extensively studied in experiments and numerical computations. Comparisons are made with historical stirring protocols, that is the blinking vortex flow (c) and the journal bearing flow (d).

and built in collaboration with Natalia KUNCIO during her Master's degree internship.

The schematic drawing in Fig. 2.4 illustrates the different parts of the experiment described below.

Stirring apparatus

The viscous fluid used here is cane sugar syrup, aka "Canadou", a beverage usually designed for the nobler use of lime rhum cocktails (see Fig. 2.5 (a)). For the physicist however, it has the additional advantage of being a cheap viscous Newtonian fluid. Its good optical transparency makes it also an ideal candidate for flow visualizations. Canadou viscosity measures made by Frédéric Da Cruz are shown on Fig. 2.5 (b): at room temperature (controlled at $19° \pm 0.5°$ in our laboratory), Canadou kinematic viscosity ν is about 250 times higher than for water.

Canadou fills a cylindrical tank (see Fig. 2.4) of 20 cm inner diameter and 10 cm height. The height of Canadou inside the tank is 9.5 cm. As the mixing pattern is visualized through the bottom of the tank, the tank is built up of a transparent plastic cylinder glued on a flat 4 mm glass plate, in order to avoid planarity defects that one can find in the bottom of a commercial glass vat. Nylon screws press the tank firmly at a fixed position against a metal frame fixed to the laboratory floor, but can also be easily removed between experiments in order to empty and clean the tank.

Canadou is stirred by a cylindrical rod plunged inside the fluid down to 1 cm of the glass plate, in order to create an approximatively 2-D flow close to the free surface [1]. Different rod diameters ($\ell = 4$, 8, 10, 12 and 16 mm) were used in our experiments. However, we will mostly concentrate in this manuscript on results obtained for $\ell = 16$ mm. The rod is driven on a figure-eight path by an ARRICKS ROBOTICS XY table that allows to control the rod movement. For each rod diameter, we performed experiments at two different linear speeds U – $1\,\mathrm{cm \cdot s^{-1}}$ and $2\,\mathrm{cm \cdot s^{-1}}$ – to test the influence of stirring speed [2]. Depending on rod diameter and speed, we explore

[1] By visual inspection through the transparent side-wall of the vessel, we observed that dyed fluid stays in a thin layer - typically 1 or 2 mm – below the free surface. We concluded that 3-D effects are negligible for the duration of an experiment, that is about 30 stirring periods.

[2] For these low velocities, the motion of the rod is slightly jerky. However, we have checked that the rod always comes back to the same position at the end of a cycle (up to a precision of one pixel). Moreover, in the low-Reynolds-number regime, Lagrangian trajectories depend only on the path travelled by the rod, and not of the speed at which it is travelled.

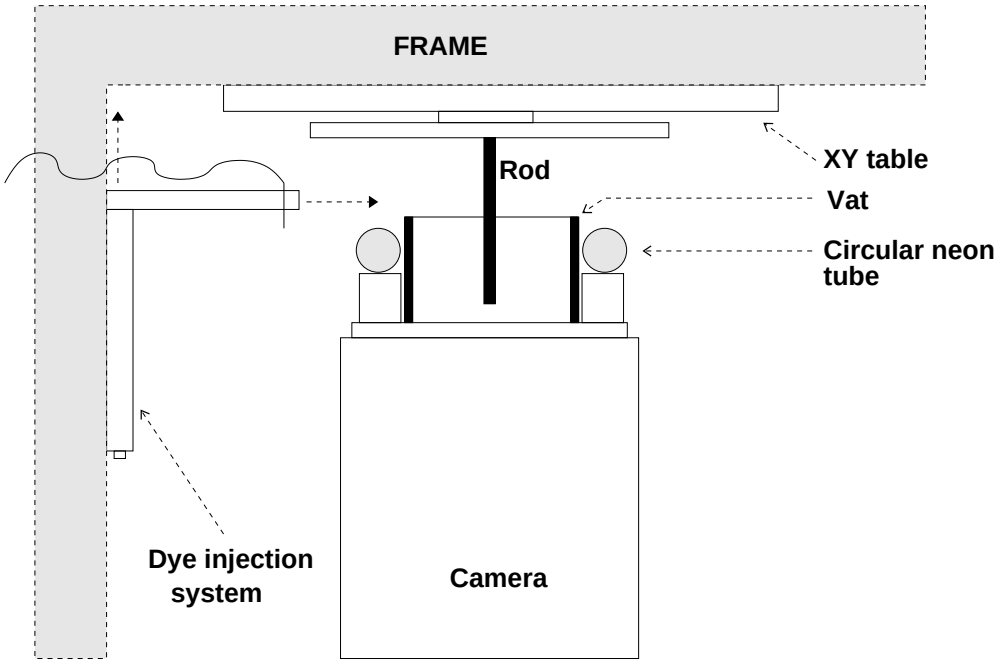

Figure 2.4: Closed-flow experimental setup. A cylindrical rod moved by a XY table stirs viscous sugar syrup inside a closed vat. At the beginning of the experiment, a spot of dye is injected just below the fluid surface. The mixing pattern is illuminated by the reflexion of a neon tube by a white plate moving with the rod, and we visualize mixing through the transparent bottom of the vat with a high-resolution digital camera.

Reynolds numbers $Re = U\ell/\nu$ ranging from 0.16 to 1.6 . The figure-eight path is made of two adjacent circles of 6 cm diameter.

Dye injection and homogenization

Our experiments consist in visualizing the homogenization of a small blob of dyed fluid that is injected just below the fluid surface, before the rod motion starts. The dye blob is made of Indian ink (Lefranc-Bourgeois brand) diluted in Canadou (we use a 2% by volume Indian ink dilution in all experiments described in this thesis). The blob is injected at 1 mm below the surface through a syringe needle. A controllable syringe pump allows smooth injection of a fixed volume of dye (2 mL) in a reproducible fashion. Again for the sake of repeatability, two perpendicular sliding tracks (see Fig. 2.4) allow to inject the blob always at the same place. Indian ink, hence dye, is lighter than Canadou: the buoyancy force thus lifts the blob

(a)

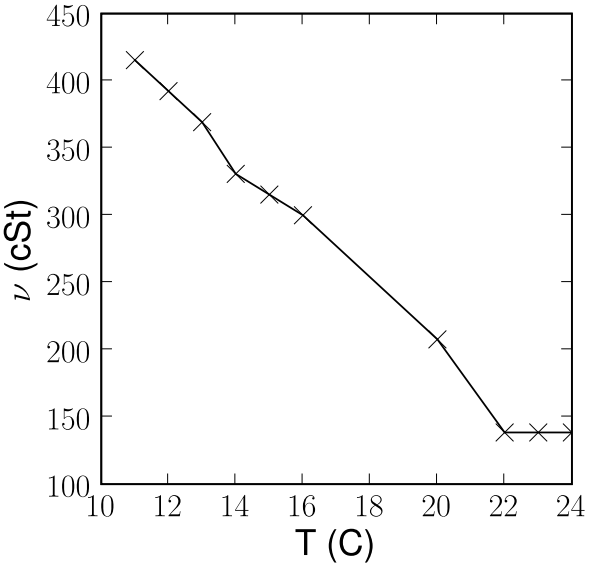

(b)

Figure 2.5: (a) Cane sugar syrup, aka Canadou, is cheap and easily commercially available. Its basic fabrication principle consists in slowly incorporating cane sugar in warm water. (b) Canadou kinematical viscosity (measures by Frédéric da Cruz) vs. temperature. At 19°C, Canadou is about 250 times more viscous than water.

to the free surface, ensuring that the initial condition is two-dimensional, with dye confined to a thin upper layer.

The choice of Indian ink was motivated by its great dyeing intensity: little dye is required to color a great quantity of Canadou, so that we might hope that dyed fluid has the same hydrodynamical properties as unmarked fluid. However, commercial Indian ink is made of an aqueous suspension of black carbon particles, stabilized by a *binder*, usually polymers which are responsible for the ink's very low surface tension. As a result, blobs with a high ink concentration tend to break up as they reach the surface, to minimize the surface tension. We therefore limit ourselves to a highly diluted ink solution, where this effect is not visible on the experiment's timescale.

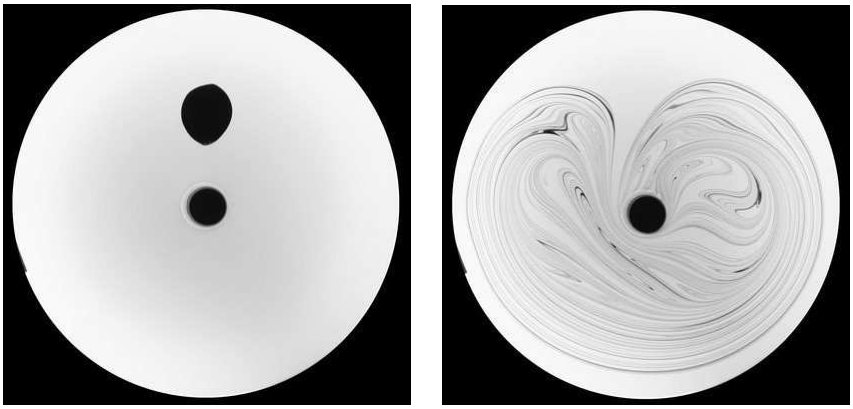

(a) (b)

Figure 2.6: (a) Initial condition: a small blob of marked fluid is released just under the free surface. (b) We follow the evolution of the mixing pattern imposed by the stirring rod.

Data acquisition

Our primary goal is to follow the evolution of the dye concentration field as the mixing process goes on. To do so, we need to access the concentration field through the greyscale intensity of pictures of the mixing pattern, in order to have an unambiguous relation between greyscale intensity and dye concentration. It is important to note that this condition imposes the use of transmission lighting. Since we observe the mixing pattern from below, all light rays must therefore come from above. Because of the XY table mechanical device, there is no room left for a light source above the fluid tank. Our light source is therefore an indirect one: a large plastic plate coated with white paint is fixed between the rod and the XY table carriage. The white plate is illuminated by a circular neon tube around the cylindrical tank (see Fig. 2.4). The inner tank border is coated with matted black film to ensure that only light reflected by the white plate can illuminate the fluid. A digital Canon EOS Mark II 1-D color camera is used to take 12 bit, 3504×2336 pictures at a fixed rate. Depending on rod velocity, we take 3 ($U = 2\,\mathrm{cm \cdot s^{-1}}$) or 6 ($U = 1\,\mathrm{cm \cdot s^{-1}}$) pictures per stirring period. We also wrap the camera in a black-cloth dark room fixed to the tank glass plate and the metallic frame to avoid any unwanted lighting of the apparatus.

Data processing

A first step for processing pictures such as Fig. 2.6 (b) consists in carefully calibrating the digital camera to obtain its response to dye concentration, i.e. the law $I(\mathbf{x}) = f(C(\mathbf{x}), I_0(\mathbf{x}))$, where $I(\mathbf{x})$ is the measured light intensity (pixel grey level), and $I_0(\mathbf{x})$ the light intensity coming from the white plate, that can be accessed by taking pictures without any dye. To do so, we fill a small transparent dish with dye dilutions of known dye concentrations (see Fig. 2.7). We take pictures of the "grey dish" at different positions, as well as reference pictures of the white plate alone. We take into account the small variation ($\sim 5\%$) of incoming light intensity with time – due to the 50 Hz oscillations of the neon tube – by rescaling the mean intensity of the reference picture with respect to a white region without dye in dish pictures. Results of this calibration are plotted in Fig. 2.8 for 12 different dilutions (dilution factors: 1, 2, 3, 4, 5, 8, 10, 12, 16, 25, 32, 125, ∞) and at 12 different spatial positions, in order to test the influence of the slightly inhomogeneous lighting. We can see that we have indeed an unambiguous relation between I/I_0, that is the amount of light dispersion due to dye particles, and dye concentration C. For small dye concentrations, there is a linear relation between C and $\log(I/I_0)$, as predicted by the Beer-Lambert law of simple diffusion. The saturation observed at higher concentrations is probably caused by a saturation of the CCD captor sensitivity. We therefore fit the relation between C and I/I_0 by:

$$\log(I(\mathbf{x})/I_0(\mathbf{x})) = \alpha \tanh\left(\frac{C(\mathbf{x})}{\beta}\right), \text{ with } \alpha = 4.90,\ \beta = 0.32. \qquad (2.1)$$

This law enables to calculate at each pixel the dye concentration of the pixel from the intensity of the pixel, using the reference light intensity of the same pixel in the absence of dye.

Pictures recorded in Canon 12-bit Raw format are first transformed into standard PPM (portable pixmap) format using Dave Coffin's open source library DCRAW (`http://cybercom.net/~dcoffin/dcraw`). PPM pictures are then read with standard scientific libraries written in the PYTHON programming language (`http://www.python.org`, `http://www.scipy.org`). All our data processing scripts are also written in PYTHON. The concentration field is directly accessed thanks to the calibration relation (2.1), where I_0 is obtained by taking pictures of the white plate alone.

Let us finally mention that calibrating the camera was a difficult step; this explains partly why very few previous mixing experiments have measured quantitatively the concentration field. To our knowledge, the only preceding experiments to have performed such direct concentration measures

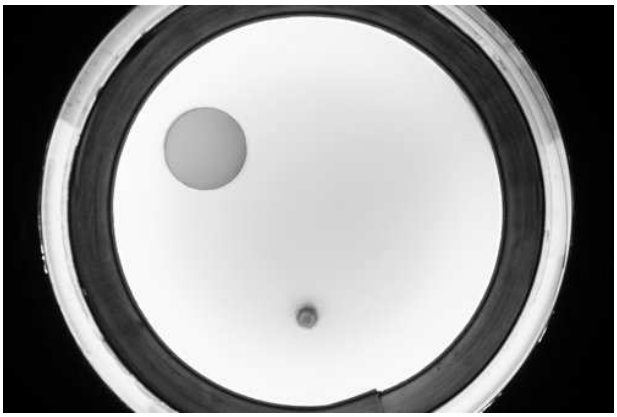

Figure 2.7: Example of picture used to calibrate the camera. A small transparent dish filled with a 1 mm-thick dye layer of known concentration value floats on the fluid surface. The layer thickness was chosen to approximate the thickness of the initial dye blob in experiments (Fig. 2.6).

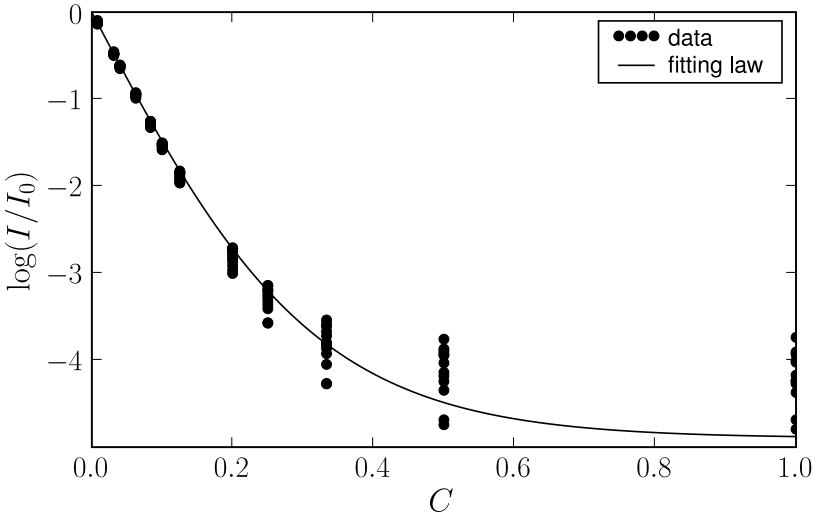

Figure 2.8: Canon camera response to the light fraction transmitted through dye (I/I_0), vs. dye concentration. Data points are fitted by a $\log(I/I_0) = \alpha \tanh(C/\beta)$ law ($\alpha = 4.90$, $\beta = 0.32$), which amounts to the Beer-Lambert law for low concentrations.

have been conducted in devices where the flow scale was much smaller than the domain scale, such as conductive fluids stirred by large arrays of magnets [95, 52]. Other notable concentration measures have been carried out in turbulent mixing experiments [125]. Although beautiful dye spreading experiments were realized in pioneering chaotic mixing experiments ([22, 61, 50]), their main purpose was do determine the size of different regions of the space phase. In contrast, our apparatus has been specially designed to obtain precise concentration measures, with an appropriate lighting and a careful calibration of the camera response to dye.

Steps of a typical experiment

To sum up, a representative experiment proceeds as follows.

- The tank is fixed to the apparatus frame and then filled with Canadou.
- A 2 mL dye blob is injected by the syringe pump just under the fluid's free surface.
- We start the rod's periodic motion together with the pictures acquisition.

Typical experiments are conducted for about $25 - 35$ periods of the stirring protocol. Weak 3-D effects in weakly stretched regions, that is close to the boundary or in non-chaotic regions, prevented us from following the mixing pattern for longer times (see Fig. 2.9). These three-dimensional effects might be due to small thermal or solutal convection movements.

2.2.2 An open-flow mixing experiment

We have built an open-flow channel, where chaotic stirring is confined in a small region of the channel. We consider here open flows stationary at infinity, where mixing is restricted to a single region of the flow, contrary to other open-flow mixing devices where fluid flows through *successive* mixing elements, as in serpentine channels [19, 62], grooved micromixers [105], or 3-D Kenics-like or partioned-pipe mixers [126]. In the latter case, fluid particles are stretched along different directions in successive mixing elements, and mixing is a multiplicative process, which is not the case in our open-flow experiments.

We describe the experimental setup below.

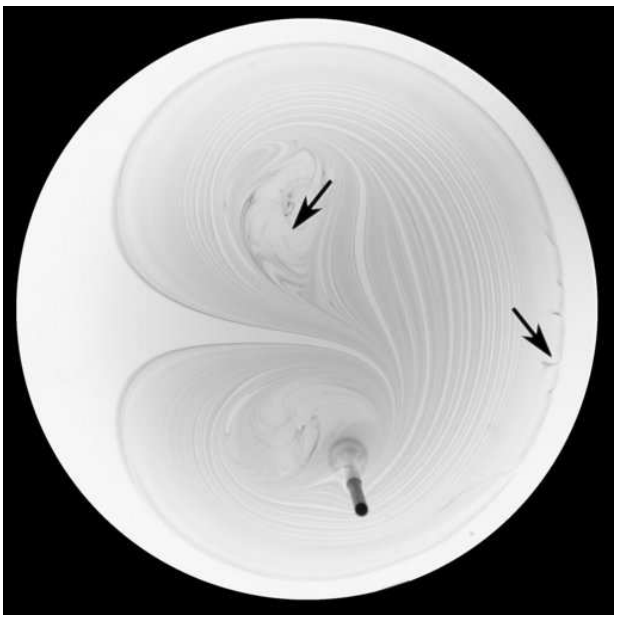

Figure 2.9: 3-D effects – In weakly stretched regions, such as the no-slip boundary or non-chaotic regions, small convection movements induce three-D effects that start spoiling the mixing pattern after about 30 periods of the stirring pattern. This is especially marked for particles close to the boundary, which are slowly advected to other parts of the domain (because of the chaotic nature of their trajectory) and contaminate the whole pattern.

Stirring device

The viscous fluid is again Canadou (see the previous section for details about this fluid). Canadou flows through a long glass channel of 2 m length (x direction), 36 cm width (y direction), and 10 cm height (z direction). Canadou fills the channel to a 5 cm height. The mixing region is situated at channel mid-length, where two rods stir fluid with the egg-beater protocol (Fig. 2.3(b)). To do so, two YAKSAWA SGDH Servo motors are fixed vertically above Canadou to a rail perpendicular to the channel direction (see Fig. 2.11). On each motor shaft, a perpendicular arm allows the rotation of a 45 mm diameter (d) nylon rod on a 140 mm diameter (D) circular path. The distance between the two motors axis is 105 mm so that the two rod paths intersect. The two rods travel at the same speed, but in opposite directions on the two circles. The motors are controlled in speed with a home-made software written by Cécile Gasquet. We have explored angular velocities Ω ranging from 1 to 8 rpm, hence Reynolds numbers $Re = 2\pi\Omega dD/\nu$ range from 2.6 to 21 . For greater velocities, surface waves start to appear.

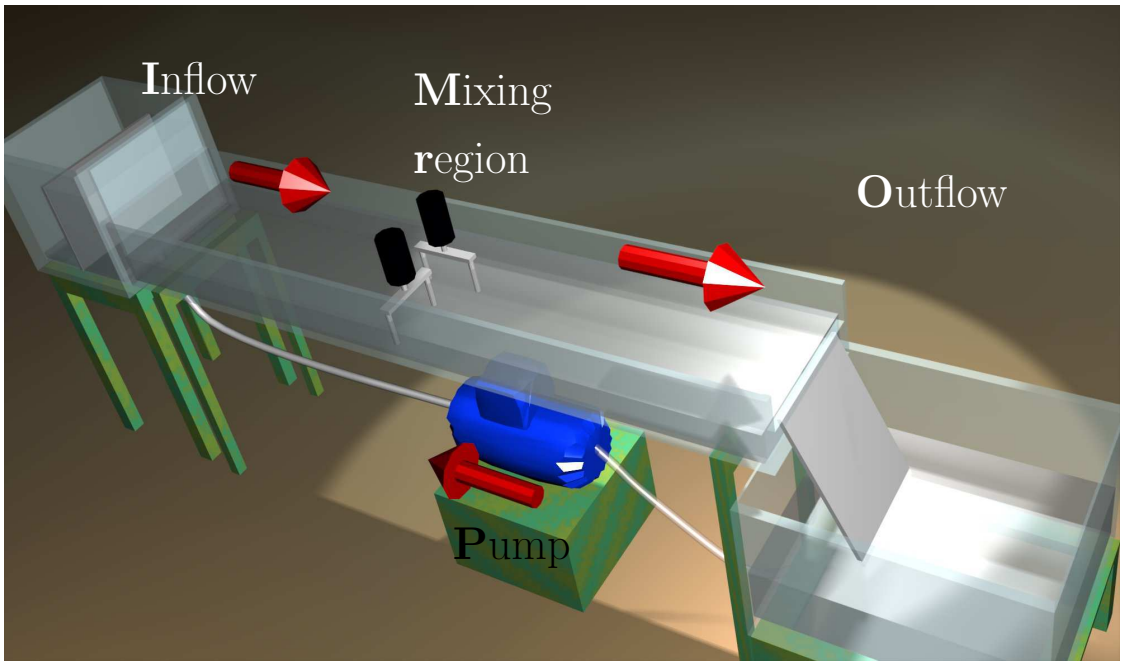

Figure 2.10: Open-flow channel experiment – Viscous fluid (Canadou) is pumped at constant rate into a long shallow channel (2 m long, 36 cm wide and 5 cm deep). Fluid flows through a mixing region where rods stir fluid in an egg-beater-like fashion. Typical experiments consist in injecting a small blob of dye upstream of the mixing region, and visualizing the mixing pattern that is created by the stirrers inside the mixing region and downstream (see Fig. 1.4). A CCD camera (not shown) records the mixing pattern through the transparent bottom of the channel. The lighting device (not represented) consists in a large light table (see Fig. 2.11).

Channel flow

Main flow (far upstream and downstream) - Canadou flows down the channel from an inflow tank (see Fig. 2.10), and flows over the 5 cm-high end of the channel into a large outflow tank that can contain all the Canadou necessary for an experiment (30 L). The glass channel and inflow tank are glued on a 1-m-high thin metallic frame, while the outflow tank lies on a lower frame (Fig. 2.10). A POLLARD pump designed for very viscous fluids closes the Canadou loop by pumping fluid from the outflow tank to the inflow tank. At such a low flowrate, no oscillations due to the pump are visible inside the inflow tank. The flowrate in the channel is therefore

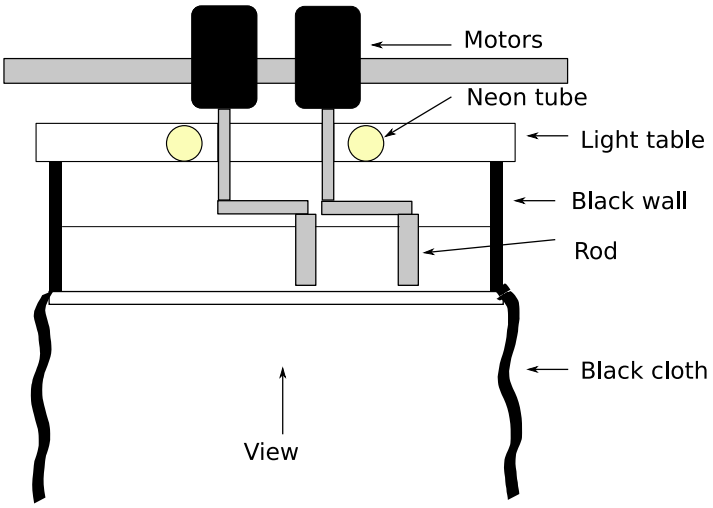

Figure 2.11: Cross-section view of the channel: schematic drawing of the stirring and lighting apparatus.

controlled by the pumping rate, which is fixed at $Q = 1\,\mathrm{L}\cdot\mathrm{min}^{-1}$ in all experiments described here. The mean velocity in the channel (averaged on a channel cross-section) is then $U = Q/hl \simeq 1\,\mathrm{mm}\cdot\mathrm{s}^{-1}$. Analytical calculations as well as numerical simulations (not included here) achieved by Franck Pigeonneau at Saint-Gobain Recherche showed that for a shallow channel, as it is the case in our device, the flow profile at the free surface ($U(y, z = h)$ is much flatter than a Poiseuille flow because of bottom effects: in a large central fraction of the channel, $U(y, z = h)$ is well approximated by a plug flow. On both sides, a boundary layer where the velocity decreases fast with the distance to the wall matches the no-slip boundary conditions on solid walls. In the absence of stirrers, we can consider that the low-Reynolds-number flow is stationary, and $x-$invariant in a region $\lambda < x < L - \lambda$, with $\lambda \sim Uh^2/\nu \sim 1\,\mathrm{cm}$ – that is along almost the whole channel length. [3]

Flow in the mixing region - The stirring motion perturbs the upstream stationary and $x-$invariant velocity field. Stirrers indeed force fluid to flow preferentially through some parts of a cross-section. As can be seen in Fig. 2.12, we can distinguish two cases depending on the rod rota-

[3] λ is the length travelled during the viscous time-scale h^2/ν by a particle of velocity U.

tion sense with respect to main flow direction. If the rods travel "with the flow" near the channel sides, and "against the flow" in the channel central region, upstream fluid reaches the downstream region by flowing preferentially along the channel sides (Fig. 2.12 (c)). Fluid can only enter the mixing region (say, the area swept by the rods) close to the intersection point of the upper rods' paths. Because of mass conservation, fluid conversely leaves the region through this point, thus forming the flower-shaped downstream pattern in Fig. 2.12 (a). However, if rods move against the flow on the sides, and with the flow in the center (Fig. 2.12 (d)), fluid flows preferentially through a funnel-shaped channel, whose width shrinks as fluid enters the mixing region (fluid is then accelerated), and widens again as fluid leaves region, since the rods move towards the side walls in the upper part of the mixing region. This results in the elongated downstream structures, and the funnel-shaped lower cusp in the mixing region visible in Fig. 2.12 (b). In an analogy between swimming styles and rods movements, we will from now on refer to the first case (Fig. 2.12 (a) and (c)) as the **butterfly** (BF) protocol, and to the second case (Fig. 2.12 (b) and (d)) as the **breaststroke** (BS) protocol. We can already see that mixing patterns are very different for the butterfly and breaststroke protocols.

Dye injection

We use the same 2% by volume Indian ink Canadou solution as in the closed-flow experiment. In a preparatory version of the experiment, we injected continuously (with a syringe pump) a dye streakline from a central injection upstream point. A resulting picture can be seen on Fig. 2.14. This kind of experiment models for instance the mixing of different fluids that are continuously fed in an open-flow mixer, a standard situation e.g. in food processing. However, we have mostly concentrated on decay experiments that consist in injecting an upstream dye blob, which is advected by the flow into the mixing region, and then into the downstream region (see Fig. 1.4 where a few steps of this process are represented). This case corresponds to a localized inhomogeneity. As we will describe later in the experimental analysis, a continuous line can be modeled by a successive chain of adjoining blobs. The analysis of the "blob case" will therefore also yield information about the "streakline case". As the dye blob is advected, some part is caught inside the mixing region by the rod's movement. However, mass conservation imposes that fluid also leaks continuously from the mixing region, so that less and less dye can be seen in the mixing region and the near downstream. This decay of dye intensity fixes the duration of an experiment: we stop the picture acquisition when the contrast starts being

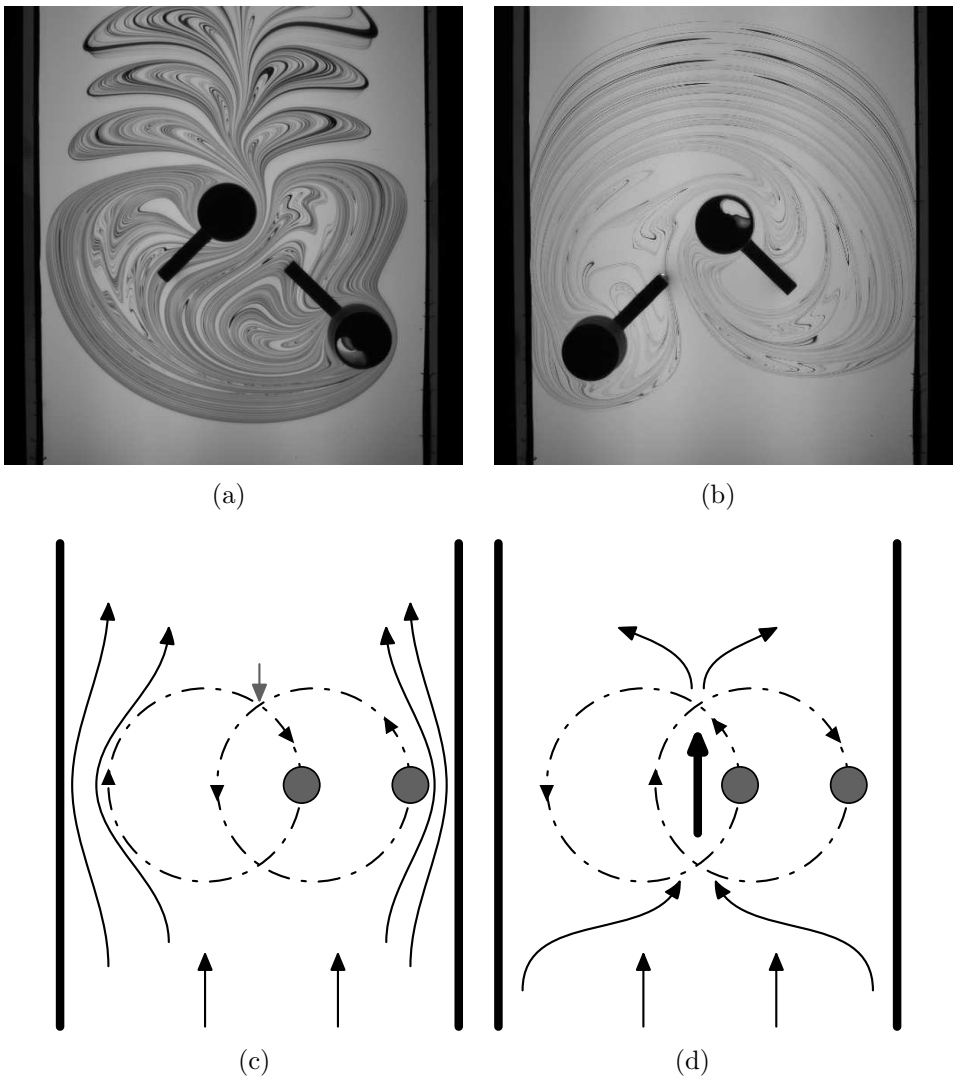

Figure 2.12: Butterfly ((a) and (c)) and breaststroke ((b) and (d)) protocols. Depending on the rod motion orientation with respect to the main flow direction, fluid chooses very different routes to cross the mixing region. If the rods travel against the flow in the center and with the flow on the channel sides, fluid flows preferentially along the sides (c). Conversely, the other orientation forces fluid to flow preferentially through a central funnel (d). Note that the resulting downstream mixing patterns are very different ((a) and (b)).

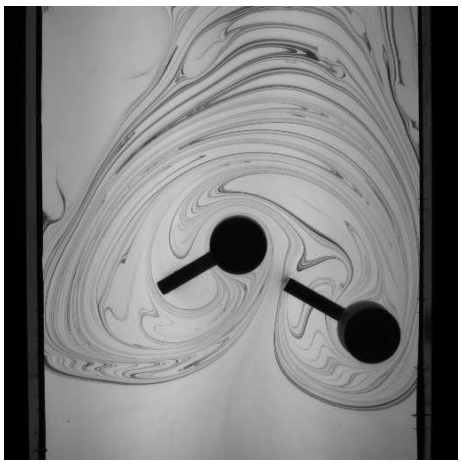

Figure 2.13: The explosion of a high-concentration downstream part of the dye blob perturbs the whole mixing pattern.

too weak.

We use new unspoiled Canadou for each experiment, and discard partly dyed fluid. Each experiment requires about 30 L of Canadou, which explains why we chose a cheap, water-based viscous fluid instead of more classical viscous fluids such as glycerol or silicone oil.

Surface tension effects responsible for frequent "explosions" of the dye blob are even more problematic than for the closed-flow experiment (see the previous section for a description), as there is a long (~ 3 min) period during which the blob travels the distance (~ 20 cm) between its injection point and the entrance of the mixing region, where it is caught and stretched by the rods. During this initial stage, the high-concentration dye blob explodes (i.e. spreads very rapidly over the surface) whenever a surface perturbation occurs, such as the blowing up of a tiny air bubble or the landing of a dust grain on the free surface. As soon as blob parts are stretched by the rods, diffusion causes the concentration levels to decay, and therefore dye to be more and more diluted, so that explosions are much less frequent. However, contrary to the closed-flow experiment, some parts of the initial blob can escape downstream almost untouched (the black stripes in Fig. 1.4 (b)) and keep a high concentration during all the duration of the experiment: they might therefore explode at any time, and perturb the whole concentration pattern, even in the mixing region (see Fig. 2.13).

To limit this effect, we use a highly diluted ink solution. This has the disadvantage of reducing the experiment duration. The pump flowrate is also fixed to a low enough value to remove cavitation bubbles. Also, Canadou slides from the channel exit inside the outflow tank on a gentle slope so that it forms a continuous film, instead of a jet that might imprison air bubbles in outflowing Canadou. An early attempt to depose a tiny

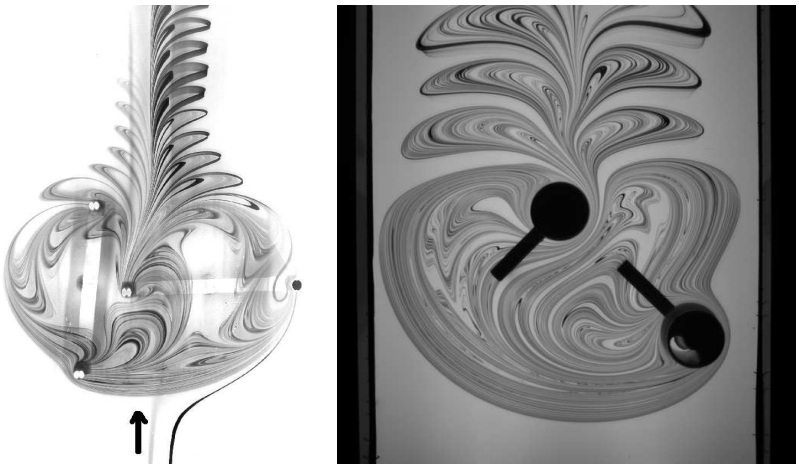

(a) (b)

Figure 2.14: Continuous dye feeding vs. decay experiment.

drop of surfactant (liquid commercial soap) on the fluid surface reduced the explosions, yet we abandoned this method after noticing that the surfactant perturbed the surface flow.

Lighting and data acquisition

As in our closed-flow experiment (see the previous section), we aim at measuring precisely the dye concentration field. As we saw, this requires an adapted backlighting and a precise calibration of the camera response to dye. Our lighting apparatus is slightly more sophisticated than for the closed-flow experiment: we use a JUST NORMLICHT photographic light table (originally designed for viewing photographic proofs) with a $35 \times 51\,\mathrm{cm}^2$ lighted area. The light table is clipped upside-down to the channel side walls and lights the Canadou directly (see Fig. 2.11). Two holes are drilled through the light table to allow the motors axis through. This configuration allows a large workable area in the pictures, as only the rods and the arms linking them to the axis are visible (see Fig. 2.12). In the same spirit as the closed-flow experiment, channel side walls are coated with matted black film, and large black cloth panels fall from the channel to the ground, thereby wrapping the camera in a dark room. For convenience, the camera is fixed to a horizontal NEWPORT MICROCONTROL optical rail and views the image of the channel reflected by a 45° mirror. The visible field can be seen on Fig. 2.12: we select a region of interest that encompasses completely the area swept by the rods – the mixing region – as well as a large

downstream strip and a smaller upstream region. This permits us to view both the arrival of the still untouched dye blob from upstream (Fig. 1.4), as well as the downstream mixed pattern, which is the final product we wish to characterize. It is also crucial to visualize what happens in the mixing region in order to understand which mechanisms give birth to the downstream mixed pattern.

We use a 12-bit 2048×2048 monochrome REDLAKE MegaPlus II ES4020 camera to acquire pictures at a 0.5 Hz rate. To do so, the camera is triggered by a signal generator in TTL mode. The acquisition time is fixed at 40 ms, that is, two full 50 Hz periods, to avoid mean lighting variations between two pictures. Camera pictures are transferred on the fly to a computer and saved in 16-bit PNG (Portable Network Graphics) format, using a LABVIEW interface.

Data processing

As for the figure-eight experiment, all data processing is realized using PYTHON scripting and programming language.

We calibrated the camera response to dye concentration using the same technique as in the figure-eight experiment, by measuring the light intensity attenuation due to samples of known concentration value. Results are shown on Fig. 2.15: we observe the same Beer-Lambert behavior for weak concentrations as for the CANON camera, as well as a saturation for higher concentration values. We therefore have an unambiguous relation between C and I/I_0 that is successfully fitted by the same law expression as for the CANON camera (see Fig. 2.15) :

$$\log(I/I_0) = \alpha \tanh\left(\frac{C}{\beta}\right), \quad \text{with } \alpha = 17.09, \quad \beta = 0.239. \tag{2.2}$$

2.3 Numerical simulations of Stokes flows

Whereas we have access to concentration field measurements through our dye mixing experiments, numerical simulations can provide complementary information. The usual Lagrangian description of chaotic advection (Sec. 1.2.3) calls naturally for following fluid particles trajectories, which is more easily realized in numerical simulations than in experiments.

The basic principle of all computations conducted here is given by the integration of a pointlike particle trajectory in a prescribed flow: $\dot{\mathbf{x}}(t) = \mathbf{v}_{\text{fluid}}(\mathbf{x}, t)$. This requires to have the expression of the velocity field $\mathbf{v}_{\text{fluid}}(\mathbf{x}, t)$

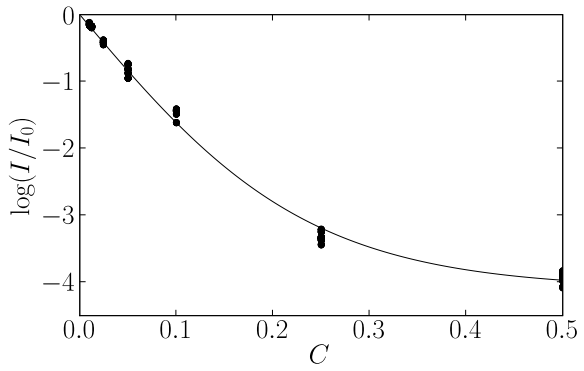

Figure 2.15: Redlake camera response to the light fraction transmitted through dye (I/I_0), vs. dye concentration. Data points are fitted by a $\log(I/I_0) = \alpha \tanh(C/\beta)$ law ($\alpha = 17.09$, $\beta = 0.239$), which amounts to the Beer-Lambert law for low concentrations.

at hand, which is given by the Navier-Stokes equations :

$$\frac{\partial \mathbf{v}}{\partial t} + \mathbf{v} \cdot \nabla \mathbf{v} = -\frac{1}{\rho} \nabla p + \nu \Delta \mathbf{v}, \quad \nabla \cdot \mathbf{v} = 0. \tag{2.3}$$

Suitable boundary conditions (imposed by moving rods or no-slip boundaries, etc.) must be used in the resolution of Eq. (2.3). For vanishingly small Reynolds numbers, that is in the Stokes flow regime, the inertia forces can be assumed to be negligible compared to viscous forces in Eq. (2.3), which simplifies to:

$$-\nabla p + \mu \Delta \mathbf{v} = 0, \quad \nabla \cdot \mathbf{v} = 0, \tag{2.4}$$

usually referred to as *Stokes equations*. Stokes flow is a considerable simplification of Navier-Stokes equations, with many remarkable properties. First, a Stokes flow has **no time-dependency** other than prescribed by time-dependent boundary conditions (e.g. moving rods or boundaries). This means that a Stokes flow is entirely determined by the motion of boundaries and can be found at any instant without knowledge of the flow at any other time: in a Stokes flow, time is only a parameter. Stokes flow is also **time-reversible**. Moreover, Stokes equation is **linear**, which allows for superposition of solutions, a useful principle while searching for the flow expression.

Flow expressions in 2D domains can be searched for using *streamfunctions methods*. It can indeed be shown that the streamfunction Ψ for a Stokes flow satisfies the biharmonic equation [71]

$$\nabla^4 \Psi = 0. \tag{2.5}$$

The challenge is then to find a suitable streamfunction satisfying both Eq. (2.5) as well as no-slip on the – fixed or moving – boundaries. This is usually

done by decomposing different elements inside the fluid domain (such as fixed or moving rods) in Stokes flow singularities such as *stokeslets* or *rotlets* [91, 40], together with an images system that satisfies the no-slip condition on the outer domain. However, such subtle methods require special care and closed-form expressions are not always available. In a circular domain, the flow due to an rotating inner cylinder was first obtained by [51]. The case of a translating cylinder was only derived recently by Finn and Cox [40]. The same authors extended their work to the case of an arbitrary number of moving rods in [38]. For more than one rod there is no closed expression for the Stokes flow: it is nevertheless possible to write the flow as a rapidly converging series with unknown coefficients, which are determined with a least-squares method on the boundaries [38]. We will make extensive use of the corresponding velocity fields for simulating rods-driven protocols. For open flows, the situation is unfortunately more complicated, as boundary conditions must be satisfied on *both* sides of the channel. We have therefore been unable to conduct numerical simulations for open flows.

Lagrangian trajectories are obtained by integrating the previously determined Stokes flow with a fourth-order Runge-Kutta scheme in a C++ implementation. Many routines used here have been written by Matt Finn and Jean-Luc Thiffeault; others were developed during this thesis for implementing specific stirring protocols.

Many useful information can be gained from integrating Lagrangian trajectories. Poincaré sections e.g. can be determined by integrating a small number of initial conditions during a large number of periods. A coarse-grained concentration field can also be studied by integrating a large number of trajectories initialized inside a small area – a dye blob – and dividing the fluid domain in boxes, which contain variable numbers of points. Interfaces lengths can also be obtained by points-insertion algorithms.

2.4 Conclusion

In this Chapter, we have presented the various apparatus that we have used. We have built two experiments aiming at recording the concentration field of a low-diffusivity, in a circular closed tank and in an open-flow channel. Chaotic advection is realized in these mixers by the motion of stirring rods. We have also described numerical simulations that will allow us to follow the motion of Lagrangian point-like particles.

The next chapter is concerned with the study of chaotic mixing from a dynamical systems and topological point of view. Starting from the basis of chaotic advection [8], that is stretching and folding, we will propose an

alternative view of mixing that relies on the topological complexity of the flow.

Chapter 3

Mixing structures from a topological and dynamical systems viewpoint

Classical tools of dynamical systems theory help to provide considerable insight into the mechanisms of mixing, as well as useful hints for a relevant characterization of the mixed state. We have already introduced *Poincaré sections* that characterize flows in a crude binarized way, by evidencing chaotic and regular regions. More refined characterizations, as well as hints of mixing mechanisms, are of course desirable. This chapter starts by a review of some useful concepts of dynamical systems, exemplified in our experiments and applied in simple maps for clarity. An original topological characterization of stretching through the entanglement of periodic points trajectories is then presented, together with implications for a simple description of the global mixing pattern. Periodic points are also highly relevant for describing mixing in open flows: we explain in the last section of this chapter how a set of bounded periodic orbits, also called *chaotic saddle*, and its manifolds, determine the mixing pattern and the residence time distribution inside our channel mixer.

3.1 Dynamical systems concepts in mixing

3.1.1 Stretching

It is now commonplace to say that chaotic mixing is a combination of exponential stretching and diffusion. In this paragraph, we describe the stretching route for typical fluid particles in a 2-D incompressible velocity field $\mathbf{v}$.

Let us consider a Lagrangian trajectory $\mathbf{x}(t)$ determined by $\mathbf{v}$. An infinitesimal vector $d\mathbf{x}(t)$ pointing from $\mathbf{x}$ evolves as

$$d\mathbf{x}(t) = \mathbf{F}(t) \cdot d\mathbf{X} \tag{3.1}$$

where $d\mathbf{X} = d\mathbf{x}(t=0)$ is the initial vector and $\mathbf{F}(t)$ is the deformation tensor. $\mathbf{F}$ can be computed from the velocity field and the integrated trajectory $\mathbf{x}(t)$ as

$$\frac{d\mathbf{F}}{dt} = \Big(\nabla \mathbf{v}(\mathbf{x}(t))\Big)^T \cdot \mathbf{F}\,; \quad \mathbf{F}(t=0) = \mathbf{I} \tag{3.2}$$

where $\mathbf{I}$ is the identity tensor. Although no analytical expression is usually available for the deformation tensor $\mathbf{F}$, Eqs. (3.1) and (3.2) can be directly integrated in numerical simulations to compute the stretching factor

$$\lambda(t;0) = \frac{||d\mathbf{x}(t)||}{||d\mathbf{X}||}, \tag{3.3}$$

that is the length stretch magnitude for the fluid particle $\mathbf{X}$ during time t. Stretching is a multiplicative process, as one can decompose the deformation in n successive steps between intermediate times t_i:

$$\lambda(t;0) = \lambda(t=t_n;t_{n-1}) \cdots \lambda(t_{i+1};t_i) \cdots \lambda(t_1;t_0=0). \tag{3.4}$$

If one considers a long time interval t, a typical chaotic trajectory visits different phase space regions and experiences different successive intensities $\lambda(t_{i+1};t_i)$. For a time-periodic flow, a classical formulation consists in choosing a stirring period T for the elementary timestep $t_{i+1} - t_i = T$. The particle $\mathbf{x}$ then samples different stretching values λ of the first-return map defined by

$$\mathcal{M} : \mathbf{x}(t) \rightarrow \mathbf{x}(t+T). \tag{3.5}$$

If we further assume that successive stretching values $\lambda_i = \lambda(t_{i+1} = t_i + T; t_i)$ are statistically independent, $\log(\lambda(t=nT)) = \sum_i \log(\lambda_i)$ is obtained from the addition of independent variables. We conclude that $\log(\lambda)/t$ converges to a single value for all chaotic trajectories, called the *Lyapunov exponent* $\bar{\Lambda}$ of the region visited by the particle [78]:

$$\bar{\Lambda} = \lim_{t \rightarrow +\infty} \frac{1}{t} \log(\lambda(t)). \tag{3.6}$$

This definition also holds for a non-periodic flow, if the limit exists. The Lyapunov exponent is simply the mean rate of stretching of a fluid particle. It is characteristic of a single phase space region (e.g. an ergodic component). Note that the above definition Eq. (3.6) also encompasses the case

of an elliptical island (a non-chaotic region), where stretching is at most algebraic, therefore $\bar{\Lambda} = 0$.

Another quantity of interest is the material line growth rate, also called *topological entropy* h: if we parametrize an initially small material line by n equally spaced points x_i ($||x_{i+1}(0) - x_i(0)|| = l_0$), the line length grows as

$$l(t) = \sum_{i=0}^{n-1} ||x_{i+1}(t) - x_i(t)|| = \sum_{i=0}^{n-1} l_0 \lambda_i(t) \tag{3.7}$$

so that for large t,

$$\frac{l(t)}{l(0)} \sim \exp(\log(\overline{\lambda(t)})) \sim \exp(ht), \tag{3.8}$$

with

$$h \equiv \lim_{+\infty} \frac{1}{t} \log \overline{\lambda(t)}. \tag{3.9}$$

h is therefore the exponential growth rate of the *arithmetic* mean stretching, whereas $\overline{\Lambda}$ represents the growth rate of the *geometric* mean stretching. This implies

$$\overline{\Lambda} \leq h. \tag{3.10}$$

Moreover, by virtue of large-deviation theory [32], the additivity of $\log(\lambda(t = nT)) = \sum_i \log(\lambda_i)$ allows us to write the probability distribution function of $\Lambda = \log(\lambda)/t$, also called *finite-time Lyapunov exponent* , as

$$P(\Lambda, t) = \sqrt{\frac{tS''(0)}{2\pi}} \mathrm{e}^{-t\mathcal{S}(\Lambda - \bar{\Lambda})} \tag{3.11}$$

where $\mathcal{S}$ is known as the *Cramer* or *large-deviation* function and has a global maximum at $\Lambda = \bar{\Lambda}$. This implies in particular that the distribution $P(\Lambda, t)$ is Gaussian in a vicinity of $\bar{\Lambda}$ for large t under the general assumptions of the central limit theorem.

In the remainder of this paragraph, we briefly illustrate these concepts by use of one of the paradigms of chaotic mixing, that is the area-preserving *baker's map*. Unlike time-continuous flows, the baker's map is a time-discrete map that transforms the unit square by

1. cutting it in two horizontal parts of heights γ and $1 - \gamma$, where $0 < \gamma < 1$,

2. stretching the two pieces with respective strains $1/\gamma$ and $1/(1-\gamma)$ to a unit height,

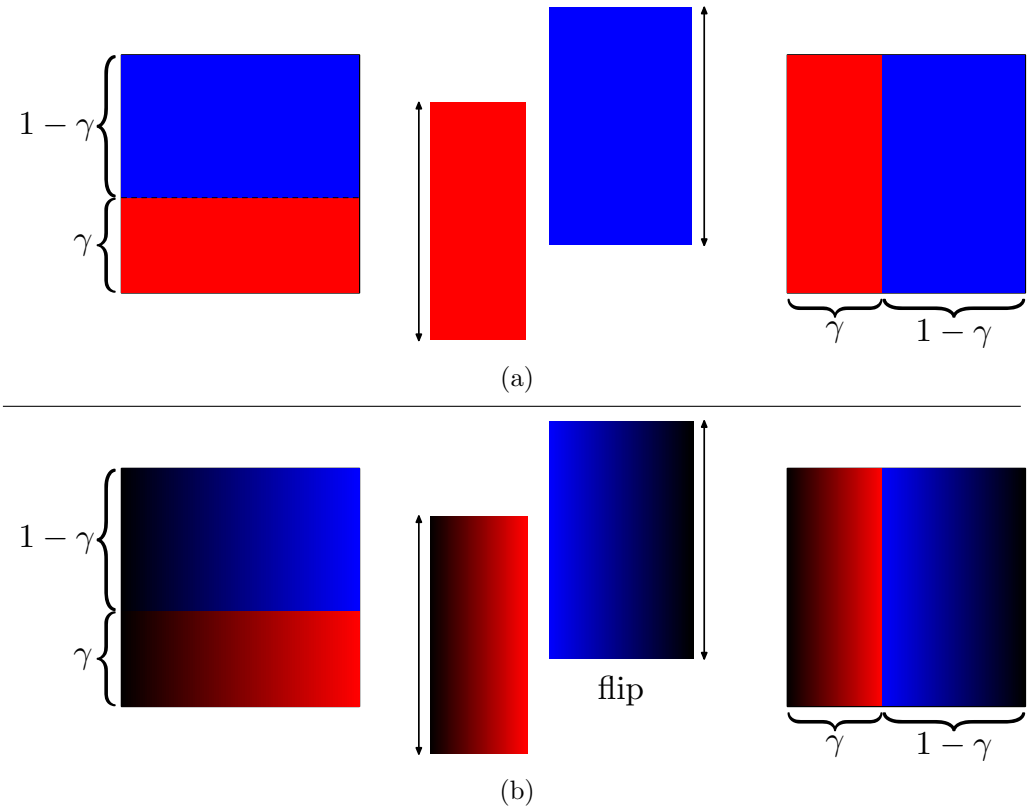

Figure 3.1: (a) Principle of the area-preserving inhomogeneous baker's map: "cut, stretch and stack". A square domain is cut in two unequal horizontal parts of (resp.) height γ and $1-\gamma$, which are then stretched along the vertical direction by (resp.) $1/\gamma$ and $1/(1-\gamma)$. The two elongated pieces are finally stacked together in the original square. (b) Flipped variant. The flip is evidenced by the x-dependent shading of the two parts.

3. and finally stacking together the two unit pieces in the original unit square.

The map is therefore written:

$$\begin{pmatrix} x_n \\ y_n \end{pmatrix} \to \begin{cases} \begin{pmatrix} \gamma x_n \\ 1/\gamma \times y_n \end{pmatrix}, & y_n \in [0,\gamma] \\ \begin{pmatrix} \gamma + (1-\gamma)x_n \\ 1/(1-\gamma) \times (y_n - \gamma) \end{pmatrix}, & y_n \in [\gamma, 1], \end{cases} \tag{3.12}$$

for a point (x_n, y_n). Despite its simplicity, this map is a useful model for stretching created by a 2-D physical flow, e.g. by a moving rod that stretches

fluid inhomogeneously. The main difference is that stretched filaments are necessarily folded to fit into the finite mixing domain, whereas we simply cut and stack them again in the discontinuous map. Throughout this manuscript, we will make extensive use of this map and several variants for illustrative purpose.

The stretching distribution is trivially computed in this simple map. A fraction γ of particles experiences a stretching $1/\gamma$, whereas the remaining $1-\gamma$ fraction is stretched by a factor $1/(1-\gamma)$. This yields immediately the Lyapunov exponent

$$\bar{\Lambda} = \overline{\log(\lambda)} = -[\gamma \log(\gamma) + (1-\gamma)\log(1-\gamma)]. \tag{3.13}$$

In the same way, the stretching distribution is derived easily by noticing that after n iterations of the map, a fluid particle has experienced a stretching $\gamma^{-k}(1-\gamma)^{k-n}$ with probability $\mathrm{C}_n^k/2^n$, $0 \leq k \leq n$. The topological entropy is given by

$$h = \log(\overline{\lambda}) = \log(\gamma \times 1/\gamma + (1-\gamma) \times 1/(1-\gamma)) = \log(2) \tag{3.14}$$

Each iteration of the map indeed transforms a vertical material line into two images of same length as the original line, hence the total length doubles at each step.

3.1.2 Periodic points

Periodic orbits of the first-return map of a stirring flow are highly pathological objects: whereas typical chaotic trajectories visit the whole chaotic region and experience different successive stretching factors, a periodic orbit is confined to a measure-zero set and does not sample the whole stretching distribution of the chaotic region. Consider for examples the two period-1 points of the Baker's map, that is $x_0 = (0,0)$ and $x_1 = (1,1)$ (the bottom-left corner of the red rectangle and the top-right corner of the blue rectangle in Fig. 3.1). A particle initialized at $x = x_0$ always stays at the same place, hence always sees the same stretching rate γ, whereas particles initialized at non-periodic points visit alternately regions of stretching γ and $1-\gamma$, so that their stretching rate converges to the Lyapunov exponent .

Nevertheless, periodic orbits are the only simple trajectories that can be characterized by a finite number of values, e.g. n successive positions for a period-n orbit. Chaotic orbits on the contrary can only be characterized by asymptotic values such as the Lyapunov exponent, or through a statistical description, such as the finite-time Lyapunov exponent distribution (Eq. (3.11)). Periodic orbits are therefore convenient tools for a finite-time

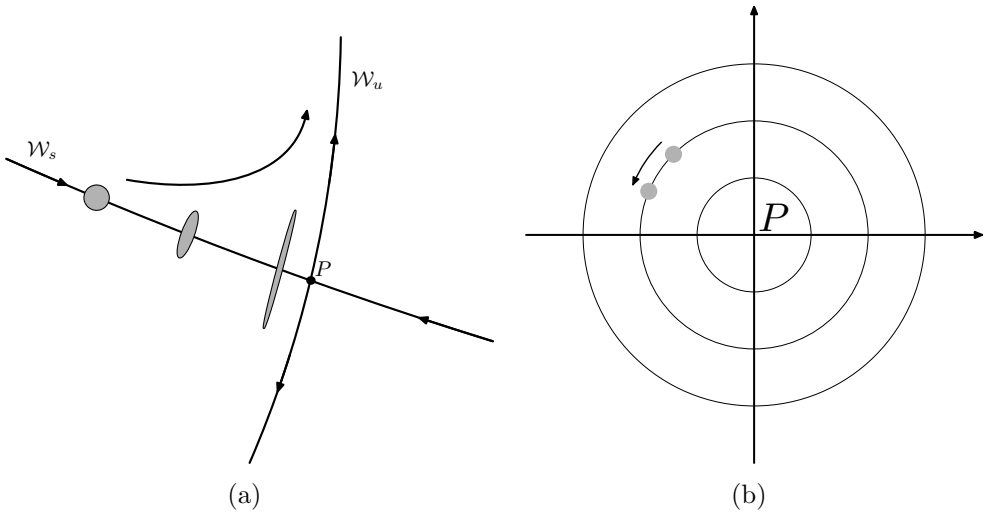

Figure 3.2: (a) Hyperbolic (unstable) point (b) Elliptical (stable) point.

description of a flow [13, 27]. There are three different kinds of periodic orbits, depending on the flow structure around the periodic point: hyperbolic, elliptic, and parabolic points. The nature of the periodic point P can be determined by linearizing the first-return (or $n-$return for an $n-$periodic point) map around this point, which transforms a point (x_n, y_n) in the vicinity of P to

$$\begin{pmatrix} x_{n+1} \\ y_{n+1} \end{pmatrix} = \mathcal{M} \begin{pmatrix} x_n \\ y_n \end{pmatrix}, \tag{3.15}$$

where $\mathcal{M}$ is a 2×2 matrix of unit determinant because of area preservation. The eigenvalues of $\mathcal{M}$ are obtained by solving

$$X^2 - \mathrm{Tr}(\mathcal{M})X + 1 = 0, \tag{3.16}$$

where $\mathrm{Tr}(\mathcal{M})$ is the trace of $\mathcal{M}$.

Three cases arise:

- If $\mathrm{Tr}(\mathcal{M}) > 2$, $\mathcal{M}$ has two positive eigenvalues λ and $1/\lambda$, and is diagonal in appropriate coordinates $(\tilde{x}, \tilde{y})$:

$$\begin{pmatrix} \tilde{x}_{n+1} \\ \tilde{y}_{n+1} \end{pmatrix} = \begin{pmatrix} 1/\lambda & 0 \\ 0 & \lambda \end{pmatrix} \begin{pmatrix} \tilde{x}_n \\ \tilde{y}_n \end{pmatrix}. \tag{3.17}$$

  An infinitesimal volume is compressed along the $\tilde{x}$ direction, and stretched along the $\tilde{y}$ direction at rate λ, as represented in Fig. 3.2. The periodic point P is called *hyperbolic* in this case. All periodic points of the Baker's map belong to this class.

- If $\mathrm{Tr}(\mathcal{M}) < 2$, $\mathcal{M}$ has two conjugate complex eigenvalues. In suitable coordinates:

$$\begin{pmatrix} \tilde{x}_{n+1} \\ \tilde{y}_{n+1} \end{pmatrix} = \begin{pmatrix} \mathrm{e}^{i\theta} & 0 \\ 0 & \mathrm{e}^{-i\theta} \end{pmatrix} \begin{pmatrix} \tilde{x}_n \\ \tilde{y}_n \end{pmatrix}, \tag{3.18}$$

  so that fluid elements loop around P without being stretched. P is therefore a stable point and is called *elliptic*. Periodic elliptic points can be found in the center of elliptic islands (two islands are visible in Fig. 1.7).

- If $\mathrm{Tr}(\mathcal{M}) = 2$, $\mathcal{M}$ is either the identity, or has doubly-degenerate eigenvalue 1 and can be written in the Jordan canonical form

$$\mathcal{M} = \begin{pmatrix} 1 & \alpha \\ 0 & 1 \end{pmatrix}. \tag{3.19}$$

  In both cases, the linearization is not sufficient to determine the flow structure near P, and non-linear terms must be taken into account. Points belonging to this marginal case are called *parabolic*.

3.2 A topological characterization of mixing in closed flows

We have seen that periodic points are good candidates for characterizing mixing with few quantities. In particular, we show in the following section that the topological study of periodic orbits in closed flows is well suited to describe the complexity of a 2-D flow.

3.2.1 The development of topological mixing

The early 2000's have seen the dawn of a new topological approach to mixing [18] that relies on powerful tools from the study of surface diffeomorphisms to describe 2-D stirring protocols. The founding work on topological mixing is presented in a 2000 paper by Boyland, Aref and Stremler, where the authors analyze elegant rod-stirring experiments in light of topological constraints induced by the rods movements. Two different time-periodic protocols with three stirring rods were used (Fig. 3.3). In both cases, the stirring period starts by exchanging the two leftmost rods during a first half-period, by moving them clockwise on semi-circles centered halfway between them. The difference between the two protocols comes in during the

second half-period: in the first protocol, the two rightmost rods are also exchanged clockwise; in the second protocol however, rods are exchanged in an *anti-clockwise* fashion. The total length traveled by rods is the same in both cases, which might seem very similar. Nevertheless, obvious discrepancies are visible in simple dye mixing experiments performed by Boyland et al. [18] (Fig. 3.3). After nine iterations of the stirring protocol, dye streaks initially attached to the wall and the three rods have experienced little stretching in the first case (Fig. 3.3 (d)) and seem to have mostly wound up around a core region where the rods move. Because of this poor stretching, diffusion has not yet blurred dye filaments, so that black and white strips retain a high contrast. On the contrary, the second protocol leads to very efficient mixing after the same number of stirring periods, as can be seen in Fig. 3.3 (e) where a large gray kidney-shaped central region is very well homogenized.

One may therefore ask what difference between these two protocols causes this striking dissimilarity. A first answer is obtained by plotting the rods' trajectories in a space-time diagram, as in Fig. 3.4. The trajectory of a material point forms a *strand*, and strands corresponding to different rods can braid together, leading to a more or less tangled weaving. This is precisely where the difference between the two protocols appears: the first protocol creates a *topologically trivial* braid with the three strands, which are simply twisted together in a global rotation by the rods' movement. This braid can be completely untangled by rotating its extremities and exhibits little complexity. The braid corresponding to the second protocol (Fig. 3.4), on the other hand, cannot be untangled by just fiddling with its extremities, and is therefore topologically complex. A closer look reveals that this braid is in fact quite familiar: it consists in crossing two adjacent strands clockwise, then crossing the two other anticlockwise – this is just the pigtail braid commonly used in hairdressing. The construction of such a braid is shown in Fig. 3.5, which roughly mimics the trajectories of stirring rods.

But how are these braids related to mixing ? Imagine a material line initially attached to two adjacent rods like the pink line in Fig. 3.4. As the rods move and braid together, the line gets also caught by the third rod but stays attached to the two other due to continuity. Our line must then follow the tangling of the three rods, so that after one stirring period, its length is much greater (Fig. 3.4). Furthermore, this stretching will take place again at the next period for each new line element extending between two rods: this stretching process is multiplicative, therefore we expect the line growth to be exponential with time. For the first protocol, though, a line that initially links two rods is not necessarily even caught by the third

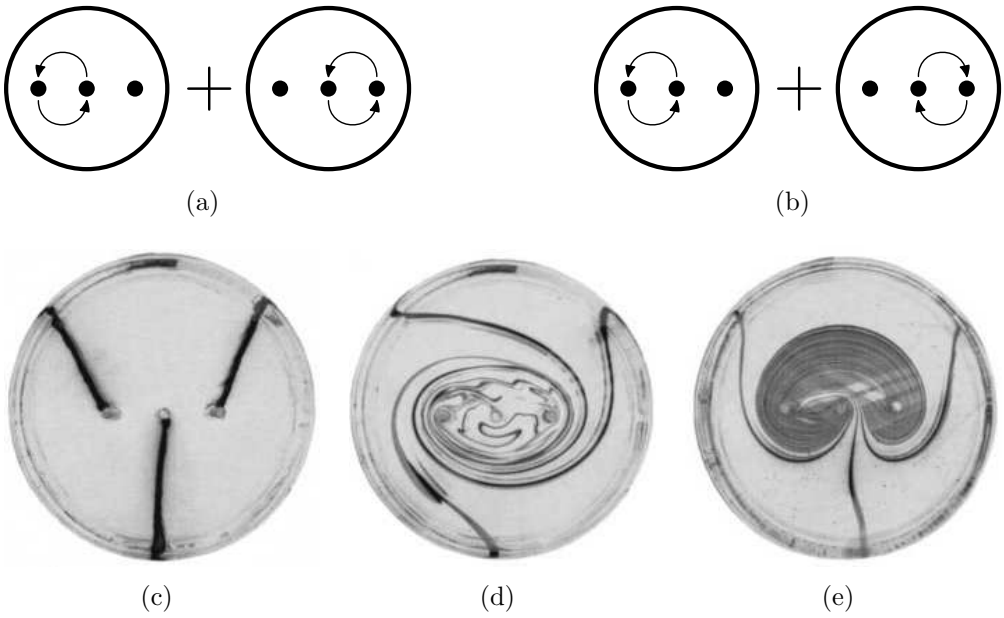

Figure 3.3: Experiments by Boyland et al. [18]. Three rods stir fluid in a periodic fashion. Elementary stirring steps consist in smoothly transposing two adjacent rods by moving them on semi-circles centered halfway between them. In a first protocol (a), the two rods on the left are moved in a clockwise fashion, then the two rods on the right are also exchanged on a clockwise fashion. In a second protocol (b) however, the first step still exchanges the two left rods clockwise, but then exchanges the two right rods *anti-clockwise*. Mixing properties of these two flows are strikingly different: if the system is prepared with three streaks of dye attached to the wall and the three rods (c), the dye pattern after 9 iterations shows little stretch for the first protocol (d), whereas the second protocol (e) has created a kidney-shaped very homogeneous mixing region. ((c), (d) and (e) were taken from [18])

rod, and no predictions can be made about its growth. Remember now that we have previously introduced the *topological entropy* of a flow h_{flow} as the exponential growth rate of a material line in the flow. In the same way, it is possible to define the topological entropy of a braid h_{braid}, which is a measure of its entanglement and basically measures the exponential rate of a material line pulled tight on the braid strands, as the pink line in Fig. 3.4. The catch is that a material line in the flow must grow at least as fast as a line pulled tight on the rods, which reads

$$h_{\text{braid}} \leq h_{\text{flow}}. \tag{3.20}$$

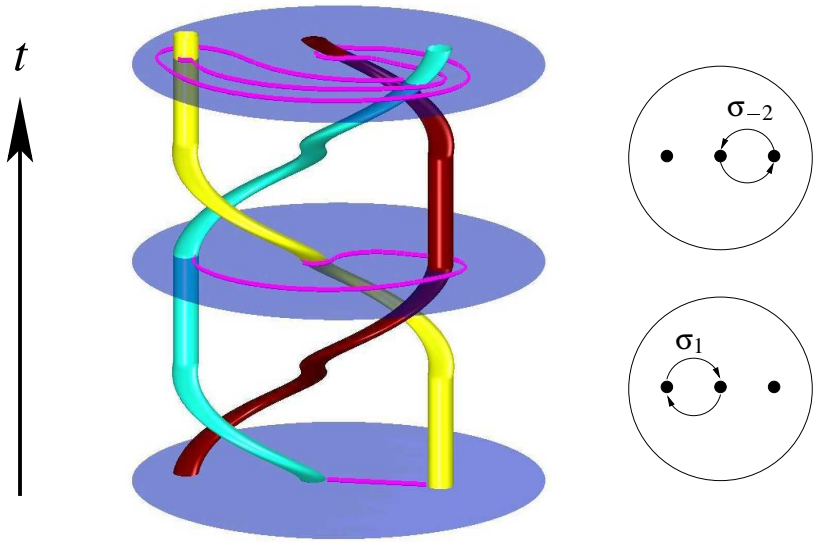

Figure 3.4: Trajectories of the rods in a space-time diagram for the protocol $\sigma_1\sigma_{-2}$ pictured on the right (σ_i refers to the exchange of rods i and $i+1$ in a clockwise fashion, whereas the interchange occurs in an anticlockwise fashion for σ_{-i}). Rods trajectories are entangled in a topologically complex braid, which forces material lines to be repeatedly stretched between the rods. Rods are indeed topological obstacles to material lines, which cannot cross them.

We now begin to glimpse the power of topological mixing: moving the rods with a protocol that has a tangled braid (i.e. $h_{\text{braid}} > 0$) ensures that a material line is stretched exponentially with time by this flow (which is just a way to say that the flow is chaotic), and moreover we have a lower bound h_{braid} for the growth rate ! Note that our crude explanations, mostly based on braids and stretching drawings, have none the less a solid mathematical basis with the Thurston-Nielsen theory of surface diffeomorphisms [118, 17]. Although the topology of surface diffeomorphisms is a well-developed field of mathematics, the true novelty of topological mixing lies in applying these ideas to physical fluid flows where, as we briefly saw, they are strikingly useful – especially for viscous flows where fluid is simply dragged, and therefore braided by the rods. This has leaded Boyland and co-authors to assert [18] that "all the configurations investigated to date have been 'too simple'" in the sense that mobile-boundaries stirring protocols studied before, such as the blinking vortex or journal-bearing flows, were too simple and less interesting than topologically complex moving rods protocols, where you know that the flow is chaotic regardless of all other parameters.

Figure 3.5: Principle of the pigtail braid. This braid is built with three strands, which is the minimal number to achieve topological complexity. The strands are braided by repeatedly (i) exchanging the two left-most strands by putting the left strand over the central one, (ii) then exchanging the two right-most strands by putting the right strand over the central one. Intuitively, this is the simplest way to braid the strands ; it has also been proved in [28] that it is the most efficient protocol (that maximizes the topological entropy per operation).

3.2.2 Topogical mixing with ghost rods

The paper inserted below presents another aspect of topological fluid dynamics. It has been published in *Physical Review E* **73**, 036311 (2006). Inspired by the work of Boyland et al. [18], we show that the flow complexity as measured by its topological entropy can in fact be described completely by the braiding of periodic structures, that is, stirring rods but also periodic points of the flow. This accounts for the positive topological entropy of one-rod stirring protocols, which can form complex braids with, for example, elliptical islands of the flow. Further complexity – i.e. a greater stretching rate – can be accounted for by considering the braiding of unstable periodic orbits.

Topological Mixing with Ghost Rods

Emmanuelle Gouillart, Jean-Luc Thiffeault,* and Matthew D. Finn

Department of Mathematics, Imperial College London, SW7 2AZ, United Kingdom
(Dated: May 22, 2006)

Topological chaos relies on the periodic motion of obstacles in a two-dimensional flow in order to form nontrivial braids. This motion generates exponential stretching of material lines, and hence efficient mixing. Boyland *et al.* [P. L. Boyland, H. Aref, and M. A. Stremler, J. Fluid Mech. **403**, 277 (2000)] have studied a specific periodic motion of rods that exhibits topological chaos in a viscous fluid. We show that it is possible to extend their work to cases where the motion of the stirring rods is topologically trivial by considering the dynamics of special periodic points that we call *ghost rods*, because they play a similar role to stirring rods. The ghost rods framework provides a new technique for quantifying chaos and gives insight into the mechanisms that produce chaos and mixing. Numerical simulations for Stokes flow support our results.

PACS numbers: 47.52.+j, 05.45.-a
Keywords: chaotic mixing, topological chaos

I. INTRODUCTION

Low-Reynolds-number mixing devices are widely used in many industrial applications, such as food engineering and polymer processing. The study of chaotic mixing has therefore been an issue of high visibility during the last two decades. A first step was taken by Aref [1], who introduced the notion of *chaotic advection*, meaning that passively advected particles in a flow with simple Eulerian time-dependence can nonetheless exhibit very complicated Lagrangian dynamics due to chaos. Chaotic advection has been demonstrated in many systems since: for a review see [2] or [3]. However, all the systems considered had a fixed geometry: even if the boundaries were allowed to move, as for instance in the journal bearing flow [4], the topology of the fluid region remained fixed.

A new aspect was recently investigated by Boyland *et al.* [5]. In an elegant combination of experimentation and mathematics, the authors introduced to fluid mechanics the concept of *topological chaos*. They studied two different periodic motions of three stirrers in a two-dimensional circular domain filled with a viscous fluid. They then used Thurston–Nielsen (TN) theory [6, 7] to classify the diffeomorphisms corresponding to the different stirring protocols. (The diffeomorphism is a smooth map that moves the fluid elements forward by one period.) As the stirrers moved, the geometry changed in time. The authors labelled the protocols using the braid formed by the space-time trajectories of the stirrers. In Figure 1 we show a space-time plot that illustrates how the trajectory of the rods can be regarded as a braid, for the same "efficient" braid presented in [5].

Boyland *et al.* then used TN theory to determine which stirring protocols generate *pseudo-Anosov* (pA) diffeomorphisms: a pA diffeomorphism corresponds roughly to exponential stretching in one direction at every point, and is thus a good candidate for efficient mixing. A relevant measure of the chaoticity of the flow is the maximum rate of stretching of material lines. In two dimensions this is equivalent to the topological entropy of the flow [8]. In the pA case the braid formed by the stirrer trajectories gives a lower bound on the topological entropy of the flow regardless of

*Electronic address: jeanluc@imperial.ac.uk

flow details (*e.g.* Reynolds number, compressibility, ...)—hence the term *topological chaos*. A pA braid can only be formed with three or more rods, since two rods cannot braid around each other nontrivially, and one rod has nothing to braid with. In stirring protocols with pA braids it is thus possible to predict a minimum complexity of the flow, as opposed to systems that require tuning of parameters to observe chaos. Such universality is of course desirable for mixing applications.

In this article we present another aspect of what was described as *topological kinematics* by Boyland *et al.* [9]. We study flows with only one stirring rod that have positive topological entropy, even though the braid traced by the stirrer is trivial. We apply the topological theory to these systems by considering the braid formed by periodic orbits of the flow as well as the stirrer itself. This allows us to account for the non-zero topological entropy of the flow. The periodic orbits (which can be stable or unstable) are created by the movement of the rods, but they are not the same as the rod trajectories, and in general will have different periodicity than the rod motions. We call the periodic points *ghost rods* because in the context of topological chaos they play the same role as rods, even though they are just regular fluid particles. Rather, they are kinematic rods that act as obstacles to material lines in the flow because of determinism—a material line cannot cross a fluid trajectory, otherwise the fluid trajectory must belong to the material line for all times. In fact, any fluid trajectory is such a topological obstacle [10], but for time-periodic systems periodic orbits are the appropriate trajectories to focus on. The idea of using periodic orbits to characterise chaos in two-dimensional systems comes from the study of surface diffeomorphisms [7]. In a related vein, periodic orbit expansions are also used to compute the average of quantities on attractors of chaotic systems [11, 12].

The study of ghost rods is important because it helps identify the source of the chaos (and hence good mixing) in a given mixer. We will show that the main contribution to the topological entropy in a system usually comes from a relatively small number of periodic orbits. This represents a tremendous reduction in the effective dimensionality of the system, and by focusing on this reduced set of orbits it will be easier to study and improve mixing devices. The ghost rods framework thus provides new tools for diagnosing and measuring mixing [10]. In addition, it also gives a new understanding of the mixing mechanisms as we can consider the mixing to arise from the braiding of material lines around the ghost rods.

The outline of the paper is as follows. In Section II we introduce the mathematical theory for braids and topological chaos. In Section III we study examples with one rod moving on different paths. We show that some periodic orbits braid with the stirrer. In Section IV we show that we can account for an arbitrary percentage of the observed topological entropy of the flow with such a braid. The main conclusions and an outlook on future research are presented in Section V.

II. BRAIDS AND DYNAMICAL SYSTEMS

A. Overview of Thurston–Nielsen (TN) Theory

The mathematical setting for studying braiding in fluids mechanics is centered on the N-punctured disk in two dimensions, R_N. The N punctures, located somewhere in the interior of the disk, represent the stirring rods. If the stirrers undergo a prescribed periodic motion, they return to their initial position at the end of a full cycle. Naturally, the rods have dragged along the fluid, which obeys some as yet unspecified equations (*e.g.*, Stokes, Navier–Stokes, Euler, non-Newtonian equations, assumption of incompressibility, ...). The position of fluid elements is thus determined by some function $\Phi(x,t)$. Since the flow is periodic with period T, $\Phi(x,T)$ is a map from R_N to itself, and we define

$$f : R_N \to R_N\,, \qquad f(x) = \Phi(x,T). \tag{1}$$

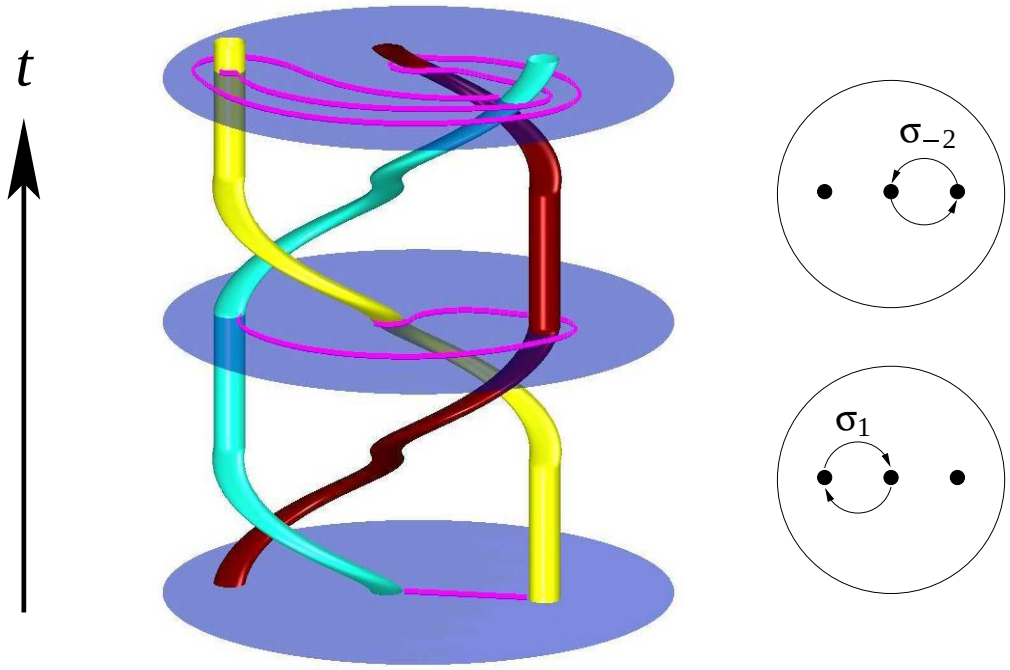

FIG. 1: The trajectories of the N stirrers define a braid on N strands in a space-time diagram (here $N = 3$), with time flowing from bottom to top. The periodic movement of the stirrers for the protocol is represented in the two pictures on the right: first (bottom) the two rods on the left are interchanged clockwise (we call this operation σ_1), then (top) the two rods on the right are interchanged anti-clockwise (σ_{-2}). Two sequences of this protocol are drawn on the 3D braid. This protocol is the pseudo-Anosov protocol described in [5].

For any realizable fluid motion, f will be an orientation-preserving diffeomorphism of R_N. The map f takes every fluid element to its position after a complete cycle. It is a diffeomorphism because the physical fluid flows we consider are differentiable and have a differentiable inverse. The map f embodies everything about the fluid movement, and it is thus the main object to be studied.

But in some sense f contains too much information: it amounts to a complete solution of the problem, and there are interesting things we can say about the general character of f without necessarily solving for it. We are also interested in knowing what characteristics of the stirrer motion must be reflected in f. This is where the concept of an *isotopy class* comes in: two diffeomorphisms are *isotopic* if they can be continuously deformed into each other. This is a strong requirement: continuity means that two nearby fluid elements must remain close during the deformation, and so they are not allowed to "go through" a rod during the deformation, otherwise they would cease to be neighbours. In that sense, isotopy is a topological concept, since it is sensitive to obstacles in the domain (the rods). The isotopy class of f is then the set of all diffeomorphisms that are isotopic to f. In fact, an entire class can be represented by just one of its members, appropriately called the *representative*. Of course, the important point here is that that not all diffeomorphisms are isotopic to the identity map. Note that the overwhelming majority of f are not allowable fluid motions (*i.e.*, they cannot arise from the dynamical equations governing the fluid motion), but any allowable fluid motion must belong to some isotopy class.

The problem now is to decide what isotopy classes are possible, and what this means for fluid motion. Thurston–Nielsen (TN) theory [6, 7] guarantees the existence in the isotopy class of f of

a representative map, the TN representative f', that belongs to one of three categories:

1. *finite-order*: if f' is repeated enough times, the resulting diffeomorphism is isotopic to the identity (*i.e.*, f'^m is isotopic to the identity for some positive integer m);

2. *pseudo-Anosov* (pA): f' stretches fluid elements by a factor $\lambda > 1$, so that repeated application gives exponential stretching;

3. *reducible*: f' can be decomposed into components acting on smaller regions of the previous two types.

A famous example of an Anosov map is Arnold's cat map [13]. A pA map is an Anosov map with a finite number of singularities. The TN theory also states that the dynamics of a diffeomorphism in a pA isotopy class are at least as complicated as the dynamics of its pA TN representative, meaning it has a greater or equal topological entropy. For a diffeomorphism, the topological entropy h gives a measure of the complexity, *i.e.* the amount of information which we lose at each iteration of the map [8]. It also describes the exponential growth rate of the number of periodic points as a function of their period. Newhouse and Pignataro [8] noticed that h also gives the exponential growth rate for the length of a suitably chosen material line. In the numerical simulations described below, we use this fact to compute the topological entropy of a flow: we consider a small blob in the chaotic region of the flow and we calculate the growth rate of its contour length.

TN theory tells us about the possible classes of diffeomorphisms that can arise from the periodic motion of the stirrers. But one can also consider the trajectories of the punctures (here the stirrers) in a 3D space-time plot (Fig. 1), where the vertical is the time axis. These trajectories loop around each other and form a physical braid. The crucial point is that such a braid constructed from the rod trajectories specifies the isotopy class of f, no matter the details of the flow. (See Refs. [5, 7, 9, 14] for further details.) As a consequence of the TN theory, the topological entropy of this braid is a lower bound on the topological entropy of the flow.

Hence, determining the isotopy class of the diffeomorphism f is equivalent to studying the braid traced by the stirrer trajectories. This is a drastic reduction in complexity, because we are free to impose relatively simple braiding on the stirrers by means of a short sequence of rods exchanges, whereas the resulting diffeomorphism obtained by solving the fluid equations can be quite complicated. In the next section we introduce the machinery needed to characterize braids.

B. Artin's Braid Group

Let us introduce now the notation for braids. The generators of the Artin braid group on N strands are written σ_i and $\sigma_i^{-1} =: \sigma_{-i}$, which represent the interchange of two adjacent strands at position i and $i+1$. The interchange occurs in a clockwise fashion for σ_i (i goes over $i+1$ along, say, the y-axis) and anti-clockwise for σ_{-i} (i goes under $i+1$). For N strands, there are $N-1$ generators, so $i \in \{1, \ldots, N-1\}$. It is thus possible to keep track of how N rods are permuted and of the way they cross by writing a *braid word* with the "letters" σ_i. We read braid words from left to right (that is, in $\sigma_1\sigma_3\,\sigma_{-2}$ the generator σ_1 precedes σ_3 temporally). For example, the pA stirring protocol described by Boyland *et al.* [5] and shown in Fig. 1 corresponds to $\sigma_1\sigma_{-2}$: it consists of first interchanging the two rods on the left clockwise (σ_1) and then interchanging the two rods on the right anti-clockwise (σ_{-2}). Note that the i index on σ_i refers to the relative position of a rod (*e.g.*, second from the left along the x-axis) and does not always label the same rod.

The generators obey the *presentation* of the braid group,

$$\sigma_i\sigma_j\sigma_i = \sigma_j\sigma_i\sigma_j \qquad \text{if} \qquad |i-j| = 1, \tag{2a}$$

$$\sigma_i\sigma_j = \sigma_j\sigma_i \qquad \text{if} \qquad |i-j| \geq 2, \tag{2b}$$

that is, the relations (2) must be obeyed by the generators of physical braids, and no other nontrivial relations exist in the group [14]. The relation (2a) corresponds physically to the "sliding" of adjacent crossings past each other, and (2b) to the commutation of nonadjacent crossings.

The braid group on N strands has a simple representation in terms of $(N-1)\times(N-1)$ matrices, called the Burau representation [15]. For three strands ($N = 3$), the topological entropy of the braid is obtained from the magnitude of the largest eigenvalue of the Burau matrix representation of the braid word. This is the technique used in Refs. [5, 9, 16, 17] to compute topological entropies. For $N > 3$ the Burau representation only gives a lower bound on the topological entropy of the braid [18], so a more powerful algorithm must be used to obtain accurate values. Here we use the train-tracks code written by T. Hall [19], an implementation of the Bestvina–Handel algorithm [20]. The train-tracks algorithm works by computing a graph of the evolution of edges between rods under the braid operations. It suffices for our purposes to say that train-tracks determine the shortest possible length of an "elastic band" that remains hooked to the rods during their motion—the minimum stretching of material lines [21].

III. EVIDENCE FOR GHOST RODS

A. Motivation

We consider here the advection of a passive scalar in a two-dimensional batch stirring device containing a viscous fluid that obeys Stokes' equation. The batch stirrer includes circular cylinders—the stirring rods—that undergo periodic motion. The exact velocity field for one circular rod in a Stokes flow was derived in Ref. [22]. For more than one rod there is no exact expression available for the velocity field, so we use instead a series expansion suggested by Finn *et al.* [17]. We use an adaptive fourth-order Runge–Kutta integrator for the time-stepping.

We study first a configuration of the translating rotating mixer (TRM) defined by Finn *et al.* [22]. The system consists of a two-dimensional disk stirred by a circular rod that moves around in the disk. The center of the rod moves on an epicyclic path (in a time period T) given by

$$\begin{aligned} x(t) &= r_1 \cos 2\pi m t/T + r_2 \cos 2\pi n t/T, \\ y(t) &= r_1 \sin 2\pi m t/T + r_2 \sin 2\pi n t/T, \end{aligned} \tag{3}$$

as shown in Fig. 2. Note that such a path can be implemented in a real mixing device using straightforward gearing. It is possible to choose very complicated trajectories by changing m and n, however we limit ourselves to the comparatively simple case $m = 1$ and $n = 2$. The other parameter values used here are $r_1 = 0.2$, $r_2 = 0.5$. The radius of the outer disk is 1 and we tested configurations with different values for the rod radius a_{in}.

There is only one rod so the one-strand braid formed by the stirrer is trivial. Topologically, the motion of this single rod does not imply a positive lower bound on the topological entropy of the flow. This does not mean that material lines cannot grow exponentially for this flow. We have plotted in Fig. 3(a) the image of a small blob, *i.e.* a circle enclosing the rod at $t = 0$, after just four periods of the flow with $a_{\text{in}} = 0.05$. The small blob has been tremendously stretched, suggesting exponential growth.

Furthermore, note some similarities with another stirring protocol, where the rod is moving on the same path but we have added two fixed rods in the regions enclosed by the moving rod's

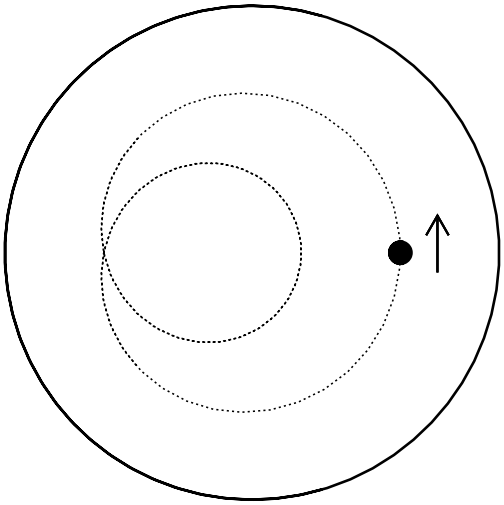

FIG. 2: A rod traveling on a epicyclic path. The trajectory of the rod encloses two different regions, a loop and a crescent.

trajectory (Fig. 3(b)). For this protocol the braid formed with the stirrers is $\sigma_{-2}\sigma_{-1}\sigma_{-1}\sigma_{-1}\sigma_{-1}\sigma_{-2}$ [17] with topological entropy $h_{\text{braid}} = 1.76$. (From now on, we shall use h_{braid} to denote the topological entropy of a braid, which is a lower bound on the corresponding flow's topological entropy, h_{flow}: $h_{\text{braid}} \leq h_{\text{flow}}$.) Thus we expect the efficient stretching displayed in Fig. 3(b). The braid's entropy is a lower bound for the entropy of the flow, and we indeed measure $h_{\text{flow}} = 2.38$. (We recall that we compute h_{flow} by calculating the exponential rate of growth of material lines in the chaotic region.)

There is thus a discrepancy in that the motion of the rod in Fig. 3(a) does not account for the observed exponential stretching of material lines, at a rate given by $h_{\text{flow}} = 2.32$. An indication of the source of the missing topological entropy is that this rate is comparable to the one observed in the protocol of Fig. 3(b), $h_{\text{flow}} = 2.38$, where extra obstacles are present. We shall see in the following sections that the "missing" topological entropy can be accounted for by looking at periodic orbits in the flow and their topological effect on material lines.

B. Elliptic Islands as Ghost Rods

In Section III A we saw that much of the topological entropy in a one-rod protocol could be accounted for by adding two fixed rods to the flow. These fixed rods modify the flow, but they do not significantly modify the topology of advected material lines compared to the single-rod case (Fig. 3). Hence, for the TRM with only one rod we observe that material lines grow *as if* rods were present inside the loops traced by the physical rod's trajectory. This justifies introducing the notion of "ghost rods": something inside the physical rod's trajectory is playing the role of a real rod, and we shall soon see that in this case elliptical islands are the culprits. These islands braid with the physical rod, and taken together they give a positive topological entropy. In general, we refer to periodic structures of the flow (islands or isolated points) as ghost rods when they play a role in determining the topological entropy. These are topological obstacles and are thus candidates for forming nontrivial braids. The topological approach puts all periodic structures—orbits and rods—on the same footing.

The introduction of ghost rods becomes even more relevant if one considers the one-rod protocol

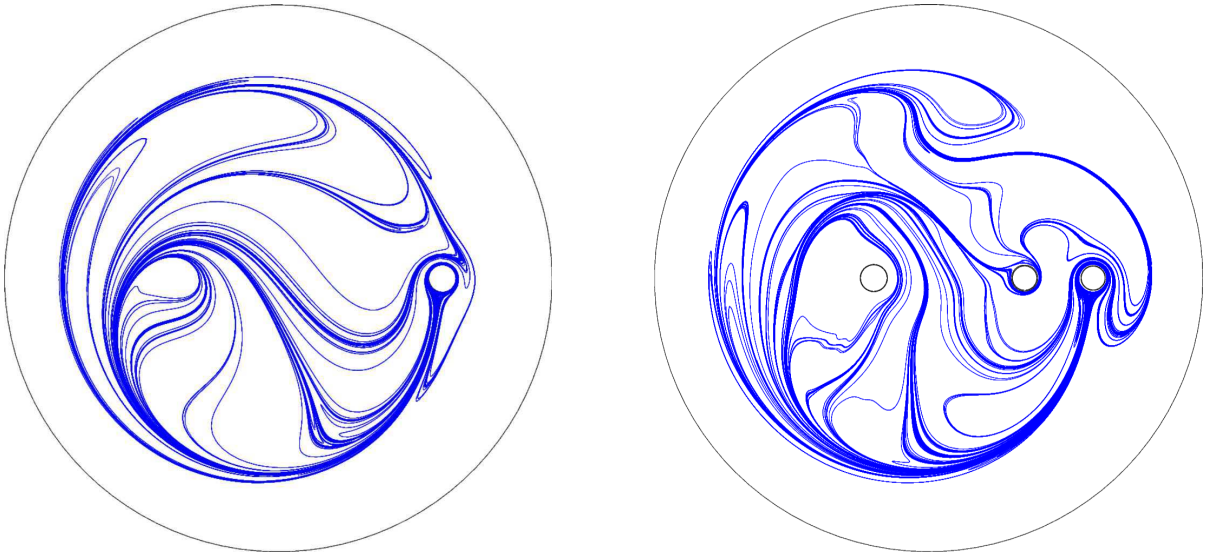

(a) (b)

FIG. 3: (a) The stretching of a small blob initially surrounding the moving rod; (b) Same as in (a), except two extra fixed rods are inserted in the flow. The patterns made by the blob in (a) and (b) look similar, suggesting that there are invisible topological obstacles in (a) as the fixed rods in (b). Note in particular the similarity between the fixed rod inside the loop in (b) and the way the line wraps itself around an invisible obstacle inside the loop in (a).

pictured in Fig. 4. The rod is moving on a figure-eight path, traveling clockwise on the left circle of the eight and anticlockwise on the right circle. A Poincaré section reveals two small islands inside both circles (see Fig. 4). Initial conditions inside these islands remain there forever and are thus topologically equivalent to a fixed rod inside each circle of the figure-eight. By studying the motion of the rod closely, it is easy to show that the braid formed by the rod and the islands is $\sigma_1\sigma_{-2}\sigma_{-2}\sigma_1$, which has a topological entropy $h_{\text{braid}} = 1.76$. Indeed, we measure a topological entropy $h_{\text{flow}} = 2.25$, which is greater than 1.76. (We shall account for the difference with the measured topological entropy of the flow later.) Hence, although elliptic islands are usually considered barriers to mixing, they can also yield a lower bound on the topological entropy of the region exterior to them. All the results presented here for the figure-eight protocol are for the parameters $a = 0.35$ (radius of the circles forming the eight), $a_{\text{in}} = 0.04$ (radius of the rod) and $a_{\text{out}} = 1$ (radius of the outer circle).

So far we have only considered period-1 islands that stay into the regions bounded by the rod's trajectory, but this is not always possible. In general we have to consider more complicated orbits. For instance, the two islands inside the eight (Fig. 4) are not present for protocols with a larger rod radius a_{in}: in that case we have not found any points that remain forever inside one of the circles. Similarly, for the epicyclic path (Fig. 2) there is an island inside the loop part of the trajectory; however any point will leave the crescent region after a finite time because of the ascending movement induced by the rod, so there are no fixed ghosts rods in that region. The Poincaré section shown in Fig. 5 suggests however other candidates for ghost rods. First, as we noted before, there is a period 1 island that remains inside the loop forever. Second, the Poincaré section reveals three islands that are part of the same period-3 structure. Two "images" of this period-3 island are inside the crescent. The braid formed by the rod and these four islands is shown

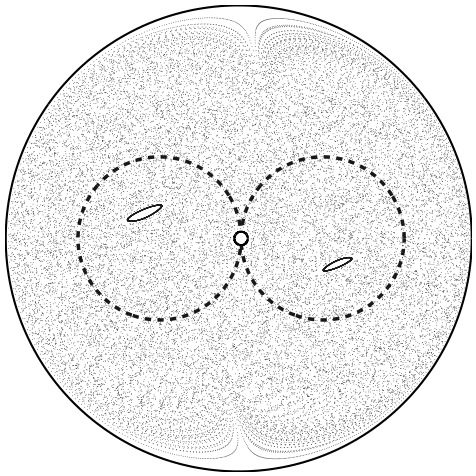

FIG. 4: Poincaré section for a protocol with one rod traveling on a figure-eight path (dashed line). Two regular islands are present inside each loop of the rod's path. They are topological obstacles that form a non-trivial braid with the rod.

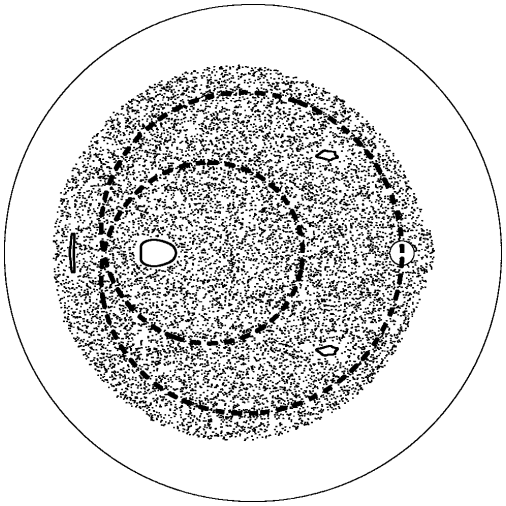

FIG. 5: Poincaré section for the TRM protocol, showing different kinds of topological obstacles. The physical rod is moving on an epicyclic path whereas a regular island stays inside the loop and three islands of period three are permuted each period. The braid formed with the rod and these islands is shown in Fig. 6

in Fig. 6.

We now have a first method of computing a lower bound on the topological entropy of a flow: look for elliptic islands and calculate the braid formed by the physical rod(s) (if any) and the islands (the ghost rods). Its entropy h_{braid} will be a lower bound on the topological entropy of the flow h_{flow}. However, this lower bound is often not a very good one: we show in the next section that it is possible to improve it by considering not only islands, but also more general (unstable) periodic orbits.

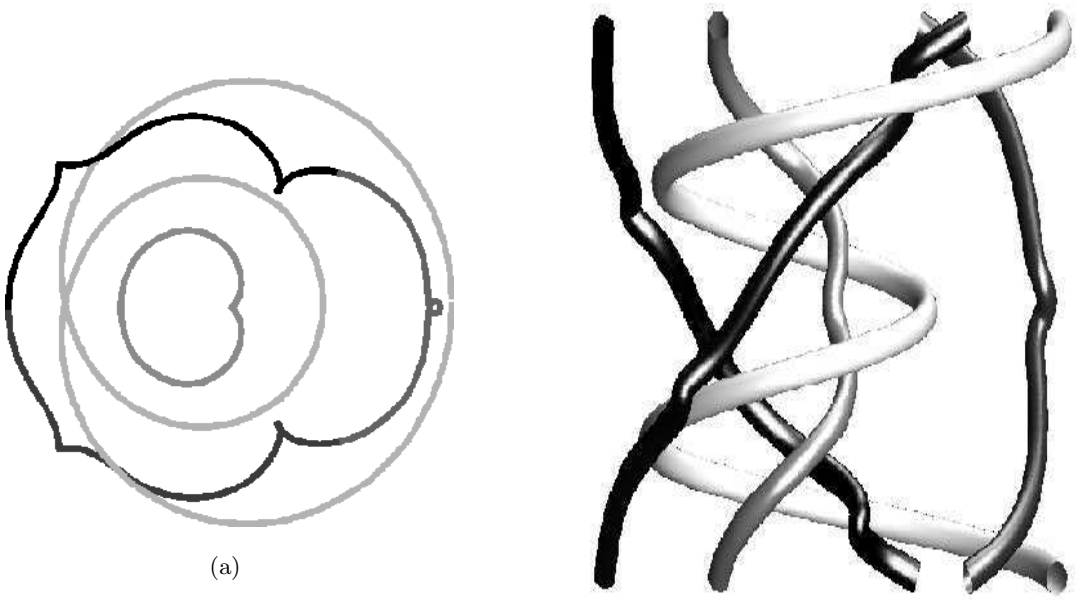

(a) (b)

FIG. 6: (a) Trajectories of the topological obstacles (the physical rod and two periodic islands) shown in Fig. 5. (b) The same trajectories in a space-time diagram form a braid with positive topological entropy $h_{\text{braid}} = 1.72$.

C. Unstable Periodic Orbits as Ghost Rods

A positive topological entropy implies a horseshoe structure [23] and thus an infinite number of unstable periodic orbits (UPO's) in the flow. These periodic points are topological obstacles as well as the physical rods (though they have zero size), and hence are ghost rods. However, most periodic points are unstable and therefore difficult to detect: a trajectory initialized near an unstable periodic point will diverge from the periodic orbit (exponentially for a hyperbolic orbit). We use the method of Schmelcher and Diakonos [24] to detect periodic orbits numerically. The method relies on finding the periodic orbits of a modified version of the flow that has the same periodic orbits, except that they are stable in the modified flow. Diakonos *et al.* [25] point out that this method selects the least unstable orbits, that is, the least unstable orbits are found first and one has to change a parameter in the algorithm and therefore increase the computing time to find more unstable orbits. Furthermore, we are dealing with systems with high topological entropy: as asymptotically the flow has roughly $\exp(h_{\text{flow}} n)$ periodic points of period n, systematic detection of periodic points is impossible for orbits of high order. We choose rather to detect only the least unstable orbits: we show in the next section that it is possible to derive an accurate value of the topological entropy of a flow from these orbits.

IV. CALCULATING THE TOPOLOGICAL ENTROPY WITH GHOST RODS

Boyland [7], using results by Katok [23], proved that for an orientation-preserving diffeomorphism of the disk there exists a sequence of orbits whose entropies converge to the topological entropy of the flow. The topological entropy can thus be obtained from the periodic-orbit structure of the flow. It should therefore be possible to find a periodic orbit whose braid has a topological

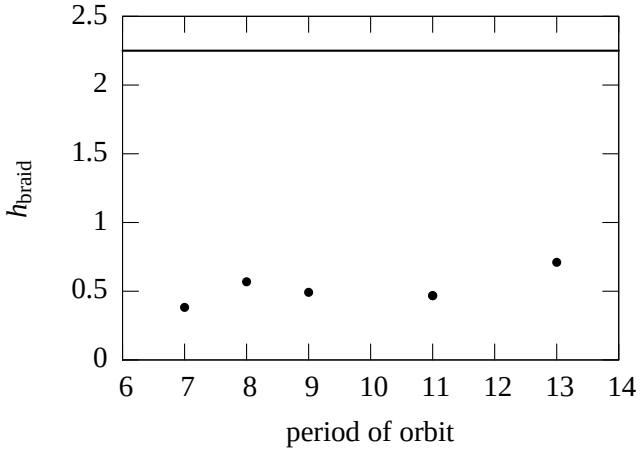

(a)

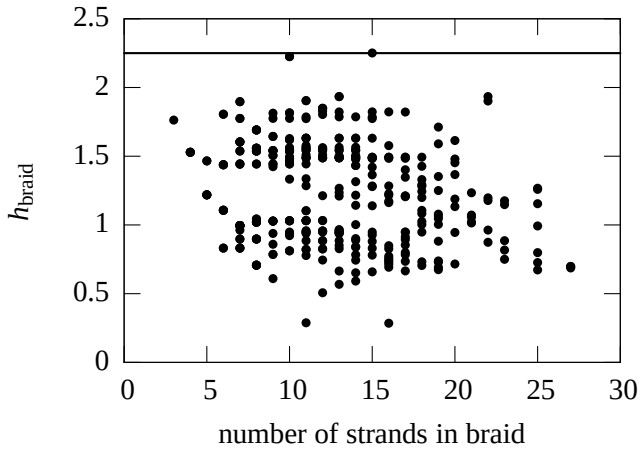

(b)

FIG. 7: (a) Some periodic orbits are self-braiding, that is, the entropy of the braid formed by all the points of the orbit is strictly positive. The entropy of the self-braiding orbits is plotted here vs their period. (b) The positive entropy of braids formed by the rod's trajectory and pairs of periodic orbits vs the number of strands in the braid. In both plots, the solid line is the measured topological entropy of the flow, $h_{\text{flow}} = 2.25$.

entropy arbitrarily close to the topological entropy of the flow. We investigate this before considering multiple periodic orbits.

A periodic orbit is *self-braiding* if the points in the orbit form a nontrivial braid when taken together. Figure 7(a) shows the topological entropy of self-braiding orbits as a function of their period for the figure-eight protocol. Some orbits indeed have a positive topological entropy, but their entropy is far from the one computed with the line-growth algorithm ($h_{\text{flow}} = 2.25$), solid horizontal line in Fig. 7(a). Furthermore very few orbits self-braid, *i.e.* have a positive entropy. Hence, it appears that looking at the topological entropy of individual orbits is not very useful: obtaining a reasonable approximation to the topological entropy requires orbits of prohibitively high order or instability.

As self-braiding orbits do not seem very convenient to approach h_{flow} we choose rather to combine several orbits together to form more complex braids. We first combine each periodic

orbit with the rod and we obtain higher values for h_{braid}, although still far from h_{flow}. We also consider the braids formed by the rod and pairs of periodic orbits, which are also invariant sets of the first return map. We consider pairs of orbits because this is the minimal number of orbits that can capture the topology determined by the rod's trajectory. As is shown in Fig. 7(b), we obtain braid entropies far closer to the value measured for the flow: some braids approximate the measured entropy to within numerical error. It is thus more efficient to consider combinations of orbits rather than only self-braiding orbits: one would surely need orbits of very high order, or very unstable, to get as close to the measured value h_{flow}. For this example we used a set of 52 periodic orbits whose positive Floquet exponent is smaller than $3/T$, where T is the period of the orbit. Note that although we did not detect all or even a large number of periodic orbits (there is an infinity of them), our combination of ghost rods provides us with a very good approximation of the topological entropy of the flow. For a given system the entropy lower bound must increase as more orbits are added to a given braid; nevertheless we see that for the system we consider, only a small number of orbits is needed to obtain a satisfactory lower bound on h_{flow}. We therefore suggest an alternative method for calculating the topological entropy of a flow: (i) detect some periodic orbits; (ii) calculate the maximum entropy of all the braids one can create with these points and the rod(s); and (iii) see if this maximum entropy converges when one increases the number of periodic orbits.

V. DISCUSSION

To summarize, we have characterized chaos in two-dimensional time-periodic flows by considering the braids formed by periodic points and calculating their topological entropy for different stirring protocols. We have demonstrated the role of periodic points in fluid mixing, and called these periodic points ghost rods because their movement stretches material lines as real stirring rods do. This work is an extension of the topological kinematics theory introduced by Boyland *et al.* [5, 7, 9], since it characterizes the mixing in a flow by studying the topological constraint induced by the ghost rods and not only stirrers. We expect this approach to develop further in the near future, and to yield new insight on efficient mixing devices.

The idea of characterizing dynamics of homeomorphisms of surfaces by puncturing at periodic orbits dates back to Bowen [30], and the study of braids formed with periodic points had already been suggested by Boyland for the general study of diffeomorphisms of the disk [7]. In addition, this technique is used in other fields such as the study of optical parametric oscillators [26]. However, the present work is to our knowledge the first study of ghost rods in fluid mechanics.

In contrast to other applications, in our systems the ghost rods are created by the movement of the physical rod, so we may hope to derive some information about ghost rods from the motion of that physical rod. For instance, let us consider the period-3 orbit for the figure-eight protocol shown in Fig. 8 (this orbit is more unstable than the ones we used in the previous section). One point of the orbit is located very close to the physical rod at $t = 0$. Its trajectory will thus be very close to the rod's trajectory at the beginning of the period. Later the rod leaves the periodic point in its trail after a time equal to about $T/3$. One period later the rod drags this point again on its trajectory as it comes close to it. This accounts for the topological similarity between the trajectory of the rod and the periodic orbit. The braid formed by these period-3 orbits is $\sigma_{-1}\sigma_2$, which is also the braid studied by Boyland *et al.* in [5]. It is actually the braid with the maximal h_{braid} that we can form with points moving on a trajectory strictly equivalent to the rod's path. Indeed we cannot form a braid with fewer than three points, and periodic points with a higher period on such a path move slower as they take longer to cover the whole path, so they have a less efficient braiding (fewer exchanges per period). We conjecture that this type of figure-eight

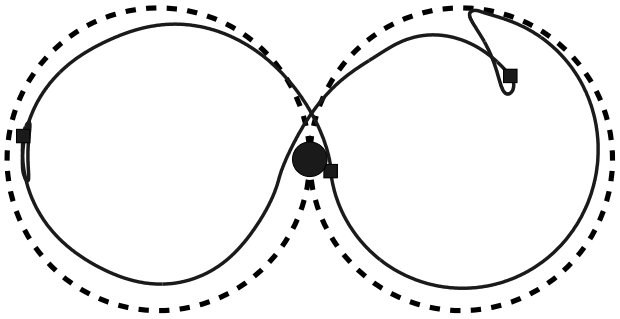

FIG. 8: The trajectory of the rod (dashed line) and three period-3 points belonging to the same orbit (solid line). The position of the rod (filled circle) and the periodic points (filled squares) at $t = 0$ is also shown.

trajectory is characteristic of all mixing protocols with a rod moving on a figure-eight path.

We have indeed found such a braid—formed by a period-3 orbit equivalent to the rod's trajectory—for all the figure-eight protocols we have tested. We have tried the protocol plotted in Fig. 4 with different radii for the rod, as well as a protocol with one rod moving on a lemniscate (a lemniscate is the more natural "figure-eight" shape [27]), and we have detected this figure-eight periodic orbit associated with the $\sigma_{-1}\sigma_2$ braid for each protocol. It is thus very tempting to conjecture that for all the Stokes flows created by the movement of a rod on a figure-eight path, the topological entropy of the flow is greater than the entropy of the braid $\sigma_{-1}\sigma_2$, that is, 0.96. If this conjecture holds, then ghost rods can be used not only for diagnosing chaos and calculating the entropy of a flow, but also topological arguments can be used to *predict* a minimum entropy just from the path of the physical rod with ghost rods in its trail. This is a generalization to ghost rods of the arguments used by Boyland *et al.* [5] to predict a universal minimum entropy from the movements of the rods for three or more physical rods. A further natural question then is which ghost rods have the best braid, that is, the braid giving the topological entropy of the flow, and could we relate these "most efficient" ghost rods to the physical properties of the flow? This will be the topic of future research.

The ghost rods approach should also be compared with recent work on nonperiodic points. Thiffeault [10] noticed that every fluid particle in a two-dimensional flow is a topological obstacle, much like a stirrer, and calculated entropies of braids formed by arbitrary chaotic orbits. As these points were not periodic points these entropies may not give a lower bound on the entropy of the flow for short times; however, they can yield finite-time information about the stretching rate of material lines. Furthermore, if one considers long time series, a randomly chosen point in an ergodic chaotic region will repeatedly come very close to periodic orbits. It should thus be possible to observe braids with similar properties as the ones formed by ghost rods.

Finally, the study of ghost rods can be used to prove that a map is chaotic in the case where some periodic points can be calculated analytically, as for the sine flow map [21, 28] or the closely-related standard map [29]. Finn *et al.* [21], for example, have shown that the sine flow map has chaotic trajectories for some parameter values.

Acknowledgments

We thank Toby Hall for use of his train-tracks code. This work was funded by the UK Engineering and Physical Sciences Research Council grant GR/S72931/01.

---

[1] H. Aref, "Stirring by chaotic advection," J. Fluid Mech. **143**, 1 (1984).
[2] J. M. Ottino, *The kinematics of mixing: stretching, chaos, and transport* (Cambridge University Press, Cambridge, U.K., 1989).
[3] H. Aref, "The development of chaotic advection," Phys. Fluids **14**, 1315 (2002).
[4] J. Chaiken, R. Chevray, M. Tabor, and Q. M. Tan, "Experimental study of Lagrangian turbulence in a Stokes flow," Proc. R. Soc. Lond. A **408**, 165 (1986).
[5] P. L. Boyland, H. Aref, and M. A. Stremler, "Topological fluid mechanics of stirring," J. Fluid Mech. **403**, 277 (2000).
[6] W. Thurston, "On the geometry and dynamics of diffeomorphisms of surfaces," Bull. Am. Math. Soc. **19**, 417 (1988).
[7] P. Boyland, "Topological methods in surface dynamics," Topology Appl. **58**, 223 (1994).
[8] S. Newhouse and T. Pignataro, "On the estimation of topological entropy," J. Stat. Phys. **72**, 1331 (1993).
[9] P. Boyland, M. Stremler, and H. Aref, "Topological fluid mechanics of point vortex motions," Physica D **175**, 69 (2003).
[10] J.-L. Thiffeault, "Measuring topological chaos," Phys. Rev. Lett. **94**, 84502 (2005).
[11] D. Auerbach, P. Cvitanović, J.-P. Eckmann, G. Gunaratne, and I. Procaccia, "Exploring chaotic motion through periodic orbits," Phys. Rev. Lett. **58**, 2387 (1987).
[12] P. Cvitanović, "Invariant measurement of strange sets in terms of cycles," Phys. Rev. Lett. **61**, 2729 (1988).
[13] V. I. Arnold, *Mathematical Methods of Classical Mechanics*, 2nd ed. (Springer-Verlag, New York, 1989).
[14] J. S. Birman and T. E. Brendle, in *Handbook of Knot Theory*, edited by W. Menasco and M. Thistlethwaite (Elsevier, Amsterdam, 2005).
[15] W. Burau, "Über Zopfgruppen und gleichsinnig verdrilte Verkettungen," Abh. Math. Sem. Hanischen Univ. **11**, 171 (1936).
[16] A. Vikhansky, "Chaotic advection of finite-size bodies in a cavity flow," Phys. Fluids **15**, 1830 (2003).
[17] M. Finn, S. Cox, and H. Byrne, "Topological chaos in inviscid and viscous mixers," J. Fluid Mech. **493**, 345 (2003).
[18] B. Kolev, "Entropie topologique et représentation de Burau," C. R. Acad. Sci. Sér. I **309**, 835 (1989).
[19] T. Hall, *Train: A C++ program for computing train tracks of surface homeomorphisms*, `http://www.liv.ac.uk/maths/PURE/MIN_SET/CONTENT/members/T_Hall.html`.
[20] M. Bestvina and M. Handel, "Train-tracks for surface homeomorphisms," Topology **34**, 109 (1995).
[21] M. D. Finn, J.-L. Thiffeault, and E. Gouillart, "Topological chaos in spatially periodic mixers," `arXiv:nlin.CD/0507023`.
[22] M. D. Finn and S. M. Cox, "Stokes flow in a mixer with changing geometry," J. Eng. Math. **41**, 75 (2001).
[23] A. Katok, "Lyapunov exponents, entropy and periodic orbits for diffeomorphisms," Inst. Hautes Etudes Sci. Publ. Math. **51**, 137 (1980).
[24] P. Schmelcher and F. K. Diakonos, "General approach to the localization of unstable periodic orbits in chaotic dynamical systems," Phys. Rev. E **57**, 2739 (1998).
[25] F. K. Diakonos, P. Schmelcher, and O. Biham, "Systematic computation of the least unstable periodic orbits in chaotic attractors," Phys. Rev. Lett. **81**, 4349 (1998).
[26] A. Amon and M. Lefranc, "Topological signature of deterministic chaos in short nonstationary signals from an optical parametric oscillator," Phys. Rev. Lett. **92**, 094101 (2004).
[27] E. W. Weisstein, Lemniscate, from MathWorld—A Wolfram Web Resource. `http://mathworld.wolfram.com/Lemniscate.html`.
[28] M. Liu, F. J. Muzzio, and R. Peskin, "Quantification of mixing in aperiodic chaotic flows," Chaos

Solitons Fractals **4**, 869 (1994).

[29] B. Chirikov, "Anomalous diffusion in a microtron and critical structure at the chaos boundary," JETP **83**, 646 (1996).

[30] R. Bowen, "Entropy and the fundamental group," in *Structure of Attractors*, Lecture Notes in Math. **668**, pp. 21–29 (Springer, New York, 1978).

3.2.3 Topological structure of the mixing pattern

3.2.3.1 Ghost rods and shape of a material line

In the previous section and the paper therein, we have described how the chaotic complexity of a flow can be accounted for by considering the braiding of periodic orbits – ghost rods – which stretch material lines around their trajectories. Ghost rods are indeed allowed to braid fluid like real stirrers, as they are topological obstacles to material lines. We have seen that all periodic structures are useful to provide a measure of chaos by computing lower bounds on the flow topological entropy, which can moreover be very accurate with a small number of orbits. However, the reader might ask how far this analogy can go, that is, if ghost rods play a role as important as real rods in the mixing process.

Physical stirrers deform material lines in an obvious way by forcing lines to *fold* around them. Fig. 3.6 shows how a small material line (initialized as a circle wrapped around the central rod) has been stretched after 5 stirring periods of the pigtail braid protocol introduced by Boyland et al. [18]. It is easy to describe the line pattern, as rods uniquely determine it: lines are strongly folded around the rods, and they have very weak curvature between rods. We will introduce later on *train tracks*, which are a simple way to encode the line pattern around rods.

However, ghost or even real rods do not all determine the pattern in such a direct way. Fig. 3.6 (b) shows how a line has been stretched by a rod moving on a figure-eight path (the central rod in the picture) around two fixed rods each located inside a loop of the figure-eight. The braid formed by the rods' trajectory is $\sigma_2^2\sigma_{-1}^2$, which has a positive topological entropy. Yet line patterns in Figs. 3.6 (a) and (b), and their relation to rods, are very different. Fixed rods in Fig. 3.6 (b) do not fold the line pattern as moving rods do. One could indeed remove the fixed rods and squash the line pattern on both sides of their location, without changing much the general structure of the pattern. Moreover, the pattern looks more complicated: additional folds are visible in the upper part of the pattern, for example, yet they are not "hooked" on real rods.

Elliptical islands are not better candidates to describe the global structure of the pattern: Fig. 3.6 (c) shows a line stretched by a single rod moved again on a figure-eight, that creates two small elliptical islands (superimposed here on the line pattern). Islands seem to play a similar role as real rods: they create a void in the line pattern, yet they do not change its topological structure by folding the line in any way. Complex folds are also visible in the upper part of the pattern but are not easily accounted for.

Finally, we have plotted in Fig. 3.6 (d) many hyperbolic periodic orbits (our numerical scheme to detect periodic orbits, described in the previous section, can only detect hyperbolic orbits). They braid in a very complicated fashion, yet the structure of the pattern in Fig. 3.6 (c) cannot be related to their position.

Except for special cases such as Boyland's braiding protocol, it is therefore difficult to describe the mixing pattern (that is, its spatial structure and not only its exponential growth coefficient) with ghost or real rods. Fig. 3.8 shows a different example where rods completely determine the line stretching and pattern. Taffy (candy) is stretched and folded by four pulling arms. However, there is no hydrodynamical flow in this taffy machine, but taffy is just stretched and pulled tight on its prongs. However, we would like to answer some questions about rods and the mixing pattern they create:

- in which situations do rods completely determine the mixing pattern as in Fig. 3.6 (a) ?
- How can we describe the line pattern created by the rods as in Fig. 3.6 (a) ? The line pattern is indeed similar in a stroboscopic map: new line segments are added by a new stretching period, yet the shape of the pattern stays the same.
- Can we find a small number of "efficient" ghost rods that determine the mixing pattern as the rods in Fig. 3.6 (a) ?

In the next paragraph, we attempt to give some hints about the answers: we show that parabolic periodic points are good candidates for efficient ghost rods, as they fold lines around them.

3.2.3.2 Parabolic points and folds

A more detailed version of this paragraph can be found in our paper [117].

Results by Katok and Boyland cited in the paper included in the previous section state that there exist a sequence of *orbits* whose topological entropy converges to the entropy of the flow. However, our method to measure the entropy of the flow combined different orbits to approach efficiently the entropy of the flow. After the submission of the paper [44], we started to use an algorithm written by Moussafir [72], which allowed us to compute rapidly the entropy of long braids an arbitrary precision. Of course, we detected only a finite number of periodic orbits (there exists an infinity of them). We found that the topological entropy of these hyperbolic orbits – that is the entropy of the braid built with the n points of period-n orbit –

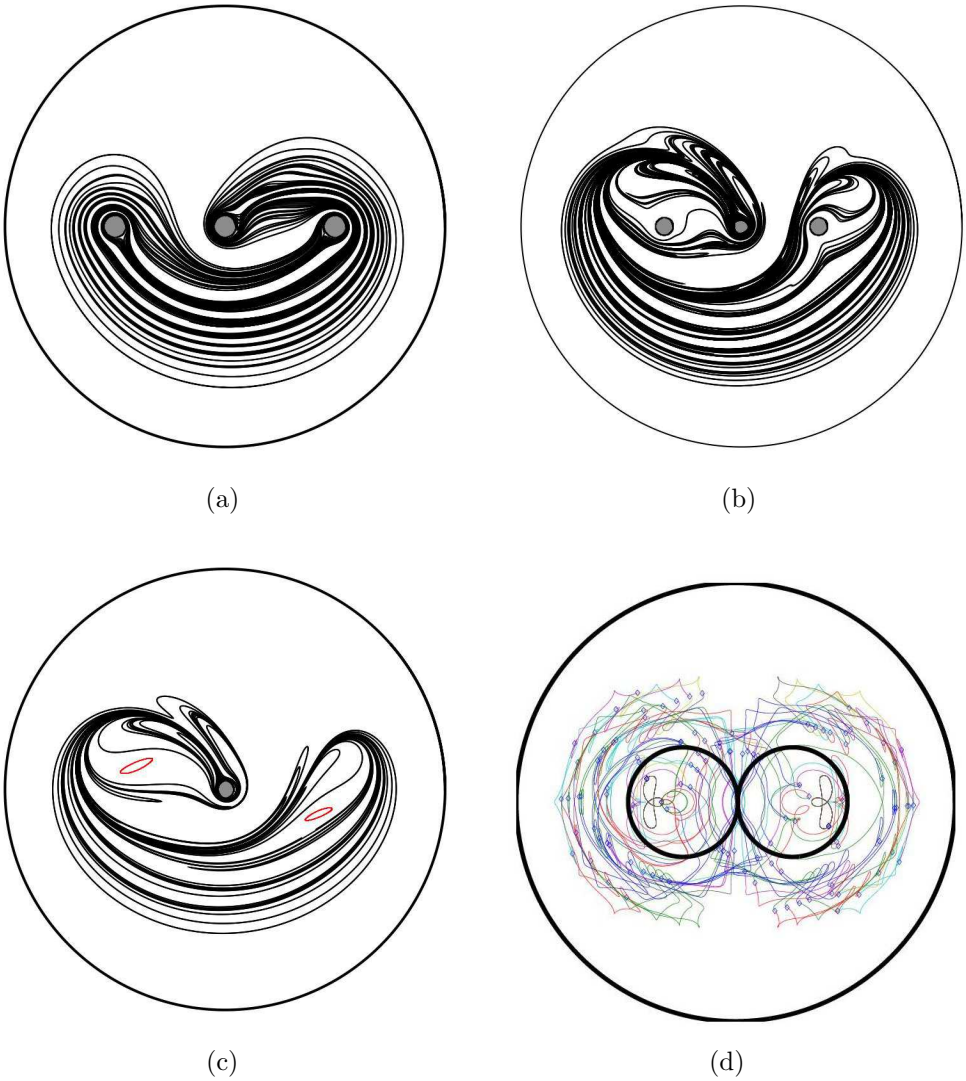

Figure 3.6: Numerical simulations of 2-D rod stirring protocols in the Stokes flow regime. (a) Shape of a material line stretched by the rods movement in the Boyland protocol (the two leftmost rods are exchanged clockwise, then the two rightmost rods are exchanged anticlockwise). The line pattern can be easily described: lines are loosely pulled tight between rods (i.e. they are parallel and have little curvature), but they are strongly folded around rods (i.e. they have a high curvature close to the rods). In a topological sense, the line pattern is therefore uniquely determined by the braiding rods. (b) Line pattern created by a rod travelling on a figure-eight path and braiding around two fixed rods inside the two loops of the figure-eight. Although the braid of the three rods is non trivial, the three rods do not completely determine the pattern as in (a) : additional folds are visible, moreover the fixed rods do not fold the pattern around them. (c) Line pattern for a single rod moving on a figure-eight path, that creates two elliptical islands around which it braids non-trivially. As for fixed rods, islands do not deform much the and additional folds are visible elsewhere in the domain. (d) Periodic hyperbolic trajectories detected numerically for the same protocol as (c). Hyperbolic points do not deform the line pattern either.

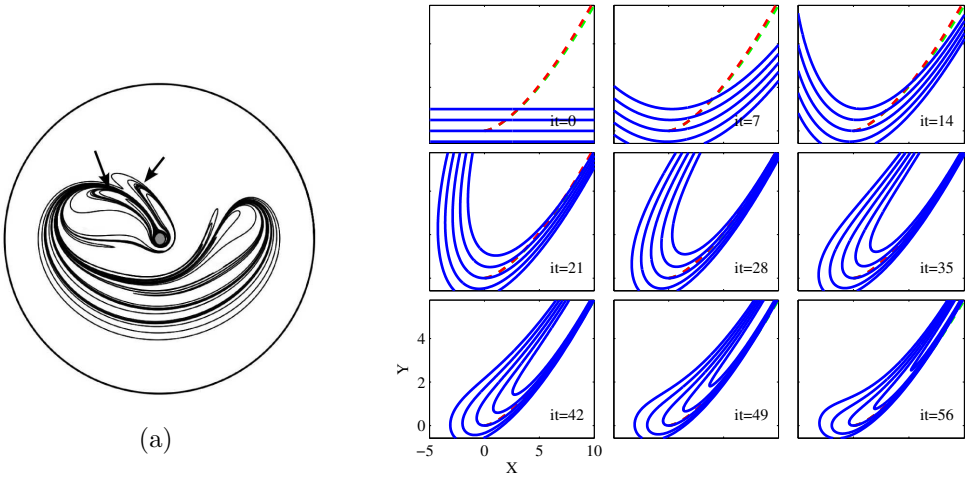

(a) (b)

Figure 3.7: (a) Line pattern for a version of the figure-eight protocol. Nested folds are visible in the upper part of the pattern. (b) Parallel lines are iterated by the map 3.24 for the case $\gamma = 1$. Lines are folded in a nested way on the unstable manifold (red dashed line) of the parabolic point at $(0, 0)$. Curvature increases near the parabolic point under successive iterations of the map. The resulting pattern is a big nested fold that can also be found in real flows as in (a). (This plot is taken from [117])

did not provide such a good estimate for the entropy of the flow compared to the entropy obtained with combinations of different orbits. Nevertheless, we know from the study of circle diffeomorphisms that orbits with entropies as close to the flow entropy as desired *do exist* – we just did not detect them. Once again, the special case of Boyland's braiding protocol is an illustrative one, as for this protocol the flow entropy measured by the line stretching rate equals (up to numerical precision) the entropy of the pigtail braid built with the three rods. We therefore expect that efficient ghost rods, i.e. orbits with a high entropy, are characteristic of the mixing pattern structure as the real rods of the pigtail protocol are. We have already mentioned that hyperbolic or elliptic periodic points are poor candidates, since material lines align with the unstable direction of hyperbolic points and avoid elliptical islands.

We are only left with the degenerate case, that is *parabolic points*. The linear part of the first-return map near a parabolic point has at least one eigenvalue equal to ± 1, leaving only two possibilities: $\mathcal{M}$ is the identity transformation, or is equal to the identity plus a nilpotent term as in Eq.

(3.19). The first case corresponds, for example, to escape points on no-slip walls and will be discussed in detail in Chapter 4. We're interested here in the second case, as we will see that such points indeed *fold* material lines around them as real rods do.

The linear part of the first-return map does not describe how material lines are deformed by the flow (this linearization leaves invariant horizontal lines $y = C$). The first non-linear terms must be taken into account, so that a general form of the first-return map reads

$$X_{n+1} = X_n + \alpha Y_n + aX_n^2 + bX_nY_n + cY_n^2 \quad (3.21)$$
$$Y_{n+1} = Y_n + dX_n^2 + eX_nY_n + fY_n^2. \quad (3.22)$$

It is explained in [117] how this general expression can be transformed into the following simpler one by a linear transformation and a near-identity area-preserving quadratic transformation:

$$X_{n+1} = X_n + Y_n + \gamma X_nY_n \quad (3.23)$$
$$Y_{n+1} = Y_n + \gamma\left(\frac{1}{2}X_n^2 + X_nY_n\right) \quad (3.24)$$

The map transforms a short horizontal segment passing through the periodic point (i.e., of equation $Y = 0$) into an arc of parabola defined by $Y = \gamma/2X^2$ – hence the term *parabolic* point. The map therefore causes a straight line to *fold*. Moreover, a set of parallel straight lines are packed together in a set of nested folds by the map, as shown in Fig. 3.7 (b). These folds look exactly like the more complex parts of the mixing pattern in stirring protocols, such as the figure-eight protocol shown in Fig. 3.7 (a). The recurrent nested structure of the folds in mixing patterns of experiments or simulations advocates the presence of a periodic point inside the folds. We are not able to detect numerically such marginally stable points. Nevertheless, parabolic points and folds are important structures: a promising direction towards a topological description of the flow would be to understand how different folded parts of the mixing pattern are swapped by the flow – and consequently braid.

In the next section, we will again consider periodic points, this time in open flows. Instead of considering their motion from a topological point of view, we will describe how periodic orbits determine transport to and from the mixing region.

Figure 3.8: Four-pronged taffy puller. In this candy machine, the four rods braid in a non-trivial way and hence stretch taffy exponentially. As taffy is pulled tight on the rods – contrary to material lines in fluid flows –, the interface growth rate is exactly the topological entropy of the rods braid.

3.3 Open flows: the chaotic saddle and its manifolds

The topological approach of mixing presented in the previous section provides (i) an original way to compute the topological entropy of a flow, and (ii) new insights for understanding mixing processes: in chaotic mixing, the complexity of a flow arises from the braiding of periodic orbits – ghost rods – which subsequently stretch material lines. In this section, we describe how periodic points are key ingredients for mixing also in open flows [111]. We relate the residence-time distribution of fluid particles inside the mixing region to a set of bounded periodic orbits that stay forever inside the mixing region. This set is called the chaotic saddle, as such orbits are highly unstable due to the main flow. A dynamical systems analysis allows us to describe transport properties in our mixer in terms of such periodic points and their invariant manifolds.

3.3.1 Chaotic saddles in open flows

While there exists a huge literature about mixing in closed flows, open flows have received comparatively less attention, and understanding of open-flow mixing processes clearly lags behind its closed-flow counterpart. This situation might stem from an intrinsic difficulty of describing mixing in open flows, where fluid particles initialized upstream of the mixing region might well experience some stretching and mixing while they stay inside the mixing region, yet they are doomed to leave it eventually to ensure flow conservation. Time-asymptotic quantities cannot be used to characterize the *transient* stretching process experienced by fluid particles before they

are swept away by the main flow, and additional framework is required. For instance, stretching experienced by fluid particles during their stay inside the mixing region do not correspond to a mean Lyapunov exponent as in closed flows.

Once again, periodic orbits of the flow are useful objects to qualify mixing. For open flows, such orbits indeed allow a description of particle histories. Chaotic advection in open flows has been associated to the set of unstable periodic orbits trapped inside the mixing region that goes under the name of *chaotic saddle* [45, 54, 109]. This zero-measure set consists of orbits that never leave the mixing region and strongly influences most Lagrangian trajectories, insofar as a fluid particle enters the mixing region along the *stable manifold* of the chaotic saddle (i.e. the set of trajectories converging to the chaotic saddle as time goes to infinity), shadows periodic trajectories for some time while in the mixing region, and finally leaves it along the *unstable manifold* of the chaotic saddle (the set of trajectories escaping from the chaotic saddle). It might seem conceptually difficult to imagine bounded orbits surviving to the main flow: the reader might try to picture the chaotic saddle as permanent whirlpools in the meanders of a river. A trivial example of never-escaping orbits consists e.g. in rods boundaries. Such orbits are found on a multifractal set of zero-measure [111]. For chaotic advection, some orbits braid in a non-trivial braid: points are topological obstacles to lines as in closed flows, thus the chaotic saddle is composed of ghost rods. Stretching imposed by braiding results in a complex dye filamentary pattern that can be seen in Fig. 3.9 (c)-(d).

Neighboring fluid particles in the far upstream might leave the mixing region at different exit times and locations – a phenomenon called *chaotic scattering* [31, 81] that has applications in many other domains such as nuclear physics. In the study of open-flow fluid mixing, much attention has been paid to the multifractal properties of the chaotic saddle and its manifolds in order to characterize the filamentary mixing patterns resulting from the stretching of an initially localized impurity [53, 87, 104, 85, 111].

In particular, the celebrated Kaplan-Yorke formula [55] conjectures the following relation between the information dimension of the unstable manifold D_1, the Lyapunov exponent λ characterizing stretching close to the periodic orbits, and the escape rate α from the mixing region:

$$D_1 = 2 - \frac{\alpha}{\lambda}. \tag{3.25}$$

A naive interpretation of this formula is easily available: the more you stretch (hence the bigger λ), the more filaments are created that fill the domain. On the contrary, particles escape this stretching process at a rate α,

hence the pattern density decreases with α. Such insights have permitted to understand the complicated shape of biological patterns, e.g. phytoplankton structures in the Gulf stream [133, 98]. Reaction rates of active advected particles can also be related to the fractal structure of the chaotic saddle [119, 111, 97, 110].

Still, quantitative description of homogenization for a diffusive passive scalar impurity, that might be of interest e.g. for industrial open mixers, is still lacking. Most previous studies have instead concentrated on numerical integration of pointlike particles trajectories [53, 87, 85, 111]. As a notable exception, Sommerer et al. [104] have realized the only – to the best of our knowledge – experimental study of chaotic mixing in an open flow. The authors have observed the fractal filamentary structure created from an initial dye blob advected in the Von-Karman alley wake of a cylinder– yet more to the purpose of proving chaotic scattering than of characterizing homogenization processes.

Here, we study the channel flow mixer described in Chapter 2: our stirring device is designed to model a realistic industrial active mixer (in e.g. food or chemical engineering), contrary to most previously studied open-flow systems [53, 104, 85, 111]. A noteworthy exception concerns mobile point vortices studied by Neufeld and Tél [76], which share similarities with our moving rods. We compare dye advection experiments for different stirring frequencies of the butterfly version of our channel mixer (experimental details are given in Chapter 2), that is, rods travel with the flow near the channel sides, and against the flow in the channel central region (Fig. 3.9). Changing the stirring frequency allows to tune the lifetime of chaos, that is the mean number of stirring periods spent by a particle inside the mixing region:

$$\alpha = \frac{d}{UT} \tag{3.26}$$

(U is the mean velocity at the channel surface, d approximates the length of the mixing region along the flow direction and T is the stirring period). We report here results for $1/T = 1.5$ to 8 rpm, yielding values of α between 3.5 and 18.7 We do not increase further the stirring frequency for two reasons: for high frequencies, (i) unwanted 3-D effects caused by waves emanating from the rods start to perturb the mixing pattern; (ii) moreover two elliptical islands are then visible inside the mixing pattern (see Fig. 3.10), as the main current is not strong enough to destabilize them. We limit ourselves here to parameters where the chaotic region is fully hyperbolic, as elliptic regions might induce more complicated effects.

Our aim in this section is to propose a mixing scenario to describe the response of an open-flow mixer to an impurity. We show that the evolution

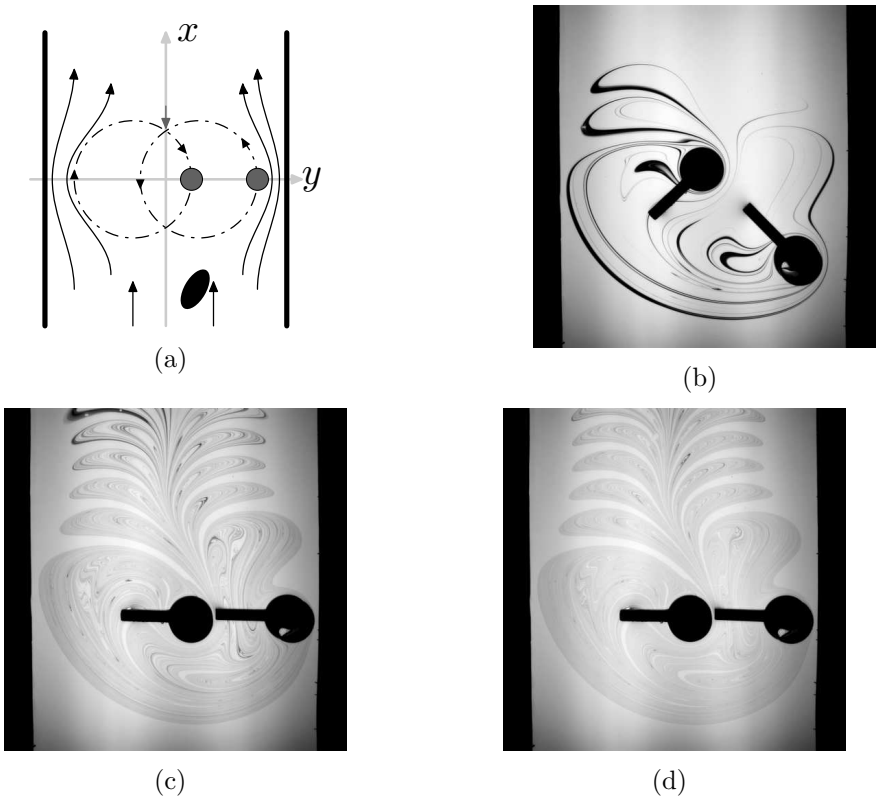

Figure 3.9: Mixing experiments conducted in an open-flow channel. (a) Flow schematic representation. Viscous fluid flows at a constant rate in a long channel. The flow is stationary far from a central mixing region where an "eggbeater flow" is realized by two cylindrical rods travelling at a constant linear speed on opposite directions on two intersecting circles. Rods travel against the flow in the central region of the channel and with the flow along its sides, so that in the rods vicinity, fluid flows preferentially along the channel sides and enters the mixing region through an injection point at its top. This results in a heart-shaped mixing region with a cusp at its top corresponding to the path along which fluid enters and leaves the mixing region ((b)-(d)). A small blob of dye is injected upstream of the mixing region; a typical evolution is shown in (b)-(d). (b) Dye pattern 5 stirring periods after dye injection. A fraction of the blob has not entered the mixing region at all, and forms thick black strips that can be seen downstream. The remainder of the blob has been caught inside the mixing region where it is stretched and folded. (c) and (d) Dye pattern after (resp.) 8 and 11 stirring periods. As time goes on, lobes of partly mixed fluid are torn away from mixing region, while new white fluid is incorporated inside the mixing pattern. Global dye intensity therefore decreases, yet a permanent mixing pattern sets in.

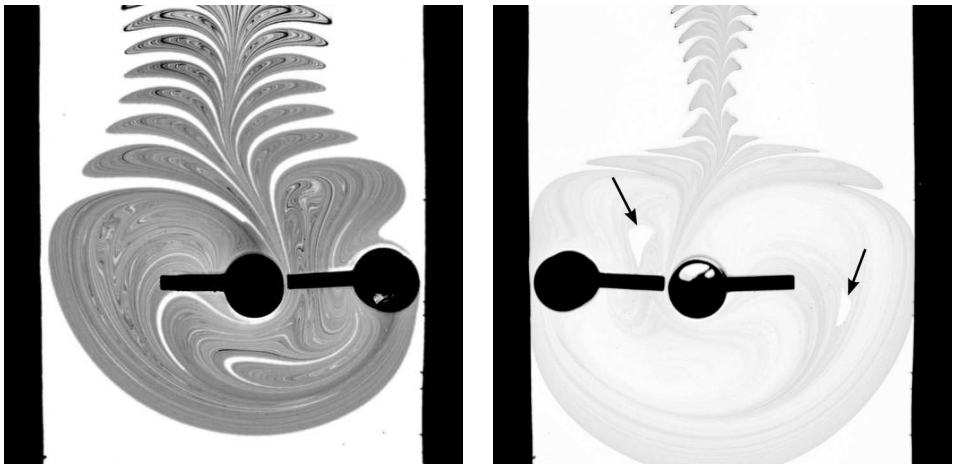

(a) (b)

Figure 3.10: (a) Asymptotic pattern for a stirring frequency $1/T = 3$ rpm. No elliptical islands are visible inside the mixing region. (b) Asymptotic pattern for $1/T = 8$ rpm: two small islands are visible inside the mixing region.

of a dye blob can be decomposed into two phases: an initial transient where dye particles escape downstream without experiencing much stretching, and an asymptotic regime when the dye pattern has converged to an invariant function with exponentially decreasing amplitude. We describe a method for determining a chart of upstream fluid particles contributing to either regime. This section is organized as follows. Residence-time distributions (RTD) obtained from dye concentration fields are presented in the next subsection. Short and long residence times are related to the structure of the chaotic saddle and its manifolds. Finally, lobe dynamics allows us to describe precisely transport mechanisms.

3.3.2 Residence-time distributions

We follow the response of the mixer to the initial blob during a large number of stirring periods (during about 15 min, corresponding to 40 to 100 periods, depending on stirring frequency). As the blob is advected by the main flow to the mixing region, a fraction of the blob is caught by the rods inside the mixing region, where it stretched and folded (see the filaments interwoven on the rods in Fig. 3.9 (b)). However, an important fraction does not enter at all the heart of the mixing region (basically the area swept by the rods), but escapes instead immediately downstream without experiencing much stretching, resulting in thick high-contrast structures that can be

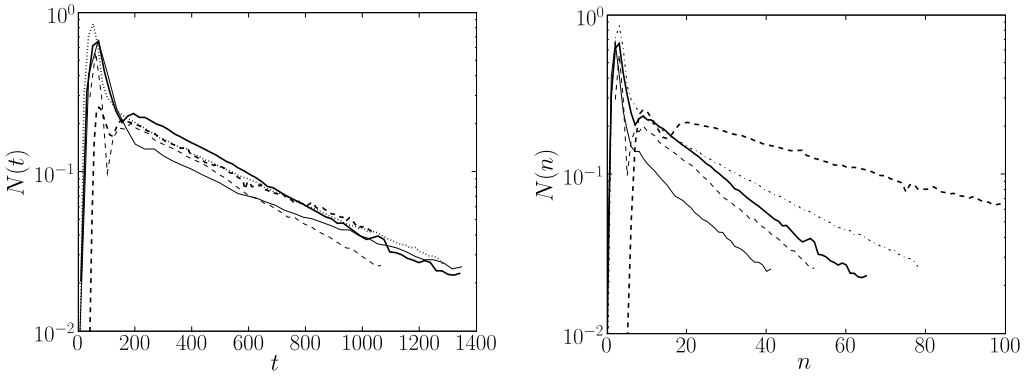

(a) (b)

Figure 3.11: (a) Fraction of the initial blob $\mathcal{N}(t)$ remaining inside the mixing region after time t, for different stirring frequencies (solid line: 2 rpm, bold solid line and dashed line: 3 rpm, dotted line: 4 rpm, bold dashed line: 8rpm). All experiments exhibit a short transient characterized by a high peak, followed by an asymptotic exponential regime. (b) $\mathcal{N}(n)$ plotted against the number of stirring periods n. More periods could be explored fore high stirring frequencies as dye contrast then decays slower with n.

seen in the downstream region in Fig. 3.9 (b). It is of high importance to characterize those elements, which contribute to the worst mixed (i.e. with highest dye contrast) state than can be measured downstream. At longer times, new pure fluid is continuously incorporated into the mixing region to be homogenized with the remaining dye, while at each period a lobe [94, 16] of the partly mixed pattern is conversely torn away from the mixing region by the main flow, resulting in the flower shape that can be seen downstream in Fig. 3.9 (c)-(d). Despite this dye mass loss, chaotic mixing inside the mixing region rearranges dye filaments on a similar pattern (consider the striking likeness of patterns in Fig. 3.9 (c) and (d)) – yet with a weaker contrast. In this chapter, we concentrate on accounting for the RTDs: a more refined description of the dye pattern, and of underlying homogenization mechanisms, will be provided in Chapter 5.

The latter typical scenario describing the history of a blob can be quantified by computing residence-time distributions (RTDs) inside the mixing region for dye particles, or equivalently the fraction $\mathcal{N}(t)$ of the initial blob remaining inside the central region after time t – which is the integral of the RTD (in his seminal work about residence-time distributions in chemical engineering, Danckwerts [30] considers both quantities). Results for

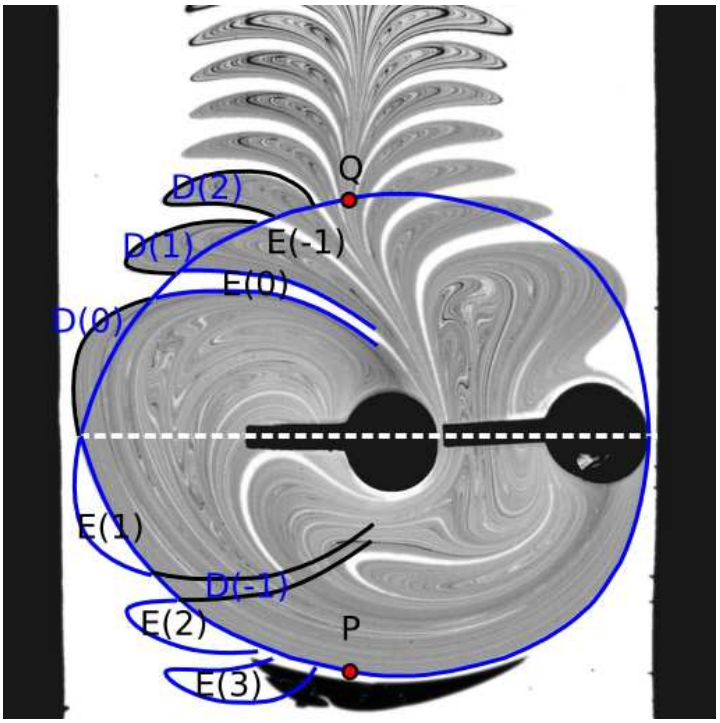

Figure 3.12: A picture of the initial dye blob (dark black spot) is superposed with the asymptotic mixing pattern. Intersections of the initial blob with mirrored images of downstream lobes along the axis $x = 0$ are eventually caught inside the mixing region, while parts between such lobes are directly advected downstream without being stretched. Indeed, the asymptotic downstream pattern traces out the unstable manifold of the chaotic saddle $\mathcal{W}_u$, which is mirrored into the stable manifold $\mathcal{W}_s$ because of flow symmetries. More precise transport properties can be predicted from the heteroclinic tangle originating from the separation point P (that separates trajectories going left or right) and its mirror reattachment point Q (see text).

Table 3.1: Decay rates and predictions

$1/T$ (rpm)	β_{exp}	UT/d	$\eta UT/d$
2	0.098	0.167	0.093
3	0.042	0.111	0.046
3	0.046	0.111	0.046
4	0.029	0.083	0.031
8	0.013	0.042	0.010

four different stirring frequencies ($1/T$ = 2, 3, 4 and 8 rpm, corresponding to $\alpha = 4.7$, 7, 9.3 and 18.7) are shown in Fig. 3.11. $\mathcal{N}$ is plotted both against time t and the number of stirring periods $n = t/T$. For each experiment, two phases are visible on these plots: a high peak for early times, corresponding to fluid that escapes very rapidly, resulting in the poorly mixed strips in Fig. 3.9 (b), and an exponential tail $\mathcal{N}(t) \sim \mathcal{N}_0 \exp(-t/\tau)$ from a few periods after dye arrival in the mixing region. This exponential regime supports the above observation based on the mixing pattern: the main flow periodically tears away a fixed area of the mixing pattern, while the stirring protocol rearranges dye filaments back on the persisting pattern. We might have therefore expected that a constant fraction β goes away with the flow at each period, resulting in an exponential RTD:

$$\mathcal{N} = \mathcal{N}_0(1-\beta)^n = \mathcal{N}_0 \exp[t/T \times \log(1-\beta)]. \tag{3.27}$$

A naive estimate of β can be gained from noticing that the fraction of the mixing region that goes away at each period is controlled by the flowrate. We may indeed consider that the main flow translates the mixing pattern by a distance UT at each period, so that the cut fraction is $\beta \sim UT/d = \alpha^{-1}$ where d is the length of the mixing region along the flow direction. This expected scaling leads to

$$\mathcal{N} = \mathcal{N}_0 \exp[t/T \times \log(1-UT/d)] \sim \mathcal{N}_0 \exp[-Ut/d] \tag{3.28}$$

for large α, that is a decay rate independent of the stirring frequency. Indeed, the log-linear plot of $\mathcal{N}(t)$ in Fig. 3.11 shows comparable slopes for different stirring frequencies. However, measured values β_{exp} for five different experimental runs are given in Table 3.1, together with the expected value UT/d: it is obvious that UT/d systematically overestimates the measured β. How can we explain this trend ? Flowrate actually only determines the flux of fluid across a channel crosssection. Mass transfer from upstream

to downstream regions does not occur only through the mixing region, but also from fluid accelerated on the sides by the rods passing. This set of escaping particles, if marked with dye, contributes to short residence times and ill-stretched structures. For long times, only unmarked fluid flows in such a way along the sides, so that the downstream lobes occupy only a fraction of the channel width. In our shallow channel, the velocity profile is almost flat at the free surface (e.g. much flatter than a Poiseuille flow). We therefore approximate that fluid flowing out the mixing region contributes a fraction $\eta = \ell_{\text{eff}}/\ell$ to the flowrate, where ℓ is the channel width and ℓ_{eff} the width of the downstream mixing pattern. We measure ℓ_{eff} as the length between the tips of escaping dye lobes, which is constant for asymptotic times. Values of the corrected prediction for the escape rate $\eta UT/d$ are given in Table 3.1 and approximate well β_{exp} (to within $\sim 10\%$). The worst matching occurs for $1/T = 8\,\text{rpm}$, as in this case the lobes pattern does not reach its asymptotic width within the picture field. Note that ℓ_{eff} decreases with increasing stirring frequency, as can be seen in Fig. 3.10.

Our crude above analysis provides a satisfactory approximation for the RTD decay rate in terms of mean flow parameters (U, T, d) and geometry of the dye pattern (ℓ_{eff}). Additional insight about the RTD and trajectories contributing to either regime can yet be gained by considering the chaotic saddle and its manifolds.

3.3.3 Towards a chart of residence times

As already stated, fluid particles enter the mixing region along the stable manifold of the chaotic saddle $\mathcal{W}_s$, follow a periodic orbit during some time, jump to another orbit, and leave the chaotic saddle along its unstable manifold $\mathcal{W}_u$ after a few iterations of this shadowing process. In particular, a fluid particle with no intersection with $\mathcal{W}_s$ never enter the mixing region, but are instead directly swept away by the flow. Characterizing these ill-mixed particles requires to determine the overlap between the initial dye blob and $\mathcal{W}_s$. $\mathcal{W}_s$ is not directly visible in our experiments ; however many previous studies [111] have pointed out that after a long time, downstream lobes come from fluid elements that have spent a long time inside the mixing region – and hence were initially close to $\mathcal{W}_s$; so that they trace out directly $\mathcal{W}_u$. Up to diffusion, pictures of the dye pattern for long times such as Fig. 3.9 provide a picture of $\mathcal{W}_u$. We now make use of symmetries in our flow: $\mathcal{W}_s$ is formally defined as the union of trajectories converging to the chaotic saddle when time goes to infinity, and $\mathcal{W}_u$ as the union of trajectories converging to the chaotic saddle when time goes backwards to minus infinity. We therefore obtain $\mathcal{W}_s$ from $\mathcal{W}_u$ by switching to backward time $t \to -t$.

What does it mean in our flow ? Actually, changing t to $-t$ reverts the direction of the main flow, as well as the direction of the rods on their paths – that is, exactly the same flow, yet mirrored along the $x = 0$ axis! We can thus picture $\mathcal{W}_s$ by "flipping" the downstream pattern along the $x = 0$ axis and searching for overlaps between the initial blob picture and the flipped lobes, i.e. $\mathcal{W}_s$. The principle is shown in Fig. 3.12, where E(2) and E(3) are the respective flipped pictures of the latest separated lobes contours D(1) and D(2) (this terminology borrowed from lobe dynamics theory [94, 16] is explained later on). We have superposed a picture of the initial blob (the black spot at the bottom) and a picture of the asymptotic pattern that allows us to determine the location of the flipped lobes. The intersection of the blob with $E(3)$ and $E(4)$ will enter the mixing region and contribute to the exponential part of the RTD; on the contrary, parts between two lobes are far from the stable manifold and contribute to the short-time peak of the RTD. The flipped image of the asymptotic pattern therefore gives a chart of initial conditions that will be well or ill mixed, whether they intersect $\mathcal{W}_u$ or not. This can be of high importance for possible applications, e.g. if one wishes to dissolve a pollutant into the main flow . Injection of the pollutant at the heart of one of the flipped lobes will lead to a far better dispersion than at a location that would only intersect partly a lobe, if at all. In particular, an initial condition located on the sides of the channel, that is for $|y| > \ell_{\text{eff}}/2$ is not caught at all inside the mixing region: Fig. 3.13 shows the pattern obtained from an initial condition with no such intersection. No part of the blob has been caught by the rods, and the resulting pattern is very badly mixed. Our chart of initial conditions sheds a new light on our previous assertion that a fraction $\eta = \ell_{\text{eff}}/\ell$ flows through the mixing region and contributes to the exponential part of the RTD: these particles come from the set of particles overlapping with the flipped lobe pattern of width ℓ_{eff}.

3.3.4 Lobe dynamics

We can describe transport mechanisms in our mixer more precisely using lobes dynamics theory [94, 16]. Two periodic points play a special role inside the chaotic saddle: a period-1 separation point which we call P at the bottom of the mixing pattern – its stable manifold corresponds to the separation between trajectories going left or right – and the symmetric reattachment point Q (see Fig. 3.12). P determines the lowest frontier of the mixing region. The unstable manifold of P, $\mathcal{W}_u$(P) is materialized by the border of the mixing pattern, as dye leaves P by being stretched along the filament at the border. Because of symmetry, $\mathcal{W}_s$(Q) is obtained by taking

the mirror image of $\mathcal{W}_u(\mathrm{P})$ along the axis $x = 0$. Both curves (represented in Fig. 3.12) intersect on the y axis. However, manifolds are invariant curves, hence the iterates of the intersection point by the Poincaré map $\mathcal{M}$ and its time-inverse $\mathcal{M}^{-1}$ still belong to both curves, resulting in a double infinite series of intersections between $\mathcal{W}_u(\mathrm{P})$ and $\mathcal{W}_s(\mathrm{Q})$ (we call *primary intersection point* the first intersection lying on the $x = 0$ axis). As a result, both curves are intricated in a very complicated way: the first intersections have been sketched in Fig. 3.12. A single intersection point therefore gives rise to a so-called *heteroclinic tangle*. This interwoven structure completely determines transport in and out the mixing region: we know how arcs of both manifolds are mapped one to another, but because of flow continuity, lobes bounded by a portion of $\mathcal{W}_u$ and another of $\mathcal{W}_s$ are also mapped one to another by the Poincaré map (see [16] or [49] for more details). As a result, an *entrained* lobe (using the terminology of [16]) $\mathrm{E}(n)$ is mapped to $\mathrm{E}(n-1)$ by $\mathcal{M}$. The portion of fluid E(3) is transformed into E(2), etc. However, as $\mathcal{M}$ preserves phase space orientation, the last lobe before the primary intersection point, $E(1)$, is mapped into $E(0)$ inside the mixing region this time. Conversely, lobes extracted from the mixing region are obtained by considering $\mathcal{M}^{-1}$, i.e. the mirror image of entrained lobes along $x = 0$, so that $\mathrm{D}(-1)$ (see Fig. 3.12) is mapped to D(1), outside the mixing region, D(1) is mapped to D(2). As iterated lobes $\mathrm{D}(n)$ come closer to Q, their intersection with $\mathcal{W}_s(\mathrm{Q})$ gets smaller: to ensure mass conservation, they have greater extension in the transverse direction, resulting in high stretching. We can now provide a more rigorous definition of the mixing region, which we choose to be bounded by $\mathcal{W}_u(\mathrm{P})$ and $\mathcal{W}_s(\mathrm{Q})$ up to the primary intersection point: indeed, fluid out of this region in the upper half-plane $x > 0$ never enters the mixing region again, but is advected downstream, whereas outside fluid in the lower half-plane is advected upstream by $\mathcal{M}^{-1}$. A measure of transport in our mixer is given by the area of one elementary lobe, which can be determined by drawing the construction of $\mathcal{W}_u(\mathrm{P})$ and $\mathcal{W}_s(\mathrm{Q})$ show in Fig. 3.12. This method proceeds along the same lines as our previous criteria relying on the width of the mixing pattern – the latter method being perhaps easier to implement.

Complicated lobe-shaped mixing patterns resulting from a heteroclinic tangle in an open flow have already been observed in simulations [86] and experiments [49], yet it is instructive to see how important features of the Poincaré map as periodic points, manifolds and transported lobes can be directly determined from the asymptotic mixing pattern. All these information can be obtained from a single picture of the pattern at long times, following a few successive steps (see Fig. 3.12):

Figure 3.13: A dye blob initialized with no intersection with $\mathcal{W}_s$ has been carried away downstream without being caught by the rods. Mixing is very inefficient for this initial condition.

- We trace the unstable manifold $\mathcal{W}_u(\mathrm{P})$ by following the border of the mixing pattern from its lower part.
- We trace its mirrored image $\mathcal{W}_s(\mathrm{Q})$.
- Q is obtained as the intersection between $\mathcal{W}_s(\mathrm{Q})$ and the central vein on which all downstream lobes accumulate. P is then obtained as the mirror image of Q.
- The intersections between $\mathcal{W}_u(\mathrm{P})$ and $\mathcal{W}_s(\mathrm{Q})$ unveil elementary transported lobes $\mathrm{E}(n)$ and $\mathrm{D}(n)$.

Simple geometric considerations based on the asymptotic mixing pattern allow us to determine a "chart" of initial conditions leading to: (i) particles that escape immediately downstream, if they do not intersect the stable manifold $\mathcal{W}_s$, (ii) or particles caught inside the mixing region. Note that a single blob that intersects $\mathcal{W}_s$ yields the whole asymptotic pattern and therefore provides a chart that can be used to predict the history of any other blob. Here, we have concentrated on elements with short residence times that lead to bad mixing; we will study in more details the asymptotic mixing pattern in Chapter 5.

In the language of chemical engineering, our device consists of a perfect mixer – the chaotic saddle contributing to the exponential part of the RTD – in parallel with a plug flow on the sides of the channel. To pursue further the analogy between chemical engineering analysis of RTDs [30, 60] and dynamical systems, elliptical islands observable inside the mixing region for high-frequency stirring are equivalent to dead zones.

It is important to note that our mixing system in its butterfly version shows a pure hyperbolic behavior that has rarely been observed before in open-flow systems: for example, the well-studied Van Karman alley takes place in the wake of a fixed cylinder whose surface is a degenerate parabolic fixed point, resulting in an asymptotic algebraic RTD (after a short exponential phase) [53, 104]. In the same way, leapfrogging vortex pairs studied by Péntek et al [86] also lead to asymptotic algebraic RTD, due to stickiness on KAM tori. On the contrary, we are able in our mixer to observe an exponential regime during up to 70 stirring periods. We will address in Chapter 5 non-hyperbolic phenomenons that can be observed in the breaststroke protocol, because of parabolic stagnation points on the channel sides.

3.4 Conclusion

In this chapter, we have first introduced the dynamical systems approach to fluid mixing, that relies in particular on characterizing the *stretching* experienced by fluid particles. In particular, finite-time stretching exponents converge asymptotically to the Lyapunov exponent of the flow. We have also introduced different kinds of periodic structures, that can be hyperbolic, elliptic, or parabolic. We have then proposed an alternative characterization of the flow complexity, that consists in computing the braiding of periodic orbits, whose topological entropy provides a lower bound for the growth rate of a material lines, that is the topological entropy of the flow. We have found that few orbits still permit to obtain good estimates for the topological entropy of the flow. This method provides an original description of chaotic advection, where mixing is described in terms of topological entanglement, contrary to the usual view based on stretching – a metric description.

Periodic orbits are also paramount in open flows: even in the case of a global advection, an infinity of unstable periodic orbits survive in the vicinity of the stirring rods, forming the so-called *chaotic saddle*. Fluid enters the mixing region along the stable manifold of the chaotic saddle, and leaves it along its unstable manifold. In particular, particles initialized regions not covered by the stable manifold escape directly downstream without being caught by the rods. Using the symmetries of the flow, we have described a simple geometric method that allows to predict whether particles in the upstream region will escape directly, or be caught in the mixing region. This partition into two sets of initial conditions also allows to estimate independently the mean residence time.

Up to now, we have only considered point-like particles that are not

submitted to diffusion . There is a major change of tack in the next two chapters, when we consider this time the homogenization of a *diffusive scalar field* by our mixing systems, both in closed and open flows. Nevertheless, we will again pay close attention to periodic structures, be them hyperbolic, parabolic or elliptic points, or manifolds of the chaotic saddle, that will be shown to have a strong influence of homogenization dynamics of the concentration field.

Chapter 4

Homogenization in closed flows

This chapter concerns the mixing of passive scalars, such as dye blobs homogenized by chaotic advection protocols described in Chapter 2. We take on here one of the most natural questions in mixing, that is: How fast does it mix ? Various approaches ranging from functional analysis [88, 64] to large-deviation analysis of the stretching distribution [5, 7], or multifractal formalism [80, 6] have provided insights into the structure of the mixing pattern and the decay rate of inhomogeneity, yet mostly for ideal systems, e.g. with random-time dependency (thereby avoiding transport barriers) or periodic boundary conditions. In particular, time-persistent spatial patterns have been observed in numerical simulations [88] as well as in dye homogenization experiments [95, 52], and these permanent structures have been related to the slowest decaying eigenmode of the advection-diffusion operator – hence the term *strange eigenmode* used to describe these structures, which was originally coined by Pierrehumbert in 1994 [88]. Eigenmodes amplitude decay exponentially with time at a rate determined by the corresponding eigenvalue, and an exponential decay of inhomogeneity variance has indeed been observed in various systems.

Our aim in this chapter is to illustrate the appearance of recurrent patterns for different time-periodic mixing protocols (that is, concentration fields at successive periods are strongly correlated). We show that such permanent fields have strong values (i.e. high departure from mean value) in regions where stretching is smallest. This occurs close to "least unstable" *periodic* structures where recurrent small stretching causes the inhomogeneity to decay slower. Persistent patterns are therefore identified with the unstable manifold of least unstable periodic structures, which can have different natures, e.g. hyperbolic, elliptic or parabolic points. While in-

homogeneity decays exponentially in a purely hyperbolic phase space, we show that non-hyperbolic structures lead to more complicated (and slower) dynamics, although recurrent patterns are still visible.

The chapter is structured as follows. In a first section, we describe how homogenization takes place through the combined action of stretching and diffusion, and we briefly review different approaches that have been employed in the literature to quantify the evolution of a scalar field homogenized by chaotic advection. Section 4.2 tackles the widely studied case of a fully hyperbolic baker's map. For this ideal system, we relate the structure of the strange eigenmode to the unstable manifold of the least unstable periodic point. Spatial stretching correlations are also shown to have a high impact on the speed of mixing. Section 4.3 contains the core of this chapter. We report on homogenization experiments conducted with the figure-eight protocol described in Chapter 2. We observe anomalously slow mixing, that is an algebraic – instead of exponential – decay of concentration variance. This behavior is shown to be generic for 2-D mixers where the chaotic region extends to fixed no-slip walls. In such systems, poorly stretched fluid escapes the wall at a slow rate (controlled by no-slip hydrodynamics) through the unstable manifold of parabolic points on the wall. These ill-mixed elements contaminate the whole mixing pattern, up to the core of the domain where stretching is bigger. A modified version of the baker's map that includes such a parabolic point on the boundary is shown to yield similar results as in the experiments and allows us to derive analytically the observed scalings for the concentration variance and distributions. Having understood the importance of boundaries for mixing dynamics, we briefly consider in Sec. 4.4 the case where a central chaotic region is protected from the wall by an annular elliptic region near the boundary. We retrieve exponential dynamics in this case. A final section offers concluding discussion.

4.1 Homogenization mechanisms

In this section, we shortly sketch how the concentration field of a passive scalar (e.g. dye) evolves from an initially segregated state towards homogeneity. For illustrative purposes, we will consider the example of a dye blob of initial scale l_{blob} smaller than the velocity field scale l_{v}, which is of the same order as the domain size L.

The evolution of the concentration field $C(\mathbf{x}, t)$ obeys to the advection-

diffusion equation.

$$\frac{\partial C}{\partial t} + \mathbf{v} \cdot \nabla C = \kappa \Delta C, \tag{4.1}$$

that is, the concentration field evolves through the combined effect of the velocity field that rearranges dye particles, and of diffusion that smoothes concentration gradient . A classical transformation of Eq. (4.1) consists in multiplying both sides by C and integrating it over the whole domain, which results after an integration by parts in the following equation for the evolution of the concentration variance $\sigma^2(C)$:

$$\frac{\partial \sigma^2}{\partial t} = -2\kappa \langle |\nabla C|^2 \rangle \leq 0. \tag{4.2}$$

Eq. (4.2) implies that the concentration variance decreases monotonically, showing that diffusion is an irreversible process. The above expression is also instructive to understand how homogenization takes place: the instantaneous variance decay rate is given by the mean square amplitude of the concentration gradients, weighted by the diffusivity κ. In an efficient stirring protocol, velocity fields are characterized by important shears that create large concentration gradients, resulting in fast homogenization.

In most cases, Eqs. (4.1) or (4.2) cannot be solved analytically, and the numerical integration of the PDE Eq. (4.1) is usually complicated by numerical diffusion. However, different approaches can be used to characterize homogenization, that are valid at different stages of the mixing process. These different steps are visible on the successive pictures of Fig. 4.1, which we had already described in Ch. 1. An initial blob (Fig. 4.1 (a)) is quickly deformed by the stirring velocity field (Fig. 4.1 (b)). At early times, the concentration spectrum evolves as finer scales are created, yet the variance is almost unchanged as the spatial scales are still too large for diffusion to be efficient (Fig. 4.1 (b)).

During a second stage (Fig. 4.1 (c)), elongated filaments are thin enough so that diffusion is efficient on the scale of a filament width . Diffusion causes the contrast of a dye filament to weaken, as can be seen in Fig. 4.1 (c) where intermediate gray levels are visible, whereas the mixing patter of (Fig. 4.1 (b)) is completely black and white. Different gray levels correspond to different stretching histories along the elongated image of the initial blob. At this stage, a successful approach consists in dividing the elongated blob in small Lagrangian chunks, and following the decay of each part in a comoving frame (see for example Refs. [23, 15] and references therein. A detailed derivation is also given in Ref. [115]. Finally, a complete experimental study and the corresponding analytical derivation for a vortex flow is performed

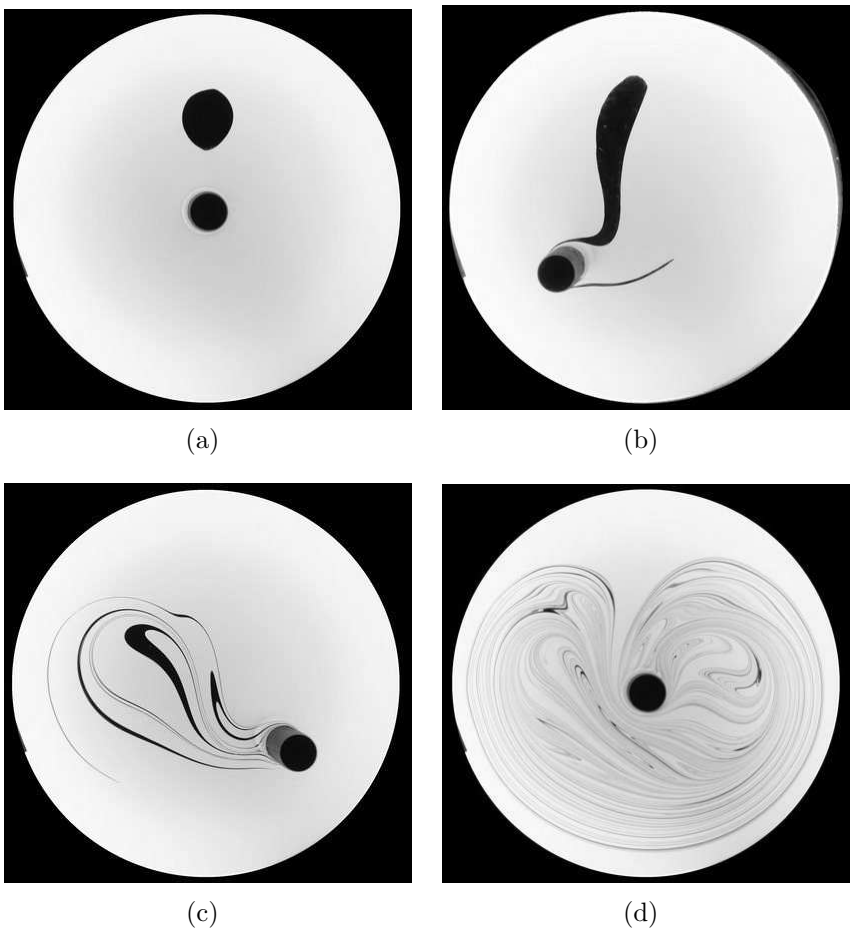

Figure 4.1: Successive homogenization steps of a dye blob by a time-periodic chaotic advection protocol. An initial blob (a) is deformed by shears in the velocity field (b). For early times, stretched filaments are still too broad for diffusion to be noticeable (b), and the concentration variance is constant. As time increases, filaments are thin enough (c) so that diffusion starts to act and dye strip fade away. Different gray levels correspond to different stretching histories. At this stage, concentration PDFs are successfully related to the distribution of stretching [7]. Later, different dye filaments start interpenetrating (d), so that the concentration field results from the averaging of concentration values coming from neighboring strips. Stretching correlations must then be taken into account.

in [125]). Very briefly, this approach consists in linearizing the velocity field $\mathbf{v}$ in the comoving frame, writing

$$\mathbf{v} = \sigma \cdot \mathbf{x} \tag{4.3}$$

where σ is the local strain tensor. A following step consists in neglecting the concentration variance along the stretching direction, and reducing the advection-diffusion equation to a 1-D equation where the concentration varies along the perpendicular direction to stretching x. Finally, introducing new dimensionless coordinates

$$\xi = x/s(t) \tag{4.4}$$

$$\tau = \int_0^t \frac{\kappa \mathrm{d}t'}{s^2(t')} \tag{4.5}$$

where $s(t)$ is the cumulated compression, yields the simple heat equation in the reduced coordinates

$$\frac{\partial C}{\partial \tau} = \frac{\partial^2 C}{\partial \xi^2} \,. \tag{4.6}$$

Given an initial condition, i.e. a concentration "step", it is easy to solve Eq. (4.6) and to obtain how the concentration profile is smoothened by diffusion . Of course, homogenization dynamics are entirely hidden in the evolution of the Jacobian of the coordinates transformation. The probability distribution of the scalar is therefore obtained from the distribution of stretching. In particular, Antonsen et al. [7] proposed a relation for the decay of variance in terms of the probability density function for finite-time Lyapunov exponents , which leads to an exponential decay for long times. Numerical studies have also shown that a good estimate of the decay rate can be derived using the global Lyapunov, in the case of a very homogeneous stretching [121].

However, the above reasoning is valid only as long as different filaments do not interact with each other. Yet, filaments are stretched, but also *folded*, so that many filaments are close to each other, and their diffusive boundaries interpenetrate ((Fig. 4.1 (d))). Let us precise this effect in the case of chaotic mixing. The width of a dye filament stretched at a constant rate stabilizes at the so-called Batchelor length $w_\mathrm{B} = \sqrt{\kappa/\lambda}$, where the effects of compression and diffusion balance (this is obtained by equating the width reduction of the mean square width due to stretching $w^2 \lambda dt$, and the broadening due to diffusion κdt during an infinitesimal time interval dt). In a realistic flow, stretching is not constant, but the width of a filament quickly adapts to the local stretching rate $\lambda(\mathbf{x})$. w_B is the smallest lengthscale that can be observed inside the concentration pattern: an initial blob has usually

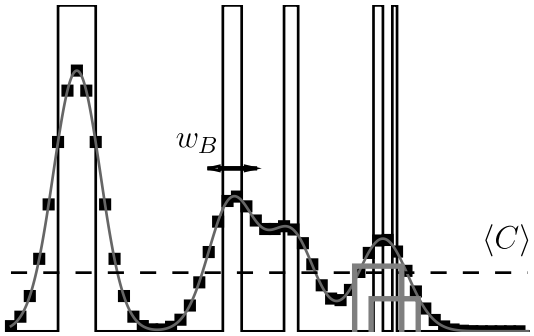

Figure 4.2: Due to the combined effect of stretching and diffusion, concentration profiles have a typical variation scale of $w_{\mathrm{B}} = \sqrt{\kappa/\lambda}$, where κ is the diffusion coefficient and λ a typical stretching rate. Stretched strips of dye (black) are smeared out by diffusion on a scale w_{B} (gray). The concentration C of a pixel x is then given by adding the concentrations coming from strips inside a box of size w_{B} around x.

a scale greater than w_{B}, so that it is stretched into many filaments that are compressed up to the diffusive scale w_{B}. After a strip has stabilized at the width w_{B}, the amplitude of the concentration profile decreases according to the further stretching experienced by the strip, to ensure mass conservation. As more and more filaments are created by chaotic stretching, the centers of neighboring dye filaments become closer and closer due to compression, so that the diffusive profiles of such filaments interpenetrate (see Fig. 4.2). Ultimately, homogenization takes place inside a box" of size w_{B} through the averaging of many strips that have experienced different stretching histories and have therefore different amplitudes.

Villermaux and Duplat [125], followed by Venaille and Sommeria [124], have proposed that the concentration field evolves by random addition of dye strips of different amplitude. Given this assumption, the concentration probability density function (PDF) evolves by self-convolution [125, 124], and the concentration variance is inversely proportional to the number of filaments averaged inside a box w_{B} (which we expect to be exponential in chaotic mixing). This approach has proved to be successful for turbulent flows [125]. However, this theory relies on the assumptions that (i) stretching is homogeneous, and (ii) neighboring strips have uncorrelated stretching histories, that are certainly not verified in physical chaotic mixing flows.

So far, the most satisfying explanation for the decay of inhomogeneity in chaotic mixing has been the *strange eigenmode* theory, initially proposed by Pierrehumbert in a 1994 paper [88]. The strange eigenmode is the second slowest decaying eigenmode of the advection-diffusion operator (the first

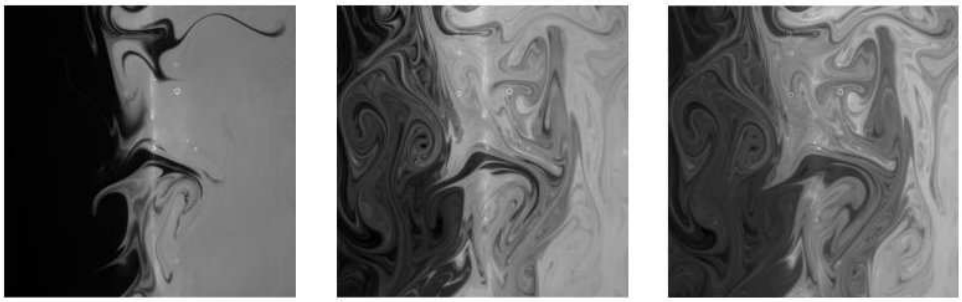

Figure 4.3: Experimental pictures of dye homogenization by a magnets array, taken from [95]. The three pictures correspond to the same experiment, as different stirring periods. The appearance of a permanent spatial pattern is clearly visible, consistently with the onset of a strange eigenmode.

trivial mode corresponds to a uniform concentration). We consider in the following the case of periodic velocity fields, where the strange eigenmode is an eigenvector of the Floquet operator . It decays at an exponential rate fixed by the corresponding eigenvalue. The projection of the initial concentration field on this eigenmode decays slower than the contributions to other eigenmodes, so that one expects the concentration field to converge rapidly to a permanent spatial pattern determined by the strange eigenmode, whose contrast decays exponentially. A simple physical picture of the strange eigenmode is given by noticing that as soon as many filaments are put in contact inside a box of width w_{B}, the filaments have visited a large part of the domain where they have experienced different values of stretching, therefore the decay rate is controlled by a *global* mode that varies on the scale of the domain and accounts for the spatial inhomogeneities of stretching [36, 48].

Since the seminal paper of Pierrehumbert, strange eigenmodes have been observed in many numerical studies [37, 131, 107, 89, 36]. The proposed evidence for strange eigenmode were (i) the onset of permanent spatial concentration patterns and (ii) an exponential decay for the concentration variance, whose rate depended only weakly on the diffusion . Recurrent spatial patterns have also been observed in experiments where a viscous fluid is stirred by an array of magnets [95, 52, 127](see also Fig. 4.3), yet the concentration decay seemed somewhat slower than exponential. In the following section, we briefly show how a strange eigenmode appears in a one-dimensional baker's map, and relate the spatial structure of the eigenmode to the regions of lowest stretching. Experimental evidence of a strange eigenmode is also provided in Sec. 4.4.

Let us note, however, that the existence of a strange eigenmode is not mathematically proved for general conditions. Indeed, the advection-diffusion operator acts in a Banach space of infinite dimension, and the existence of a weakest non-degenerated Floquet solution is not insured (for a rigorous discussion of this problem see Refs. [107, 64] and references therein). More precisely, for smooth velocity fields and non-zero diffusivities, it has been shown that the operator spectrum is discrete, yet eigenvalues might be degenerated (see [107]). It has also been suggested [25, 24, 59] that mixing dynamics might be slower than exponential in a domain bounded by no-slip walls. This has been recently observed in numerical simulations [96]. A detailed experimental and analytical study of this case is provided in Sec. 4.3.

4.2 Mixing in fully hyperbolic systems: the onset of strange eigenmodes

In this section, we describe how periodic points of a fully chaotic map affect the concentration field $C(x,t)$ of a low-diffusivity scalar, insofar as they determine the spatial structure of the observed strange eigenmode.

For simplicity, we will use one of the most-studied paradigms of fluid chaotic mixing, that is the inhomogeneous incompressible baker's map [35, 80, 6]. We will consider transformations of one-dimensional concentration profiles defined on the unit interval $[0,1]$ by two different variants of the map:

- the "classical" discontinuous baker's map g, which reads

$$g(x) = \begin{cases} g_1(x) = & \gamma x \\ g_2(x) = & \gamma + (1-\gamma)x \end{cases} \tag{4.7}$$

- and its "flipped" continuous variant f

$$f(x) = \begin{cases} f_1(x) = & \gamma x \\ f_2(x) = & 1 - (1-\gamma)x \end{cases} \tag{4.8}$$

  (represented in Fig. 4.4(a)).

The concentration profile evolves as

$$C(x, t+1) = C\Big(\mathcal{M}^{-1}(x), t\Big), \tag{4.9}$$

where the map $\mathcal{M}$ stands for f or g. Both maps therefore transform the concentration profile $C(x,t)$ at time t into two images "compressed" by respective factors γ and $1-\gamma$ ($0<\gamma<1$). However, f "flips" the "right" image before stacking it again with the 'left" image.

Two main ideas are presented here: we first show that the concentration pattern obtained from an initial segregated condition after successive iterations of the map is determined by the least unstable periodic point of the map, and its multifractal unstable manifold. We remark in a second subsection that the decay rate of concentration fluctuations depends on stretching spatial correlations and cannot be explained by the sole stretching distribution. This work is strongly inspired by the very rich literature on chaotic map and scalar mixing, yet the simplicity of the baker's map allows us to describe mixing processes in a plain and pedagogical way which might help the reader to develop an intuition about such mechanisms.

4.2.1 Strange eigenmodes trace out unstable manifolds of least unstable periodic points

First, we compute numerically the evolution of an initial "blob" under the action of f: we choose an initial concentration profile such that $C(x)=1$ for $0<x_a\leq x\leq x_b<1$ and $C=0$ elsewhere. Diffusion is mimicked by letting the concentration evolve during a unit-time-interval diffusive step, where C evolves according to the heat equation with diffusivity κ. We use periodic boundary conditions. Fig. 4.4 (b) shows the concentration profile after 17 iterations of f and corresponding diffusive steps for a typical simulation with $\gamma=0.4$. We see that the system is quite well mixed, insofar as fluctuations of C around its mean value $\langle C\rangle$ (which is conserved by the map) are very weak compared to the initial segregated blob. A closer inspection reveals that fluctuations of C have more important values at some points, so that the concentration pattern has a distinctive "spike shape". Remarkably, we have observed that the spatial pattern visible in Fig. 4.4 seems permanent, i.e. further iterations of the map do not change the form of C. Despite the global decay of fluctuations amplitude, high spikes or low-amplitude fluctuation regions indeed "stay" at the same places. Our example is therefore an illustration of a strange eigenmode, i.e., a spatial pattern converging very rapidly to an eigenfunction of the advection-diffusion operator. Strange eigenmodes in baker's map have been studied in detail in Refs. [37, 131, 42]. Our approach here is to provide a simple way to characterize the spatial organization of the strange eigenmode, that has not been proposed before to the best our knowledge. We describe below

how the strange eigenmode pattern traces out the unstable manifold of the lowest stretching periodic point of the map.

The map g has two period-1 points at the origin and $x_f = 1/(2-\gamma)$. For $\gamma < 0.5$ ($\gamma = 0.4$ in Fig. 4.4), the second fixed point is "least unstable" than the first one, as the compression factor at this point is smaller. We notice on Fig. 4.4 that the highest spike in the concentration pattern is located at $x = x_f$, whereas spikes of decreasing height are located at iterates of x_f: $f_1(x_f)$, $f_2(f_1(x_f))$, ...: the unstable manifold of x_f represents the backbone of the concentration pattern.

A closer look at the mechanisms leading to the concentration pattern can provide a first explanation for this structure. After n iterations of f, the initial blob has been transformed into 2^n strips compressed by factors γ^n, $\gamma^{n-1}(1-\gamma), \ldots, (1-\gamma)^n$. However, diffusion imposes that the width of an elementary strip saturates at the Batchelor width $w_{\rm B}$ where diffusion balances stretching

$$\sqrt{\frac{\kappa}{1-\gamma^2}} \leq w_{\rm B} \leq \sqrt{\frac{\kappa}{1-(1-\gamma)^2}}$$

(We therefore approximate $w_{\rm B} \sim \sqrt{\kappa/(1-\Gamma^2)}$, where

$$\log\Gamma = \frac{1}{2}\Big[\log(\gamma) + \log(1-\gamma)\Big]$$

is the Lyapunov exponent.) As a result, the concentration profile of Fig. 4.4 has a typical variation scale of $w_{\rm B}$. Under repeated compression and diffusion steps, each elementary strip takes the shape of a Gaussian of width $w_{\rm B}$ (and amplitude $\sim 1/(w_{\rm B}\lambda)$ to satisfy mass conservation, where λ is the multiplicative compression experienced by the strip), centered on iterates of the initial blob center x_c. The concentration C measured at a point x therefore results from the addition of slightly shifted strips whose centers are all iterates of x_c that fit into a "box" of size $w_{\rm B}$ centered on x (Fig. 4.2). As the concentration mean is locally conserved, fluctuations of $C(x)$ around $\langle C\rangle$ are inversely proportional to the number of Gaussians in the box. Therefore, high spikes in the pattern will correspond to "boxes" with relatively few contributing strips – i.e. images of the initial domain that have experienced relatively low compression. One can easily convince oneself that the iterate closest to x_f is the strip that has experienced the lowest compression factor, $(1-\gamma)^n$: this particular strip contributes most significantly to fluctuations. However, neighboring iterates must also be considered, as for large n the contribution to $C(x)$ results from the addition of a very large number of strips. On average, these iterates have also experienced compressions

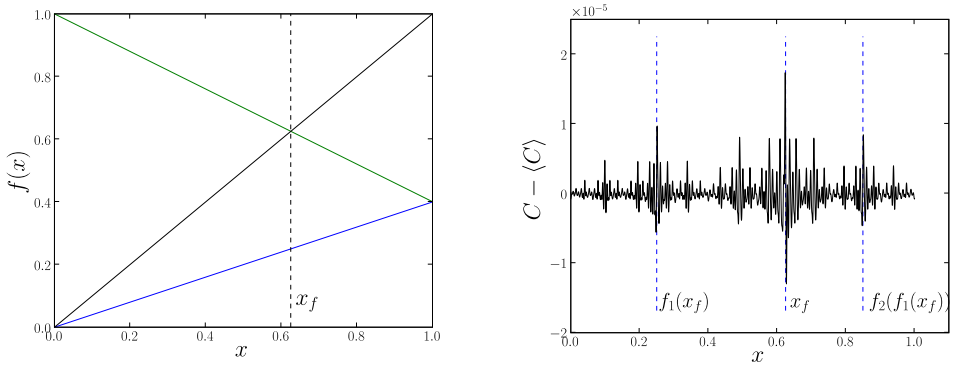

(a) (b)

Figure 4.4: (a) "Flipped" 1-D baker's map f. f has two fixed points at $x = 0$ and $x = 1/(2-\gamma)$. For $\gamma < 1/2$ the most stable fixed point is $x_f = 1/(2-\gamma)$. (b) Concentration profile obtained for an initial blob transfomed by 17 iterations of f ($\gamma = 0.4$, $\kappa = 10^{-5}$). Important "spikes" of the profile are located at x_f and (with decreasing amplitude) around its iterates (of decreasing stability).

smaller than the mean compression Γ^n. This is where the periodic nature of x_f comes in: iterates present around x_f have in fact only experienced $1-\gamma$ factors during the last steps of the process while converging to the attractive point x_f. This explains why the sharpest fluctuations are visible around x_f, with decreasing amplitude around iterates of x_f of decreasing stability. For example, all iterates around $f_1(x_f)$ have experienced a large number N of successive $1-\gamma$ compressions, and an additional γ compression during the latest iteration. In contrast, iterates around x_b have experienced $(N+1)$ $(1-\gamma)$ compression steps, and fluctuations are greater. A further description would require to define a "super-stretching" factor that characterizes a point x by dealing with all different stretching factors for iterates inside a box of size w_{B} centered around x, i.e. an "integrated" stretching factor. However, one encounters several difficulties while attempting such a definition, mostly because boxes of size w_{B} do not coincide with compressions of the whole mixing pattern at an earlier time.

We have illustrated how the strange eigenmode of a chaotic map traces out the multifractal unstable manifold of its least unstable periodic point. Regions of low stretching control the structure of the concentration pattern. This behavior has already been illustrated for the case of mixed phase (with elliptical islands or weakly connected chaotic domains) [89, 90], but also holds for purely hyperbolic domains with uneven stretching.

4.2.2 Decay rate of strange eigenmodes: the importance of stretching spatial correlations

Now that we have described how fluctuations of the spatial pattern evolve with time, we analyze the mixing pattern more quantitatively. A quantity of interest for strange eigenmodes is the decay rate of the concentration variance. Strange eigenmode theory indeed predicts that the concentration profile converges to an eigenfunction C_∞ of the advection-diffusion operator $\kappa\Delta - \mathbf{v}\cdot\nabla$, that is

$$C(x,t) = \exp(-\alpha t)\, C_\infty(x). \tag{4.10}$$

Predicting the decay rate α is a recurring topic in the chaotic advection literature. Some studies have tried to relate α to the stretching distribution in the flow [7, 115]. As we mentioned earlier, fluctuations are inversely proportional to the number of compressed "strips" that overlap because of diffusion, and it seems natural to connect this number with the stretching distribution. However, it has been shown that this prediction often provides poor estimates for the decay rate observed in experiments [127] or simulations [37]. For the case of a specific torus map, it has even been proven [116] analytically that both quantities were different.This discrepancy has been attributed to large-scale patterns causing the failure of a "local theory" relying on statistics of finite-time Lyapunov exponents [115].

We briefly demonstrate in this section that stretching statistics cannot provide an accurate estimate for α, which is shown to depend strongly on stretching spatial correlations. For this purpose, we consider the mixing rate for the two versions of the baker's map, that is the "classical" and the "flip case" (Eqs. (4.7) and (4.8)) with $\gamma = 0.4$. We perform numerical simulations for the same diffusivity $\kappa = 10^{-8}$. The evolution of the concentration variance for both cases is shown in Fig. 4.5 (c). Three phases are visible on this plot: (i) at early times, diffusion has not yet started to blur compressed dye strips and variance is constant; (ii) when compressed strips reach the diffusion scale w_B, the concentration variance decays superexponentially during a transitory phase; (iii) when different strips start overlapping, the concentration profile approximates the strange eigenmode and variance decays exponentially. We note that both maps have the same variance evolution during the two first phases; however, the two curves diverge strongly during the exponential asymptotic phase. A least-squares fit yields $\alpha = -0.59$ for the classical baker's map g, and $\alpha = -0.90$ for the flip map f. The flip map therefore mixes nearly two times faster than its variant without flip ! Yet, both maps have exactly the same stretching distributions...

We have shown in the previous section that highest fluctuations of the concentration profile are located around the least unstable periodic point of the map, that is $x_f = 1/(2-\gamma)$ for f and $x_f = 1$ for g. For permanent patterns, it is equivalent to study the rate of decay for the peak around x_f to characterize α. We notice in Fig. 4.5 that concentration patterns of g and f are remarkably dissimilar. Whereas the pattern seems organized in a roughly symmetric fashion around x_f for f, the pattern for g is highly assymetric. In the neighborhood of $x_f = 1$ and its iterates, concentration gently rises from the left side of the periodic point, yet the profile brutally decreases on its right side, forming abrupt "cliffs". This discrepancy is easily traced back to the map principle itself: at each iteration, f "pushes" strips with highest compression factors (that yield weak fluctuations) to both ends of the domain, whereas x_f is an attractive point at which the slope of the map is negative, therefore strips weakly compressed by successive $(1-\gamma)$ factors converge to x_f while jumping from one side of the point to the other, yielding this more symmetric pattern. However, in the absence of flip, g "puts together" strips having experienced weak compression (on the left side of x_f iterates) and points having experienced tremendous compression (on the right side of such points). This is illustrated on the schematic drawings of Fig.4.6 which zoom into a neighborhood of x_f or one of its iterates for both cases. For the classical baker's map g, the right side of the greater peak at x_f is very flat, contrary to its left side. However, fluctuations decrease at each iteration because neighboring concentration values are averaged at each compression and diffusion step, which forces neighboring peaks to overlap. Roughly, a positive (resp. negative) fluctuation peak of size w_{B} (Fig. 4.6) is dampened by its two neighboring negative (resp. positive) peaks on both sides at each iterations. If one of the neighboring peaks is almost zero, like the right one in Fig. 4.6 (b), the cancellation is smaller than for important peaks on both sides, as in Fig. 4.6 (a). This explains why fluctuations decay at a smaller rate in the classical baker's map than in the flip map.

We conclude that spatial stretching correlations play a very important role for predicting the variance decay rate. This idea was already hinted at in a study by Wonhas and Vassilicos [131], as well as in recent work [116, 112], nevertheless our example allows to "see" how these correlations step in. The importance of correlations is a distinctive feature of chaotic mixing, compared to turbulence: it seems therefore questionable to us to use turbulence models such as Kraichnan flows to predict mixing dynamics of chaotic mixing.

Our basic example has provided a first example of concentration patterns dominated by the periodic structures of least stretching. In the remainder of this chapter, we will see how different phase portraits lead to similar

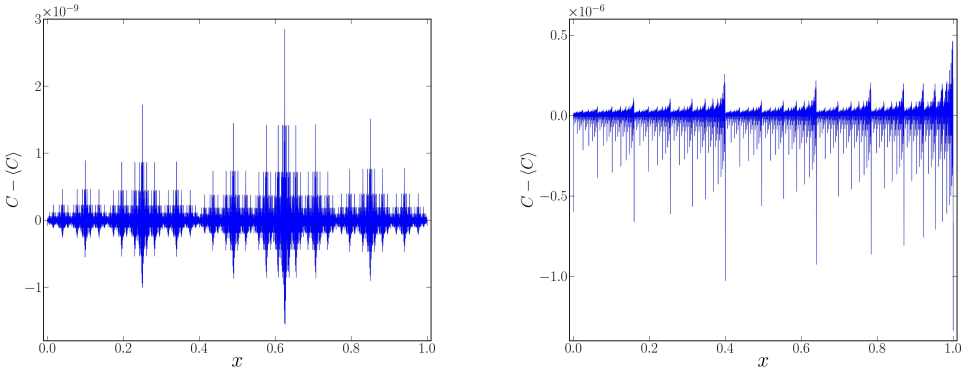

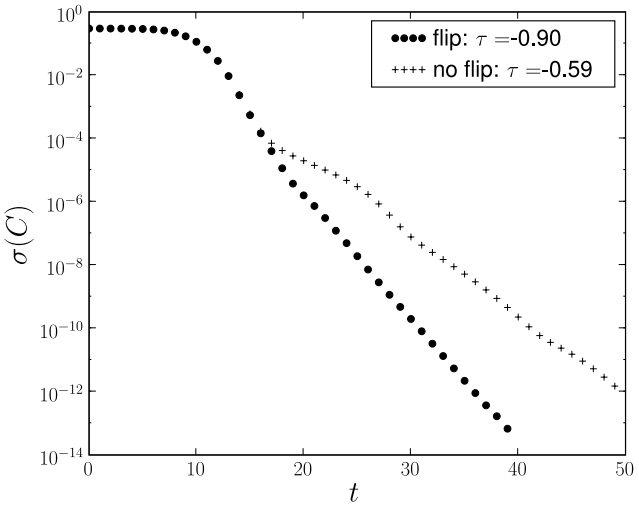

Figure 4.5: Concentration patterns for two realizations of the baker's map with same stretching distribution but different stretching spatial dispersions. (a) "Flipped" baker's map f with $\gamma = 0.4$ ($\kappa = 10^{-8}$). (b) "Stacked" baker's map g, $\gamma = 0.4$ ($\kappa = 10^{-8}$. Both patterns trace out the unstable manifold of the most stable periodic point, that is $x^{(0)} = 0.625$ for the flipped map and $x^{(0)} = 1$ for the stacked map. ((a) + (b): patterns are described inside the text.) (c) Evolution of the concentration variance for two blobs respectively evolved with f and g (log-lin coordinates). Although both maps show an exponential variance decay after an initial transient, the flip map produces surprisingly faster decay than its variant without flip.

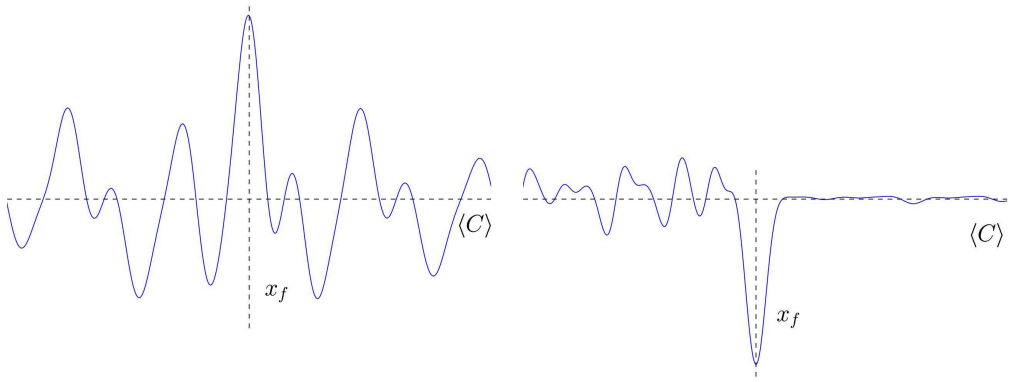

Figure 4.6: Typical concentration pattern around x_f (and its iterates) for the baker's map with (a) and without (b) flip. Description in the text.

conclusions. The next section concerns the experimental and analytical study of mixers where the structure with weakest stretching is a parabolic point on a no-slip boundary.

4.3 Mixing in bounded domains fully covered by a chaotic region

4.3.1 Algebraic mixing observed in experiments

In this section, we report results of dye homogenization experiments conducted in a closed mixer where a single rod stirs fluid with the figure-eight protocol described in Chapter 2. In this physical system, the phase portrait is not purely hyperbolic as it was in the baker's map: we describe how parabolic points on the walls appear due to no-slip hydrodynamics. These low stretching regions are shown to slow down mixing and to contaminate the whole mixing pattern up to its core, far from the wall.

Let us first shortly describe a typical experiment. An initial blob of black dye is transformed into a complicated filamentary pattern after a few iterations of the periodic 2-D stirring protocol (see Fig. 4.7). Each loop of the rod on its figure-eight path transforms the mixing pattern as follows: the rod catches a whole bunch of packed parallel strips (Fig. 4.7 (c)), stretches them and folds a part of the mixing pattern back on itself. Also, each time the rod comes back to its central position at the end of

a loop, it traps some white fluid from outside the mixing region, that is inserted between the newly folded parts of the mixing pattern (see Fig. 4.7 (b) and (c)). Since fluid keeps being added to the mixing pattern, the heart-shaped pattern grows slowly towards the domain wall as time increases. The annular unmixed white region near the wall shrinks conversely.

We measure the concentration field inside a large rectangle (shown in Fig. 4.8) that belongs completely to the partly mixed pattern after a few iterations of the protocol. The resulting variance and concentration probability distributions functions (PDF) are plotted in Fig. 4.9. We observe an algebraic evolution of the concentration variance $\sigma^2(C) \sim t^{-m}$, where we measure $m \sim 3.2$. These results are quite counter-intuitive and not consistent with the exponential evolution of an eigenmode of the advection-diffusion operator. This behavior persists until the end of the experiment (35 periods), by which time the variance has decayed by more than three orders of magnitude. We also note that concentration PDFs have a surprisingly wide shape, with power-law tails on both sides of the maximum (see Fig. 4.9 (b)). Moreover, concentration PDFs are highly asymmetrical. A persistent white peak at zero-concentration values slowly transform into a large shoulder at weak concentration values. This implies that the light-gray wing of the peak, corresponding to concentration values smaller than the most probable value, is more important than the dark-gray wing on the other side of the peak. Finally, the most probable value decreases slowly with time.

4.3.2 Transport mechanisms

In order to understand these surprising scalings, let us first consider the various mechanisms at play during the mixing process. We describe in this paragraph how the observed slow mixing appears from a subtle combination of the phase portrait nature, and hydrodynamics. A Poincaré section obtained numerically for a Stokes flow of the same stirring protocol is shown in Fig. 4.8. The chaotic region spans the whole domain, and no transport barriers are visible for this protocol (elliptical islands might appear inside both loops of the figure-eight for a smaller rod, but for large enough rods we did not detect such islands at all). In particular, trajectories initialized close to the wall boundary also belong to the chaotic region. Thus they end up escaping from this peripheral region to visit the remainder of the phase space, yet after a long time as trajectories stick to the zero-velocity non-slip wall. This escape process takes place along the white cusp of the heart-shaped mixing region, as can be seen in Fig. 4.7. Since stretching is very low close to the wall, fluid sucked into the heart of the chaotic region

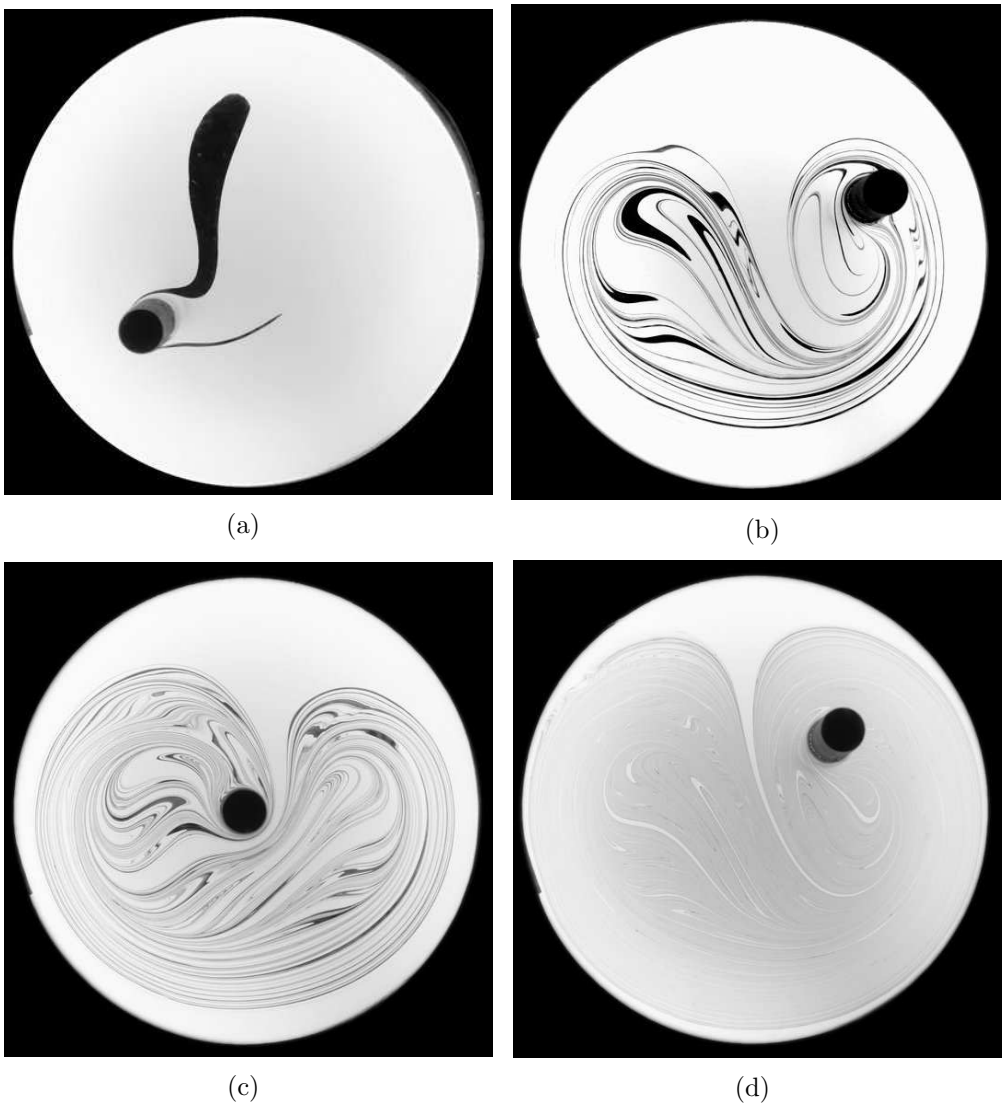

(a) (b)

(c) (d)

Figure 4.7: Successive step dye homogenization in the figure-eight mixer. The rod catches the dye blob (a), stretches and folds it repeatedly in a baker's map fashion, while it also inserts periodically a strip of white fluid coming from the boundary at the core of the mixing pattern (b-d). As a result of this mass injection, the filamentary pattern grows slowly towards the boundary with time. White fluid is injected along the unstable manifold of a parabolic point in the upper part of the wall – this manifold is traced by the thin white filament in (d).

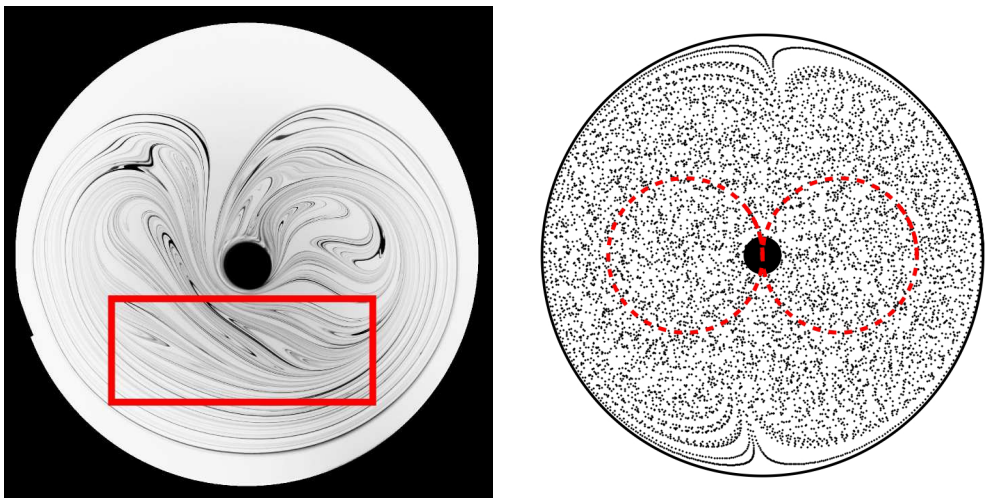

(a) (b)

Figure 4.8: (a) Dye pattern, and region of interest (red rectangle) where we measure the statistical properties of the concentration field. No elliptical islands are visible from the dye pattern in (a) (also see Fig. 4.7). Although there remains an annular unmixed region in the vicinity of the boundary, the partly mixed pattern grows towards the boundary with time (see Fig. 4.7). This purely chaotic phase portrait is confirmed by the Poincaré section in (b), where a single trajectory fills the entire domain. Two parabolic points can be inferred from the small cusps on top and bottom of the boundary. They correspond to the separation point along whose unstable manifold fluid gets injected in the bulk, and to the symmetric reattachment fluid towards which dye filaments slowly converge.

from the wall keeps a high variance at the time when it is injected, contrary to fluid that has spent some period in the heart of the mixing region. As we inject the initial dye blob far from the boundary, poorly stretched fluid injected from the boundary to the heart of the chaotic region consists of zero-concentration white strips that are inserted between folded parts of the mixing pattern (see Fig. 4.7).

Hydrodynamics near the no-slip wall allow us to describe more precisely such white strips. To this aim, consider the velocity field $\mathbf{v}$ near the vessel boundary. The wall can be considered locally flat and we define local coordinates $x_\parallel$ and $x_\perp$ that denote respectively the distance along the wall and to the wall. No-slip boundary conditions impose $v_{x_\parallel} = 0$ for $x_\perp = 0$ (on the

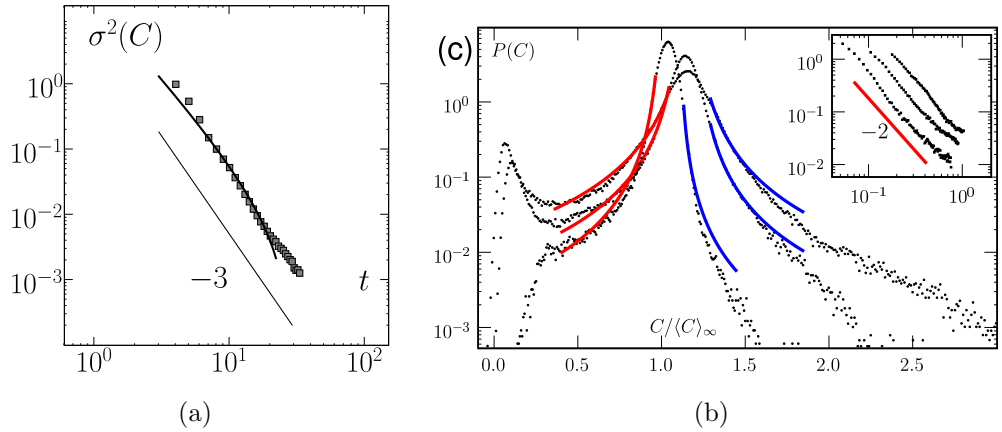

Figure 4.9: Statistical properties of the concentration field measured in a central (i.e. partly mixed) area for the figure-eight mixer. (a) The concentration variance (plotted here in a log-log diagram) has a power-law-like evolution. A t^{-3} law has been represented as a guide for the eye. The variance behavior is much slower than an exponential behavior characteristic of a strange eigenmode. (b) Concentration PDFs after 13, 17 and 31 stirring periods, plotted in log-lin coordinates. Both sides of the peak can be fitted by power laws $(C_{max} - C)^{-2}$ (red and blue plots). Inset: left (light-gray) tail of the peak, $P(C)$ against $|C_{max}(t) - C|$ in a log-log plot. Also note the persistence of a white peak at $C = 0$, that transforms into a remarkably high shoulder fat weak concentration values for larger times.

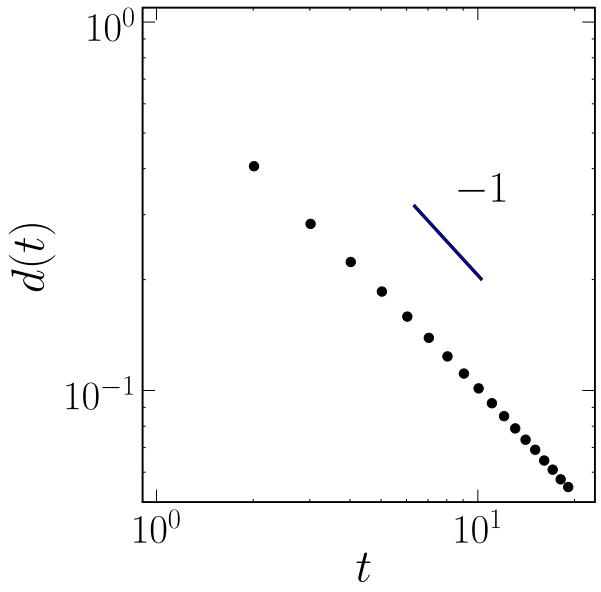

Figure 4.10: Distance $d(t)$ between the dye pattern and the wall (measured in experiments of the figure-eight protocol on a vertical diameter, as the distance between the boundary and the farthermost dye filament). $d(t)$ agrees well with a t^{-1} law predicted by no-slip hydrodynamics on the wall.

wall) and the corresponding first-order linear scaling for small $x_\perp$:

$$v_{x_\parallel} \propto x_\perp. \tag{4.11}$$

Incompressibility writes in such coordinates:

$$v_{x_\parallel,x_\parallel} + v_{x_\perp,x_\perp} = 0. \tag{4.12}$$

Combining Eqs. (4.11) and (4.12) yields

$$v_{x_\perp} \propto x_\perp^2. \tag{4.13}$$

A positive prefactor corresponds to regions where fluid particles come closer to the wall (e.g. the lower part of the domain, see Fig. 4.7), and a negative one to regions where fluid escapes from the boundary (i.e. in the upper part of the domain). Mass conservation imposes that the net flux of $v_\perp$ through a concentric circle is zero. We obtain the evolution of a passive particle near the wall by integrating Eq. 4.13, which reads

$$\dot{x}_\perp = v_{x_\perp} = Ax_\perp^2, \tag{4.14}$$

hence

$$x_\perp = \frac{x_0}{1 - Atx_0}. \tag{4.15}$$

Note that Eqs. (4.14) and (4.15) are somehow inexact, as they neglect the variation of $v_\perp$ with $v_\parallel$. However, we're mostly interested in determining a mean evolution in the wall region and not in individual trajectories details. Eq. (4.15) predicts that the distance between the wall and a particle in the lower part of the domain (where $v_{x_\perp} < 0$) shrinks as $d(t) \sim 1/t$ for large t. Fig. 4.10 shows the evolution of the distance between the wall and the mixing pattern, measured by the position of the farthermost dye strip: $d(t)$ is indeed well approximated by a power law scaling $d(t) \sim 1/t$. To ensure mass conversation, a quantity of unmixed white fluid scaling as $\dot{d}(t) \sim t^{-2}$ is injected periodically in the mixing pattern. As each newly injected white strip has approximately the same length (determined by the extent of the rod path), the width of a strip injected at time t must scale as $\dot{d}(t) \sim t^{-2}$ also. We now start to grasp the origin of our slow scaling: the mixing pattern may well be stretched and folded at each half-cycle of the rod movement in a baker's map like fashion – yet the folded parts are not stacked directly onto each other but *separated by the newest injected white strip*. As this white strip has a large width – that evolves algebraically with time –, we might expect that the concentration variance evolution is slowed down by this variance injection. We also note that the folded part of the

mixing pattern attached to the rod has experienced more stretching than the one left behind. Dominant transport and stirring effects can be summed up as follows: (i) chaotic stretching imposes that the typical width of a dye filament in the bulk shrinks down exponentially down to the diffusion or measurement scale, yet (ii) wide strips of unmixed fluid of width $\dot{d}(t) \sim t^{-2}$ are periodically inserted between these fine structures.

We will flesh out later this simple phenomenological description with a more quantitative analysis; to confirm first that we have drawn the relevant effects, we perform numerical simulations of "dye homogenization" for a different stirring protocol with similar transport mechanisms. We consider a viscous version of the blinking vortex flow [8, 50], that is two contra-rotative vortices alternatively switched on and off. Following Jana et al. [50], we study below a realistic version of this protocol consisting of two fixed rods placed on a diameter of a circular domain (see Fig. 4.11). To mimic the blinking vortices, the two rods are rotated one after the other in a contrarotative fashion. This mixer bears some resemblance with the figure-eight one, as the counter-rotating movement of the vortices imposes that fluid is sucked from the boundary in some part of the domain ($v_\perp > 0$), whereas it is pushed towards the boundary in the other part ($v_\perp < 0$). The flow parameters are $\theta = 270°$ (angular displacement of one rod at each half period), $a = 0.7$ (distance between the rods), $a_{in} = 0.2$ (radius of the rods), $a_{out} = 1$ (radius of the outer cylinder). A Poincaré section shows (see Fig. 4.11 (b)) that the chaotic region spans the entire domain for this protocol as well. We compute the positions of 10^6 particles – initialized inside a small area in the center of the domain – during 75 periods. The heart-shaped mixing pattern shown in Fig. 4.11 (b) is very similar to the figure-eight one. We can indeed observe the injection of white strips inside the bulk, which causes the mixing region to grow. We checked that the distance of the blob to the boundary decreases as $1/t$ as expected from hydrodynamics at the no-slip wall. We compute a coarse-grained concentration field in a large area far from the boundary (the red rectangle in Fig. 4.11). The coarse-graining scale plays the role of the diffusive cut-off scale w_{B}. Again, we observe an algebraic evolution of the concentration variance (shown in Fig. 4.11 (c)) that is well fitted by a $t^{-2.9}$ law from period 15.

Both protocols have in common a chaotic region that spans the entire domain, which imposes the presence of one (or possibly more) *parabolic point* on the boundary [50, 46]. Indeed, because of incompressibility the radial component of the velocity field is much smaller than the component parallel to the wall (we have seen that $v_{x\perp} \propto x_\perp^2$ whereas $v_{x_\parallel} \propto x_\perp$). Fluid therefore escapes from the boundary only in the vicinity of the separation profiles attached to the boundary at points where the sign of $v_{x_\parallel}$ changes

(see Fig. 4.13 (b)). Recently, such separation profiles have been investigated in great detail in Ref. [46]. A Taylor expansion of the velocity field near a separation point reads:

$$v_{x_\parallel} = -\alpha x_\parallel x_\perp \tag{4.16}$$

$$v_{x_\perp} = \frac{1}{2}\alpha x_\perp^2. \tag{4.17}$$

The linear part of the flow vanishes at such a point, which is therefore parabolic. Parabolic points inside the bulk considered in Chapter 3 had a non-zero nilpotent linear part, and therefore different resulting dynamics in their vicinity: here dynamics are controlled by no-slip boundary conditions. The signature of a parabolic separation point ($\alpha > 0$) and of the corresponding reattachment point ($\alpha < 0$) can be seen in the cusps on the boundary in the Poincaré sections for both the figure-eight and the blinking vortex protocols (see Fig. 4.8 (b) and Fig. 4.11 (b)). Rod paths with more intersections could possibly yield phase portraits with many separation and reattachment parabolic points.

4.3.3 Simplified 1-D model

We now wish to derive quantitative predictions to explain the observed algebraic scaling for the concentration variance. To this purpose, we simplify the 2-D problem by characterizing only 1-D concentration profiles $C(x,t)$ along a secant to the stretching direction with which dye filaments align – the dashed segments in Fig. 4.13. This basically amounts to neglecting the variation of the concentration while following a dye filament until it folds – that is on a scale comparable to the vessel size. The effect of the figure-eight mixer during a half-period boils down to the action of a one-dimensional discrete-time map, that transforms concentration profiles by inserting an unmixed strip of fluid scaling as $\dot{d}(t)$ from a parabolic point on the boundary at the heart of the mixing pattern. This strip is injected between two inhomogeneously compressed images of the mixing pattern at the previous timestep. We therefore feel entitled to mimick the behavior of our mixer with a one-dimensional map f, in the spirit of Sec. 4.2. The map f is defined on $[0,1]$ for simplicity; it evolves concentration profiles as $C(x,t+1) = C(f^{-1}(x),t)$ and meets the following requirements: (i) it is a continuous double-valued function to account for the stretching/folding process; (ii) $x = 0$ is a marginally unstable (i.e. parabolic) point of f^{-1}; the correct dynamics close to the wall are then reproduced by imposing $f^{-1}(x) \simeq x + ax^2 + \cdots$, $a > 0$ for small x; (iii) because of mass conservation, at each x, the local slopes of the two branches add up to 1. Other

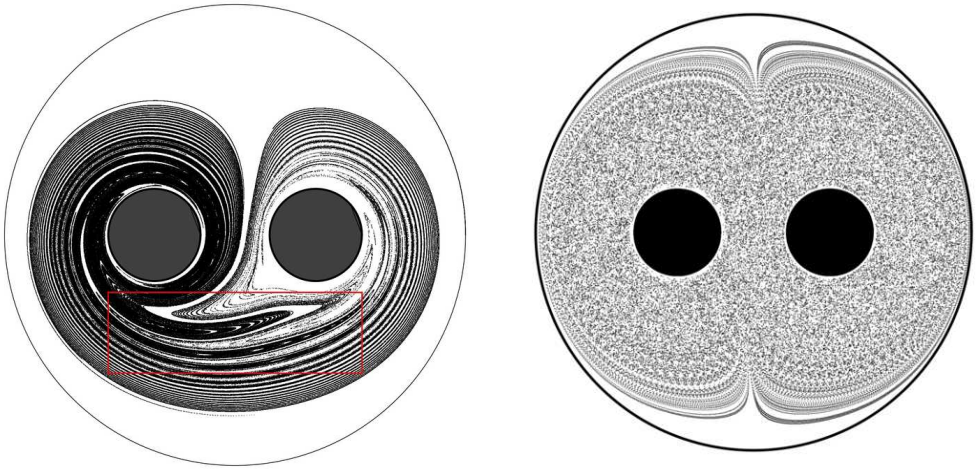

(a) (b)

Figure 4.11: Numerical simulations of a contra-rotative viscous blinking vortex protocol [8, 50]. Two fixed rods are alternately rotated contra-rotatively while the other is kept at rest. Flow parameters are as follows: $\theta = 270^\circ$ (angular displacement of one rod at each half period), $a = 0.7$ (distance between the rods), $a_{in} = 0.2$ (radius of the rods), $a_{out} = 1$ (radius of the outer cylinder). (a) "Dye" filamentary pattern obtained from an initial small square blob formed by 10^6 points. We measure the concentration field inside the large red rectangle for successive iterations of the protocol. The dye pattern bears a strong resemblance with the figure-eight-one: the upper cusp corresponds to a parabolic injection point on the boundary, while in the lower part of the pattern filaments are nicely packed in a parallel fashion. (b) Poincaré section of the flow: as for the figure-eight protocol, the chaotic region spans the entire domain. Again, the upper and lower cusps are fingerprints of parabolic points on the wall.

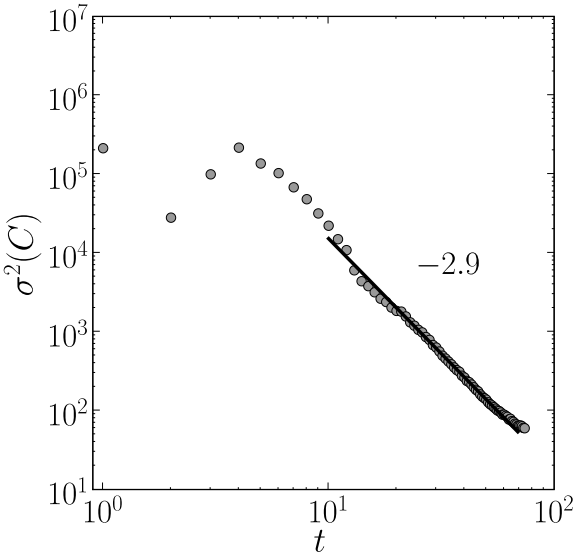

Figure 4.12: Concentration variance measured in a central region in simulations of the blinking vortex protocol. A power-law evolution $\sigma^2(c) \propto t^{-2.9}$ fits well the data from period 15.

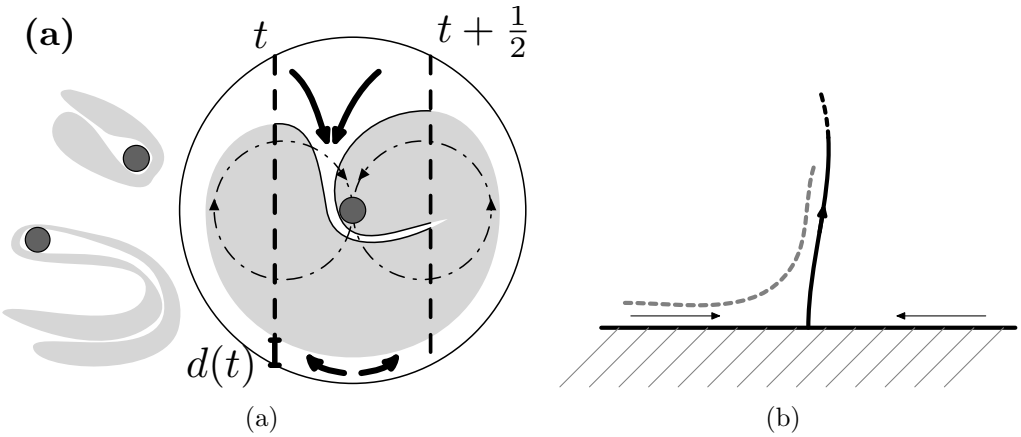

Figure 4.13: (a) Transport mechanisms in the figure-eight protocol. Each loop of the rod on its path stretches and folds the dye pattern like a baker's map, yet new unmixed fluid from the boundary is periodically inserted between the two folded parts. This fluid injection in the bulk is due to the "up/down" asymmetry of the rod movement on its path, as it sucks fluid inside the mixing region in the upper part of the domain, while it stretches and pushes fluid downwards in the lower part. This enables a particle to wander through the whole domain, including the wall vicinity, and therefore the chaotic region to span the entire domain. (b) Fluid from the boundary is then reinjected along the unstable manifold of a marginally unstable (parabolic) point, where the velocity component along the wall cancels.

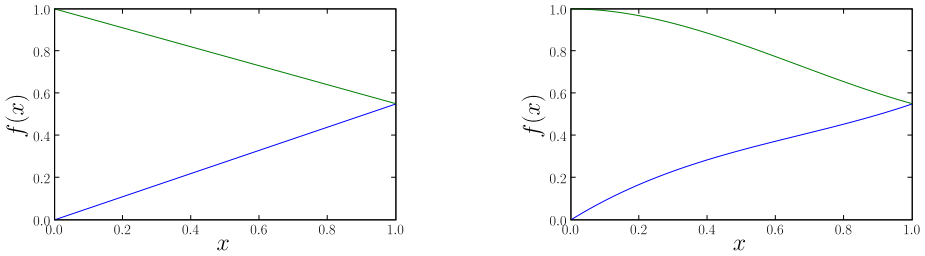

(a) (b)

Figure 4.14: Illustration of the one-dimensional baker's map (a), and a modified version with a parabolic point at $x = 0$. Both maps transform the unit interval into two unevenly compressed images, $f_1([0,1])$ and a flipped image $f_2([0,1])$. While the baker's map is purely hyperbolic, the parabolic point at $x = 0$ in the second map has a strong influence on mixing dynamics. In particular, a point x close to zero is transformed by $f_1(x) \simeq x - ax^2$, so that its distance to the wall decreases with the number of iterations n as $1/n$ (it would decrease exponentially in the classical baker's map). This reproduces no-slip hydrodynamics in the vicinity of a wall in a real physical mixer. The second map is therefore a good candidate to model two-dimensional protocols displaying chaotic advection, where the chaotic region extends to a no-slip wall.

details of f are unessential for our discussion. Diffusion is mimicked by letting the concentration profile diffuse between successive iterations of the map (with no-flux boundary conditions). This model is a modified baker's map [35], with a parabolic point at $x = 0$, whereas the dynamics are purely hyperbolic in a classical baker's map.

We perform numerical simulations by evolving concentration profiles for the specific choice for f:

$$f_1(x) = x - ax^2 + (\gamma - 1 + a)x^3 \quad (4.18)$$
$$f_2(x) = 1 - ax^2 + (\gamma - 1 + a)x^3, \quad (4.19)$$

with $\gamma = 0.55$ and $a = 0.9$. We fix $\kappa = 10^{-7}$. A plot of f is shown in Fig. 4.14, where we compare the map with a plot of the classical baker's map with uneven stretching γ and $(1 - \gamma)$. In our map $f(1) = \gamma$, hence γ represents the mean stretching realized by f_1 as in the baker's map, and $(1 - \gamma)$ the mean stretching realized by f_2 – although stretching is not constant along the two branches. Our initial condition is a concentration

step of width δ

$$C(x) = \begin{cases} 1 & \text{for } x \in [1/2 - \delta/2, 1/2 + \delta/2] \\ 0 & \text{outside.} \end{cases} \tag{4.20}$$

Concentration profiles obtained after several iterations of the map are shown in Fig. 4.15. Strong similarities are observable between concentration profiles obtained in the experiment (Fig. 4.15 (a)) and from the map (Fig. 4.15 (b) and (c)). In both cases a thin layer of "white fluid" ($C = 0$) is present at $x = 0$. Its width decreases as $1/t$ due to the parabolic point on the boundary. In the experiment, the concentration pattern in the bulk (far from $x = 0$) is characterized by sharp spikes at zero or low concentration values, whereas fluctuations seem quite weak elsewhere. Sharp spikes correspond to white strips recently injected from the boundary into the bulk. For the map also, the bulk pattern is clearly dominated by a set of thin spikes, which are recently injected white strips – that is images of the boundary region at $x = 0$ by f_2, then successive iterates by f_1 of f_2.

The validity of our model is also strengthened by statistical properties of the obtained concentration field, which follow closely the behavior observed in the experiment. We have represented the concentration variance (measured in a central region) in Fig. 4.16 (b), superimposed with experimental data for the concentration variance : again we find a power-law evolution. Moreover, there is a strong resemblance between the concentration PDFs depicted in Fig. 4.16 (b) and the experimental ones shown in Fig. 4.9 (b), as they share in particular power-law tails.

The simplicity of our model now allows us to derive analytical predictions for statistical properties of the concentration field. We first consider the simple case of an initial uniform blob, for which we characterize the concentration pattern by plainly counting iterates of injected white strips which have been shown to dominate the concentration pattern. In a further paragraph, we will envisage more general initial conditions and discuss the possible onset of a strange eigenmode for very long times.

4.3.4 Analytical derivation of the concentration PDF and variance

We concentrate here on characterizing the concentration pattern inside a central region where the concentration profile seems at least partly mixed – that is far from $x = 0$. Concentration PDFs and variance presented above have for example been measured in the range $[0.2, 0.9]$.A finer description that includes in particular the concentration field near $x = 0$ will be provided in the next subsection.

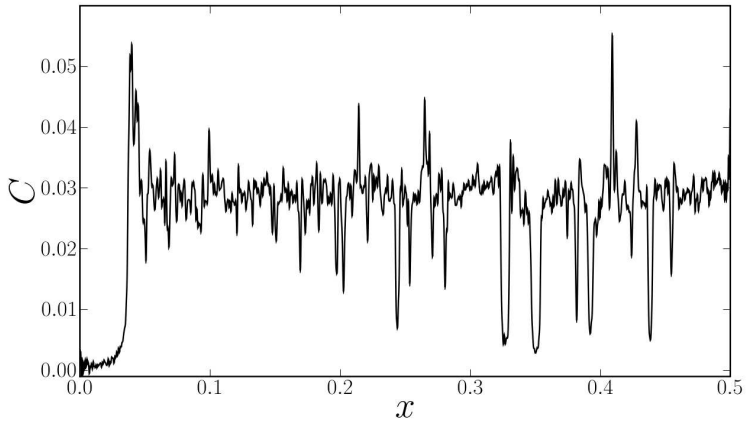

(a)

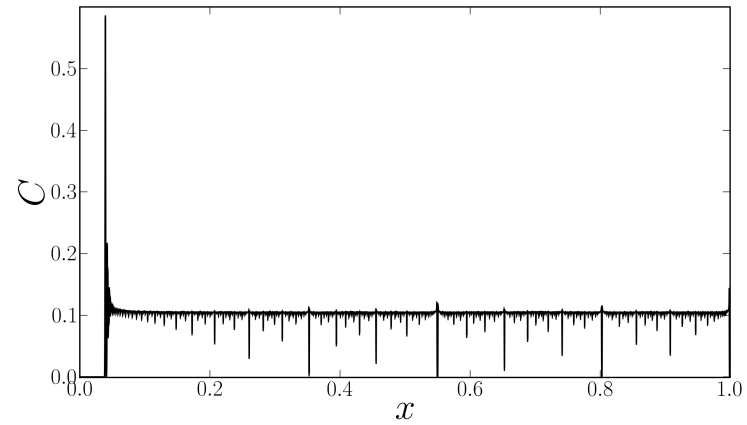

(b)

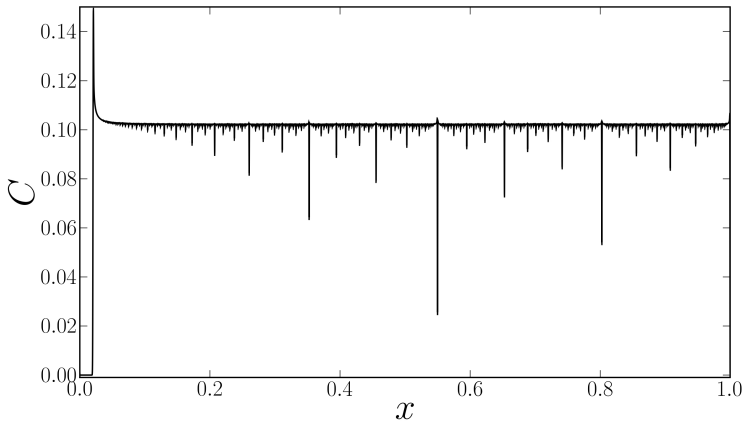

(c)

Figure 4.15: Concentration profiles obtained in the figure-eight experiment after 13 stirring periods (a) and using the 1-D model ((b) and (c), after respectively 25 and 50 iterations of the map).

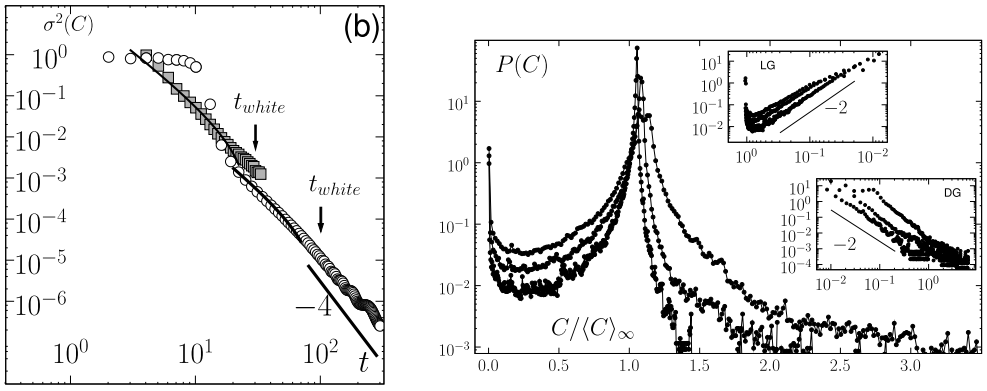

(a) (b)

Figure 4.16: Variance and PDFs of the concentration field measured in a central region for a blob of dye transformed by the modified baker's map. (a) The concentration variance (circle symbols) displays a power-law evolution comparable to results obtained in experiments of the figure-eight experiments (square symbols). (b) Concentration PDFs have wide power-law tails on both sides of the peak. Nevertheless, the dark-gray tail corresponding to high concentration values decays much faster than the light-gray one, that is weak concentration values, which is continuously feeded by the injection of white fluid from the boundary.

The map transforms an initial blob of dye of width s_0 into an increasing number of strips with widths $s_0\lambda_1 \cdots \lambda_t$, resulting from different stretching histories inside the mixed region, where λ_t is the compression experienced at time t. White strips also experience this multiplicative stretching from their injection time. Because of diffusion , a strip of dye or white fluid is only compressed down to the diffusive Batchelor scale w_B , that is, a strip stabilizes at a width $w_\mathrm{B} = \sqrt{\kappa/(1-\lambda(x)^2)}$ parametrized by the local stretching rate $\lambda(x)$. We choose in the following to neglect the weak variation of w_B with x for $\lambda(x)$ sufficiently far from 1, that is far from the boundary region. We estimate the diffusive scale as

$$w_\mathrm{B} = \sqrt{\frac{\kappa}{1-\Gamma^2}}, \tag{4.21}$$

where

$$\Gamma = \exp\left(\left\langle -\log\left(\left|\frac{\partial f^{-1}(x)}{\partial x}\right|\right)\right\rangle\right) \tag{4.22}$$

and the mean is taken over the measure region. Γ is the geometric mean of the compression, which makes $\log(\Gamma)$ the equivalent to a Lyapunov exponent

. For a moderate stretching inhomogeneity in the bulk, we expect Γ to be close to 0.5. $w_{\rm B}$ is the smallest observable scale in the mixing pattern. In experiments as in simulations, we probe the concentration field on a pixel, or box size, which is smaller than $w_{\rm B}$. For long times, the concentration measured at a pixel x might be the average of many overlapping dye and white strips that have been compressed down to $w_{\rm B}$ and whose profiles have therefore superimposed in a box of size $w_{\rm B}$ (see Fig. 4.2).

Different measured values of C correspond to a different combination of superimposed white or dye strips. We characterize $P(C)$ by considering the different combinations of strip widths that one might find in a box of size $w_{\rm B}$. We will distinguish between three generic cases corresponding to three different regions of the histogram $P(C)$ (see Fig. 4.9 (b) and Fig. 4.16) (b): a white (W) peak at $C = 0$ corresponding to recently injected white strips still wider than $w_{\rm B}$, light gray (LG) and dark gray (DG) tails corresponding to respectively smaller and larger concentrations than the peak (mean) concentration. Once we have quantified the proportion of boxes contributing to these different values of C, the variance will be readily obtained as

$$\sigma^2(C) = \int (C - \langle C \rangle)^2 P(C) {\rm d}C = \sigma_W^2 + \sigma_{LG}^2 + \sigma_{DG}^2. \qquad (4.23)$$

4.3.4.1 White pixels

Let us start with white (zero) concentration measures that come from the stretched images of white strips injected before t. White strips injected at an early time have been stretched and wiped out by diffusion , that is their width has become smaller than $w_{\rm B}$. A white strip injected at time t_0 has been compressed to a width $\dot{d}_{t_0}\lambda_{t_0+1}..\lambda_t$ at time t (for convenience we write the positive strip width $\dot{d}_t = |\dot{d}(t)|$). We neglect the spatial variation of $\lambda(x)$ and approximate $\lambda_{t_0+1}..\lambda_t \sim \Gamma^{t-t_0}$. The oldest white strips that can be observed have been injected at the time $t_i(t)$ such that

$$\dot{d}_{t_i}\Gamma^{t-t_i} = w_{\rm B}. \qquad (4.24)$$

Note that from $t_{\rm white}$ defined by

$$\dot{d}_{t_{\rm white}} = w_{\rm B}, \qquad (4.25)$$

the injected white strip is smaller than $w_{\rm B}$ and no white pixels can be observed. Before $t_{\rm white}$, we can observe all white strips that are images from strips injected between $t_i(t)$ and t, and the number of white pixels is

proportional to

$$n_W = \sum_{n=t_i(t)}^{t} \dot{d}_n = d_{t_i(t)} - d_t. \tag{4.26}$$

We now use the expression of $d(t)$ determined by no-slip hydrodynamics $d_t \sim 1/at$, which yields for large t

$$n_W \simeq (t - t_i)(at_i t)^{-1}. \tag{4.27}$$

From the definition of $t_i(t)$,

$$t - t_i \simeq (2\log at + \log w_\mathrm{B})/\log\Gamma \tag{4.28}$$

for large t, therefore

$$n_W \simeq (2\log at + \log w_\mathrm{B})/(\log\Gamma \times t^2). \tag{4.29}$$

The fraction of white pixels n_W is plotted versus time in Fig. 4.17. We find excellent agreement between the data and the expression Eq. (4.29) for n_W, up to t_white. Note that during the first iterations n_W is constant: this correspond to the initial phase when dye strips are still wider than w_B and diffusion is almost ineffective (i.e. up to t such that $\delta \times \Gamma^t = w_\mathrm{B}$). During this phase, the concentration variance is also almost constant, so we will not worry about this initial phase. We deduce the contribution of the white pixels to the concentration variance for $t < t_\mathrm{white}$

$$\sigma_W^2 = n_W \langle C \rangle^2 \simeq \delta^2 \times \frac{2\log at + \log w_\mathrm{B}}{\log\Gamma \times t^2} \tag{4.30}$$

Of course $\sigma_W^2 = 0$ after t_white.

4.3.4.2 Light-gray tail

We now concentrate on the distribution of light gray values corresponding to white strips that have just been compressed below the cut-off scale w_B. At its injection time, a white strip is injected between images of the mixing pattern where fluctuations are lower (see Fig. 4.15). Fluctuations measured in a pixel are therefore mostly due to a recently injected white strip that is superimposed with low-fluctuation profiles. We propose to approximate the measured value C as the average of the biggest white strip with width $\lambda < w_\mathrm{B}$, and mixed "gray" fluid whose concentration is close to the most probable concentration C_g. A box with a white strip of scale λ thus bears a concentration

$$C_\lambda = C_\mathrm{g}(1 - \lambda/w_\mathrm{B}), \tag{4.31}$$

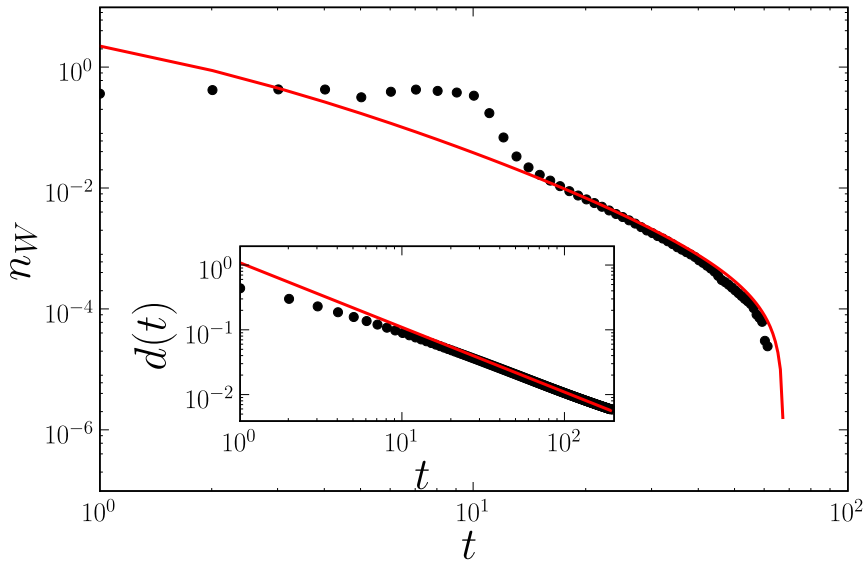

Figure 4.17: Simulations of dye homogenization by the map. Fraction of white pixels (where $C = 0$) n_W as a function of time-iteration (full circle symbols). For early times diffusion has not started yet to broaden dye filaments and n_W remains approximatively constant. When n_W starts to decay, it closely follows the law $n_W = (2 \log t + \log w_{\rm B})/(t^2 \times \log \Gamma)$ (solid line plot) obtained by counting the images of injected white strips that have not yet been compressed down to the diffusion scale $w_{\rm B}$. Inset: the distance between the dye pattern and the wall (measured by the position of the first peak in Fig. 4.15) evolves as $d(t) = 1/at$ (solid line plot).

and we can relate $P(C)$ to the distribution of widths of the images of the injected white strips $Q(\lambda)$ in the following way:

$$\begin{aligned} P(C) &= Q\Big(\lambda = w_{\rm B}(1 - C/C_g)\Big)\left|\frac{d\lambda}{dC}\right| \\ &= \frac{w_{\rm B}}{C_g}\, Q\Big(\lambda = w_{\rm B}(1 - C/C_g)\Big). \end{aligned} \tag{4.32}$$

$Q(\lambda)$ is easily retrieved from standard combinatorial arguments. A white strip injected at t_0 is transformed into 2^{t-t_0} images with scales $\dot{d}_{t_0}\Gamma^{t-t_0}$ (once again we consider only the mean stretching Γ, which amounts to matching a given concentration to a unique injection time). In a "quasi-static" approximation, we neglect the algebraic dependence of λ (hence C) with t_0 in the factor d_{t_0}, compared to the exponential dependence in Γ^{t-t_0}.

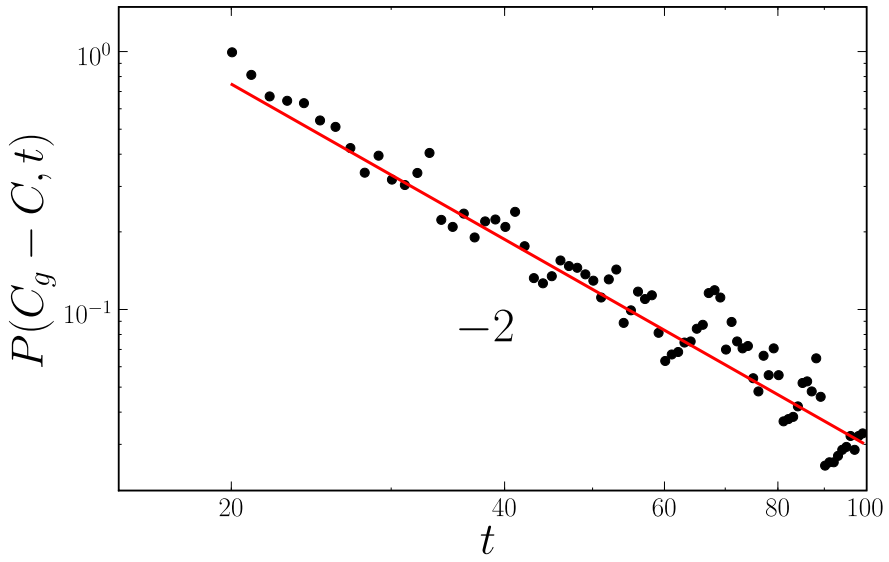

Figure 4.18: Probability of a light-gray concentration level with a given distance to the peak, i.e. probability that $\Delta - \epsilon \leq C_g - C \leq \Delta + \epsilon$ ($C_g \sim 0.1$, $\Delta = 3 \times 10^{-2}$, $\epsilon = 10^{-3}$, as a function of time. $P(C_g - C)$ agrees well with the t^{-2} evolution predicted by Eq. (4.35), that has been also plotted as a guide to the eye.

Therefore

$$Q(\lambda) = (\lambda/\dot{d}_{t_0})^{\log(2)/\log(\Gamma)} \times (1/\lambda \log \Gamma), \tag{4.33}$$

resulting in

$$\begin{aligned} P(C) &= \dot{d}_t^{\log 2/\log(\Gamma^{-1})} \frac{w_{\mathrm{B}}}{C_{\mathrm{g}}(t)} \left[w_{\mathrm{B}}(1 - \frac{C}{C_{\mathrm{g}}}) \right]^{\frac{\log 2}{\log \Gamma} - 1} \\ &= g(t) \left[C_{\mathrm{g}} - C \right]^{(\log 2/\log \Gamma) - 1} . \end{aligned} \tag{4.34}$$

$P(C)$ thus has a power-law tail in the light gray levels whose exponent depends on the mean stretching Γ. We observe satisfactory agreement between this prediction and both experimental data and numerical 1-D simulations (see Fig. 4.9 (b) and Fig. 4.16 (b)). For this tail indeed we measure $P(C) \propto (C - C_{\mathrm{g}})^{-\alpha}$ with $\alpha \lesssim 2$, consistent with $\Gamma \lesssim 0.5$, a rather homogeneous stretching. Also note that the amplitude of the light-gray tail decreases with time as a power law

$$g(t) \propto \dot{d}_t^{\log 2/\log(1/\Gamma)} \propto t^{-2(\log 2/\log(1/\Gamma))}. \tag{4.35}$$

We have plotted in Fig. 4.18 the probability of a concentration value with constant distance from the maximum. The observed evolution scales as a power-law t^{-2} as expected from our calculation. We deduce the contribution of light-gray pixels to the concentration variance

$$\sigma_{LG}^2 = g(t) \int_{C_{\min}}^{C_{\rm g}} (C_{\rm g} - C)^{2-\alpha(\Gamma)} {\rm d}C \tag{4.36}$$

where $\alpha(\Gamma) = 1 - \log 2/\log \Gamma$, and $C_{\min}$ is the smallest concentration observed ($C_{\min} = 0$ for $t < t_{\rm white}$ and $C_{\min} = C_{\rm g}(1 - \dot{d}_t/w_{\rm B})$ for $t > t_{\rm white}$). For $t < t_{\rm white}$ the integral is constant and $\sigma_{LG}^2 \propto g(t) \propto \dot{d}_t \propto t^{-2}$. On the other hand, for $t \geq t_{\rm white}$,

$$\sigma_{LG}^2 = \frac{g(t)}{2 + \alpha(\Gamma)} [C_{\rm g} - C_{\min}]^{3-\alpha(\Gamma)} \propto t^{-(6+2\frac{\log 2}{\log \Gamma})} . \tag{4.37}$$

For $\alpha(\Gamma) \sim 2$ as we observed, the exponent in the above power law is about -4.

4.3.4.3 Dark-gray tail

Let us now turn to the dark-gray part of the PDF. In our case, high concentration values correspond to black dye strips that have not experienced much compression, so that they have not been canceled out by being superimposed with many other strips. This time, it is not sufficient to consider only the mean stretching Γ to characterize such strips as we did before, since stretching histories far from the mean are involved. Looking at the concentration profiles in Fig. 4.15, we observe that highest concentration values come from the reinjection of black strips pushed to the pattern boundary where they have experienced lower stretching than inside the pattern core. Such a positive concentration fluctuation is then mixed with the remainder of the pattern as successive images are compressed by a factor of order Γ, in the same way as injected white strips. Many images of the initial blob may have aggregated inside a box of size $w_{\rm B}$. If the decay of this highest concentration "cliff" is slower than Γ^t – the decay of an injected fluctuation inside the bulk –, we may apply the same method for computing the shape of the dark-gray tail as we did for white strips and the light-gray tail. Writing

$$C_\lambda = C_g(1 + \lambda/w_{\rm B}), \tag{4.38}$$

and relating the width λ to the injection time t_0 as we did before, leads again to a power-law shape $(C - C_g)^{-2}$, for the dark-gray tail also. This is in good agreement with the observed scalings for both experimental and

numerical PDFs (see Fig. 4.16). We now turn to evaluating the amplitude of the highest concentration fluctuation on the pattern boundary, which determines the tail global decay. Note that the contribution of the dark gray tail is very small compared to the light gray one, as after a few periods, only a few boxes of size w_B on the border of the pattern have an amplitude noticeably greater than the mean (see Fig. 4.15 (b) and (c)), whereas the width of the remaining white pool is much larger. Moreover, we show below that this amplitude decays faster than the contribution of white strips.

We have plotted in Fig. 4.19 the decaying amplitude of the greatest fluctuation in the pattern, that is of the leftmost box in the mixing pattern (Fig. 4.15 (b) and (c)). The evolution during 200 periods reveals a first exponential decay, whose rate increases with the diffusivity, followed by a power-law phase with an exponent of order 3. Let us perform a simple analysis to understand this evolution. The number of images of the initial dye blob that superpose inside a box of side w_B at the pattern boundary is given by w_B/Λ, where $\Lambda \simeq \prod_{i=1}^{t} f_1'(f_1^i(1))$ is the compression factor experienced after t periods at the pattern boundary (i.e. by the leftmost blob image) (This is true until the distance between the pattern and the wall is greater than the diffusion scale at the boundary. We will discuss this final phase later). For early times dye strips do not feel yet the effect of the wall, and the stretching factor Λ can be approximated by γ^t (we use γ instead of Γ for evaluating the compression by repeated iterations of f_1), and we expect the decay to be exponential with a rate $\log \gamma$. This behavior is indeed observed for large enough diffusivities (Fig. 4.19 (a)). For small diffusivities, few dye strips are homogenized before the mixing pattern borders reaches the region where no-slip hydrodynamics dominate. For long times $f_1^i(1) \simeq (ai)^{-1}$, $f_1'(f_1^i(1)) \simeq 1 - 2/i$. The compression Λ can be approximated by

$$\Lambda \simeq \gamma^{n_0} \prod_{n_0+1}^{t} (1 - 2/i). \tag{4.39}$$

The two terms in the equation above account for (i) the exponential compression by successive factors of order γ inside the bulk, and (ii) a weaker compression by factors converging slowly to 1 as the pattern frontier gets close to the boundary and experiences a compression determined by no-slip hydrodynamics. The product $\prod_{n_0+1}^{t}(1 - 2/i)$ converges to a power-law $\propto t^{-2}$ for long times. The observed exponent is greater; this might come from a crossover between an exponential phase and the t^{-2} phase that we predict.

From the above analysis, we see that the contribution of the dark gray tail to the concentration variance is very small compared to the light gray

tail, therefore we neglect it in the following computation of the variance.

In our experiments, additional contributions to the dark-gray tail come from dye particles trapped during some time in folds of the pattern where stretching is weak (notice the dark folds in Fig.4.7 (b) and (c)). This 2-D effect is not present in our map. The dark gray tail is therefore built by contributions from the border of the pattern, but also from these folds. Nevertheless, we have checked that this contribution is small compared to the light-gray tail, and decays rapidly with time.

4.3.4.4 Concentration variance

We finally sum all contributions from different parts of the PDF to obtain $\sigma^2(C)$. In the experiment, the crossover t_{white} is estimated as 30 periods. However, 3-D effects inside the fluid prevented us from conducting experiments for more than 35 periods. For this early regime, fitting the data with $\sigma^2_W \propto (2\log t + \log w_{\text{B}})/t^2$ (black line on Fig. 4.9 (a)) gives good results, except close to t_{white} where the contribution of the light gray tail starts to dominate. In contrast, in numerical simulations we observe (Fig. 4.16 (b)) both the $(2\log t+\log w_{\text{B}})/t^2$ behavior (black line) , which can be interpreted as in the experiment, and the t^{-4} decay after t_{white} (100 periods for the case studied) given by σ^2_{LG}. For long times, the observed power-law arises from the specific way of incorporating white strips whose width scales as t^-2 inside the mixing pattern.

4.3.4.5 Longer times: the appearance of a strange eigenmode

We now consider the asymptotic regime, when it is not valid any more to approximate the injected variance by the contribution of a white strip of width $1/at^2$, as the mixing pattern is close enough to the wall $x = 0$ so that diffusion blurs the white layer at the boundary. For such large times, the mixing pattern can be described as an inverted half-Gaussian centered on $x = 0$ (see Fig. 4.20 (b)) that decays with time as fluid keeps being reinjected in the bulk. At this time, fluctuations are very small in the rest of the pattern, and they are only controlled by the amplitude of the half-Gaussian. The width of the half-Gaussian w_0 is determined by the point where stretching and diffusion balance:

$$w_0 = \sqrt{\frac{\kappa}{1 - f_1'(w_0)}}. \tag{4.40}$$

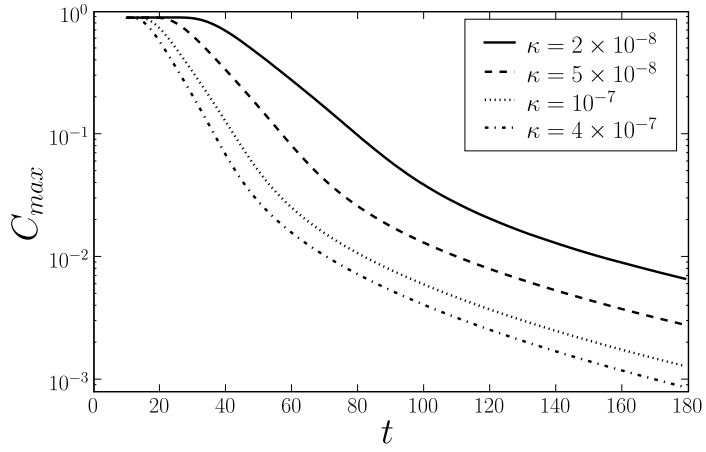

(a)

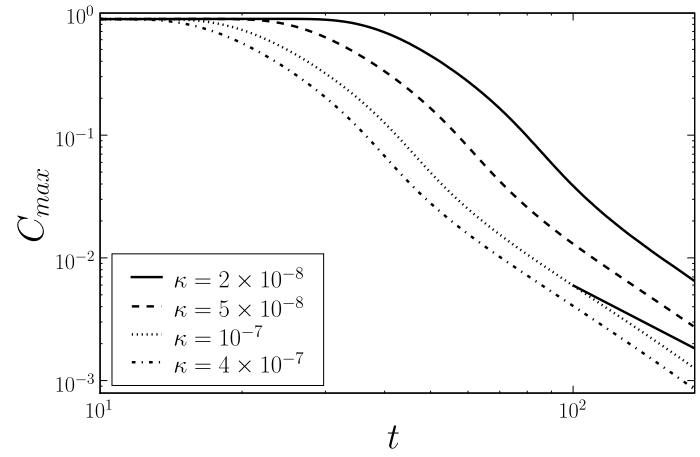

(b)

Figure 4.19: Amplitude C_{max} of the maximum positive concentration fluctuation, in log-linear (a) and log-log (b) coordinates, for different diffusivities. This corresponds to the amplitude of the leftmost spike of the concentration pattern, that has experienced weaker stretching than images of the initial blob in the core of the pattern. An exponential decay followed by a power-law evolution are observable on these plots. A line of slope -2 corresponding to the asymptotic expected evolution has been drawn for comparison.

Thus, with $f_1'(w_0) = 1 - 2aw_0$, we obtain for a small diffusivity

$$w_0 = \left(\frac{\kappa}{4a}\right)^{1/3}. \tag{4.41}$$

Once the concentration at $x = 0$ starts rising, which occurs for $d(t) = 1/at \sim w_0$ (i.e. 350 periods for a diffusivity $\kappa = 10^{-7}$!), the stabilized half-Gaussian decays exponentially at a rate $-\log(f_1'(w_0)) = 2aw_0$, which scales as $\kappa^{1/3}$. We have verified this scaling in numerical simulations of the model (see the inset of Fig. 4.20 (a)). Note that this is one of the very few examples where one can predict analytically the decay of a strange eigenmode (another noteworthy situation is the torus map considered in Ref. [116]). However, this strange eigenmode is somehow frustrating, as we only observe it when fluctuations are completely negligible in the bulk. Its structure is also quite trivial: it consists of the half-Gaussian at $x = 0$, and of very small spikes centered on the iterates of $x = 0$ in the bulk.

4.3.5 Other initial conditions

For the sake of completeness, we have realized numerical simulations for different initial conditions than a blob of dye. In particular, we have simulated two different situations:

- a cosine profile, corresponding to an initial condition

$$C(x, t = 0) = 1 + \cos(4\pi x), \tag{4.42}$$

- and a random profile where we attribute to each pixel a random value between 0 and 1. This rapidly varying profile is rapidly smoothened everywhere on the local Batchelor scale.

The main difference between the two protocols may be assessed as follows: for the cosine profile, the initial scale of variation for the scalar field is much greater than the Batchelor scale at the boundary w_0, whereas for the random initial condition, the scalar field varies already on the smallest possible scales.

In the first case, as for the dye blob, the scale of variation of the profile close to the boundary is large, of order $f_1^t(1) \sim 1/(at)$ (see inset of Fig. 4.21 (a)). This case is therefore analogous to the dye blob case. After a short time, most important fluctuations are concentrated in the leftmost image of the initial unit interval, that was iterated only by f_1. Other iterates have wandered in the bulk where stretching is much more efficient, so that

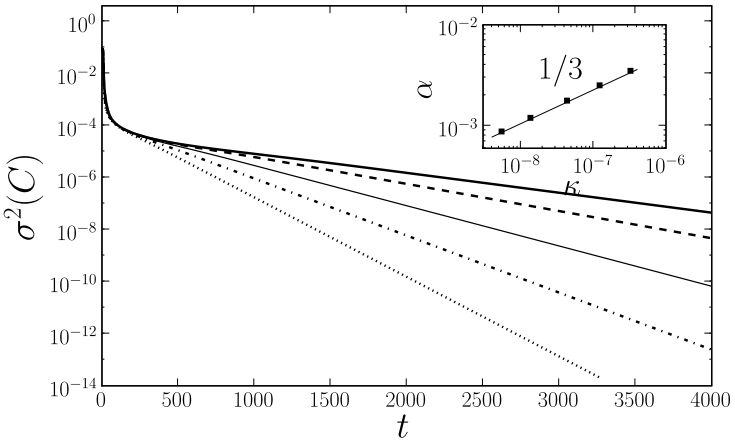

(a)

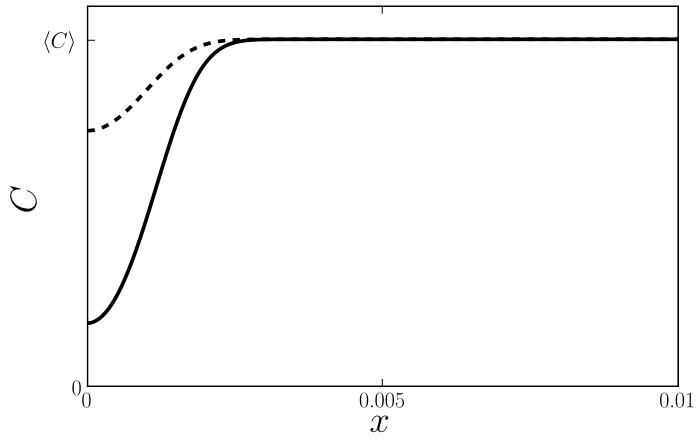

(b)

Figure 4.20: (a) Concentration variance measured in the whole unit interval $[0, 1]$ for different diffusivities (the thick solid, dashed, solid, dot-dashed and dotted lines correspond respectively to the following values of κ: 5.4×10^{-9}, 1.3×10^{-8}, 4.3×10^{-8} 1.2×10^{-7} and 3×10^{-7}.). For long times, the evolution of the variance is exponential, corresponding to the onset of a strange eigenmode: $\sigma^2(C,t) = \sigma_0^2 \exp(-\alpha t)$. As expected from Eq. (4.41), α scales as $\kappa^{1/3}$ (inset). (b) Structure of the strange eigenmode: an inverted half-Gaussian of width w_0 decays exponentially at a rate $-\log(f_1'(w_0)) = 2aw_0$.

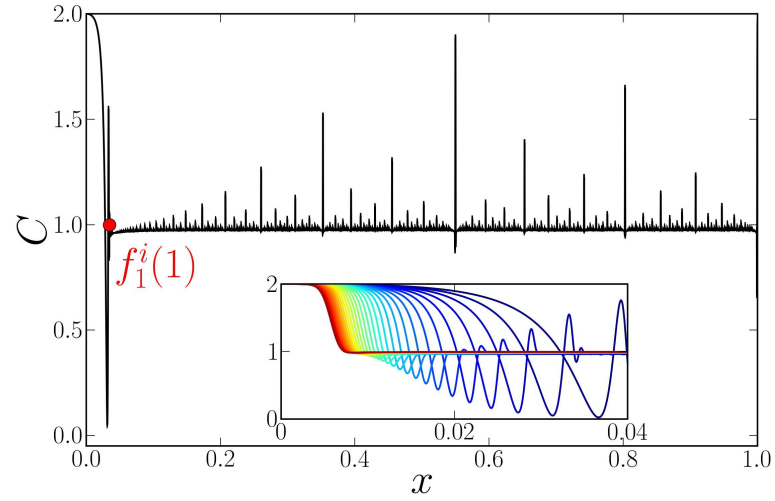

(a)

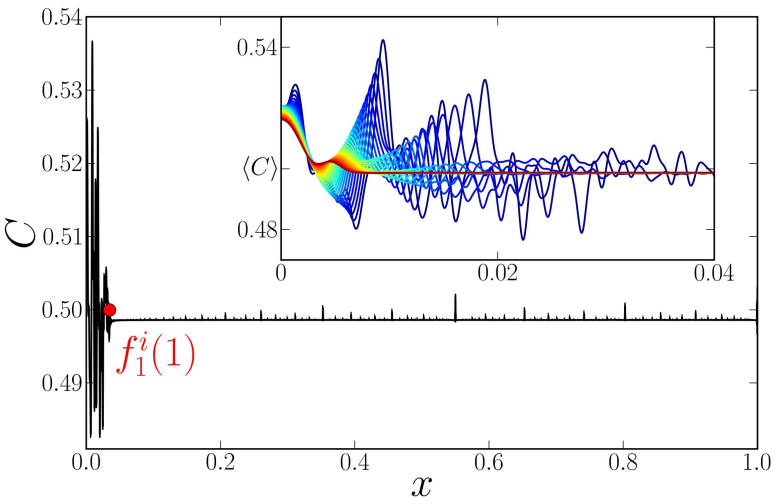

(b)

Figure 4.21: Homogenization for two different initial conditions: (a) $C(x, t = 0) = 1+\cos(4\pi x)$, (b) random initial profile. The scale of variation of the initial profile is much greater than w_0 in the first case, whereas it is of order w_0 close to the boundary in the random case. Main axes: concentration profile after 30 iterations of the map. Note that all variance is contained in the leftmost image of the unit interval (always transformed by f_1), and around the iterates of $x = 1$. Inset: zoom on the border region for periods 30 (dark blue) to 180 (red), represented every fifth period.

all fluctuations have died out – except for newly reinjected iterates (whose history can be coded as a sequence $F \circ f_1 \circ f_2 \circ f_1^k$ where F stands for the last few iterations), which correspond to the reinjection inside the bulk of fluctuations at the left boundary. Even the leftmost iterate feels the spatial heterogeneity of stretching (see inset in Fig. 4.21 (a)), as fluctuations initially close to $x = 1$ have been more compressed, and they have overlapped and averaged. After some time, the profile at the boundary (inset in Fig. 4.21 (a))) has a value significantly different from the mean concentration only at one or two "oscillations", which is exactly what we observe for the dye blob case (see Fig. 4.15). As for the dye blob case, we observe a power-law decay for the variance evolution, which can be accounted for with the same reasoning.

For the random profile case, the concentration profile at the boundary (inset in Fig. 4.21 (a))) is much less coherent over successive periods. Indeed, the scale of variation of the concentration profile saturates immediately at the local Batchelor scale in the whole domain. The strips reinjected in the bulk result from the averaging of many strips at the boundary, and their amplitude is more difficult to predict. We measured a non-monotonous decay of variance in this case, as the averaging of strips close to the wall depends on the instantaneous height of many neighboring strips (Fig. 4.21 (b)). Yet, the strange eigenmode regime is only reached once fluctuations have died out everywhere, except for the leftmost box of size w_0 and around the iterates of $x = 0$, so that there is a long transient phase also in this case.

However, many features seem to persist for all initial conditions we checked:

- the spatial organization of the bulk profile is dominated by the unstable manifold of the parabolic point at $x = 0$, where fluctuations subsist for longer times. As can be seen in Fig. 4.22, the cross-correlation coefficient of the bulk profile at successive periods is very high.

- as stretching is lower close to the boundary, the reinjected fluctuations are almost similar over successive periods. The same reasoning as for the dye blob case yields concentration PDFs with power-law $|C - \langle C \rangle|^{-2}$ tails, which are indeed observed in all cases.

Finally, let us briefly consider as a gedanken-experiment an experimental initial condition where half of the circular region is black, and the other is white, so that a half-black/half-white sandwich is reinjected inside the filamentary pattern at each period, instead of a purely white strip as in our experiments. This time the concentration mean in a central region may

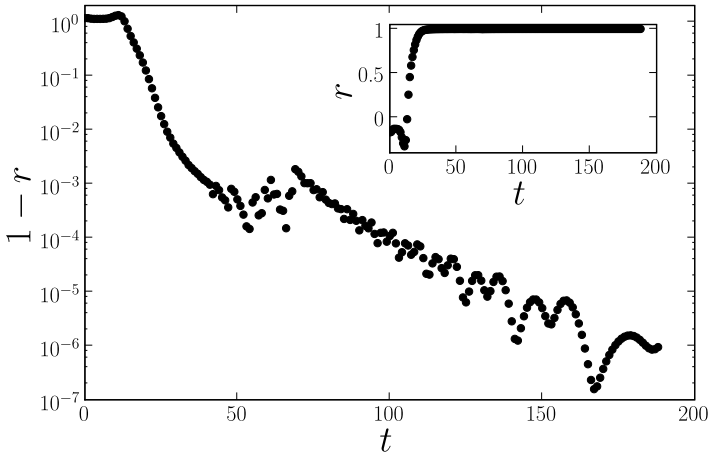

Figure 4.22: Inset: time cross-correlation of the concentration pattern $r(t) = \mathrm{Cov}\left(C(t), C(t+1)\right) / \left(\sigma(t)\sigma(t+1)\right)$, measured in a central region (initial dye blob case). The cross-correlation coefficient approaches 1 very rapidly. Main axes: deviation from the asymptotic value $1-r$ in log-log coordinates. Although the concentration profile has not yet converged to an eigenmode, the correlation between profiles at different times is very high: indeed, the concentration pattern is completely dominated by the unstable manifold of the parabolic point at $x = 0$, which forms the backbone of the profiles.

be constant in time, contrary to our experiments, yet the injection of the poorly-mixed sandwich would slow down mixing dynamics as well. It is important to notice that the slow dynamics of the variance observed in our experiments do not result only from the algebraic injection of white fluid (that changes the mean concentration in a central region), but from the injection of *variance* that is afterwards transported to smaller scales by the subtle combination of stretching and folding, and diffusion.

4.3.6 Discussion

Using a 1-D baker's map with a parabolic point on the boundary, we have explained how the concentration pattern is completely dominated by the parabolic point, which "stores" high-variance fluid, and its unstable manifold along which unmixed fluid is slowly reinjected. To sum up, our study has highlighted the importance of a set of different scales, that is

- the Batchelor scale in the bulk w_{B}, which characterizes the smallest scale of the concentration profile inside the bulk .

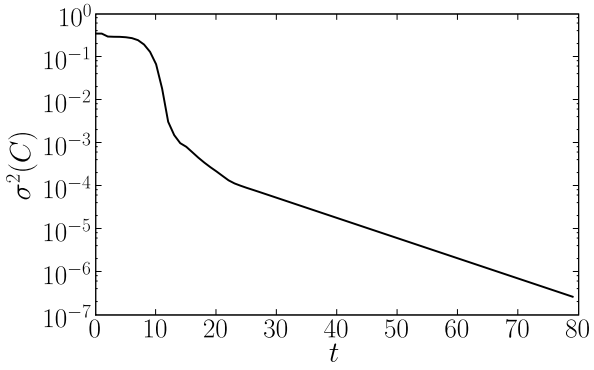

Figure 4.23: Decay of variance measured in a central region for a large value of a ($a = 200$). We observe two exponential stages: the first one corresponds to the decay of fluctuations due to stretching inside the bulk, while the second is the signature of a strange eigenmode dominated by the parabolic point.

- the size of the leftmost image of the initial profile, $d(t) \simeq 1/(at)$. For an initial dye blob, this corresponds to the size of the remaining white pool. Variance is stored in this slowly shrinking region.
- the Batchelor scale at the wall $w_0 = \sqrt{\kappa/(1 - f_1'(w_0))}$, which controls the asymptotic strange eigenmode.
- the size of the wall region compressed to a box of size w_B when it is reinjected in the bulk $W = \sqrt{w_B/(\gamma a)}$. All fluctuations inside W are averaged when they are reinjected.

Our analysis shows that the only way to reduce the effect of the wall is to increase the coefficient a so that the distance between the mixing pattern and the wall $d(t) = 1/at$ decreases faster. This can be achieved in an experiment by taking a stirring rod closer to the wall (this corresponds to "scraping the bowl" while making a cake!). If fluctuations corresponding to strips injected from the boundary are smaller than concentration fluctuations coming from the averaging of dye strips, the effect of the wall will not be visible during a first phase.

Results of a simulation realized for $a = 200$ are plotted in Fig. 4.23. (We have used a modified version of the model, that is $f_1(x) = x - ax^2$ for $x < (1 - \gamma)/a$ and $f_1(x) = \gamma x$ for $x \geq (1 - \gamma)/a$ in this simulation.) After a short superexponential decay of variance, we observe two distinct exponential regimes. The first one correspond to the decay of fluctuations due to stretching inside the bulk, while the second phase of smaller slope is the signature of the strange eigenmode dominated by the boundary. Notice that increasing a also increases the decay rate $\alpha = 1 - 2a(\kappa/4a)^{1/3}$ of this strange eigenmode. No power-law decay is visible in this case, as fluctuations due to stretching in the bulk are higher than fluctuations coming from

injected white strips during the phase where such strips have a power-law scaling – that is before the onset of the strange eigenmode.

In the course of writing this manuscript, we became aware of another recent independent approach to characterize the effect of no-slip hydrodynamics on mixing. Salman and Haynes [96], using theoretical arguments initially developed by Chertkov and Lebedev [25, 24, 59], wrote an effective diffusion equation for the concentration field of a passive scalar, averaged on many realizations of a short-correlation flow. Using the structure of the effective diffusion tensor close to a no-slip wall, combined with an order-of-magnitude analysis of the effective advection-equation equation, the authors distinguished 4 stages of homogenization in the whole domain:

- a first stage during which filaments are compressed down to the bulk Batchelor scale w_{B} (using the notations we defined),
- a second mixing step where strips of scale w_{B} average *until the bulk field is completely smooth*. Salman and Haynes suggest an exponential decay of concentration variance during the phase.
- a power-law decay of the variance in the whole domain, as a shrinking pool of unmixed fluid remains in the boundary region.
- eventually, an exponential decay once the width of the unmixed pool is of the order of magnitude of the diffusive length. This final step is discussed in details in the following paragraph.

Although our analysis shares some features with the scenario of Salman and Haynes, we disagree on a central point: because of the reinjection of unmixed fluid along the unstable manifold of the parabolic point, variance is not exponentially exhausted in the bulk. We indeed measure a power-law decay of the variance in the whole domain scaling as t^{-1}, as fluctuations are trivially dominated by the remaining unmixed pool, which scales as $1/t$. However, we have also shown that the concentration field inside the bulk – where exponential stretching is at play – also has non-trivial power-law dynamics, a distinctive spatial structure born by the unstable manifold of the parabolic point, and resulting typical concentration distributions. This behavior in the bulk is of particular interest, e.g. for industrial applications: the effect of no-slip boundaries is not felt only in a boundary layer that could be discarded while manufacturing the final mixed product; walls rather contaminate the whole mixing domain up to its high-stretching core because of the reinjection process.

The asymptotic appearance of a strange eigenmode is also mentioned in the study of Salman and Haynes [96]; however, our model permits an

explicit analytical calculation for the decay rate of the eigenmode, and its scaling with the Péclet number κ, which are new results as far as we know.

4.4 Bounded domains where the chaotic region is "protected" by an elliptic region encircling the wall

We have seen in the previous section that the influence of no-slip walls is spectacular as long as the chaotic region extends to the wall, since (i) no-slip hydrodynamics impose that homogenization is very slow close to the wall, moreover (ii) ill-mixed fluid is continuously reinjected inside the bulk and contaminates the mixing pattern even in the high-stretching region.

We have looked for a way to "protect" the chaotic region from being infected by the no-slip wall. To this purpose, we have used our closed-flow mixing apparatus to study another type of mixing protocol , which is depicted in Fig. 4.24 (a). This time, the cylindrical rod is moved on a *epitrochoid*, that is a circle with an inward loop. The rod path equation is given by

$$z = x + iy = r_i \exp(2\pi i t) + r_o \exp(4\pi i t) \tag{4.43}$$

with $r_i = 0.19$ and $r_o = 0.48$. Some topological mixing aspects of this protocol are studied in [38, 44].

The Poincaré section in Fig. 4.24 (a) shows that the resulting phase portrait is separated in two regions: a large central chaotic region, and an annular regular region encircling the wall, where trajectories are roughly circular. As a rule of thumb, such a topology of the Poincaré section arises when particles close to the wall "see" a global rotation, either when the wall itself is moving, or as in our case when the rod travels always with a continuous direction on the outer envelope of its path. As a result of the nature of the Poincaré section, fluid particles initially close to the wall never go inside the central chaotic region, notwithstanding diffusion between the two regions, which is negligible for the duration of an experiment. We therefore expect different homogenization dynamics.

The dye pattern of Fig. 4.24 (b-d) confirms the nature of the Poincaré section obtained from numerical simulations. Indeed, a blob of dye is stretched and folded in many filaments under successive iterations of the protocol, yet it is only dispersed up to the frontier of the chaotic region. We measure the concentration field inside a large square inside the chaotic

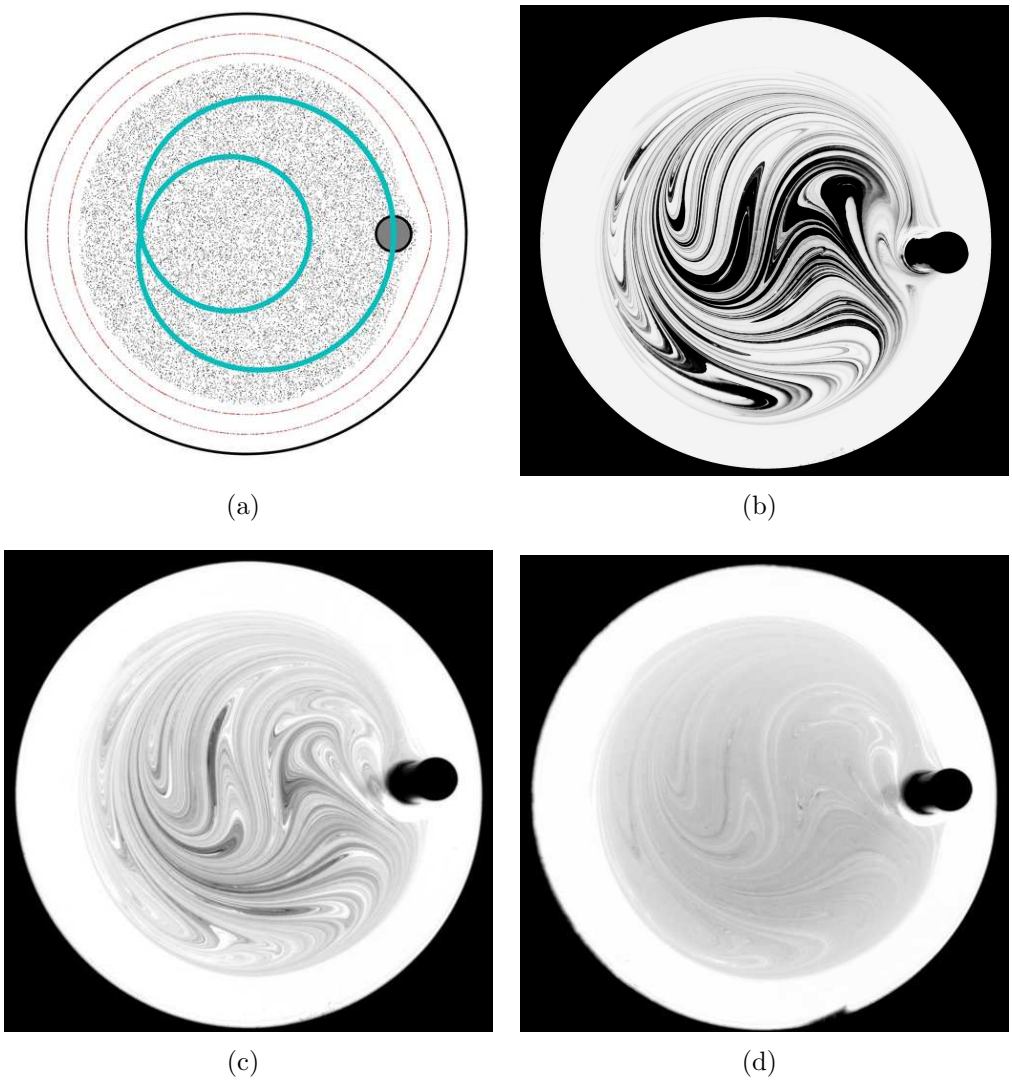

(a) (b)

(c) (d)

Figure 4.24: (a) Poincaré section of the epitrochoid protocol (i.e. a rod is moved periodically on an inwards looping path). The phase portrait is separated into a central circular chaotic region, and a regular region around the wall. The radius of the chaotic region is broadly determined by the greatest distance between the rod and the domain center. (b)-(d) Successive homogenization steps. Note the resemblance between the observed concentration patterns.

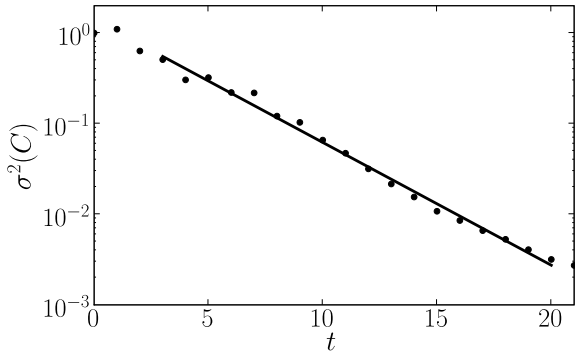

Figure 4.25: Concentration variance measured inside the chaotic region for the epitrochoid protocol. We measure an exponential decay $\sigma^2(C,t) \simeq \sigma_0^2 \exp(-\alpha t)$, with $\alpha \simeq 0.31$.

region. This time, the variance decays exponentially as

$$\sigma^2(C,t) \simeq \sigma_0^2 \exp(-\alpha t) \tag{4.44}$$

with $\alpha = 0.31$. Moreover, concentration PDFs have a very different shape than for the figure-eight case (see Fig. 4.26(a)): PDFs are much more symmetric, have a Gaussian core around the maximum value and exponential tails. White concentrations have a negligible value after a few periods, as no white fluid source is present in this case. The appearance of exponential rather than Gaussian tails indicates the importance of stretching correlations, which permit rare events (high fluctuations from the mean) to survive. After 10 periods, the shape of the PDF becomes approximatively self-similar, as can be seen on Fig. 4.26(b), consistently with the onset of a strange eigenmode. We indeed observe a permanent spatial pattern after a few periods (Note that this does not prove the existence of a strange eigenmode: a protocol with a parabolic point on its boundary also yields a recurrent spatial pattern, dominated by the unstable manifold of the parabolic point).

Let us note that there have been very few observations, be they experimental or numerical, of a strange eigenmode in a physical flow (by physical flow we mean a deterministic flow that can be obtained in an experiment). Precise measures of concentration fields have been performed in dye homogenization by magnets arrays [95, 52, 127], yet no exponential decay was clearly evidenced (plots of the variance evolution in [95], [127] and [52] on a linear scale seem slower than exponential). We therefore believe our protocol is a good candidate to study strange eigenmodes.

Our results are consistent with the simulations of Salman and Haynes [96], where an exponential decay was obtained with solid slip boundaries. Further understanding of our experiment would require to relate the mixing rate α to dynamical or topological properties of our flow. Finding such

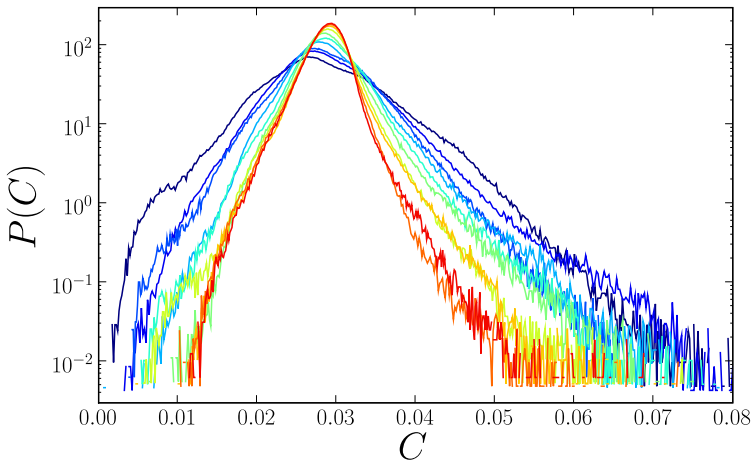

(a)

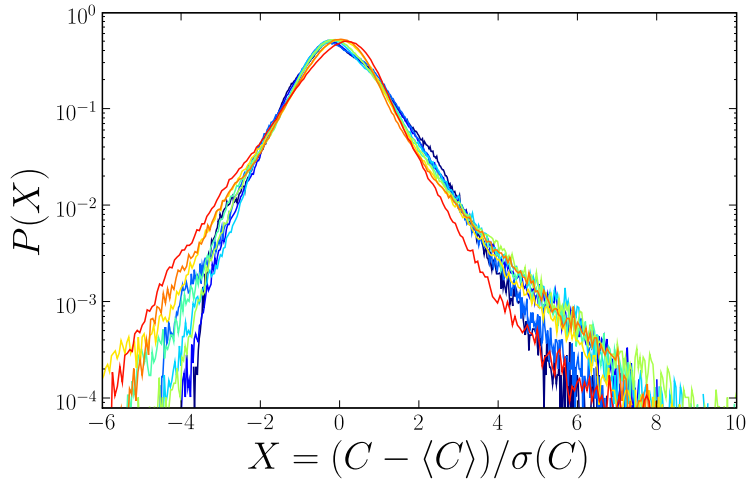

(b)

Figure 4.26: Concentration PDFs for the epitrochoid protocol from periods 7 to 23, in log-linear plots. (a) $P(C)$. (b) PDF of the rescaled concentration $X = (C - \langle C \rangle)/\sigma(C)$. These experimental PDFs display a Gaussian core as well as approximatively exponential tails on both sides, and are broadly self-similar. Note the striking difference between the rescaled shape and the PDFs for the figure-eight-case (Fig. 4.9 (b)).

relations has the subject of much recent research about strange eigenmodes [37, 131, 116, 112, 48], but no general theory for physical flows exists yet. In the following paragraph, we shortly sketch some hints to understand the structure of the observed eigenmode. No rigorous proof is provided here, and this discussion shouldn't be regarded as more than a bit of science-fiction. Yet, we hope these suggestions might fuel some future developments.

We have seen in Sec. 4.2 how the concentration eigenmode is dominated by the periodic point of weakest compression in the case of a fully hyperbolic baker's map. However, the inhomogeneity decay rate results from a subtle averaging of neighboring dye strips that is highly dependent on stretching correlations, and finding the expression of the decay rate is problematic. In our protocol, we believe the equivalent of this periodic point is played by the periodic structures with lowest stretching, that is some periodic parabolic points inside the chaotic region. Such parabolic points give rise to "fat" folds visible in the mixing pattern (see Fig. 4.24 (b)). In Chapter 3, we have suggested that parabolic points play a special role in the mixing pattern, as they allow bunches of dye filaments to be *folded*. We have therefore proposed that efficient ghost rods must be searched among periodic parabolic points. Moreover, there is a trade-off between stretching and curvature in incompressible flows [63, 21, 113], therefore folded strips keep a larger width than elongated parallel ones. More precisely, a scaling law $\Lambda \propto k^{-1/3}$ between the cumulated stretching Λ of a filament, and the curvature of the line k, has been evidenced in Ref. [113]. Material lines therefore experience little stretching close to parabolic points, where they are repeatedly folded. It has been shown recently [115] that the maximal curvature of a material line attached to a periodic parabolic point grows linearly with time, as

$$k = an, \tag{4.45}$$

where the strength of the parabolic point a is related to the importance of non-linear terms in the Poincaré map. The width of a dye filament close to a periodic parabolic point then decreases very slowly (as $t^{-1/3}$ asymptotically). We therefore expect the mixing pattern to be determined by a specific orbit of periodic parabolic points and their unstable manifold. This is confirmed by the experimental pictures (see Fig. 4.24), yet quantifying this assertion will require further understanding of stretching dynamics close to a parabolic point. Fortunately, the singularity of parabolic points might allow to make crude simplifications as we did for the figure-eight protocol, whereas the hyperbolicity of the baker's map imposes to take into account complicated spatial correlations for stretching. The holy grail, of course,

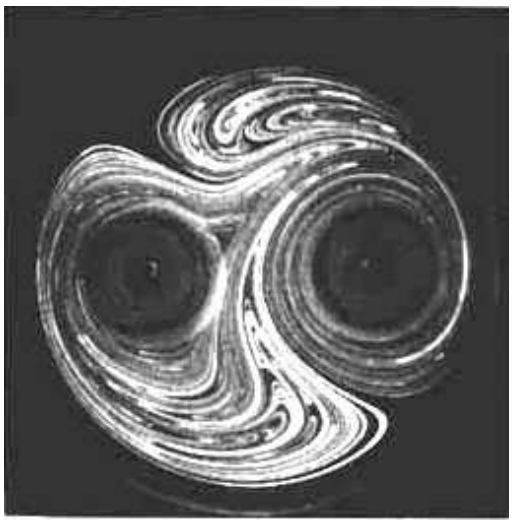

Figure 4.27: Dye homogenization experiment in a co-rotative blinking vortex, taken from Jana et al. [50]. Two cusps at the border the dye pattern reveal the presence of two parabolic points on the boundary. This is a variant of the figure-eight protocol where there is only one parabolic point on the wall.

would be to relate the concentration decay rate to topological properties of a braid formed with parabolic points. This will be the subject of future research.

4.5 Discussion

The results of this chapter can be summarized as follows. First, we have demonstrated the importance of the phase portrait in the vicinity of a no-slip wall for homogenization dynamics in a closed flow. We have described a universal mixing scenario for mixers where the chaotic region extends to the solid wall. No-slip hydrodynamics in the wall region impose that poorly mixed fluid is slowly reinjected in the bulk along the unstable manifold of a parabolic point. (Note that phase portraits with many injection points are also possible, as can be seen in Fig. 4.27. This shouldn't affect the validity of our arguments.) Mixing dynamics are then controlled by the slow stretching at the wall, which contaminates the whole mixing pattern up to its core. A second universality class correspond to a phase portrait separated into a central chaotic region, and a regular region encircling the wall. This is a trick to retrieve "slip" boundary conditions for the chaotic region, and experiments realized for this class indeed yield an exponential decay of fluctuations, consistent with the observation of a strange eigenmode. Predicting the topology of the phase portrait for a given stirring protocol is therefore of high importance. As can be seen in Fig. 4.28, the topology of stirring rods trajectories does not suffice for this purpose. It is our hope that the braiding of ghost rods [44] might provide more relevant

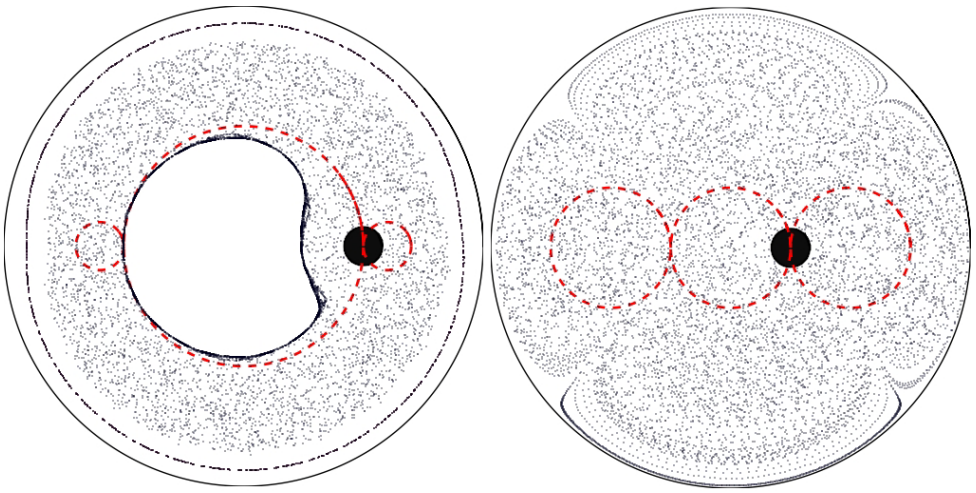

Figure 4.28: The topology of a rod trajectory does not determine the phase portrait close to the wall. We show here two Poincaré sections for two versions of a protocol characterized by three-loop trajectory of the stirring rod. In the first protocol, both sides loops are small enough so that the wall sees only a global rotation corresponding to the central bigger loop. This gives a Poincaré section with a regular region encircling the wall. However, the same path topology with three loops of equal size produces a chaotic region that extends to the wall, with two parabolic injection points (the corresponding reattachment points are also visible in the section).

information – the basic idea being to distinguish between protocols which induce a global rotation or not.

Also, our study has highlighted the role of periodic structures with lowest stretching in the construction of a time-coherent mixing pattern, dominated by their unstable manifold. This applies to the least unstable periodic point in the baker's map (thus a hyperbolic point), to the wall parabolic point for the figure-eight case, and probably to the bulk parabolic points for the epitrochoid case. The importance of elliptic region for limiting mixing dynamics has been emphasized in other studies [89, 90].

Chapter 5

Homogenization in open flows

Throughout the previous chapter, we have focused on mixing mechanisms in bounded systems, where homogenization arises through the averaging of different filaments which are stretched as they wander through the chaotic region. We have proposed different mixing scenarios, depending on the nature of the Poincaré section, and we have highlighted the crucial role of no-slip walls for homogenization dynamics.

Here, we address the question of scalar mixing in open flows. We wish in particular to relate statistical properties of the scalar concentration field to specific Lagrangian transport resulting from open-flow dynamics. For that purpose, we analyze homogenization experiments in the open-flow channel mixing device, where a concentration fluctuation – a blob of dye – injected upstream of the mixing region is advected by the main flow, and then stretched and folded into a complex mixing pattern, both in the mixing and downstream regions as it is gradually washed away by the main current. We focus here on generic mechanisms governing homogenization dynamics; relevant measures to characterize this mixing processes, and the mixers themselves, will be discussed in the next chapter. It turns out that the approach developed for closed flows can be adapted efficiently to open flows, and we will make extensive use of the knowledge gained in the previous chapter to describe mixing in our channel flow. It should be kept in mind that by "open flows", we refer to throughflow systems where the velocity field is stationary far from a spatially limited mixing region. Such terminology is also employed for successive mixing elements as in micromixers e.g., but that is not what we aim at describing here.

In a first section, we briefly sketch distinctive features of fluid transport realized by butterfly and breaststroke protocols. We show that regarding the role of no-slip side walls, the former can be mapped to the closed-flow figure-eight protocol, while the latter is the open-flow equivalent to the epitrochoid

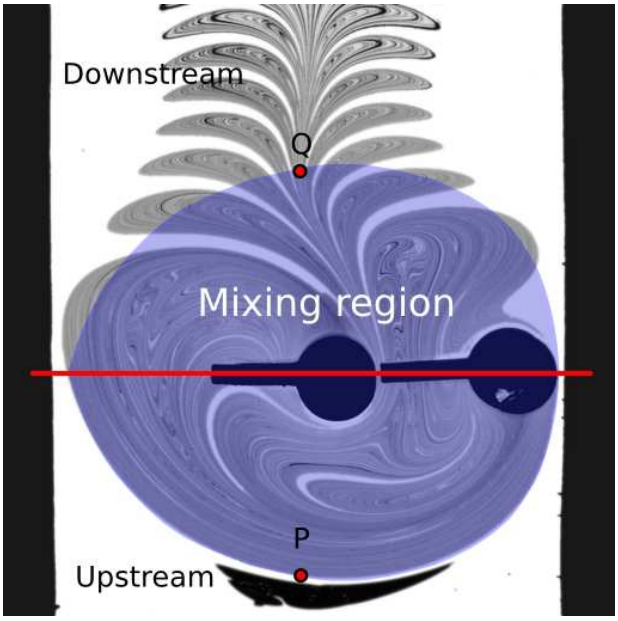

Figure 5.1: Phase portrait for a butterfly open-flow protocol. The extent of the mixing region can be determined from the first crossings of the stable and unstable manifold of the separation point P – the furthermost upstream point of the chaotic saddle. See Fig. 3.12 in Ch. 3 for more details. Note that the mixing region is well separated from the side walls.

protocol. Section 5.2 addresses the butterfly case, where free trajectories shield the mixing region from the effect of the walls. We illustrate the appearance of an open-flow strange eigenmode, that is a recurrent spatial pattern of decaying contrast. A simple 1-D model is introduced to flesh out this scenario. In section 5.3, we study the breaststroke case where parabolic stagnation points on no-slip side walls store poorly stretched fluid for long times, and result in modified residence time distributions, and mixing dynamics.

5.1 Introduction – similarities with homogenization in closed flows

In open flows, efficient mixing – that is repeated stretching and folding – takes place in the vicinity of the bounded unstable orbits of the chaotic saddle [109]. As in closed flows, these periodic orbits braid forever in a non-trivial way and stretch significantly dye particles in their vicinity: topologi-

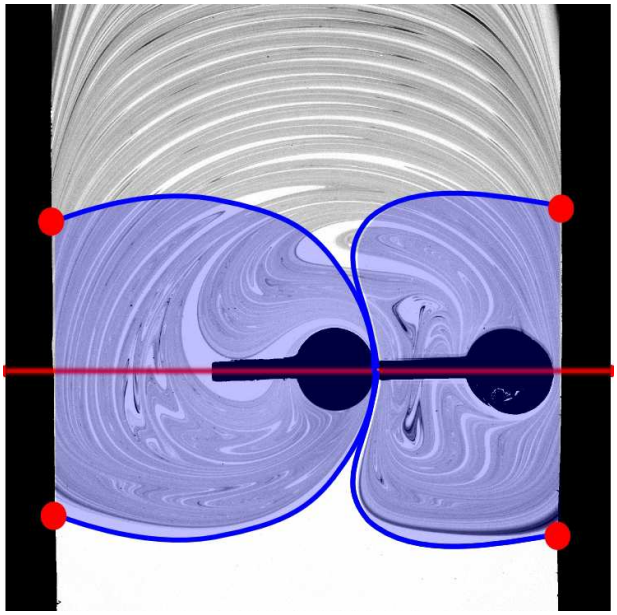

Figure 5.2: Plot of the mixing region for a breaststroke protocol. The mixing region is delimited by the manifolds of two parabolic stagnation points on the side walls, that arise from the competition between the main flow and the rods motion near the walls.

cal chaos exists in open flows as well. However, from a Lagrangian point of view, mixing only occurs during the limited time a point-like particle spends inside the mixing region. One should first wonder about the geometry and extent of the mixing region. Since particles eventually escape downstream, Poincaré sections are not relevant tools to characterize the phase space for transient chaos. As chaotic bounded orbits fill a dense bounded set [109], it is yet possible to define a "chaotic region" as the closure of such orbits, to which we refer as mixing region in the following. One illustrative example has been drawn in Fig. 5.1 for a butterfly protocol. Using flow symmetries, we have described in Chapter 3 how to obtain the extent of the chaotic saddle from the intersection of its stable and unstable manifolds – the latter being traced out by dye particles that have spent a long time inside the mixing region. Such a definition allows to distinguish as well an upstream region where fluid particles have never entered yet the mixing region, and a downstream region where fluid particles will never enter again the mixing region. Such a definition is not unique as some particles might never enter the mixing region at all; the cartoon in Fig. 5.1 corresponds to the most symmetric solution.

Butterfly and breaststroke protocols yield different topologies of the mix-

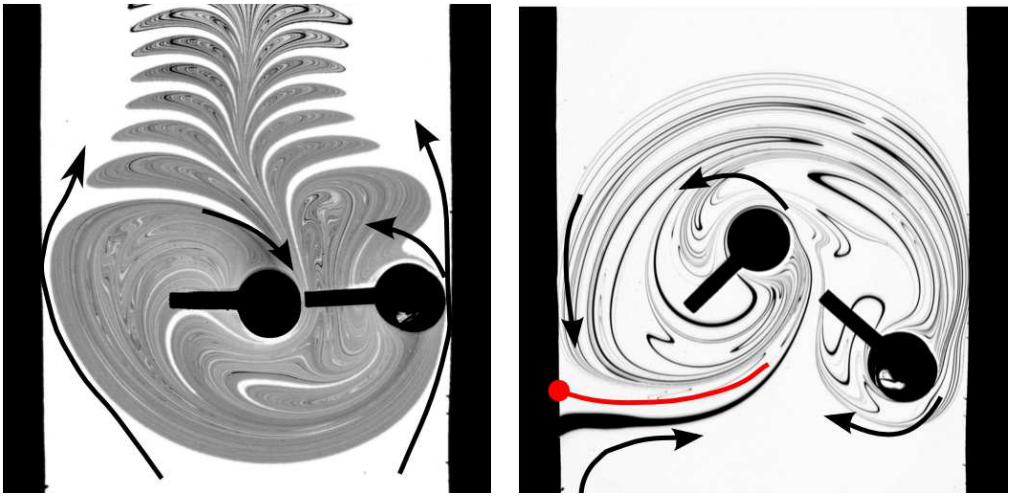

(a) (b)

Figure 5.3: Transport properties of the butterfly and breaststroke protocols. (a) In the butterfly case, rods travel with the main flow along the channel sides, so that they help fluid to cross from upstream to downstream. The induced phase portrait consists a thin layer of free trajectories parallel to the wall, where no bounded orbits of the chaotic saddle can exist. and of the mixing region – the closure of the chaotic saddle –, which is here well separated from the side walls. (b) In the breaststroke case, rods travel with the main flow in the center, yet against the flow along the channel sides. This results in a phase portrait with two stagnation points on each side, which are parabolic for no-slip boundary conditions. Here the mixing region extends over the whole channel width, and fluid enters the mixing region along the unstable manifold of the stagnation points (in red).

ing region, as can be seen in Figs. 5.1 and 5.2. For the butterfly version, the chaotic region is well separated from the channel sides, where *free* trajectories are allowed to follow the side walls, and never visit the mixing region. Basic transport features of the flow account for this situation: along the channel sides, rods travel in the same direction as the main flow, so that they help fluid to reach the upstream region (Fig. 5.3 (a)). This favors the existence of free trajectories that shield the mixing region from the side walls. This situation appears to be quite similar to the epitrochoid closed-flow protocol studied in the previous chapter, where a central chaotic region is shielded from the wall by an annular regular region. Here, the mixing region plays the role of the chaotic ergodic region, and the free trajectories layer corresponds to the regular region.

Fig. 5.2 shows the approximate location of the mixing region for the breaststroke protocol, which is again obtained by following the lower boundary of the dye pattern for long times, and joining it with its symmetric image with respect to the $x = 0$ axis (see Section 3.3 for more details about this method). This time, the mixing region extends to the side walls, and new fluid enters the mixing region only through the funnel-shaped cusp that separates the two left and right parts of the mixing region (Fig. 5.2). Once again, this can be traced back to the motion of the rods with respect to the main flow. Along the channel walls, rods travel against the main flow. Two stagnation points, one on each side wall of the channel, stem from this competition (red circles in Fig. 5.2). The unstable manifolds of these points are transport barriers and delineate the lower frontier of the mixing region (see Fig. 5.3 (b)). As in the closed-flow case, these stagnation points are parabolic, and we expect the same scalings for the velocity field near the parabolic point to hold (Eqs. (4.11), (4.13) and (4.15)), as they ensue directly from no-slip hydrodynamics on the wall. Thus, there is on each side of the channel a parabolic injection point, from which fluid is transported to the core of the mixing region, and a symmetric parabolic reattachment point at the frontier with the downstream region, where parallel filaments pile up (see Fig. 5.2). This phase portrait is strongly reminiscent of the figure-eight closed-flow protocol, and more generally of closed flows where the chaotic region goes to the wall. We expect these parabolic points to store for long times poorly stretched fluid, as they do in closed flows [43].

Taking advantage of this strong analogy between closed and open flows, we will first study the butterfly case, which we expect to be more ideal as stretching is more homogeneous in the mixing region, and then we will take on the breaststroke case and examine the role of no-slip walls. Note that by "ideal", we refer to the nature of the phase portrait rather than to the efficiency of mixing. The breaststroke case should be a better candidate for most industrial applications than the butterfly one, as the dye pattern covers the whole channel width; yet its effects are more difficult to understand because of the presence of stagnation points on the walls.

5.2 Butterfly case: bulk-only chaotic saddle and open-flow strange eigenmodes

5.2.1 Phenomenological description

Over the three first chapters of this manuscript, we have described many times the typical advection scenario for a dye blob injected upstream of

the mixing region. As the blob arrives is advected towards the mixing and downstream region, some part of it escapes immediately downstream and therefore stays "unmixed", while the remainder is caught by the rods inside the mixing region (see Figs. 1.4 or 3.9 for illustration of this process). In Chapter 3 (Sec. 3.3), we have concentrated on quantifying the fraction of fluid escaping rapidly, and we have shown how this quantity could be evaluated geometrically, using an asymptotic image of the downstream pattern which shadows the unstable manifold of the chaotic saddle. Here, we aim at describing the evolution of the concentration field after this short initial transient.

From visual inspection, the evolution of the concentration field inside the mixing region can be decomposed in two steps.

- As dye enters the mixing region in the wake of a rod, fluid particles are repeatedly stretched and folded by the rods into thinner and thinner filaments. Dye filaments are dispersed all over the mixing region as fluid particles visit the vicinity of different orbits of the chaotic saddle (as such orbits are unstable, point-like particles jump from one orbit to another. This results in a complex network of elongated dye filaments between such orbits.) Very quickly (typically, after two or three periods), the frontier of the mixing region seems invariant – this means that some dye particles have come close to the separation point P (see Fig. 5.1) and are elongated along its unstable manifold.

- As in closed flows, diffusion limits the thinning process at a typical Batchelor scale where diffusion and stretching balance. Once filaments have reached this diffusion scale, they fill out an invariant domain where many filaments overlap. This domain is the intersection with the mixing region of the unstable manifold of the chaotic saddle, that is, dye can be found close to periodic orbits and along their unstable manifolds, as such orbits are unstable. It has been shown that the unstable manifold of the chaotic saddle is a fractal set [111]. The fractal structure of the pattern is apparent in Fig. 5.1 or 5.4. Large white holes in the pattern correspond to the incorporation of unmixed fluid from upstream, at places where no periodic orbits can survive. This white patches are then stretched and folded, so that they are squeezed between also elongated dye filaments: the stretching process in responsible for the scale-invariance characteristic of fractal objects. Here the unstable manifold is fattened up by diffusion, so that the pattern has a finite measure, contrary to the fractal set.

The permanent coverage of the fattened unstable manifold by dye is easily understood, yet quantitative dynamics of the concentration field are more difficult to predict. In the following, we show that the concentration field converges to a permanent self-similar field with exponentially decaying contrast, as could be guessed from visual inspection. We give a phenomenological description of this pattern, and describe its variations with stirring frequency.

5.2.2 Pattern description

Asymptotic concentration patterns are shown in Fig. 5.4 for different stirring frequencies (f = 1.5, 2, 3, 4, and 8 rpm). As bounded trajectories trapped in the mixing region can survive further from the rods for a relatively weaker global advection, the size of the mixing region increases with the stirring rate. The total size of the mixing region (defined as the size of the blue-shaded area in Fig. 5.1) is plotted in Fig. 5.5. The growth of the area with stirring frequency saturates for high frequencies, as radial growth is limited by the channel side walls for high frequencies.

Significant evolution with increasing stirring frequency is also visible for the geometry of the downstream concentration pattern. The spatial periodicity of the pattern is entirely governed by the stirring period (remember that we fix the global flowrate), so that more lobes are visible in the region of interest for higher stirring frequencies. The balance between the main flow, that takes away fluid downstreamward, and the flow created by the rods, which brings fluid back in the center of the channel, is responsible for the lateral extent of the lobes, which decreases with f. In Chapter 3, we have related the typical residence time inside the mixing region to this lateral extent.

Beyond geometry, it is also interesting to characterize the concentration distribution inside the mixing region or in the downstream lobes. Global contrast variations may decay with time, as less and less dye remains inside the mixing region, yet fluctuations normalized by the remaining amount of dye seem to be stable in the Poincaré map (this will be confirmed later by quantitative measures of the concentration field). Large fluctuations are of two natures.

- White strips correspond to holes in the fractal dye pattern, which are images of newly injected upstream fluid, and are therefore always observed at the same locations in the Poincaré map. Thinner strips have been injected earlier and then stretched and folded.

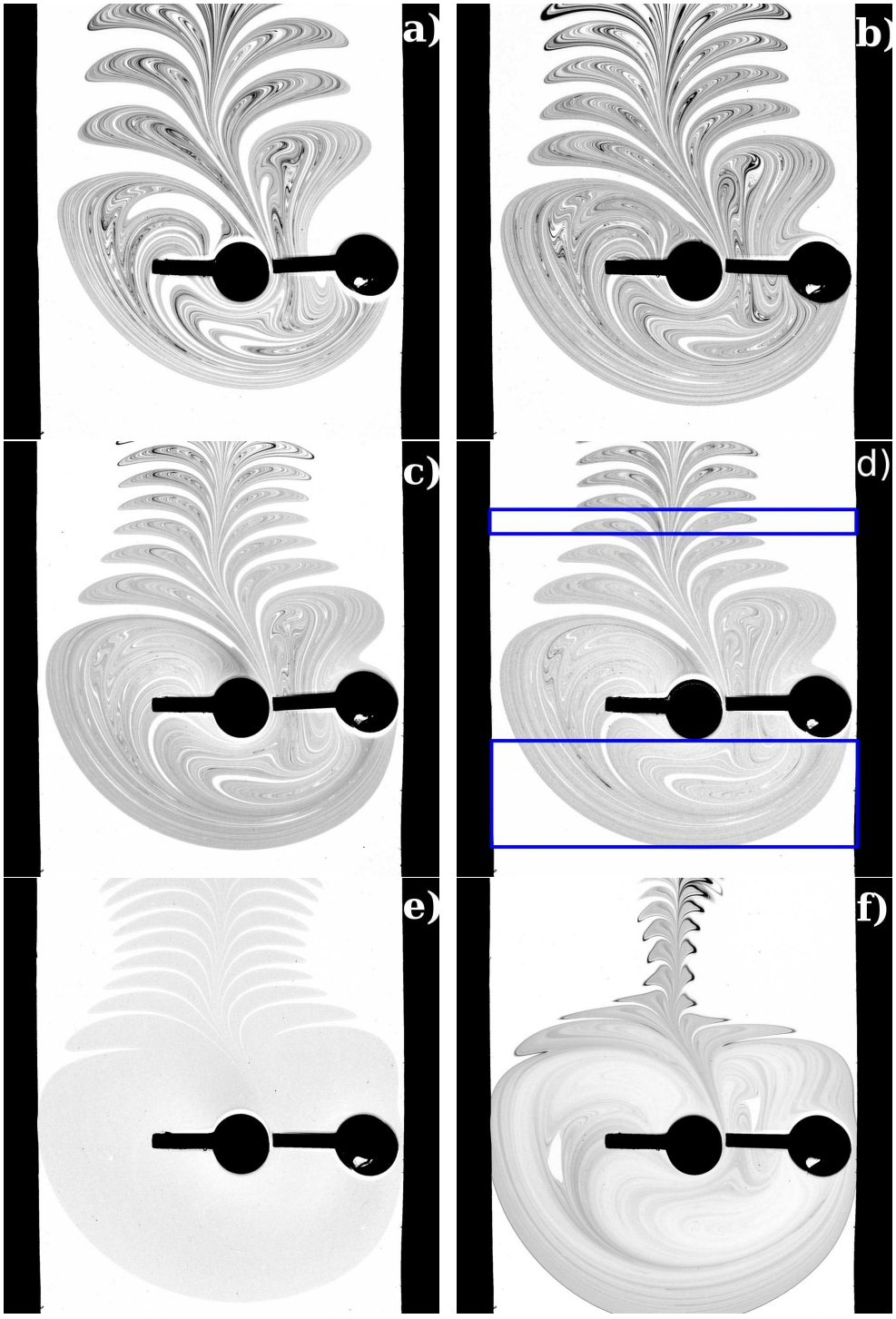

(For caption see opposite.)

Figure 5.4: (Previous page) Asymptotic concentration pattern for different stirring frequencies: $f = 1.5$ (a), 2 (b), 3 (c) and (d), 4 (e) and 8 (f) rpm. Beyond the global flower-shaped aspect, obvious differences and trends are visible on these pictures. First, the size of the mixing region increases notably with the stirring rate. Also, the lateral extent of downstream lobes globally decreases with stirring frequency. Homogeneity inside the filamentary mixing pattern varies with f in the following way: (i) a larger fraction of white holes is visible for smaller stirring rates (this corresponds to a smaller fractal dimension of the unstable manifold $\mathcal{W}_u$), (ii) the mixing pattern seems globally more homogeneous for higher stirring frequencies, except for $f = 8\,\mathrm{rpm}$ where two elliptical islands might perturb homogenization processes. For all frequencies, high contrast black zones are visible in the vicinity of folds, i.e. bulk parabolic points where stretching is low.

.

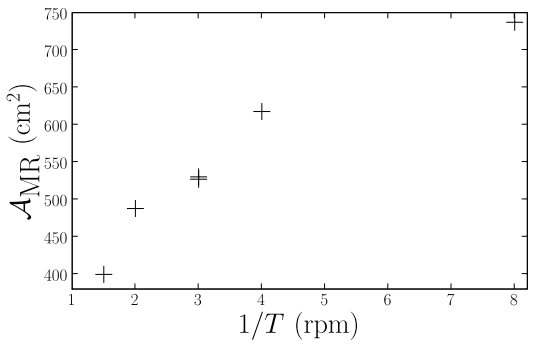

Figure 5.5: Mixing region area vs. stirring frequency. As can also be seen in Fig. 5.4, the size of the mixing region increases noticeably with stirring frequency. However, this growth saturates for $f = 8$, as side walls limit the radial growth at play for small stirring frequencies.

- Dark filaments that bear a concentration greater than the mean value are visible near large folds inside the pattern, where stretching is small and bulk parabolic points are nested. The separation point P (see Fig. 5.1) is also one of the structures where stretching is smallest, as it is far from the rods. This results in a darker boundary region for both the mixing region and the lobes torn away.

Finally, we note the appearance of two small elliptical islands for $f = 8$ rpm (Fig. 5.4 (f)). Three darker "branches" emanating from each island determine partly the structure of the mixing pattern, and the paths along which these low-stretching regions contaminate the remainder of the field. We have observed that these islands survive and even get bigger for higher stirring frequencies (however, 3-D effects become apparent at such high

stirring rates, so we did not measure the concentration field for these frequencies).

All in all, the mixing pattern inside the mixing region seems to become more homogeneous while increasing the stirring rate up to 4 rpm, but is less homogeneous at $f = 8$ rpm (and presumably for $f > 8$ rpm), where elliptical islands may be responsible for larger concentration fluctuations that are observed. It is interesting to note that there seems to be an optimal stirring rate for mixing quality. In order to characterize the homogeneity of the downstream pattern, one must take into account the homogeneity inside the lobes, but also the relative area occupied by the lobes. Once again, a better homogeneity is achieved for higher stirring rates, except for $f = 8$ rpm. We quantify this evolution in the next section.

5.2.3 Statistical properties of the concentration field

Measures – We measure and analyze the statistical properties of the concentration field in two different regions: a large rectangle that extends over the channel width and encloses the lower part of the mixing region, up to the lower part of the rods, and a downstream rectangle determined by the channel width and the spatial period of the pattern – it therefore contains one lobe on each half of the channel. We will refer to the former as the mixing region concentration field, and to the latter as the downstream concentration field.

We present below results for the evolution of the concentration mean, variance and PDFs with time. Such quantities are obtained using the relation between light intensity as recorded by the camera, background light intensity, and dye concentration as determined by the calibration of the camera. Pictures taken with the camera used for open-flow experiments suffer from a weak but noticeable Gaussian white noise, delta correlated in space and time. This results in a statistical error of $\sigma_{\text{noise}} = 10^{-4} C_0$ for the concentration field, where C_0 is the dye concentration of the initial blob. Linear quantities such as the concentration mean are not affected by this noise, contrary to the variance. However, cumulants of uncorrelated signals simply add, so that we retrieve the concentration variance as $\sigma^2(C) = \sigma^2_{\text{measured}} - \sigma^2_{\text{noise}}$. In the same way, we use a Wiener filter to reduce the amount of noise while computing concentration PDFs.

Results – We have plotted in Fig. 5.6 the evolution of the concentration mean and standard deviation in the mixing and downstream regions for different stirring frequencies. For $f \in \{1.5, 2, 3, 4\}$, all quantities display

an asymptotic exponential evolution. Remarkably, the mean and standard deviation share the same characteristic time $1/\alpha$:

$$\langle C\rangle_{\mathcal{R}} \simeq C_{\mathcal{R}} \exp(-\alpha n) \tag{5.1}$$
$$\sigma_{\mathcal{R}}(C) \simeq \sigma_{\mathcal{R}} \exp(-\alpha n), \tag{5.2}$$

where $\mathcal{R}$ stands for the mixing or downstream region and n is the number of stirring periods. $1/\alpha$, as determined by the mean concentration evolution, represents the mean number of periods spent by a particle inside the mixing region. We have studied in Chapter 3 its evolution with stirring rate, and we have shown that α scales as $1/f$ to conserve flowrate, with a geometric correction that accounts for the partial coverage of the channel width by the stable manifold of the chaotic saddle. The observed parallel evolution of the first moments hints at the onset of a self-similar concentration field, that is of an open-flow strange eigenmode. This will be confirmed and justified later on.

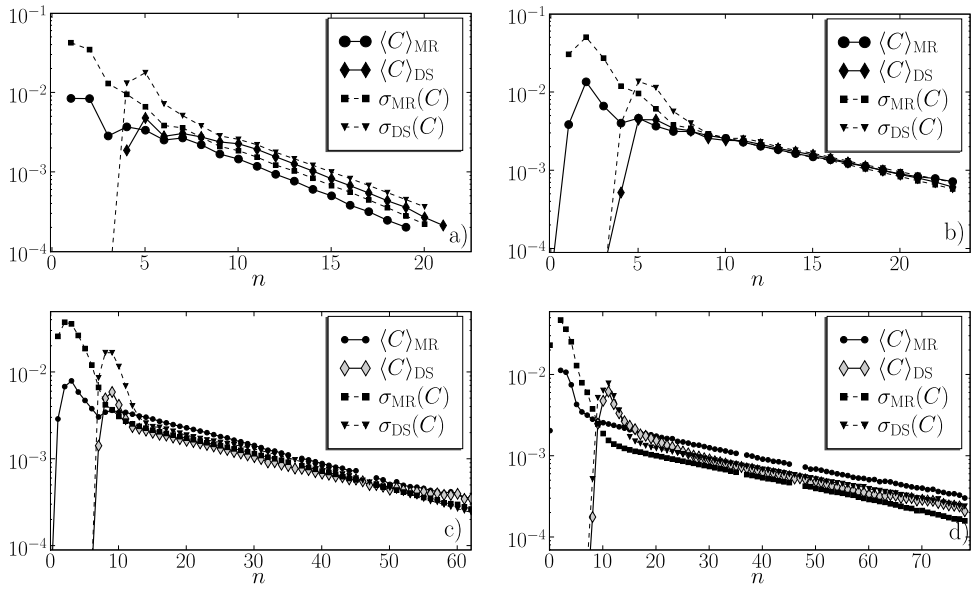

Figure 5.6: Concentration mean and standard deviation in the mixing and downstream regions, plotted against the number of stirring periods n for stirring frequencies $f = 1.5$ rpm a), 2 rpm b), 3 rpm c) and 4 rpm). For all experiments, mean and standard deviation in the two regions show an asymptotic exponential evolution with the same characteristic time. The relative position of the curves representing the mean and standard deviation measures the homogeneity of the pattern.

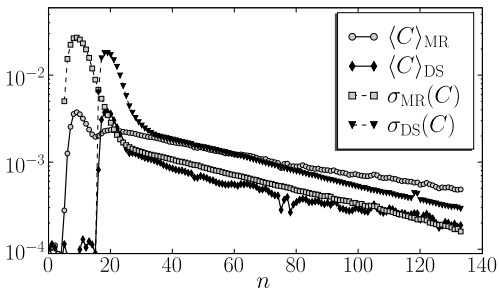

Figure 5.7: Concentration mean and standard deviation in the mixing and downstream regions, for $f = 8$ rpm. After a long exponential regime, we observe for long times a second phase where the evolution of the mean and standard deviation are not parallel any more. This may be attributed to elliptical islands.

A first evaluation of mixing efficiency is given by the relative intensity of fluctuations normalized by the concentration mean $I = \sigma_{\mathcal{R}}(C)/\langle C\rangle_{\mathcal{R}} = \sigma_{\mathcal{R}}/C_{\mathcal{R}}$, which can also be read from the relative positions of the mean and standard deviation plots in Figs. 5.6 and 5.7. In accord with the above visual observation, we notice that concentration patterns are more homogeneous for higher stirring frequencies, and that downstream fields are less homogeneous than in the mixing region, because of the limited lateral extent of the lobes.

For $f = 8$ (Fig. 5.7), the evolution of concentration mean and standard deviation are still exponential and parallel during the first 70 periods, but for longer times the mean concentration decays slower than the variance. This crossover might be due to elliptical islands, and the hierarchy of KAM tori surrounding them where fluid can be trapped for times much longer than the mean residence time. It is still possible to define an instantaneous relative importance of fluctuations: using the definition $I(t) = \sigma_{\mathcal{R}}(C)/\langle C\rangle_{\mathcal{R}}$, we see that despite a good homogeneity inside the mixing region, mixedness is poor in the downstream region because of the small lateral size of the lobes. Other studies have evidenced an asymptotic power-law residence time distribution for chaotic saddles with elliptical islands [58, 103] that is not observed here. We speculate that this power-law regime might be seen only for very long times in our experiments, as our blobs are initialized far from the islands.

For a complementary analysis, we have plotted in Figs. 5.8 concentration distributions measured in the mixing region for different stirring rates. We have also represented PDFs of the concentration normalized by the instantaneous mean value $\langle C\rangle(t)$. We observe that the concentration histograms converge to an invariant self-similar shape for long times: PDFs of the renormalized concentration $C/\langle C\rangle$ collapse on a single curve. This curve characterizes the asymptotic partly homogenized state: it is wider for

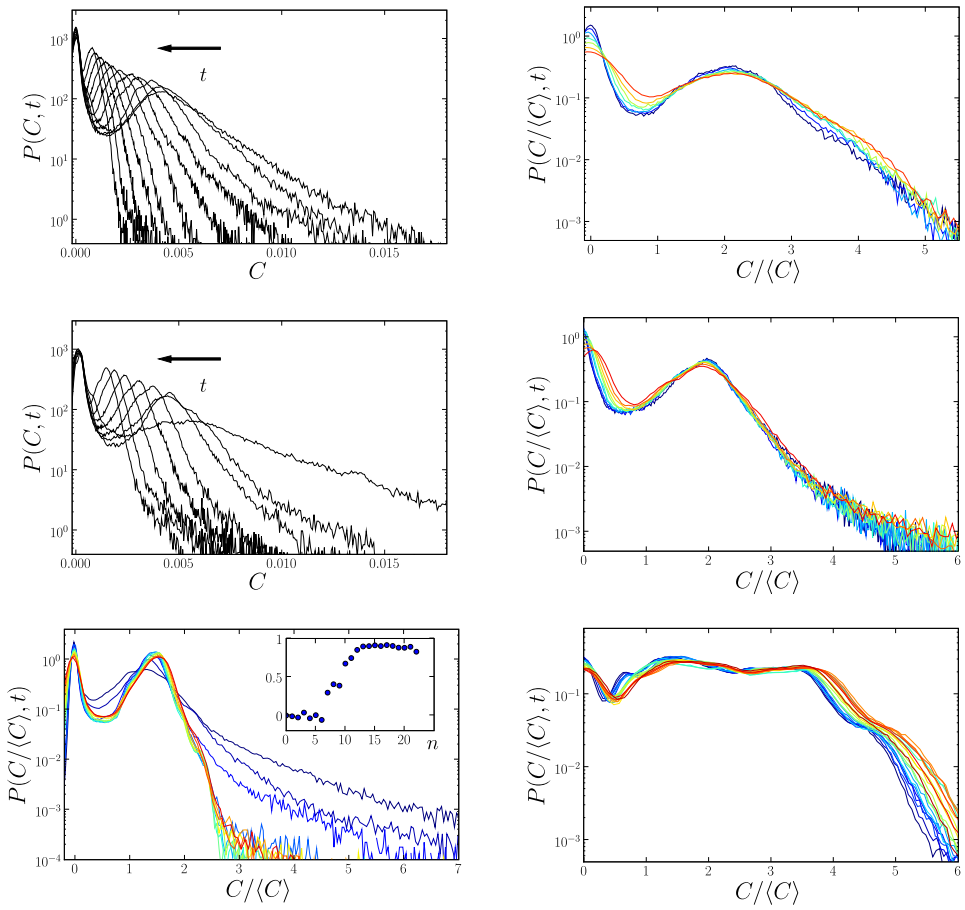

Figure 5.8: **From left to right and top to bottom. (a) and (b)** $f = 1.5$ – Concentration PDFs at periods 9 to 20, and PDFs of the renormalized concentration $C/\langle C\rangle$ at periods 13 to 20, showing the onset of a strange eigenmode. Renormalized histograms have a wide shape, with an approximately exponential right tail. **(c) and (d)** $f = 2$ – PDFs at periods 7 to 23, every 2^{nd} period, and $P(C/\langle C\rangle)$ at periods 13 to 23. The asymptotic histogram is narrower than for $f = 1.5$, which denotes a better homogenization. An exponential right tail on about two decades is also visible. **(e)** $f = 3$ $P(C/\langle C\rangle)$ at periods 9 to 31, every 2^{nd} period. The asymptotic curve is narrower than for $f = 1.5$ and $f = 2$, which is the fingerprint of a more efficient homogenization. An approximately exponential right tail is also visible. Inset: we have plotted the cross-correlation coefficient r between images of the concentration pattern at successive periods. r converges quickly to values close to 1, which also hints at the onset of a strange eigenmode (although non self-similar concentration fields could also yield strongly correlated patterns). **(f)** $f = 8$ $P(C/\langle C\rangle)$ at periods 39 to 60, every 2^{nd} period. We observe a very wide strange eigenmode with a humpy shape that can be traced back to the complicated structure of the concentration pattern in Fig. 5.4 (f). The last iterates shown here do not collapse very well on the master curve, especially for high-concentration values. This departure from the strange eigenmode regime is probably due to elliptical islands inside the mixing region (Fig. 5.4 (f)), and was also visible from the moments evolution in Fig. 5.7.

more heterogeneous patterns (here fore small stirring rates, and also $f = 8$). A roughly exponential tail for values greater than the mean indicates the persistence of rare events, i.e. important concentration values in the vicinity of periodic structures with low stretching (e.g. parabolic points). Note that for very long times, noise amplitude cannot be neglected any longer compared to the mean concentration, and the measured PDF results from a convolution between the real concentration PDF and the Gaussian noise PDF. Collapse on the characteristic curve is then poorer compared to earlier times. It is important to note that the asymptotic PDF shape appears to depend on the stirring frequency, and no universal shape can be extracted from our experiments. We might have expected such observation, as the strange eigenmode strongly depends on the structure of the unstable manifold of the chaotic saddle and on the stretching distribution inside the mixing region.

For $f = 8$, we observe an apparent strange eigenmode in the time interval where standard deviation and mean value are parallel, but later PDFs diverge from this strange eigenmode, probably as a result from the action of elliptical islands.

We now have clear evidence for an open-flow strange eigenmode, i.e. a self-similar field whose relative fluctuations are permanent despite a global exponential decay. This work is to our knowledge the first observation of a strange eigenmode in open-flow chaotic mixing. Recurrent structures have been observed in many experimental [104] or numerical studies [53], and they have been linked to the unstable manifold of the chaotic saddle, yet quantitative evolution nonlinear moments or PDFs of the concentration field of a scalar to mix has never been described before. In the remainder of this section, we justify the appearance of such an eigenmode, using a simplified 1-D map as we did for closed flows.

5.2.4 1-D model: an open-flow baker's map

Model – We now wish to derive a simple model that reproduces the principal mechanisms responsible for homogenization in our mixer, that is (i) a main flow that feeds continuously new fluid into a mixing region, and conversely tears away a fraction of the mixing region, (ii) a stretching and folding process inside the mixing region, and (iii) molecular diffusion that determines the smallest scale of stretched filaments.

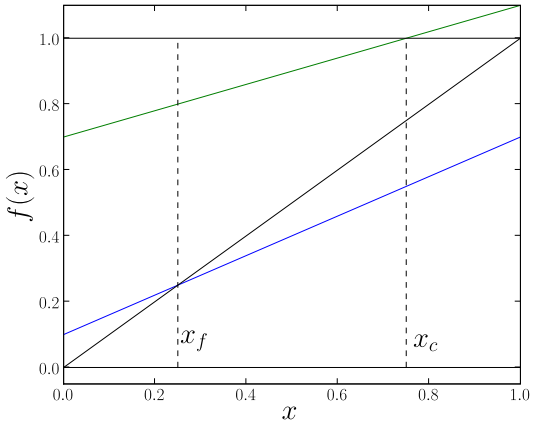

Figure 5.9: Open-flow 1-D baker's map f. Outside the unit interval (not shown on the plot), f translates fluid particles by a distance U at each iteration and thus mimicks the far upstream and downstream channel flow with flowrate U. Inside the unit interval, f acts as an inhomogeneous baker's map with two branches of respective stretching γ and $1-\gamma$, and a shift by U. A fraction $1-\gamma$ of fluid particles in the interval $[x_c, 1]$, where $f_2(x_c) = 1$ will be taken away downstream at the next iteration. Note that f has a fixed point $x_f = U/(1-\gamma)$.

We propose the following 1-D map of the real-axis:

$$\left\{ \begin{array}{rcl} f(x) & = & x+U \quad \text{for } x \in]-\infty, 0] \cup [1, \infty[\\ f(x) & = & \left\{ \begin{array}{ll} f_1(x) = & U+\gamma x \\ f_2(x) = & U+\gamma+(1-\gamma)x \end{array} \right. \quad \text{for } x \in [0,1] \end{array} \right. \tag{5.3}$$

where $U > 0$ is the flowrate, and $0 < \gamma < 1$ and $1-\gamma$ the two stretching coefficients undergone by the two images of the unit interval (A plot of f is shown in Fig. 5.9). The map f evolves 1-D concentration profiles as $C(x, t+1) = C(f^{-1}(x), t)$. The relation $|f_1'(x)| + |f_2'(x)| = 1$ insures mass conservation, or, in other words, incompressibility. At each iteration of the map, a strip of width U of upstream fluid (i.e. contained in the negative part of the real axis) arrives in the unit interval. On the other hand, the interval $[x_c, 1]$, where

$$x_c = 1 - U/(1-\gamma) \tag{5.4}$$

is mapped downstream under the action of f_2, so that a fraction $1-\gamma$ of the mass inside this interval disappears at each iteration. Fluid remaining in the mixing region is stretched by factors γ and $(1-\gamma)$.

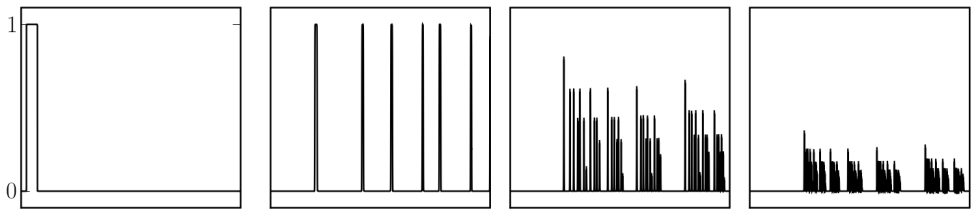

Figure 5.10: Typical evolution of the concentration profile in the interval $[0, 1]$ for the injection of a blob (left). The blob is stretched into a growing number of filaments, which are wider than the diffusive scale w_{B} during a first stage (second picture). As filaments reach w_{B}, neighboring filaments superimpose. Since fluid keeps leaving the interval, the global amplitude of the profile decreases.

As in the channel flow experiments, we inject a blob of dye of width δ in the upstream region, that is we choose an initial profile:

$$C(x,0) = \begin{cases} 1 & \text{for } x \in [x_0 - \delta/2, x_0 + \delta/2] \\ 0 & \text{outside,} \end{cases} \tag{5.5}$$

where $x_0 + \delta/2 < 0$. The blob is translated until it reaches the mixing region, where it is stretched and folded into many filaments, whereas some fraction of the blob is advected downstream at each period. After each iteration of the map, we perform a diffusive step by letting the concentration profile evolve according to the diffusion equation with diffusivity κ and free boundary conditions.

A typical evolution of the concentration profile inside $[0, 1]$ is shown in Fig. 5.10. As the blob enters the mixing region, it is transformed by iterations of the map into a growing number of thinner filaments. In a closed-flow baker's map, 2^n images of the initial blob would be present in the mixing region after n iterations. However, some iterates escape downstream at each iteration in the case of a positive flowrate U, and are no further replicated, so that fewer filaments are present in the mixing region. Once compressed filaments reach the diffusive Bachelor scale w_{B}, diffusion smoothes the profile and neighboring filaments start to superimpose and maximal concentration values decay. Meanwhile, new white upstream fluid keeps being injected in the mixing region; iterates of these white slices are visible as white holes inside the filamentary dye pattern. As time progresses further, more fluid escapes from the mixing region; we observe a self-similar profile, yet with decreasing amplitude.

Chaotic saddle – Our simple model allows to shed some more light on somewhat abstract concepts such as the chaotic saddle and its manifolds.

First note that the map f has one fixed point x_f such that

$$x_f = \frac{U}{1-\gamma}. \tag{5.6}$$

x_f is an attractive point of f_1, so that dye strips compressed by f_1 converge to x_f. Fig. 5.11 shows a typical profile obtained after 20 iterations of the map for an initial dye blob: the support of the dye pattern starts only at $x = x_f$, as all strips initially in the range $[0, x_f]$ have converged to x_f. Because of diffusion, all these strips eventually aggregate inside a box of size w_B, where w_B is the Batchelor scale at which diffusion and compression balance. Since the fixed point is the upstreammost periodic orbit that can survive inside the mixing region, that is the upstreammost point of the chaotic saddle, it plays a role equivalent to the separation point P in the butterfly experiments, at the lower end of the mixing region. The end of the pattern is also located at a periodic point x_e of higher period; x_e is 2-periodic in the case of Fig. 5.11. However, all periodic points are highly unstable. Iterates of a periodic point by cycles different from the one that stabilizes them – e.g. f_1 for x_f – are non-periodic points that eventually vanish downstream. These iterates form precisely the unstable manifold of the periodic points.

Concentration field: onset of an open-flow strange eigenmode – The qualitative evolution of the concentration field by the map reproduces closely our experimental results. We observe an exponential evolution for the decay of the mean concentration measured in the unit interval (shown in Fig. 5.12),

$$\langle C \rangle \simeq C_0 \exp(-\alpha t), \tag{5.7}$$

showing an exponential residence time distribution (RTD) inside the mixing region. Remarkably, higher moments of the concentration field have also an exponential evolution with the same exponent α, as shown in Fig. 5.12:

$$M_i(t) = \left| \int_0^1 (C(x) - \langle C \rangle)^i \mathrm{d}x \right|^{1/i} \simeq A_i \exp(-\alpha t). \tag{5.8}$$

This scaling of moments is consistent with the observation of self-similar concentration PDFs $P(C,t) = \hat{P}(C/\langle C \rangle)$ (Fig. 5.13) and of a permanent spatial pattern. An example of such a permanent pattern is plotted in Fig. 5.11.

All the above results support the claim that an open-flow strange eigenmode sets in after a few periods. We now wish to provide convincing evidence that the concentration profile must become self-similar rapidly, and to explain the structure of this eigenmode in our simple map.

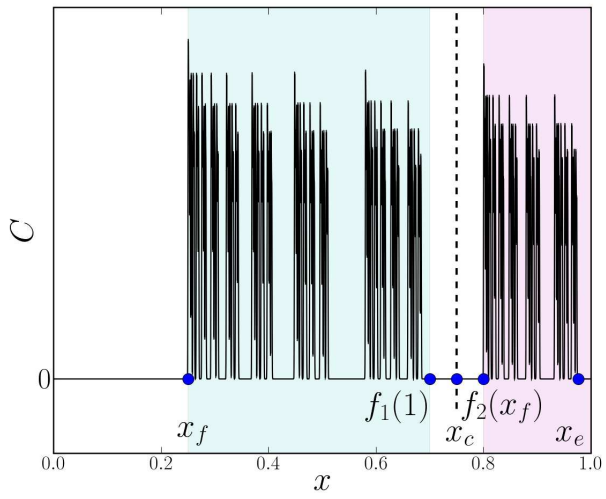

Figure 5.11: Asymptotic permanent concentration profile for the open-flow baker's map with parameters $U = 0.1$, $\gamma = 0.6$, $\kappa = 10^{-7}$. The support of the eigenmode starts at the fixed attractive point x_f, which is also the leftmost point of the chaotic saddle. The fraction of the profile after x_c so that $f_2(x_c) = 1$ will be advected downstream by f_2 by the next iteration of the map.

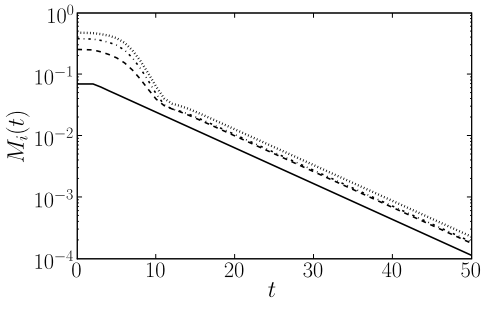

Figure 5.12: Mean concentration (solid line), and first moments of the concentration field $M_i(t) = \left| \int_0^1 (C(x) - \langle C \rangle)^i \mathrm{d}x \right|^{1/i}$ (dashed line: $i = 2$, dash-dot line: $i = 3$, dotted line: $i = 4$), in a log-linear plot. The concentration field was obtained by simulating the 1-D baker's map with parameters $U = 0.1$, $\gamma = 0.6$, $\kappa = 10^{-7}$.

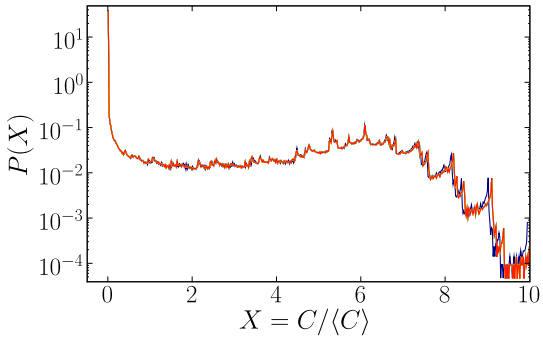

Figure 5.13: Probability distribution function of the concentration normalized by its mean, from periods 20 to 100, every 10th period. All curves superimpose very well; this self-similarity is the fingerprint of a strange eigenmode. Parameters used for this simulation: $U = 0.1$, $\gamma = 0.6$, $\kappa = 10^{-9}$.

Evidence for a strange eigenmode – For simplicity, we will first focus on a particular realization of the map (5.3), with $U = 0.1$ and $\gamma = 0.6$. The resulting concentration pattern is shown in Fig. 5.11. We have chosen the parameters U and γ in a range where $f_1(1) < x_c$ and $f_2(x_f) > x_f$. Under this condition, the concentration profile can be divided into two main blocks (shaded in blue and mauve in Fig. 5.11), which will allow us to build a simple description of the action of the map, irrespective of its details. We call the two blocks in Fig. 5.11 L (left) and R right. We also call L_t and R_t the amount of dye contained respectively in L and R at time t:

$$L_t = \int_0^{x_c} C(x,t)\mathrm{d}x \tag{5.9}$$

$$R_t = \int_{x_c}^{1} C(x,t)\mathrm{d}x. \tag{5.10}$$

The condition $f_1(1) < x_c$ imposes that an iteration of f_1 compresses L and R into the interval $[0, x_c]$, whereas, since $f_2(x_f) > x_c$, f_2 advects R away downstream and compresses L into an interval on the right of x_c. This yields the following symbolic dynamics

$$L_{t+1} = \gamma\,[L_t + R_t] \tag{5.11}$$

$$R_{t+1} = (1-\gamma)L_t. \tag{5.12}$$

Here, the endpoint x_e of the concentration profile is a 2-periodic point. Noting $D_t = L_t + R_t$ the amount of dye remaining in the mixing region at time t, we obtain the following evolution law

$$D_{t+1} = \gamma D_t + \gamma(1-\gamma)D_{t-1}. \tag{5.13}$$

This gives the asymptotic scaling

$$D_t \sim D_0 r^t \tag{5.14}$$

for $t \to \infty$, with

$$r = \frac{\gamma + \sqrt{\gamma^2 + 4\gamma(1-\gamma)}}{2}. \tag{5.15}$$

(Note that r is half the golden ratio for $\gamma = 0.5$.) Symbolic dynamics therefore determine the exact value of the decay rate α of the concentration mean

$$\alpha = -\log\left(\frac{\gamma + \sqrt{\gamma^2 + 4\gamma(1-\gamma)}}{2}\right). \tag{5.16}$$

Note that the value of α results only from simple geometrical considerations yielding the symbolic dynamics Eq. (5.12); in particular, α does not depend on the diffusivity κ. Also note that the symbolic dynamics (5.12), hence the value of α (5.16), are observed for a finite-measure range of flowrates U where $f_1(1) < x_c$ and $f_2(x_f) > x_f$, that is

$$\frac{(1-\gamma)^2}{3-2\gamma} < U < \frac{(1-\gamma)^2}{2-\gamma}. \tag{5.17}$$

This condition is dictated by the definition of the map, and has no direct equivalent in the experiments. Other symbolic dynamics can be observed for the map; another example with three symbols is given in the following. Formally, we know from the study of 2-D diffeomorphisms [18] that it is possible to define symbolic dynamics also in the experiments (in the absence of elliptical islands, though), that is to decompose the mixing region into a finite number "blocks", where each block mapped onto a finite number of blocks by the Poincaré map of the flow. Such a partition into blocks is called the *Markov partition* of the flow [56, 1, 18]. However, it might be very difficult to guess the Markov partition from experimental pictures, whereas it is more easily found in the map, where the partition is determined by the relative positions of the iterates of x_f and x_e.

The exponential regime for the decay of concentration mean is attained as soon as the ratio between L_t and R_t is close to its asymptotic value, that is when the "right proportion" is found in each block; this convergence depends only on the large-scale evolution of the profile. Conversely, local fluctuations of the profile inside the blocks contribute to higher moments of the concentration field. This explains why the exponential regime sets in earlier for the mean concentration than for higher moments in Fig. 5.12 (as a rule of thumb, for higher moments, the exponential regime is attained when filaments reach the diffusion scale w_{B}).

We now proceed to link the large-scale evolution of the concentration field, that we have characterized using symbolic dynamics, to the small-scale

evolution. As we already noticed for closed flows, the typical scale of variation of the concentration profile is the Batchelor scale $w_B \sim \sqrt{\kappa/(1-\Gamma^2)}$, with the mean stretching $\Gamma = \sqrt{\gamma(1-\gamma)}$, at which diffusion balances stretching. Let us consider a box of size w_B. After a typical time $t \sim \log(w_B)/\log(\Gamma)$, many images of the unit interval have been compressed into the box. Suppose for example that our box contains at time t the image of the whole unit interval $\mathcal{U}$ at time $t-n$. This iterate contains an amount of dye $C_t = D_{t-n}\Lambda^{(n)}$, where $\Lambda^{(n)}$ is the compression factor undergone by $\mathcal{U}$ during n periods to fit into the box. However, at the next iteration of the map, the box will contain this time the image of $\mathcal{U}$ at time $(t-n+1)$ iterated n times, which contributes to the measured concentration by an amount

$$C_{t+1} = D_{t-n+1}\Lambda^{(n)} = r \times C_t. \tag{5.18}$$

We therefore expect the concentration measured in the box, and hence the whole concentration profile, to decay by a multiplicative factor r at each iteration of the map. Thus, the origin of the strange eigenmode can be traced back to the global geometrical decay which cascades down to the smallest scale w_B because of the stretching and folding process.

The structure of the strange eigenmode can also be interpreted as follows: let us consider at time t a box of size w_B, and the largest image of the unit interval that fits into the box (for sufficiently long times). Hence, there exists $n < t$ such that

$$\Lambda^{(n)} \sim w_B, \tag{5.19}$$

where $\Lambda^{(n)} = \lambda_{t-n+1}..\lambda_t$ ($\lambda_i = \gamma$ or $1-\gamma$) is the cumulative stretching experienced by the image of $\mathcal{U}$ that has just collapsed into the box. Suppose now that $\gamma > 0.5 > 1-\gamma$. (5.19) implies that stretching histories with mostly γ factors will need more symbols than a more efficient compression sequence with mostly $(1-\gamma)$ factors. The image of $\mathcal{U}$ for a low stretching history (mostly γ) will thus correspond to the concentration pattern at an earlier time $t-n$, and it will contain more dye, as the total amount of dye decays with time. We therefore expect the concentration pattern to have higher values at the least unstable periodic points, as for concentration fluctuations in a closed flow. The highest values of the concentration profile depicted in Fig. 5.11 are indeed found around the periodic point x_f (which is the least unstable periodic point for $\gamma > 0.5$) and its next iterates.

We have demonstrated the existence of an open-flow strange eigenmode in a simple case where symbolic dynamics on only two symbols L and R are available. However, we expect our reasoning to extend to more complicated cases. We have computed the decay rate $r = -\log(\alpha)$ for $\gamma = 0.5$ and 240

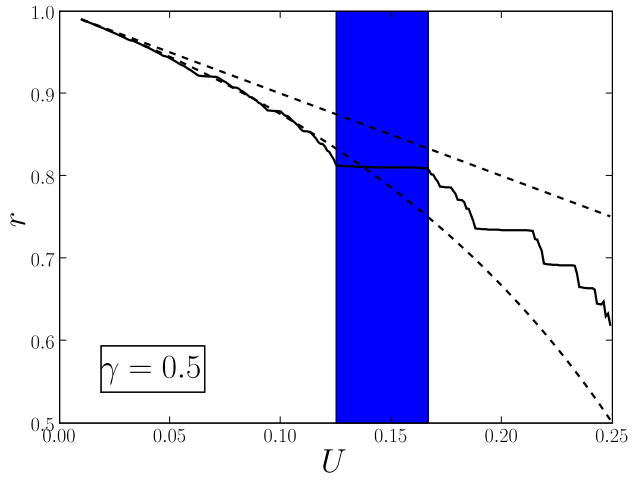

Figure 5.14: Decay rate $r = -\log(\alpha)$ of the concentration mean: $\langle C \rangle(t) \simeq C_0 r^t$, for $\gamma = 0.5$. Also shown in dashed plots are the naive guesses for the remaining fraction $1-(1-\gamma)x_c$ and $1-(1-\gamma)x_c/(1-x_f)$. The shaded area corresponds to the range of U determined by Eq. (5.17), where the symbolics dynamics (5.12) are valid and yield a decay rate $r = (1+\sqrt{5})/4$ independent of U.

values of U ranging from 10^{-2} to 0.25. The evolution of r with U is plotted in Fig. 5.14. A first observation shows that the remaining fraction of dye r is correctly approximated by the naive guesses (represented as dashed curves in Fig. 5.14), corresponding (i) to a purely geometric evaluation of the fraction of the unit interval $\mathcal{U}$ advected away, irrespective of the repartition of dye in $\mathcal{U}$, or (ii) with a correction which takes into account that the concentration support start only at x_f. This reads

$$r = 1 - (1-\gamma)(1-x_c) = 1 - U, \tag{5.20}$$

or for the more precise guess

$$r = 1 - (1-\gamma)\frac{1-x_c}{1-x_f} = 1 - \frac{U(1-\gamma)}{1-\gamma-U}. \tag{5.21}$$

However, the evolution of $r(U)$ is quite complicated and has a Devil-staircase behavior , that is, it is a continuous, monotonically decreasing function that is constant almost everywhere. In Fig. 5.14, we have shaded in blue the range of U where Eq. (5.17) is verified, and hence symbolic dynamics (5.12) are observed. Increasing U in such a range translates the 2-periodic

to the right, but the same 2-block structure is observed for the concentration profile. As the escape rate $1-r$ depends only on the form of symbolic dynamics, we observe a plateau of constant r in this range of U. In the same way, each plateau visible in Fig. 5.14 corresponds to some specific symbolic dynamics that are observed as long as an n-periodic point x_e marks the end of the chaotic saddle. As far as we know, there is no general rule for finding the partition into blocks; our method consists in following the n iterates of the last periodic point x_e, on the period-n orbit that stabilizes x_e. We have represented in Fig. 5.15 another type of symbolic dynamics, this time on three symbols with the following evolution rules

$$L_{t+1} = \gamma\left[L_t + M_t\right] \tag{5.22}$$
$$M_{t+1} = \gamma R_t \tag{5.23}$$
$$R_{t+1} = (1-\gamma)L_t. \tag{5.24}$$

The decay rate r is given by the largest eigenvalue of the transition matrix

$$\begin{pmatrix} \gamma & \gamma & 0 \\ 0 & 0 & \gamma \\ (1-\gamma) & 0 & 0 \end{pmatrix}, \tag{5.25}$$

that is 0.73 for $\gamma = 0.5$, which is indeed the height of the second largest plateau in Fig. 5.14. For all symbolic dynamics, we can adapt the above reasoning to prove (i) a global exponential decay of the mass inside the unit interval, governed by the largest eigenvalue of the transition matrix between symbols, and (ii) a permanent profile that sets in as small scale concentration values come from the compression of the whole interval profile, which has an exponential decay.

We have evidenced the apparition of an open-flow strange eigenmode in butterfly protocols, and we have illustrated this phenomenon using a fully hyperbolic model. In the next section, we investigate whether non-hyperbolic structures such as parabolic points on no-slip walls modify this evolution.

5.3 Breaststroke case: the importance of no-slip side walls

We now turn to the description of mixing mechanisms in the breaststroke case, where the mixing region extends over the whole width of the channel, and is limited by the manifolds of parabolic stagnation points on the side walls.

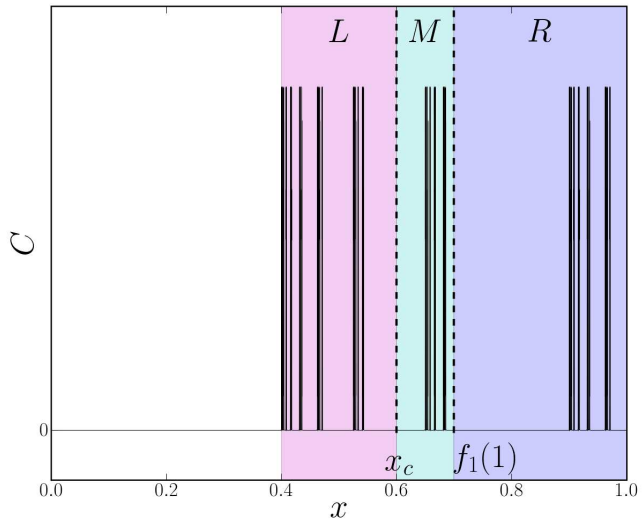

Figure 5.15: Asymptotic permanent concentration profile for the open-flow baker's map with parameters $U = 0.2$, $\gamma = 0.5$, $\kappa = 10^{-8}$. (See text for a description of symbolic dynamics evolving the three blocks L, M and R.)

5.3.1 Pattern description

Fig. 5.16 shows the asymptotic concentration patterns obtained for long times from an initial dye blob injected upstream. It is important to note that this invariant coverage of the surface by dye filaments and white holes is reached much more slowly than in the butterfly case. This is due to the presence of parabolic points on the walls: the lower frontier of the mixing region traces approximately the unstable manifold of the lower parabolic points, that is dye must first come close to the parabolic points before it can reach the frontier. We expect such dynamics to be governed by no-slip boundary conditions, and thus to be algebraic as in the closed-flow case. This means that the funnel-shaped cone at the lower end of the mixing region slowly collapses on an asymptotic shape. However, a remarkable difference between the closed an open cases is that, here, the asymptotic cone has a finite size to let upstream fluid enter the mixing region, whereas it shrank to zero in the figure-eight experiments.

The motion of the rods in the upper part of the mixing region creates parallel elongated filaments that can be seen in Fig. 5.16. These filaments stay parallel as they are further advected by the main flow in the upstream region. However, the ends of the filaments stay attached inside the mixing region, where they are compressed along the side walls as they collapse

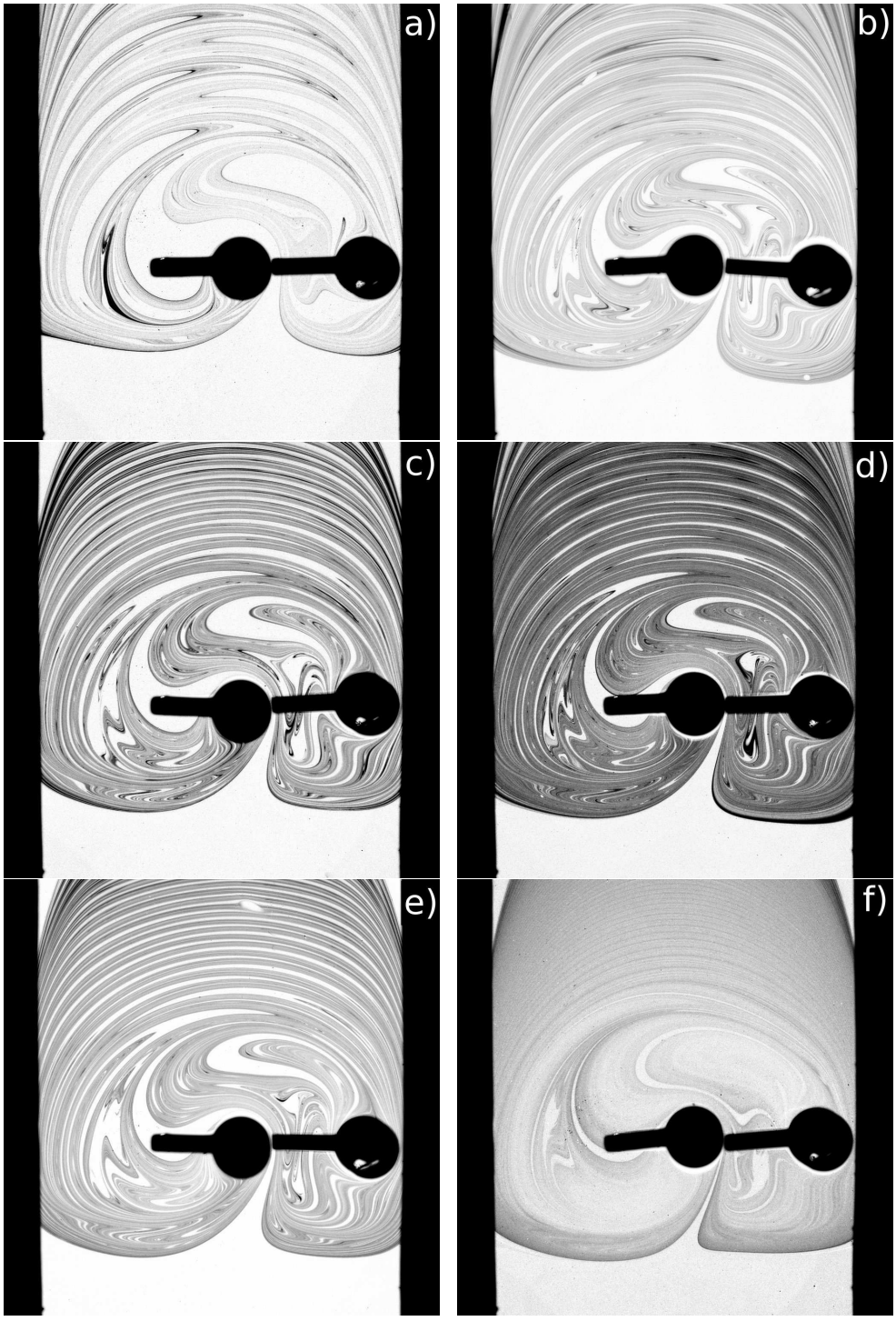

(For caption see next page.)

Figure 5.16: Asymptotic concentration patterns for breaststroke experiments realized at different stirring frequencies: $f = 1.5$ (a), 2 (b), 3 ((c) and (d)), 4 (e) and 8 (f) rpm. Contrary to the butterfly protocol, the downstream pattern extends over the whole width of the channel. It consists of parallel filaments that are transverse to the channel axis in the middle of the channel, but bend in the walls vicinity to be almost parallel to the walls. This is due to no-slip hydrodynamics, and to the presence of a parabolic reattachment point (see Fig. 5.2) at the upper frontier of the mixing region, where filaments pile up to be parallel to the wall (the unstable manifold of this parabolic point). As a result, the downstream pattern is not completely periodic, as it is more deformed along the walls. As expected, the spatial period of the downstream pattern (measured e.g. along the channel axis) decreases with stirring frequency. White holes also become thinner, so that the pattern looks more homogeneous for greater stirring frequencies: white holes even disappear completely for $f = 8$, as they are smaller than the diffusive cut-off scale. Note that two small elliptical islands are visible for $f = 8$, as in the butterfly case. High-contrast dark concentration values are visible on the frontier of the white holes: they correspond to the unstable manifold of the lower parabolic points on side walls (see Fig. 5.2), where dye is stored and slowly reinjected as in closed flows.

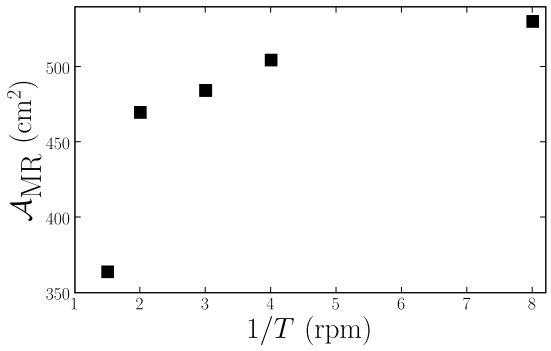

Figure 5.17: Size of the mixing region (blue-shaded area in Fig. 5.2) as a function of stirring frequency. Note that the size of the mixing region is smaller than in the butterfly case.

along the stable manifold of the upper parabolic points. The downstream pattern is therefore bent in a vicinity of the walls, and it not strictly spatially periodic. Anyhow, an upstream pattern that extends over the whole width of the channel cannot be space-periodic, as particles move faster in the center of the channel than close to the walls. The resulting pattern displays thinner filaments near the walls than in the channel center, as filaments experience further shear near the walls even after their departure from the mixing region. Also, the vicinity of the walls is filled very slowly with the dye pattern in the downstream region because of the very-low velocity close to the walls.

Increasing the stirring frequency results in a more densely striated pattern, as a smaller white area then enters the mixing region at each period, to be "sandwiched" between dye filaments whose width is of the order of the Bachelor scale. Higher frequencies therefore correspond to a concentration pattern with thinner strips, and a smaller fraction of white holes.

We have plotted in Fig. 5.17 the evolution of the mixing region size (i.e. the area of the blue-shaded zone in Fig. 5.2) with stirring frequency. We notice that the mixing region is smaller than for the butterfly protocol (Fig. 5.5), at all frequencies. For higher frequencies, the relative importance of the rod velocities, as compared to the main flow velocity, allows the stagnation points to be pushed back further, hence to increase the size of the mixing region.

Qualitative information about the pattern contrast can also be gained from the pictures in Fig. 5.16. High contrast regions correspond to (i): empty white regions that are iterates of white upstream fluid still wider than the diffusion scale w_{B}, and (ii) dark filaments emanating from the vicinity of the side walls where stretching is slow (as in closed flows).

These observations are investigated in more details in the next paragraph, where we study statistical properties of the concentration field for different stirring frequencies.

5.3.2 Statistical properties of the concentration field

As for butterfly protocols, we measure the statistical properties of the concentration field in two different rectangular regions: a large rectangle that extends over the channel width and encloses the lower part of the mixing region, up to the lower part of the rods, and a downstream rectangle determined by the channel width and the spatial period of the pattern, as measured along the channel central axis.

We have represented in Fig 5.18 the evolution of the mean concentration and of its standard deviation, measured both in the mixing and down-

stream region. For all experiments, the evolution of the mean concentration is roughly exponential after a short transient, although a slight downward curvature can be observed in Fig. 5.18(b). This exponential regime is consistent with the following purely geometric interpretation: because of the time-periodicity of the flow, the same subarea of the mixing region is taken away at each period, whereas remaining dye is reshuffled by the rods in the whole mixing region. Neglecting the spatial distribution of dye in this area, we might expect an exponential evolution. For early times, it is instructive to note that the transient "bump" for the concentration mean that can be observed during the first periods is much smaller than in the butterfly experiments (see Fig. 5.6). This bump corresponds to dye particles that escape downstream very rapidly. Its importance is related to the structure of the manifolds of the chaotic saddle. In the butterfly case, fluid that flows along the sides of the channel (more precisely, in the fraction of the channel width not occupied by the mirror image of the downstream lobes) crosses the mixing region rapidly and accounts for the importance of the transient bump. For breaststroke experiments, the unstable (and stable) manifold goes over the channel width. The only elements of the initial blob that may escape quickly correspond to the intersection of the blob with the mirror image of the filamentary white "holes" in the downstream pattern for long times (remember that the area covered with dye converges slowly to its asymptotic shape because of the parabolic points).

However, contrary to the butterfly experiments, the evolution of the standard deviation does not always follow the mean concentration decay for small stirring frequencies. We do not have yet a convincing modeling of this behavior, as the one derived in the previous chapter for mixing dynamics inside the figure-eight mixer. Nevertheless, many elements can contribute to this complicated behavior.

- The white area inside the mixing region decreases slowly with time – yet to a fixed value, contrary to the close-flow case. This shrinkage corresponds to the convergence of dye filaments to the side walls, from which they escape along the unstable manifolds of the parabolic points. As the spatial distribution of dye changes under this process, one might expect a different evolution for the mean and standard deviation of the concentration field.

- Also, parts of the original blob that are pushed quickly to the side walls undergo few stretching, because of no-slip hydrodynamics close to the wall. These dye elements stay inside the mixing region much longer than the average residence time. As a result, the frontier of the mixing region, along which they are reinjected, looks comparatively

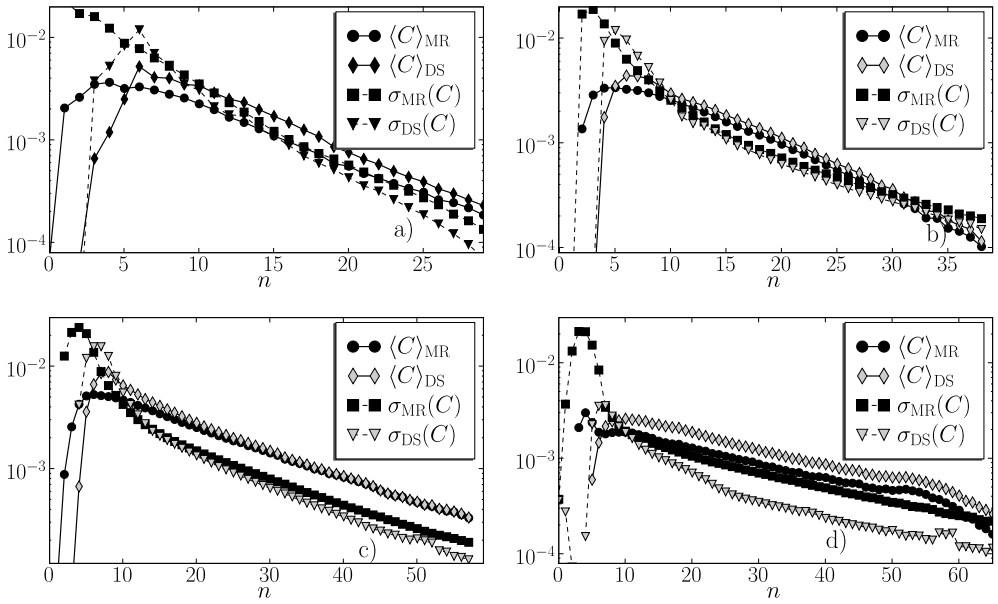

Figure 5.18: Concentration field mean and standard deviation as a function of the number of stirring periods n, measured in the mixing and downstream region for different stirring frequencies. (From left to right, and top to bottom)**a)** $f = 2$ – The first moments of the concentration field display an exponential evolution, yet with slightly different exponents for $\langle C\rangle$ and $\sigma(C)$. This shows that the evolution of the concentration field is not completely self-similar. **b)** $f = 3$ – Although the mean concentration evolution looks exponential, $\sigma(C)$ is slightly curved here. **c)** $f = 4$ and **d)** $f = 8$ – For higher frequencies, we retrieve a parallel exponential evolution for the mean and standard deviation of the concentration.

darker and darker. This storage of dark fluid causes the pattern to look more and more heterogeneous (if normalized by the decreasing mean concentration), whereas the former point – the collapse of the white cone – favors a better relative homogenization. There might be a competition between the two effects, that should be investigated in more details.

It is important to note that in open flows, the effect of wall parabolic points – that has yet to be elucidated – seems less dramatic than in closed flows. Despite the complicated structure of the mixing pattern, that may be strongly influenced by the slow stretching dynamics close to the wall, the main flow imposes that the same subarea is advected away at each period. Although the normalized concentration distribution might vary with time

inside this area, there is a "first-order" geometric term that explains why we may have observed decay of variance slower than exponential (Fig. 5.18 (b)), but always faster than power laws.

Most surprisingly, results from different experiments conducted at the same stirring frequency do not always yield the same behavior for different initial locations of the dye blob. For all experiments, we have injected the initial blob in the central part of the channel, except for one case described below. Figs. 5.19 (c) and 5.19 (d) correspond respectively to an injection of the blob in the central region of the channel ($y \simeq 0$), and near the channel walls, as shown in Fig. 5.19 (a) and (b). However, fluid is injected much more slowly along the wall than in the center – this means than in the second case, there is still some dye outside the mixing region a long time after the first entrance of dye particles inside the mixing regions. We have chosen to inject the same dye volume – hence the same area – for all experiments. As all dye particles do not enter the mixing region at the same period, the concentration field results from the superposition of filaments with very different stretching histories. In particular, the residence time distribution results from the convolution of the residence time distribution for a tiny blob that would be sucked into the mixing region in one period, with the entrance time distribution. That might explain why the concentration mean looks more exponential for an injection along the wall than for an injection in the central region, as more entrance times contribute to the evolution in the former case.

This "convolution" of blobs with different entrance times might also be responsible for the more exponential behavior for greater stirring frequencies. The initial blob can be sliced in different parts that will enter the mixing region at successive periods (this can be effectively done by flipping the asymptotic image of the downstream pattern. Filaments are more packed close to the wall, so this confirms our intuition that a given area of fluid will have a broader distribution of entrance times along the wall than in the center). As the blob area does not change, greater frequencies correspond to more slices, hence more convolution.

Concentration histograms are shown in Fig. 5.20. Many features of the PDFs complete our above observation. Although PDFs are quasi self-similar for long times, collapse on a single curve is not as good as for butterfly experiments. We observe wide power-law tails that reveal the persistence of dark concentration values. This hints again at the storage of poorly stretched fluid near the walls.

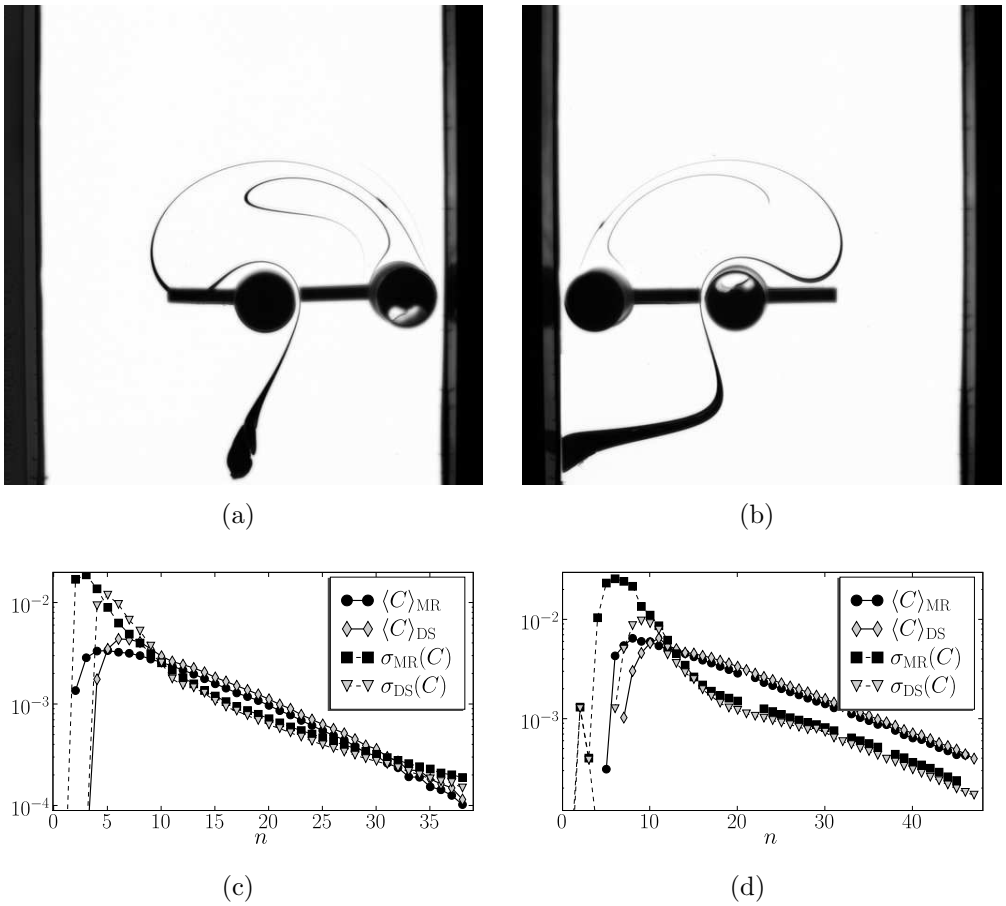

Figure 5.19: We have tested the influence of the location of the initial dye blob by realizing two distinct experiments at the same stirring frequency ($f = 3$), yet with a blob injected close to the channel axis in the first case (a), and close to the wall in the second experiment (b). Resulting concentration fields display important differences, as can be seen from the evolution of mean and standard deviation displayed in (c) and (d).

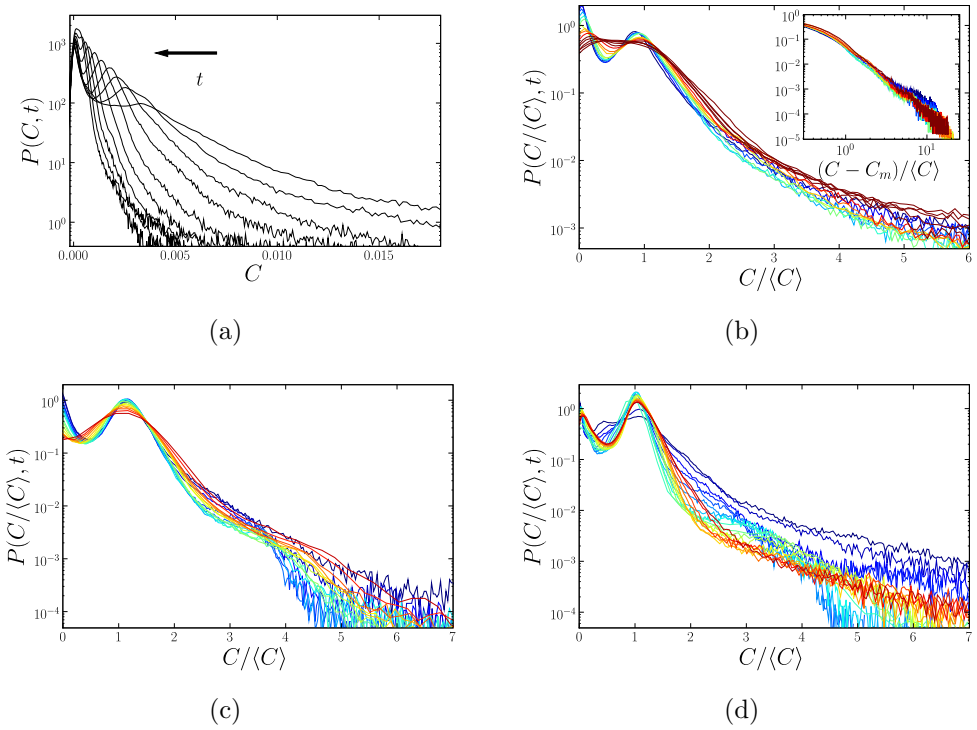

Figure 5.20: $f = 2$, (a) Concentration PDFs at periods 8 to 28, every second period. (b) PDFs of the renormalized concentration at periods 14 to 28. PDFs have a very wide shape and display in particular a power-law tail for dark values, that might be linked to the persistence of dark fluid in the wall region. As time increases, values close to the mean concentration are more important (the camera noise might be partially responsible for this phenomenon, but cannot account completely for this widening around the main peak, when compared to other experiments). This may be attributed to the convergence of the white cone to its asymptotic shape: less white fluid is then injected at each iteration than for earlier periods. This collapse of white fluid contribution might explain why $\sigma(C)$ decays faster than $\langle C\rangle$ for this experiment (Fig.5.18 (a)). **c)** $f = 3$, $P(C/\langle C\rangle)$ at periods 13 to 30. For this experiment, PDFs a very wide shape (compared to butterfly experiments, in particular). Collapse on a single curve is poor for relative high concentration values: as time progresses, high-concentration relative fluctuations seem to become more and more important. This might be attributed to parabolic points on the side walls, where fluid is stored for longer times than the average residence time in the whole mixing region.

5.4 Conclusion

In this chapter, we have analyzed homogenization experiments conducted in the open-flow channel, where a dye blob is released in the upstream region and gives birth to a complicated filamentary pattern observable for long times, both in the mixing and downstream regions – although dye keeps being swept away by the main flow. Whereas we had studied in Ch. 3 the fraction of the blob that escapes fast downstream without being caught by the rods – and is therefore poorly mixed – we have concentrated here on the long-time concentration field.

We have first focused on the butterfly protocol, where stirring rods help the global advection along the channel sides, but travel in the opposite sense in the center. In this case, the chaotic saddle, i.e. the union of all periodic orbits, that determine the extent of the asymptotic dye support, is well shielded from the side walls by a layer of free trajectories. Butterfly protocols are therefore the open-flow equivalent of the epitrochoid protocol studied in the preceding chapter. For all stirring frequencies where no elliptical islands where visible, we have observed an open-flow strange eigenmode, that is a permanent concentration field which repeats self-similarly every period, although its amplitude decays exponentially. The parallel evolution of the mean and standard deviation of the concentration, as well as the self-similarity of the PDFs, confirmed our visual inspection. We have observed that the relative homogeneity of the pattern increases for greater stirring frequencies, where thinner slices of upstream fluid are injected inside the mixing region at each period (so that less periods inside the mixer are necessary to compress them to the diffusion scale). However, for the greatest stirring frequency studied, that is $f = 8$ rpm (and presumably for higher frequencies as well), two elliptical islands modify the concentration pattern, which is less homogeneous; we have also observed a departure from the self-similar evolution of the concentration field for long times.

We have then took on the analysis of breaststroke protocols, where the rods accelerate the main flow in the center, and conversely go against it along the channel sides. Due to the latter competition, a stagnation parabolic point is located on each side wall, at the frontier between the upstream region and the chaotic saddle. As in the closed-flow figure eight protocol, the chaotic region – i.e. the chaotic saddle – goes to the no-slip walls, where poorly stretched fluid is stored for long times, and then escapes along the unstable manifolds of the parabolic points. This phenomenon is clearly visible on the mixture pictures, where darker filaments emanate from the walls. We have observed some departure from an exponential evolution of the moments, and self-similarity of the PDFs, that we have attributed to

the wall parabolic points. However, the global advection imposes a dominant evolution, as the same subarea of the mixing region is taken away downstream at each period, and we have found the effect of the walls to be less dramatic than in closed flows. Also, for higher frequencies the mixing pattern was formed by the convolution of slices of the initial blob injected at different times: this might explain why a strange-eigenmode behavior was observed for high stirring frequencies. Nevertheless, a satisfying modeling of homogenization dynamics is still lacking. Further research should concentrate on this aspect.

Now that we have gained some insights into the mechanisms governing mixing in open flows, we will consider in the next chapter some characterizations of mixing quality, that appear to be relevant from our understanding of open-flow mixing processes.

Chapter 6

Measures of mixing in open flows

In the previous chapter, we have described some mechanisms of transport and resulting mixing in our open-flow channel. We now investigate how to characterize such an open-flow mixer, in order to evaluate the quality of the mixing achieved by the mixer. Designing new mixing devices requires indeed to have at hand a way to compare different realizations – the goal being to optimize the mixing criterion, under some practical constraints that might vary from one application to another. Many measures of mixing quality have been proposed in closed flows; for that matter, their variety reflects the difficulty of proposing a single relevant measure of mixedness. However, such issues have been seldom mentioned, and much less addressed in open flows. Traditionally, the study of open-flow mixing, and underlying structures such as the chaotic saddle, has been motivated by the understanding of puzzling phenomenons in marine ecosystems [65, 133, 110], such as plankton bloom. In environmental systems, flow parameters are imposed, so that more emphasis has been laid on describing general mechanisms, than on deriving precise mixing criteria that are yet of paramount importance for industrial applications.

In a first section, we review some traditional measures of mixing that can be found in the mixing literature (mostly for closed flows, though). After mentioning some specificities of open flows, we then take on the derivation of quantitative mixing criteria for open flows: starting from an open-flow version of the intensity of segregation introduced by Danckwerts [29] for closed flows, we discuss the variation of this measure with diffusivity, and the upstream scale of heterogeneity. Related alternative measures are then discussed. We also consider spatial characterizations of mixing that aim at determining a typical scale for inhomogeneity. A brief discussion ends

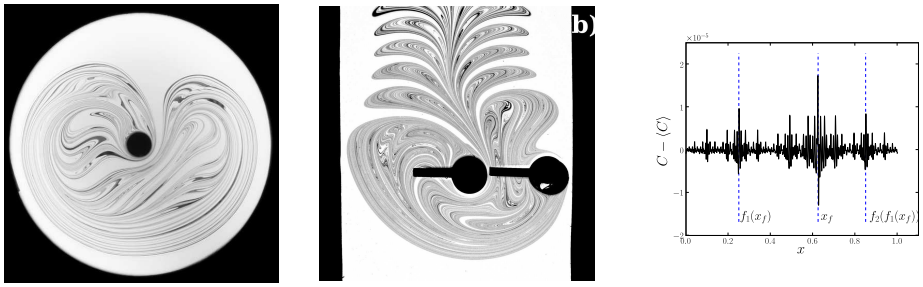

Figure 6.1: Concentration patterns obtained in experiments (a-b) or simulations (c), involving the figure-eight mixer (a), the butterfly open-flow mixer (b), and an inhomogeneous baker's map (c). These concentration patterns may be used to (i) extract an instantaneous information about the level of homogeneity, (ii) predict the further evolution of fluctuations, and, if possible (iii) characterize the efficiency of the mixer itself, independently of the realization of a specific mixing experiment.

this chapter. The reader should be warned that our description is far from exhaustive; there exists a huge variety of mixing measures in closed flows, but we have only described a few here, in the hope that they could be adapted to open flows. Concerning open flows, we have focused on simple measures that follow directly from our understanding of mixing mechanisms.

6.1 Usual strategies for characterizing mixing

6.1.1 What is a good measure of mixing ?

For the engineer as for the physicist, measuring mixing may aim at different goals, involving different levels of ambition... and difficulty. Consider for example the pictures shown in Fig. 6.1, that all represent the concentration field of a passive scalar to homogenize, obtained for a given initial condition at a given time. From such pictures, one may want to extract different information about mixing properties of the systems.

- A first obvious characterization of mixing consists in quantifying the degree of inhomogeneity of the represented field – that is, an instantaneous measure of mixing for a specific initial condition. This end-product characterization is necessary for industrial applications where one has some specific requirements for the degree of homogeneity of

the finished product. However, it does not provide any other information about how the quality of mixing would change if one e.g. stirred the mixture a little longer.

- Further characterization implies to describe the *evolution* of homogeneity for a given initial condition. One may record the state of mixedness at different instants and derive therefrom empirical laws, as we did for the variance of the concentration field for the figure-eight and epitrochoid mixers. Also, our understanding of mixing processes can enable us to extrapolate the evolution of mixing quality without actually measuring it. For example, we *know* that once the concentration profile of Fig. 6.1 (c) has converged to the strange eigenmode shape – which can be observed from noticing that no structure larger than the diffusion scale is visible, or that an exponential phase for the decay of variance has set in –, the evolution of the concentration field is completely self-similar, with a global exponential decay of fluctuations amplitude. This explains the emphasis put during the previous chapters on the description of mixing *mechanisms*.

- Finally, one may want to evaluate the mixer itself, independently of the initial condition chosen. An industrial mixing device might be used for different spatial repartitions of the initial inhomogeneity. For example, we have seen that in the channel flow mixer, the fraction of a dye blob that escapes immediately downstream depends of its intersection with the stable manifold of the chaotic saddle. Yet, we would like to have at hand a characterization of the mixer that accounts for all possible such intersections patterns, and not only one that corresponds to a specific experiment. Also, the same mixing device can be used with different fluids that have e.g. different diffusivities – we have seen that homogenization dynamics depend on the amplitude of diffusion. As far as spatial scales are concerned, it is also possible that different applications impose different requirements for the scale at which inhomogeneity is present in the end product. This must also be characterized. Of course, there is no way we can test all initial conditions, diffusivities or observation scales for a given device. Once again, we have to make extensive use of our knowledge on mixing processes to extrapolate the limited amount of information at hand.

In all cases, a measure of mixing involves reducing the dimensionality of the available information – e.g. extract numbers from a field. The underlying goal is to compare different mixing devices, that is, define a (global, if possible) order relation for mixing systems.

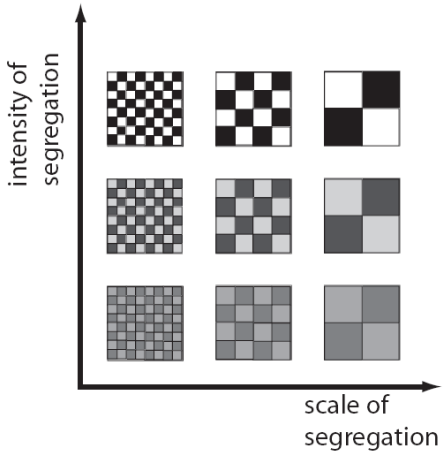

Figure 6.2: (Taken from the work of Tucker [123]) A concentration field can be characterized by the intensity of the inhomogeneity, and the typical scale of homogeneity. The two measures are independent for a non-diffusive scalar field.

Since the pioneering work of Danckwerts [29], it has become traditional to analyze the concentration field of a mixture using two distinct approaches. Their combination amounts to characterizing the intensity of the homogeneity, and the scale at which it is present: a schematic illustration is given in Fig. 6.2. A first set of mixing measures describes *statistical properties* of the field: classical examples include the variance of the concentration field, or its probability density function. Second, the spatial distribution of inhomogeneity is of paramount importance: the first column of Fig. 6.2 "looks" better mixed than the last one, regardless of the black and white contrast. Smaller scales therefore correspond to a better mixing quality. In the next paragraphs, we review classical mixing measures associated to statistical, and then spatial measures.

6.1.2 Statistical measures

Concentration variance – In closed flows, the mean concentration of a scalar field is conserved in the absence of sources or sinks. The first non-trivial moment of the concentration field is therefore its second moment or equivalently its variance $\sigma^2(C) = \langle (C - \langle C \rangle)^2 \rangle$, which characterizes directly the inhomogeneity.

In order to characterize the mixing device itself, and not only one mixing history, it seems natural to normalize the variance of the field by its initial variance and consider $\sigma^2(C,t)/\sigma_0^2$. One of the most commonly used mixing measures, the **intensity of segregation** introduced by Danckwerts in 1952

[29], is defined in a similar way as:

$$I_C = \frac{\sigma^2(C,t)}{\langle C\rangle(1-\langle C\rangle)}. \tag{6.1}$$

It corresponds to the variance normalized by the variance of a black and white initial condition like the upper row of Fig. 6.2, where the maximal (resp. minimal) value of the concentration is 1 (resp. 0). Many practical situations correspond to such an initial condition, yet the definition

$$I_C = \frac{\sigma^2(C,t)}{\sigma_0^2} \tag{6.2}$$

seems preferable to us, as it is more general.

The concentration variance has many noticeable advantages: first, it is a direct global measure of inhomogeneity; second, it can be extracted from the concentration field with reasonable precision (contrary to higher order moments). In the absence of sources or sinks, the variance decreases monotonously with time in closed flows, so that a measure of variance at a given time provides a lower bound on mixing quality for all future instants. Finally, the simplicity of its definition may allow in some cases to derive its evolution easily from a given modeling of mixing processes. One of the first tests of a mixing model consists often in checking the behavior of the concentration variance against reality [7, 95, 96, 125, 112, 43]. Throughout this manuscript, we have concentrated on this quantity to describe the evolution of mixing, and assess its quality.

Concentration PDFs – If available, concentration probability distributions (PDFs), or nonlinear moments, provide additional information compared to the variance. PDFs describe how all levels of inhomogeneity are populated. For instance, a purely black and white concentration field of variance σ^2 might be considered as less mixed than a concentration field with a Gaussian histogram of width σ. Some applications might e.g. require concentration fluctuations smaller than a given value: contrary to variance, PDFs allow to check whether the quality of mixing is satisfying using this criterion. Also, concentration PDFs provide some information about the mixing processes at play. For example, wide tails of the histogram such as the power-law tails in the figure-eight mixer (Fig. 4.9 (b) in Chapter 4) or exponential tails in the epitrochoid mixer (Fig. 4.26 in Chapter 4), suggest the persistence of rare fluctuations that might be associated with strong time-correlations of stretching.

However, in most cases it is difficult to obtain concentration PDFs with a satisfying accuracy, be it in experiments or simulations. PDFs have therefore been less described than low moments of the concentration, with some notable exceptions [107, 125, 124].

Rényi entropies – Rényi entropies [93] provide an alternative set of statistical measures that allow to put different weights on different levels of fluctuations. They are defined for $\alpha \geq 0$ by

$$S_\alpha = \frac{1}{1-\alpha} \log \left(\sum_i^N p_i^\alpha \right), \tag{6.3}$$

where

$$p_i = \frac{C_i}{\sum_j C_j} \tag{6.4}$$

is the fraction of the total concentration present in the box or pixel i. N is the total number of pixels. For a perfectly mixed system, $p_i = 1/N$ and $S_\alpha = \log N$, otherwise $S_\alpha < \log N$. On the contrary, if all scalar is concentrated in a single box, $S_\alpha = 0$. For characterizing mixing, one often considers the reduced entropy [129]

$$\tilde{S}_\alpha = \frac{1}{\log N} S_\alpha, \tag{6.5}$$

which is a number between 0 and 1, 1 denoting a perfect mixing. Entropies corresponding to different values of α provide different information about the concentration field. $\tilde{S}_0$ gives the fraction of boxes where the scalar is present, and provides a binary measure of mixing. When the support of dye is a fractal set, as it is the case for an open flow with a hyperbolic chaotic saddle [111], $\tilde{S}_0$ is the fractal dimension of the set, normalized by the Euclidean dimension of the embedding space. $\tilde{S}_1$ is the classical Shannon information entropy, defined by

$$\tilde{S}_1 = -\sum_i p_i \log p_i \tag{6.6}$$

(the limit of Eq. (6.3) for $\alpha \to 1$) and S_2 is called the correlation entropy. For a given field, S_α is a – possibly slowly – decreasing function of α. Generally, higher values of α give more importance to higher fluctuations from the mean: depending on the application, one may choose to use an entropy with high α to eliminate mixers where high fluctuations subsist. However, for higher values of α, S_α is also more sensitive to statistical

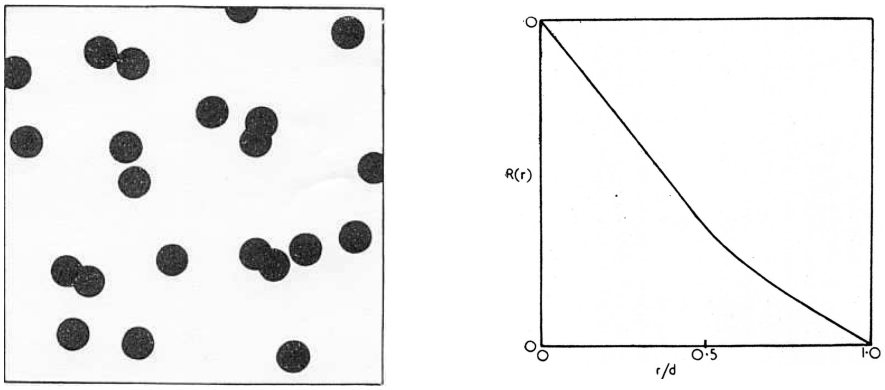

(a) (b)

Figure 6.3: (Taken from the work of Danckwerts [29]). (a) Mixture pattern, and (b) associated correlogram $R(r)$.

errors for rare events, so that one should not expect measures of entropies for very high α to be of much relevance.

Rényi entropies have been used in particular to characterize mixing in polymers processing [129].

6.1.3 Spatial measures

Another set of mixing measures is related to the spatial distribution of inhomogeneity: one would like to know which scales are present in the mixture. We briefly review some measures here; some long-used measures can be applied to a wide class of systems, while other are more closely connected to specific properties of chaotic mixing.

Scale of segregation – This measure of the typical scale in a mixing pattern was introduced by Danckwerts in 1952 [29]. Let us first consider the correlation function

$$R(r) = \frac{\langle (C(\mathbf{x}) - \langle C \rangle)\,(C(\mathbf{x}+\mathbf{r}) - \langle C \rangle)}{\langle (C(\mathbf{x}) - \langle C \rangle)^2} \tag{6.7}$$

that describes the correlation of the pattern at scale r. $R(0) = 1$ (the mixture is very correlated at small scales), and because of Cauchy-Schwartz inequality, $R(r) \leq 1$. Values of $R(r)$ close to 1 mean that pixels separated by a distance r have on average the same concentration value, while values close to 0 correspond to uncorrelated values. $R(r)$ can also take negative values, especially if the pattern displays some kind of coherent structure.

The evolution of $R(r)$ for a simple "clumped" pattern is shown in Fig. 6.3 (b). The **scale of segregation** is traditionally defined by

$$s = \int_0^\infty R(r)\mathrm{d}r, \tag{6.8}$$

or

$$s = \int_0^{r^*} R(r)\mathrm{d}r, \tag{6.9}$$

where r^* is the first value where $R(r)$ cancels (this avoids cancellations by negative –anti-correlated – parts of the integral). s gives the typical scale of unmixed clumps in the pattern. s is particularly suited to describe simple patterns such as the one shown in Fig. 6.3, where the mixture is clearly segregated with a typical length scale. However, we do not expect this measure to be as relevant for a pattern with a complicated hierarchical structure, as is often the case for chaotic mixing.

Power spectrum

Fourier power spectra have often been used [6, 7, 95, 52] to characterize the evolution of a scalar fields in terms of spatial scales. For example, the signature of the stretching process associated to chaotic mixing is visible in the power spectra, where it corresponds to a rise of the high-frequency tail during the first iterations of the stirring process. The shape of the high-frequency tail – power-law or not – also provides a diagnosis for the stirring mechanisms at play.

Nevertheless, Fourier spectra do not account completely for the spatial structure of the concentration field.

Stretching distributions

In an attempt to describe the transverse scale of the dye filaments that can be seen in typical chaotic mixing pictures, numerous studies [75, 2, 73, 127] have considered the distribution of finite-time Lyapunov exponents, as well as associated statistical quantities such as the Lyapunov exponent or the topological entropy (these quantities have been introduced in Chapter 3). The basic idea behind this measure is that a strip that has experienced a cumulated stretching λ has a typical width of w_0/λ, where w_0 is the original width of the blob. This method is quite successful for describing the first stages of mixing, that is before strips reach the diffusive scale and start to interpenetrate. However, it fails to account for the strange eigenmode phase where many strips with different stretching histories accumulate inside a single visible structure.

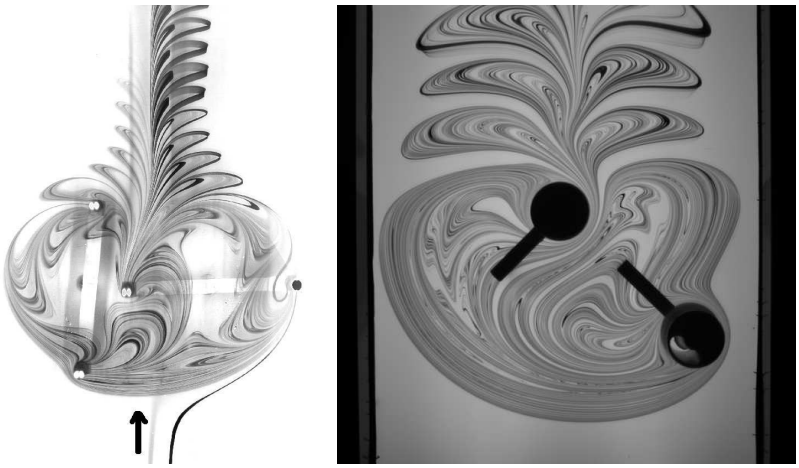

(a) (b)

Figure 6.4: Continuous dye feeding vs. decay experiment.

It is important to note that these kinematic quantities are more easily derived in numerical simulations. However, stretching distributions have also been determined in experiments where special care was taken to control the periodicity of the flow with very good accuracy [127].

6.2 Quantifying mixing in open flows

6.2.1 Typical mixing experiments

One conceptual difficulty that arises when characterizing mixing in open flows is to choose a set of relevant injection histories. Indeed, we have seen that the chaotic saddle inside the mixing region is responsible for a broad – exponential – distribution of residence times, so that a small patch of downstream partly mixed fluid results from the addition of fluid particles that have entered the mixing region at very different times – with a typically exponential distribution. The situation is somewhat simpler in closed flows, where one chooses an initial condition once and for all (characterized e.g. by a spatial repartition of inhomogeneity). For open flows, two relevant classes of experiments can be considered.

- **Decay experiments**, that correspond to the injection of a limited blob of inhomogeneity. This type of experiments allows to study the percussional response of the mixing device to an initial inhomogeneity. It also gives directly access to important structures as the manifolds

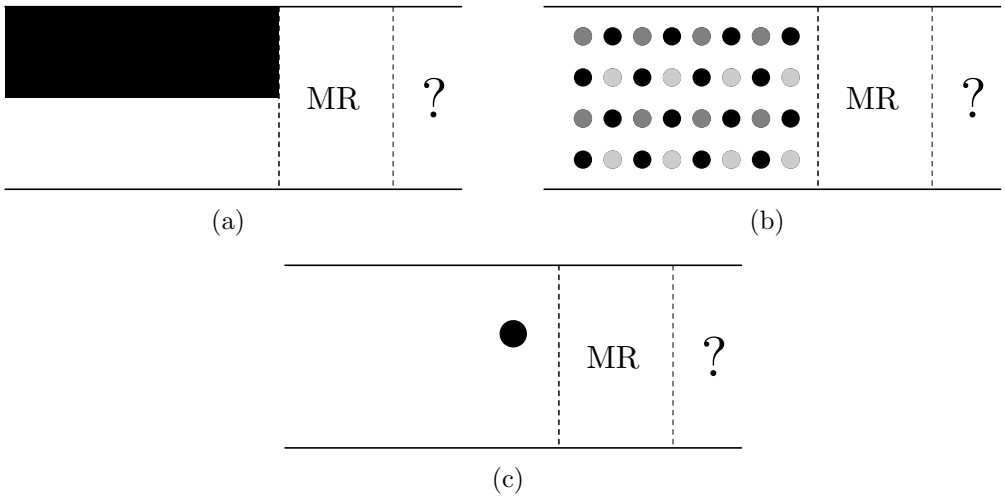

Figure 6.5: Different upstream fields to be homogenized inside the mixing region (MR). (a) and (b): for many industrial applications, the upstream concentration field is inhomogeneous and varies with time, but possesses some stationary properties, such as the auto-correlation function of the field, or equivalently its typical variation scale. In some cases, one even injects a stationary upstream field, like in (a). Picture (c) corresponds to a decay experiment, where one studies the response of the mixer to a localized inhomogeneity.

of the chaotic saddle, whose fractal properties can be extracted from the mixing patterns. Such experiments have permitted us to shed some light on transport and homogenization mechanisms, such as the onset of a permanent open-flow strange eigenmode, or the corrections due to parabolic points located on walls. Important quantities such as residence time distributions inside the mixer are directly extracted from this kind of experiments. As far as mixing applications are concerned, this situation corresponds to the dispersion of patches of pollutant that have to be dispersed as much as possible to be less harmful.

- **Continuous injection experiments** – We can also consider stationary mixing experiments, where the open-flow mixer is continuously fed with inhomogeneous fluid – a classical situation in food engineering, e.g. In this case, the upstream concentration field is inhomogeneous and varies at all times. However, it is reasonable to assume stationary statistical properties of the field, that can be defined by its auto-correlation function, or equivalently by its typical length scale. A

relevant characterization of mixing amounts to finding the transfer function of the device, that is to determine the downstream properties of the field (characterized e.g. by the auto-correlation function, which measures both the intensity and the scale of inhomogeneity), as a function of the upstream ones.

It is important to note that both cases are linked: the upstream field can be decomposed in successive slices of width UT, where U is the flow mean velocity and T is the stirring period. Using the linearity of the advection-diffusion equation, the concentration measured at some point inside the mixing or downstream regions is the addition from the contributions of all slices that have previously entered the mixing region. For example, a decay experiment for the homogenization of a single blob, that is an upstream field:

$$C(x, t = 0) \begin{cases} C_0(x) & \text{for } -x_1 \leq x \leq -x_2 \\ 0 & \text{elsewhere,} \end{cases} \tag{6.10}$$

yields directly the stationary downstream field corresponding to a continuous injection of the field C_0, repeated with a spatial period UT. In particular, we obtain the stationary downstream field corresponding to a succession of blobs by adding all successive concentration fields stroboscoped a each period for the injection of a single blob, as in our experiments. (In theory, this requires to add an infinite number of periods. However, as the mean concentration decays exponentially inside the mixing region, the error made by truncating the series can be made very small.) In the following, we will make extensive use of this relation to switch from one paradigm to the other: although we are perhaps more interested in the continuous case that models more closely industrial applications, the decay case is more simple, as its properties are strongly influenced by the chaotic saddle. We note Ψ the decay strange eigenmode that was evidenced in Chapter 1, and ϕ the steady-state concentration field resulting from a continuous injection.

In the remainder of this section, we study some statistical and spatial characterizations of ϕ and Ψ. For pedagogical reasons, we will mostly concentrate on the simplified one 1-D model, where analytical calculations can be performed to test the relevancy of our characterization.

6.2.2 Statistical characterizations

Variance – intensity of segregation

We first characterize the inhomogeneity of the downstream concentration field by considering its variance. For decay experiments, the variance of the strange eigenmode can be normalized by the mean concentration as

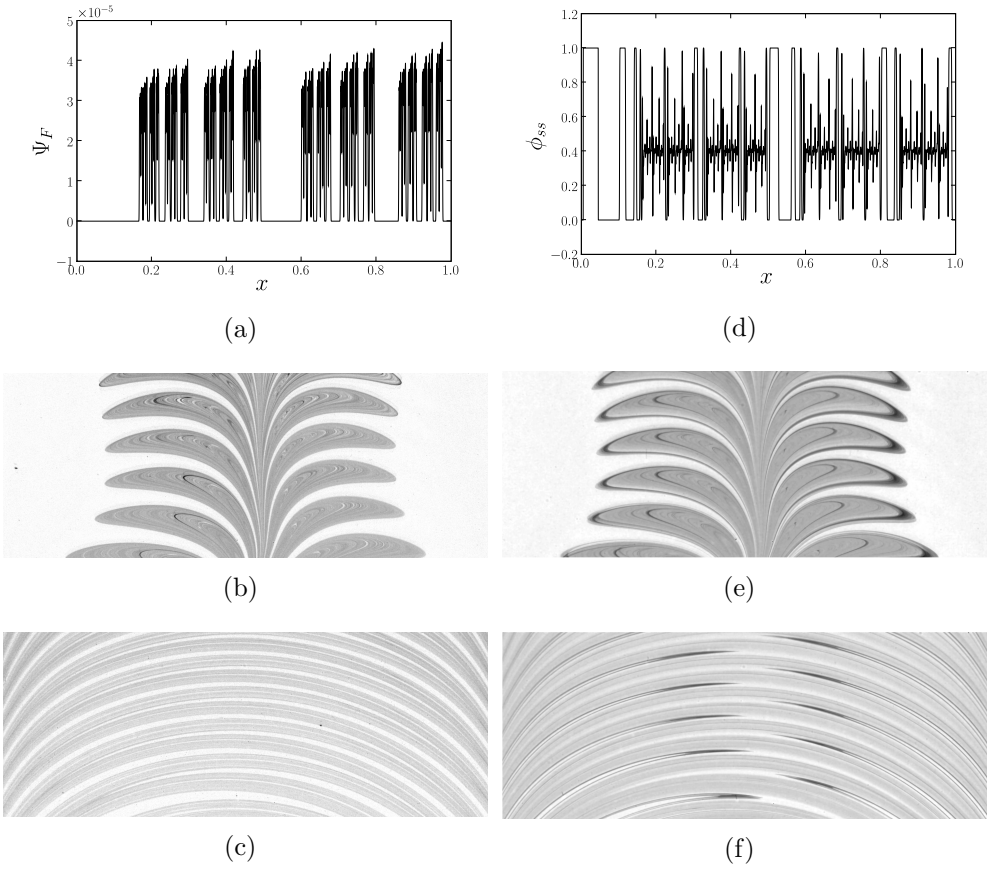

Figure 6.6: Decay strange eigenmode Ψ (left column), and steady-state continuous field ϕ (right column), for a version of the 1-D model (a-d), the butterfly protocol (b-e) and the breaststroke protocol (c-f). There is an obvious link between Ψ and ϕ, as parts of the ϕ-pattern with highest variance (or contrast) are precisely located in the holes of the support of the strange eigenmode Ψ.

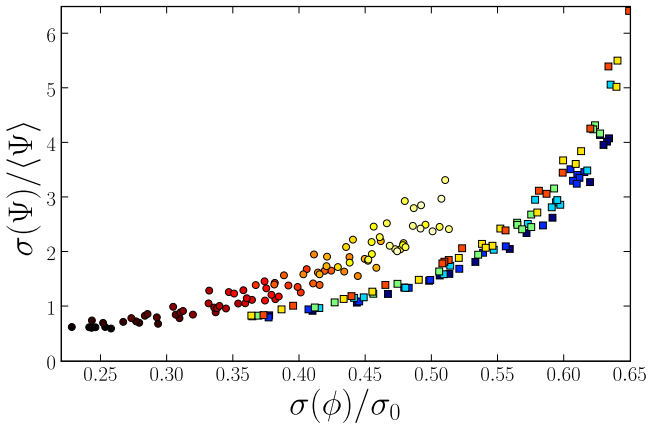

Figure 6.7: (a) Variance of the decay eigenmode $I(\Psi) = \sigma(\Psi)/\langle\Psi\rangle$ as a function of the continuous eigenmode variance $I(\phi) = \sigma(\phi)/\sigma_0$. Square and circle correspond to respective diffusivities $\kappa = 10^{-9}$ and 10^{-7}. We have varied U between 0.05 and 0.2, and γ between 0.4 and 0.6. For the $\kappa = 10^{-7}$ set of results (circle symbols), the colormap codes increasing values of U for lighter colors, while for the $\kappa = 10^{-9}$ group, blue (resp. red) symbols correspond to lower (resp. higher) values of γ. For a given value of κ, there is clearly a relation between $I(\Psi)$ and $I(\phi)$, despite some dispersion. However, changing κ also changes the master curve describing the relation between $I(\phi)$ and $I(\Psi)$.

follows:

$$I(\Psi) = \frac{\sigma(\Psi)}{\langle\Psi\rangle}. \tag{6.11}$$

For a continuous injection, it is preferable to normalize the downstream variance by the upstream one: defining

$$I(\phi) = \frac{\sigma(\phi)}{\sigma_0} \tag{6.12}$$

gives a measure of how much inhomogeneity disappears under the action of the mixer.

One may first wonder if the two quantities are related. As can be seen in Fig. 6.6, largest strips of the steady-state pattern ϕ are located in the holes of the decay eigenmode Ψ, that is in the largest holes of the fractal unstable manifold of the chaotic saddle , up to the diffusion or measurement scale. This corresponds to fluid particles that have recently entered the mixing region and have been less compressed. Older iterates of the upstream pattern compressed under the diffusion scale w_{B} add up with all older iterates and almost do not contribute to the variance. This specific

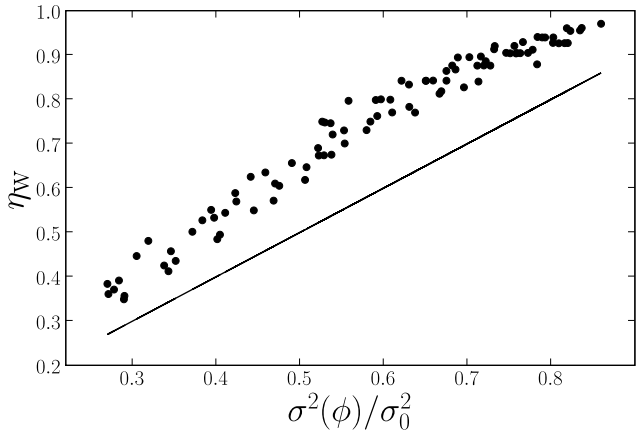

Figure 6.8: 1-D model, same set of parameters as in Fig. 6.7, with $\kappa = 10^{-9}$. Fraction of white holes in the strange eigenmode pattern η_W, plotted against the continuous pattern variance $I(\phi)$. A straight line $y = x$ has been traced for comparison. As expected, both quantities are strongly correlated, although η_W slightly overestimates $I(\phi)$. This further reinforces the picture that high-variance regions of ϕ are found in the holes of the multifractal decay pattern.

structure is also visible in the experimental pictures in Fig. 6.6. The strange eigenmode Ψ corresponds to the asymptotic dye pattern, and we have artificially computed ϕ by adding all stroboscoped iterates of the initial blob. ϕ is composed of the superposition of an almost uniform "background" situated on the fattened unstable manifold (that is, the support of Ψ), and of higher variance strips that have been hardly compressed.

We have plotted in Fig. 6.7 $I(\Psi)$ against $I(\phi)$. Both quantities have been computed for different realizations of the open-flow map where the parameters U and γ are varied. We have also used two different values of the diffusivity κ. For each value of κ, all data collapse on a master curve, despite some dispersion. Measuring the variance of Ψ therefore allows to classify the efficiency of different mixers as measured in the continuous injection sense by $I(\phi)$. However, different values of κ yield distinct master curves, which means that $I(\phi)$ and $I(\Psi)$ evolve differently with κ (this is discussed further below). As expected, $I(\phi)$ and $I(\Psi)$ increase with U, as for larger flowrates larger slices of upstream fluid are incorporated in the mixing region at each period, which creates bigger holes in the chaotic saddle. The effect of γ is less obvious, although $I(\phi)$ and $I(\Psi)$ slightly increase with γ on average. In our model, the size of the hole on the left of the chaotic saddle is determined by the position of the fixed point $x_f U/(1-\gamma)$, which

increases with γ. We do not expect this effect of γ to be generic for real flows.

Another quantity correlated to the intensity of segregation $I(\phi)$ is given by the fraction of holes in the Ψ-pattern, η_{W}. We obtain η_{W} by binarizing the profile of ϕ. A rough guess of $I(\phi)$ is given by saying that the original variance of the upstream field is conserved in all the holes of the decay pattern larger than the diffusion scale, and vanishes for smaller scales. This reads $I^2(\phi) \simeq \eta_{\mathrm{W}}$. Note that this reasoning is only valid for an initial profile with only large-scale variations (small-scale fluctuations will be annihilated quicker as the iterates are compressed). The dependence of $I(\phi)$ with the length scale of the initial profile is examined later. We have plotted in Fig. 6.8 η_{W} and $I^2(\phi)$ for the same set of simulations as in Fig. 6.7. One can see that η_{W} slightly overestimates $I^2(\phi)$ (this comes from the fact that white holes in the Ψ pattern do not correspond to a single image of the upstream slice, but to a juxtaposition of images of slices injected at different times – some may be thinner than w_{B}). However, the correlation between both quantities is clear, and η_{W} is a relevant alternative for characterizing mixing efficiency. In addition, η_{W} does not require a high-quality sampling of concentration values, as it can be computed from binarized black and white data.

We do not expect the correlation between $I(\phi)$ and $I(\psi)$, or $I(\phi)$ and η_{W} to be so good in the limit of small U or large κ, that is when holes in the strange eigenmode pattern are very small, if visible at all. However, this corresponds to the very good mixing limit, where a very precise characterization is maybe not that important.

Variation of $I(\phi)$ with the measurement and initial scales

It is important to know how the statistical properties of Ψ and ϕ vary with the pixel size at which the fields are probed, or equivalently with the diffusivity which determines the Batchelor scale. Statistical measures of mixing are often criticized for depending on the scale at which they are probed. As a remedy, multi-scale measures of mixing have been proposed [68, 100], that average e.g. the coarse-grained variance of the concentration field at different scales. Here, we advocate instead to determine the evolution of $I(\Psi)$ and $I(\phi)$ with the measure scale.

We have plotted in Fig. 6.9 the profile of the steady-state pattern ϕ for four different diffusivities, while keeping the other parameters (U and γ) constant. When the diffusivity is increased, the smallest visible holes of the decay pattern Ψ are filled by strips overlapping on a larger scale $w_{\mathrm{B}}(\kappa)$. There is then less space for high-variance patches in the steady-state pattern

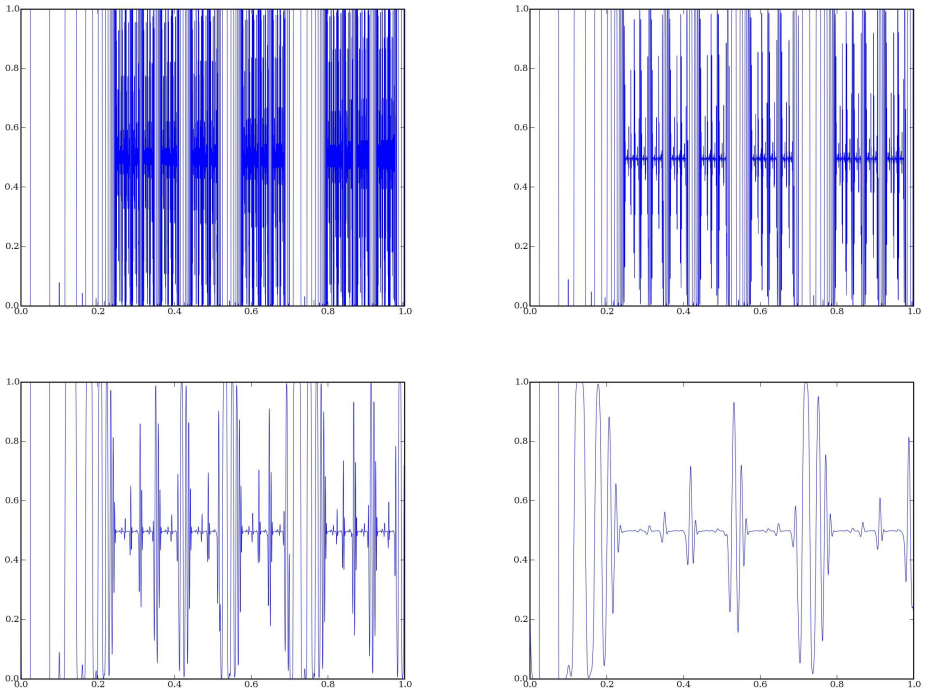

Figure 6.9: 1-D model with parameters $\gamma = 0.6$ and $U = 0.1$. Continuous permanent profiles Ψ are plotted for increasing values of the diffusivity ($\kappa = 10^{-9}$, 2×10^{-8}, 3×10^{-7}, and 4×10^{-6}). Increasing κ amounts to reducing the number and width of holes in the unstable manifold fattened by diffusion. As high-variance concentration are mostly observable in such holes, where strips have experienced few stretching, it globally decreases the concentration fluctuations.

ϕ, which shows less fluctuations.

We first concentrate on the simple case $\gamma = 1/2$, where $I(\phi)$ can be analytically calculated. In the absence of diffusion or coarse-graining, the concentration profile of ϕ is the juxtaposition of compressed images of the upstream profile that have entered the mixing region at all prior iterations, and have stayed therein despite the global advection. For an upstream profile with a large correlation scale (as the crenel profile in Fig. 6.10), we can decompose the interval $[0, 1]$ into two complementary subsets, which contribute in a different way to the global variance. We first introduce the critical number of iterations N necessary to compress the slice of fluid injected at each period up to w_{B}:

$$U\gamma^N = w_{\mathrm{B}}. \tag{6.13}$$

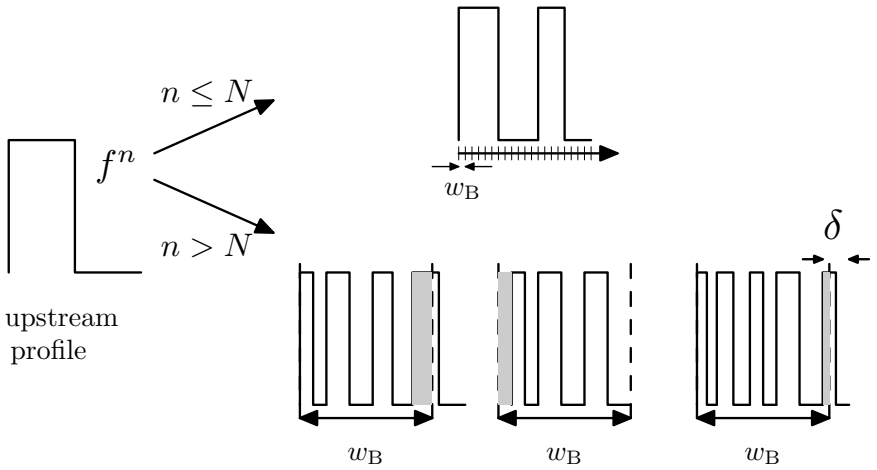

Figure 6.10: A slice of width U of the upstream profile is compressed by successive iterations of the map. Iterates that have experienced few compression steps (upper row) are much wider than the diffusion scale w_{B}. Boxes on the support of such iterates sample values from the initial profile. However, for iterates smaller than w_{B} (lower row), the measured value is the average of many iterates so that fluctuations are typically smaller than in the initial profile.

The first subset corresponds to boxes where the concentration value comes from an iterate "younger" than N, that is still larger than the width of the box where we measure the concentration (upper row in Fig. 6.10), whereas the second set is the union of boxes that contain many iterates of the upstream (lower row in Fig. 6.10) profile, which are thus "older" than N. In the first subset, we sample the same concentration values as in the upstream profile (e.g. 0 and 1 for the crenel profile in Fig. 6.10), as diffusion has not started yet to smooth the profile. The variance measured on this set is the initial variance σ_0^2.

For the second set, the concentration C measured inside a box comes from the averaging of all iterates compressed inside the box, and the squared difference from the mean is given by

$$(C(x,t) - \langle C \rangle)^2 = \left(\frac{1}{w_{\mathrm{B}}} \int_{x-w_{\mathrm{B}}/2}^{x+w_{\mathrm{B}}/2} \tilde{C} \mathrm{d}x \right)^2 - \langle C \rangle^2, \tag{6.14}$$

where $\tilde{C}$ is the diffusionless profile before the coarsening operation (represented inside the boxes in the lower row of Fig. 6.10). The only iterates inside the box that contribute to the difference from the mean are the ones cut by the box frontier, as in general there is not an integer number of iterates inside the box (in Fig. 6.10, only the area shaded in gray contributes

to the integral above). One can therefore approximate

$$(C(x,t) - \langle C \rangle)^2 = A \times \sigma_0^2 \left(\frac{\delta}{w_\mathrm{B}} \right)^2, \tag{6.15}$$

where δ is the width of the compressed iterate cut by the frontier, and A is a geometrical factor of order 1 that depends on the initial profile. For simplicity we fix $A = 1$ in the following. Fluctuations measured in the second set are therefore typically smaller than σ_0.

We now have to estimate the contribution of each set, that is, determine their measure by counting the respective widths of all iterates of the upstream profile that belong to either set. A slice of width U that enters the mixing region is transformed into h^n iterates of width $U\gamma^n$ after n periods, where h is the topological entropy (Remember that in Ch. 3, we introduced h as the growth rate of the length of a material line, measured in a fixed region. For a 1-D map, the length of the line is simply given by the number of iterates.). For a closed-flow baker's map, $h = 2$ as all iterates stay inside the mixing region. Here $h < 2$, since some iterates escape downstream and are not further replicated in more images. It turns out that h can be calculated using the symbolic dynamics that encode transport by the map, which were introduced in the previous chapter. As the replication of the blocks dictates the increase of the number of filaments, the number of iterates remaining inside the mixing region can be calculated recursively as

$$\mathcal{N}_{n+1} = \mathbf{M}\mathcal{N}_n, \tag{6.16}$$

where $\mathbf{M}$ is the $p \times p$ (for dynamics on p symbols) that code the mapping of the symbols by an iteration of the map. For example, the dynamics on two symbols of Fig. 5.11 have a transfer matrix

$$\begin{pmatrix} 1 & 1 \\ 1 & 0 \end{pmatrix}$$

The topological entropy is given by the largest eigenvalue of $\mathbf{M}$ [1]. (For the dynamics on two symbols, the topological entropy is the golden ratio $h = (1 + \sqrt{5})/2$.)

We can now derive the contribution of the first set to the variance, which is given by the initial variance weighted by the measure of the set. We write

[1] From Eq. (6.16), h can also be interpreted on the growth rate of the allowed words on p symbols coding the trajectory of a particle. This is in fact the original definition of the topological entropy: h codes the mean amount of information carried by each symbol.

this measure as the complementary to one of the measure of the second set, so that

$$\sigma_1^2 = \sigma_0^2 \left(1 - \sum_{N+1}^{\infty} U h^n \gamma^n\right). \tag{6.17}$$

The contribution of the second set is

$$\sigma_2^2 = \sigma_0^2 \int \left(\frac{\delta}{w_{\mathrm{B}}}\right)^2 \mathrm{d}\mu(\delta) \tag{6.18}$$

where $\mu(\delta)$ is the probability of cutting an iterate of width δ with the frontier of a gliding box of size w_{B} (see Fig. 6.10) – there is less chance of cutting a small crenel than a bigger one. We obtain

$$\sigma_2^2 = \sigma_0^2 \sum_{N+1}^{\infty} U \gamma^n h^n \left(\frac{U\gamma^n}{w_{\mathrm{B}}}\right)^2. \tag{6.19}$$

Computing the geometric series and adding the two contributions yields the final expression:

$$\sigma^2(\phi) = \sigma_0^2 \left\{1 - U\left[\frac{h\gamma}{1-h\gamma} - \frac{h\gamma^3}{1-h\gamma^3}\right]\left(\frac{w_{\mathrm{B}}}{U}\right)^{1+\frac{\log h}{\log \gamma}}\right\} \tag{6.20}$$

where we have used the expression of N (6.13).

This relation is easily generalized to any moment $M_m = \int_0^1 |C(x) - \langle C\rangle|^m \,\mathrm{d}x$ as follows:

$$M_m = M_m^0 \left\{1 - U\left[\frac{h\gamma}{1-h\gamma} - \frac{h\gamma^{m+1}}{1-h\gamma^{m+1}}\right]\left(\frac{w_{\mathrm{B}}}{U}\right)^{1+\frac{\log h}{\log \gamma}}\right\}. \tag{6.21}$$

Eq. (6.20) shows that the fraction of the variance lost in the mixer, $1-I(\phi)^2$, increases as a power-law of exponent $1+\log h/\log\gamma$ with the scale at which the concentration is probed. As represented in Fig. 6.11, simulations for $\gamma = 0.5$ confirm our results as the exponent is in good agreement with the value of h calculated from symbolic dynamics. Departure from the power-law regime occurs only for very small values of κ, when the coarse-graining scale in the simulations is bigger than w_{B}, and for very large values of κ or w_{B} where the first iterates are smaller than the diffusion scale ($N = 0$)– again, this regime is not very interesting, because mixing is almost perfect.

Note that the two terms inside the square brackets in Eq. (6.20) represent the contributions to the variance of the two sets that we have previously defined. The first set corresponds broadly to the largest holes of the unstable manifold, whose total measure gives η_{W}. In our first attempts to

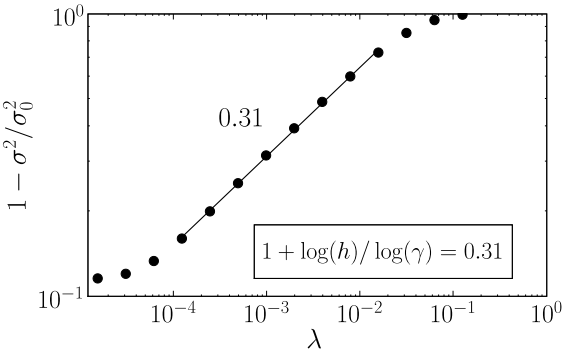

Figure 6.11: Evolution of $1 - I^2(\phi)$ with the diffusion scale λ, for a realization of the 1-D map with parameters $\gamma = 1/2$ and $U = 0.14$. The fraction of the variance lost in the mixer varies as a power law with λ, whose exponent agrees very well with $1 + \log(h)/\log(\gamma)$.

compute $I(\phi)$, we have neglected the contribution of images smaller than w_{B}. For the example shown in Fig. 6.11, the second term in the square brackets is almost 17 times smaller than the first one, which justifies this approximation (and in any case, the ratio between the two terms is bounded from above by γ^2).

The calculation performed above is trickier for a general value of γ. Results of simulations conducted for a set of values of U and γ yielding the same symbolic dynamics on two symbols (this ensures that all protocols have the same topological entropy) are presented in Fig. 6.12. Again, we observe power laws for the evolution of $1 - I(\phi)^2$ with the measurement scale, but the exponent is a function of γ (plotted in the inset of Fig. 6.12). We observe that the exponent of the power law decreases for γ farther from $1/2$: this means that diffusion is less efficient to fill the holes for a large distribution of hole widths.

This power-law behavior is of course very interesting for evaluating mixing: measuring $1 - I(\phi)^2$ for two scales or two diffusivities allows to predict the value of $1 - I(\phi)^2$ for all other scales.

Furthermore, the same above reasoning can be extended to predict the evolution of $1 - I(\phi)^2$ with the initial variation scale of the profile – say that each newly injected slice consists of a series crenels of width λ_i. This is confirmed by results shown in Fig. 6.13, where we observe a power-law with the same exponent for the evolution of the initial scale as for the measurement scale: $1 - I(\phi)^2 \propto \lambda_i^{-(1+\log h/\log\gamma)}$.

Note that the scalings derived above are only valid if the variance is measured in a domain where stretching and folding applies everywhere. For a phase portrait separated in distinct regions, as in butterfly experiments where we have a free region on each side of the channel, and a central mixing region from which fluid escape on the unstable manifold of the chaotic saddle, we expect these scalings to hold only in the central region.

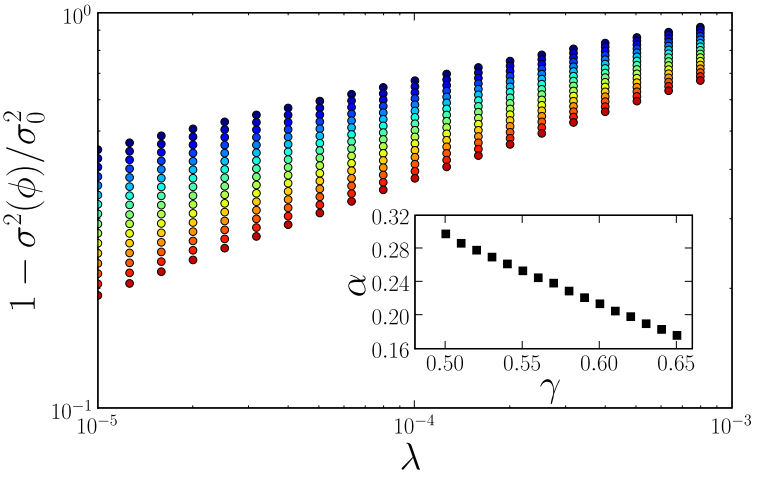

Figure 6.12: 1-D model – Evolution of $1-I(\phi)^2$ as function of the measurement scale λ. We have used 16 values of γ regularly spaced between 0.65 (blue) and 0.5(red), and corresponding values of U regularly spaced between 0.08 and 0.14. All these maps can be described by the same symbolic dynamics on two symbols. For all cases, we observe a power law, whose exponent decreases for γ further from 0.5.

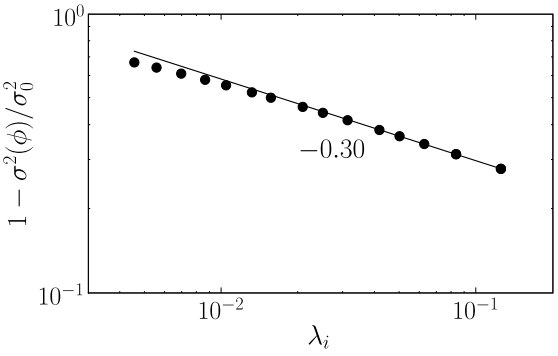

Figure 6.13: 1-D model with parameters $U = 0.14$, $\gamma = 0.5$. Evolution of $1-I(\phi)^2$ as a function of the initial profile length scale λ, for a fixed measure scale. The upstream profile chosen here is a series of crenels of width λ_i.

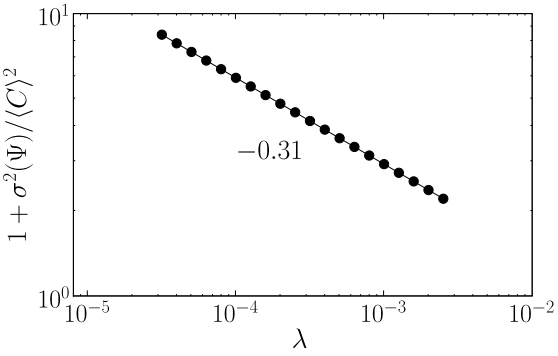

Figure 6.14: 1-D model with parameters $U = 0.14$, $\gamma = 0.5$, $\kappa = 10^{-10}$. Normalized variance of the decay strange eigenmode Ψ as a function of the measurement scale. The exponent of the observed power-law is given by the correlation dimension D_2 of Ψ.

Variation of $I(\Psi)$ with the measurement scale – multifractal spectrum

We now turn to characterizing the relative variance of the decay strange eigenmode $I(\Psi) = \sigma(\Psi)/\langle\Psi\rangle$. The support of Ψ is the multifractal unstable manifold of the chaotic saddle (constituted by all iterates of the periodic points of the chaotic saddle), fattened by diffusion to a minimal scale $w_{\rm B}$. Ψ therefore shadows the multifractal set, up to the scale $w_{\rm B}$ below which multifractal properties are no longer observed [120]. Note that fractality of Ψ follows directly from the symbolic dynamics described in the previous chapter, which ensure that the same structure is observed on every scale.

In particular, it is easy to show that $I(\Psi)^2$ is closely related to the correlation dimension D_2 of the set. Assuming that the concentration is measured at a scale λ, we may write

$$I(\Psi)^2 = -1 + \frac{\langle C^2\rangle}{\langle C\rangle^2} \tag{6.22}$$

$$= -1 + \frac{\sum_{N(\lambda)} C_i^2}{\left(\sum_{N(\lambda)} C_i\right)^2} \tag{6.23}$$

where the sums are performed on all boxes of size λ. The correlation dimension is defined as

$$D_2 = \lim_{\lambda\to 0} \frac{\log\left(\sum_{N(\lambda)} p_i^2\right)}{\log\lambda}, \tag{6.24}$$

where $p_i = C_i/\sum C_i$ is the fraction of the total mass in the box i. For small λ, we have

$$1 + I(\Psi)^2 \simeq A\lambda^{D_2}. \tag{6.25}$$

One can see in Fig 6.14 that this prediction is in good agreement with the observed variation of $1 + I(\Psi)^2$ with the measurement scale (this was expected, as we have used the very definition of the correlation dimension...).

It is important to note that Rényi entropies are more relevant for the characterization of Ψ than for ϕ, as Ψ is a scale-invariant (multifractal) object. For a small probing scale, Rényi entropies amount to the spectrum of multifractal dimensions [47]:

$$D_q = \lim_{\lambda\to 0} \frac{1}{q-1}\frac{\log\sum p_i^q}{\log\lambda}. \tag{6.26}$$

D_q is a decreasing function of q, so that in particular $D_0 \gtrapprox D_1 \gtrapprox D_2$. Depending on the available data, one should preferably compute one of

these three dimensions: D_0 gives the fractal dimension of the covered set for binarized black and white data, while D_1 is easily obtained from a continuous concentration profile (as the experiments e.g.). Finally, D_2 is well suited to compute the dimension of a set covered by points (that can be obtained in numerical simulations).

6.2.3 Spatial measures

Now that we have established that the intensity of segregation $I(\phi)$ is a robust criterion for evaluating mixing quality, we wish to account for the complicated spatial structure of ϕ (see for example Figs. 6.6 or 6.9). This task might seem especially difficult in open flows, where the pattern of ϕ results from the juxtaposition of strips with very different residence times – and consequently different numbers of stretching steps. Strips that spend few periods inside the mixing region are hardly compressed – these are of course the worst structures that must be characterized. Strips that have aggregated on the unstable manifold, on the other hand, have reached a scale of order w_B and are less problematic. We must therefore find a relevant way to process our concentration field, that accounts for this very wide distribution of scales. We start by considering an ideal case where the distribution of scales can be derived analytically; several measures are then tested against this exact prediction.

Length scale distributions for an ideal case

Let us first consider the 1-D open-flow map with even stretching ($\gamma = 1/2$). Using the notations of the previous paragraph, an injected slice of width U is transformed into iterates of widths $U\gamma^i$, up to some critical iteration N defined by $U\gamma^N \sim w_\mathrm{B}$. All further iterates contribute to the scale w_B. We define the energy of a scale l by the total contribution of all structures (e.g. crenels) of width l to the variance of the profile. For $l > w_\mathrm{B}$, the energy is simply given by the measure of all iterates of the upstream slice with width l, whereas for $l \leq w_\mathrm{B}$, one must also consider that such structures yield smaller fluctuations (as many iterates are averaged inside a box of size w_B), and contribute less to the variance. We therefore obtain the following "energy spectrum" $E(l)$:

$$\left\{ \begin{array}{rcl} E(U\gamma^n) & = & U(\gamma h)^n \quad \text{for } n \leq N \\ E(w_\mathrm{B}) & = & \sum_{N+1}^{\infty} \left(\frac{U\gamma^n}{w_\mathrm{B}}\right)^2 U(\gamma h)^n \end{array} \right. . \tag{6.27}$$

Eq. (6.27) allows in particular to compute a typical scale as $\langle l \rangle = \sum E(l) \times l$.

Fourier spectrum and scale of segregation

We have represented in Fig. 6.15 a correlogram (Fig. 6.15 (a)) and a Fourier spectrum (Fig. 6.15 (b)) for the steady-state concentration field ϕ, obtained by iterating the 1-D map with parameters $\gamma = 0.6$ and $U = 0.1$ (correlogram), and $\gamma = 0.5$ and $U = 0.125$ for the power spectrum. We can see that the correlogram has a very complicated evolution; this is due to the multi-scale structure of the pattern. Anti-correlations impose to use the second definition of the segregation scale Eq. (6.9). However, this is dangerous, as scales greater than r^* are not considered in the computation of the typical scale s. We find actually a value of s (2×10^{-3}) much smaller than the mean scale based on the distribution Eq. (6.27) ($\langle l \rangle \sim 7 \times 10^{-2}$): this discrepancy can be attributed to the non-physical cut-off performed on the length scales when computing s.

The Fourier power spectrum in Fig. 6.15 (b) indicates a broad distribution of scales, as is indeed the case. Small wave numbers contribute significantly to the energy, hinting at the presence of large-scale structures. However, Fourier power spectra might not be the best tool to describe precisely the width distribution for elementary dye strips, as we wish to do. The Fourier transform develops the field on a basis of periodic functions, and is therefore inherently non-local. It does not seem very natural to consider our concentration profile as a sum of sinusoidal functions, that interfere in a non-intuitive way to construct the particular crenel-shaped profile of ϕ. It seems therefore preferable to use a local analysis, such as wavelet transforms which are used in the following paragraph. Also note that the nonsmoothness of the profile is responsible for a very noisy Fourier spectrum.

Wavelets – We do not provide here a comprehensive introduction to wavelets; the reader is referred to the exhaustive literature on the subject (a 1992 article by M. Farge [34] on wavelets in turbulence might be of special interest for the fluid dynamics physicist).

Suffice it to say that wavelets are a space and scale analysis, where the signal is decomposed on a basis of functions that are localized in space (contrary to the space-filling sinusoidal functions). This basis relies on a *mother wavelet*, that is compressed (scale analysis) and translated (space analysis) to construct the whole basis. An example is shown in Fig. 6.16. The mother wavelet here is called the *Haar wavelet* , which is a simple crenel:

$$\begin{cases} H(x) = 1 & \text{for } 0 \leq x \leq 1/2, \\ H(x) = 0 & \text{elsewhere.} \end{cases} \tag{6.28}$$

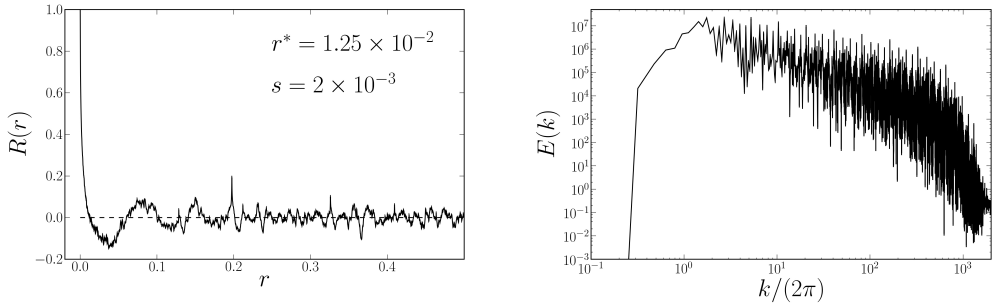

(a) (b)

Figure 6.15: (a) Correlogram $R(r)$ of ϕ for the 1-D map with parameters $U = 0.1$ and $\gamma = 0.6$. (b) Fourier energy spectrum of ϕ for the 1-D map with parameters $U = 0.125$ and $\gamma = 0.5$.

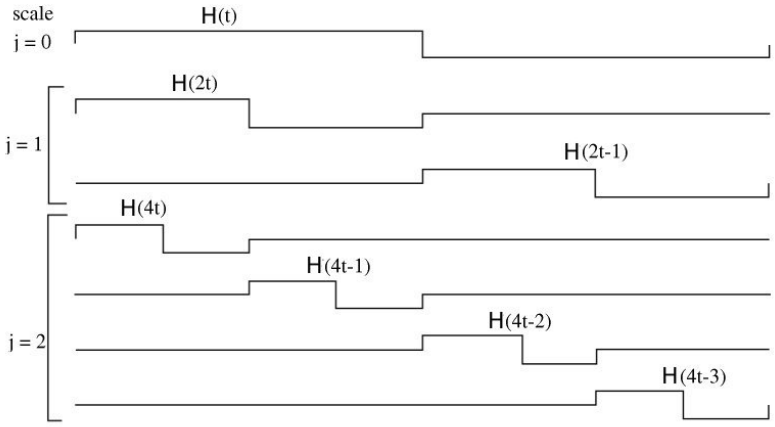

Figure 6.16: Construction of the Haar wavelet basis by rescaling and translation of the original crenel profile H.

We consider here the *discrete wavelet transform* (DWT, as opposed to the *continuous wavelet transform*), where a discretized field $C(x_i)$ is decomposed as

$$C(x_i) = \sum_{l,m} \tilde{h}_{lm} H_{lm}(x_i). \tag{6.29}$$

The basis H_{lm} is generated from the mother wavelet as

$$H_{lm}(x) = H(2^l x - m), \tag{6.30}$$

where $l \in \mathbb{N}$ and $m \in [0, 2^l - 1]$. Plots of H_{lm} are shown in Fig. 6.16 for l =0, 1, 2. The sum of H_{lm} functions is an orthogonal basis, and the $\tilde{h}_{lm}$ coefficients are simply obtained from a scalar product:

$$\tilde{h}_{lm} = \frac{1}{A} \sum_i C(x_i) H_{lm}(x_i), \tag{6.31}$$

where A is a normalization constant. The physical interpretation of the wavelet coefficients $\tilde{h}_{lm}$ is particularly interesting for characterizing the concentration profile: $\tilde{h}_{lm}$ tells us if the concentration profile around the position $m/2^l$ is locally correlated with a crenel of width 2^{-l}: this is precisely the kind of structures we wish to detect. Moreover, the logarithmic hierarchy of scales $\lambda = 2^{-l}$ seems well suited to describe a multiplicative stretching process.

The wavelet spectrum $\tilde{h}_{lm}$ is traditionally represented in a space-scale plot, where the amplitude of $\tilde{h}_{lm}$ is color-coded. Here, we will consider a scale-only information averaged over space. Due to the orthogonality of the wavelet basis, the conservation of energy writes:

$$\sigma^2(C) = \sum_l \sum_m |h_{lm}|^2. \tag{6.32}$$

Defining the wavelet power spectrum at scale 2^{-l}, $E(l) = \sum_m |h_{lm}|^2$, we obtain the "Parseval formula"

$$\sigma^2(C) = \sum_l E(l). \tag{6.33}$$

This is analogous to the Parseval formula for the Fourier transform; it is yet important to note that both spectra are not distributed in the same way – only their sums are equal. We expect $E(l)$ to account for the energy of the strips of widths between 2^{-l} and $2^{-(l+1)}$. We have represented $E(l)$ in Fig. 6.17 for the 1-D map with parameters $\gamma = 0.5$ and $U = 0.125$, and different diffusivities. For these simulations we have used an initial profile

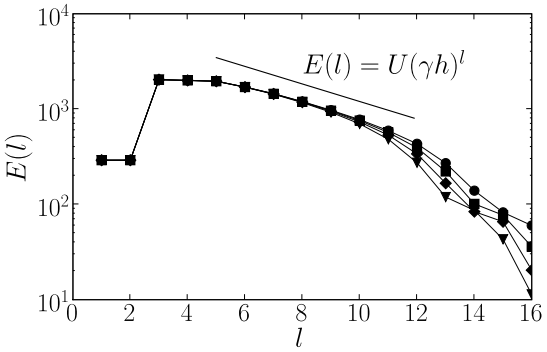

Figure 6.17: Wavelet power spectrum for different realizations of the $1-D$ map with parameters $\gamma = 0.5$, $U = 0.125$ and diffusivities 10^{-10}, 2×10^{-10}, 4×10^{-10} and 4×10^{-10}.

that consists of successive crenels of width U. We observe that $E(l)$ has significant values only for scales smaller or equal than the largest strip U, which is a desirable feature. As can be seen in Fig. 6.17, the power-law decay of the energy spectrum for smaller scales (greater l) is in very good agreement with the power-law $E(l) = U(\gamma h)^l$ derived in Eq. (6.27): as expected, the wavelet spectrum counts the number strips of widths in the range $[2^{-l}, 2^{-(l+1)}]$. The rapid decay for even smaller scales is due to the diffusive cut-off: no structures smaller than w_{B} are visible in the pattern. Increasing the diffusivity does not change the wavelet spectrum for large scales, but shifts the diffusive cut-off to larger scales (see Fig. 6.17). We have also observed (results not shown here) that changing the typical scale of the initial pattern changes only the large scale (right) part of the spectrum. Finally, the typical length scale $\lambda = \sum E(l)2^{-l}$ agrees very well with the mean scale that can be computed analytically.

The reader might have noticed that the value of $\gamma = 1/2$ might seem artificially chosen to fit with the wavelet crenels of width 2^{-l}. For an inhomogeneous stretching, the width of a strip falls typically between two values 2^{-l} and $2^{-(l+1)}$. The wavelet power spectrum shown in Fig. 6.18 for a simulation with $\gamma = 0.65$ is indeed less regular – yet it has a global power-law evolution on a wide range of scales, accounting for the multiplicative stretching process, and it provides a coarse-grained distribution of length scales, of variable coarse-graining size $2^{-(l+1)} - 2^{-l}$. Further developments could consider a continuous version of the wavelet transform which would avoid this coarse-graining and provide more precise measures.

In conclusion, we are quite confident that wavelets are a relevant tool to characterize the distribution of strips widths. For the 1-D model, wavelet analysis has permitted us to derive a spatial transfer function of the mixer, that is the answer of the map to a profile of typical length scale λ in terms of scales present in the mixing region profile. Such an analysis is very

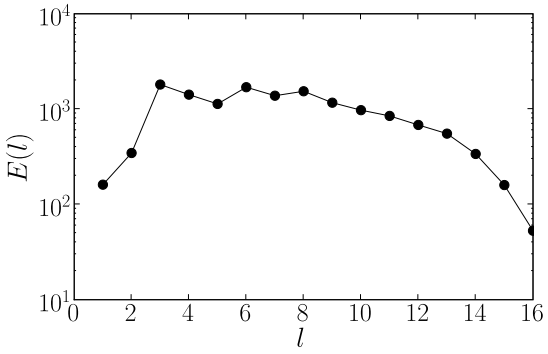

Figure 6.18: Wavelet power spectrum for a realization of the $1-D$ map with parameters $\gamma = 0.65$, $U = 0.08$ and diffusivity 10^{-10}.

important if one would envisage e.g. to consider a series of successive mixing elements.

6.3 Conclusion

In this final chapter, we have considered different measures of mixing in open flows. Our selection of mixing criteria follows directly from our understanding of mixing processes, as we wish to choose measures that are robust to a change of initial condition, or measurement scale. After a short review of usual mixing criteria in closed flows, we have revisited the classical intensity of segregation $I(\phi)$ in the case of a continuous injection of inhomogeneity. Using our open-flow 1-D model, we have first showed that, for a fixed measurement scale, $I(\phi)$ is strongly correlated to the relative variance $I(\Psi)$ of the decay strange eigenmode Ψ, observed for long times for the injection of a single dye blob. This is due to the specific structure of the mixture patterns in open-flows, that are strongly determined by the chaotic saddle and its unstable manifolds: Ψ traces out the fractal unstable manifold of the chaotic saddle, fattened to the diffusion scale w_{B}, while large (i.e. high-variance) structures of ϕ are locate precisely in the holes of the unstable manifold, as they have experienced little stretching and are therefore far from the unstable manifold. A good approximation of $I^2(\phi)$ is thus given by counting the measure of the holes of the decay pattern Ψ. This has been checked for a large set of simulations of the model, for different flowrates and stretching inhomogeneity.

We have then proposed a more refined description of the ϕ profile, by distinguishing between images of the upstream profile wider or smaller than the diffusion scale w_{B}. We have demonstrated that the fraction of the initial variance lost in the mixer, $1 - I^2(\phi)$, evolves as a power law with the scale λ at which the concentration is measured. This reasoning carries

over to the initial scale of the profile. Conversely, the relative variance of the decay profile is related to the correlation dimension of the multifractal unstable manifold, so that $1 + I^2(\Psi) = \lambda^{D_2}$ – a different evolution with the measurement scale.

Next, we have wondered how to describe the spatial distribution of the concentration profile ϕ, which is specific to open flows, as newly injected large structures live amongst older images, some of which have reached the Batchelor scale: a wide distribution of lengthscales stems from to the wide (exponential) distribution of residence time (or stretching times) inside the mixing region. We have suggested that wavelets may be efficient tools to describe these structures and emphasized the need for a *local* scale analysis.

Mainly because of lack of time, no attempt has yet been made to test these measures in the open-flow experiments and we have instead focused on the 1-D model. The next step for future developments will be of course to validate our measures for experimental fields, and to adapt them for 2-D fields (e.g. construct adapted 2-D wavelet bases). In real flows, care must also be taken to detect the phase space organization, as different mixing is expected in different regions. For butterfly protocols e.g., the chaotic saddle is not responsible for the concentration field in the layers of free trajectories along the channel sides, and the scalings derived here for the intensity of segregation $I(\phi)$ may hold only in the central region. The total variance is readily obtained as the sum of the variances in the different regions, which have however different scalings with the measurement scale.

Chapter 7

Conclusions

In this last chapter, we start by summarizing our goals, and the approach used in this work. We proceed to summing up the results presented in the thesis. A few important points that can be drawn from our work are highlighted in a third section. Finally, we suggest some possible directions for future work.

7.1 Summary of approach

We have carried out a study of mixing mechanisms in various rod-stirring devices, both in closed and open low-Reynolds-number 2-D flows. With industrial applications in mind, our primary goals were to understand the mechanisms at play during the homogenization process, to derive generic laws accounting for the dynamics of mixing, and to have at hand criteria to evaluate the degree of mixing. When choosing the mixing devices, our concern lay in studying systems that could be used for industrial applications, while being generic enough.

Our approach has combined different ways used in the literature to explore laminar mixing. 2-D incompressible laminar flows achieved in our experiments and simulations are well captured in the standard framework of chaotic advection [82], and it is common to relate characteristics of the phase space – which is also the real physical space – such as elliptical islands or chaotic regions, periodic points and their manifolds, to the stretching of Lagrangian fluid particles and to the resulting mixing. We have also explored another classical – at least for closed flows – direction, which concentrates on describing the evolution of a scalar (e.g. dye) concentration field towards a coherent pattern [88].

With regard to the literature on chaotic mixing, which consists mostly in theoretical or numerical studies, we have invested much experimental effort on obtaining quantitative data for the concentration field of a scalar field, in various closed- and open-flow systems; of course such experimental methods have already been employed in other studies (see e.g. [95, 52, 127, 125]), but we have made systematic use of this approach here. Although our approach is in the first place experimental and numerical, we have made extensive use of the formalism of Hamiltonian dynamics or 2-D diffeomorphisms, which provide powerful tools. Moreover, we have found that the phenomenons observed in the experiments could often easily be transposed in simple 1-D models, all based on modifications of the baker's map, which provide toy models where a wider range of situations can be explored.

7.2 Summary of results

Our work has contributed to the identification of several mixing mechanisms, and has shed a different light on some classical situations.

7.2.1 Topological and kinematical description of mixing

In the context of topological mixing, an approach developed recently [18], we have first proposed in Chapter 3 to consider 2-D chaotic mixing as the braiding of periodic points, that we have called *ghost rods*. All periodic structures, be they regular elliptical islands or unstable hyperbolic or parabolic points, are topological obstacles to material lines and stretch them as real rods do, at a rate (called the topological entropy of the flow) greater or equal than the complexity of the entanglement created by the motion of a set chosen among these points, that is the topological entropy of the corresponding braid. Using Stokes-flow numerical simulations of realistic rod-stirring protocols, we have shown that detecting a limited number of orbits (60 in our study) allows to compute efficiently the topological entropy of the flow, i.e. to determine the growth rate of an interface in the flow. We have suggested that parabolic points might be the most "efficient" ghost rods, i.e. the ones that account best for the topological complexity of the flow, as they are nested inside the folds that are characteristic features of a given mixing pattern.

7.2.2 Dye homogenization in closed and open flows

Besides this kinematical description of mixing, we have also carried out dye mixing experiments, where we have studied the homogenization of the concentration field under the combined action of stretching and diffusion. Although this is a well-established approach in closed flows, open flows where mixing results from the action of a chaotic saddle had never been studied before with the homogenization of a scalar field in mind: numerous studies have instead related the multifractal properties of the chaotic saddle, and its manifolds, to the scattering of point-like passive tracers [53, 104] or the filamentary structure of the tracers pattern observed for long times. Others have concentrated on extracting flow structures such as the unstable manifold of the chaotic saddle from Lagrangian data, with the application to environmental flows in mind [98, 110].

Although our primary interest was more focused on open flows, we have shown that mechanisms leading to the homogenization of a concentration field, or the dispersion of an initial blob of inhomogeneity, have striking similarities in closed and open flows. A long-lived view describes stirring as the combination of complex stretching and folding of scalar filaments, whereas diffusion completes the mixing process at finer scales. In the course of this thesis, we have come to a related conception of mixing, where the inhomogeneity of such patterns comes from the periodic structures of the phase space with lowest stretching, i.e. where homogenization is slowest, and is visible mostly along their unstable manifold, that is on the paths along which low-stretching structures contaminate the whole space.

In particular, we have demonstrated in two different closed-flow experiments the importance of the phase portrait in the vicinity of a no-slip wall. In the figure-eight mixer, where the chaotic region extends to the no-slip wall, we have observed a slow – algebraic – decay of the concentration variance, even in the core of the filamentary pattern. As we have shown, no-slip hydrodynamics near the wall impose that poorly mixed fluid is stored for long times in the vicinity of the wall, but it is later reinjected in the bulk along the unstable manifold of a parabolic point. This imposes that mixing dynamics are slowed everywhere by the wall, up to the core of the pattern. We expect such mechanisms to be valid for any 2-D mixer with a chaotic region that extends to a solid wall, in the case of no-slip boundary conditions.

Using the epitrochoid protocol, we have then evidenced a second "universality class" where the chaotic region is shielded from the wall by a regular region. In this experiment, we have retrieved an exponential evolution of

the concentration variance and observed the onset of a strange eigenmode [88], i.e. a self-similar concentration field where fluctuations decay exponentially with time. Greatest fluctuations of the pattern are observed in the folds of the pattern, presumably at the locations of parabolic points and their unstable manifolds.

We have pointed out that the nature of the phase portrait near the side walls is of paramount importance in open flows as well. We have distinguished between butterfly and breaststroke versions of the egg-beater motion of the rods. In the butterfly case, the chaotic saddle and its manifolds are confined to a finite portion of the channel width, as the chaotic saddle is shielded from the no-slip walls by a layer of free trajectories. This more ideal case is close to some other open flows studied before, such as leap-frogging pairs [87], yet it is the first time that homogenization of a concentration field performed by this kind of open-flow mixers has been investigated in details. Following the evolution of the concentration field generated by the release of a dye blob in the upstream region, we have evidenced the onset of an open-flow strange eigenmode, that is a self-similar concentration field recurrent in the Poincaré map, yet with an amplitude decaying exponentially. Using a simplified 1-D model, we have described how the strange eigenmode arises as a result of the global advection and the stretching process, which compresses the whole mixing region to a width comparable to the diffusive scale, so that the global decay of concentration is transported to small scales. The support of this decay strange eigenmode is the unstable manifold of the chaotic saddle, fattened to the diffusion scale. Holes inside the pattern correspond to images of slices of upstream fluid that are injected inside the mixing region. As could be expected, we have found that decreasing the stirring period compared to the timescale of the global advection yields thinner white holes, and hence a more homogeneous pattern inside the mixing region (as measured by its relative variance, normalized by the concentration mean). However, the homogeneity of the downstream pattern is poorer than inside the mixing region, as it is segregated in two layers of free trajectories, where no dye is visible for long times, and a lobe pattern emanating from the mixing region. Also, we have observed that the saying "the faster you stir, the better you mix" failed to be true in this case. For high frequencies, two effects reduce the efficiency of mixing in the butterfly case: (i) lobes occupy only a small fraction of the channel width, and (ii) two elliptical islands appear inside the mixing region and store poorly mixed fluid in their vicinity, so that the mixing region pattern is also less homogeneous.

For breaststroke protocols, the chaotic saddle extends to the side walls of the channel, where we have observed stagnation points that appear be-

cause of the competition between the main flow, and the action of the stirring rods. These breaststroke experiments are to the best of our knowledge the first study where the chaotic saddle and its manifolds cover such a large part of the flow domain. This is important for industrial applications, to ensure that no large-scale fluid pieces can escape to the stretching process. However, this desirable good coverage has some side-effects. As in the closed-flow figure-eight protocol, poorly stretched fluid is stored for long times near the walls, and then escapes in the form of darker filaments along the unstable manifolds of the stagnation points, which are parabolic. We have observed some departure from an exponential evolution of the moments, and self-similarity of the PDFs, that we have attributed to the wall parabolic points. However, the global advection, combined to the shuffling of the pattern by the rods, imposes a "first-order" evolution, which is close to exponential. The effect of the walls is therefore less dramatic than in closed flows. It is instructive to note that although we have always observed stagnations points on the side walls, using the breaststroke sense of rotation with smaller rods, or a smaller lateral extent of the rods' trajectories, should eliminate the stagnation points and permit fluid to leak along the channel sides. We would then retrieve a situation comparable to the butterfly case, yet with parallel filaments and a free layer as thin as wanted, if one fiddles with parameters such as the trajectories of the rods. One should be aware that the topology of the phase space, i.e. the extent of the chaotic region relative to the walls, cannot be predicted for sure beforehand, without explicitly computing the Poincaré section of the flow, or looking at the dye pattern; this is true both in closed and open flows.

With respect to preceding open-flow studies which have mostly concentrated on the long-time evolution of a blob, we have tried to consider in parallel the short-time and the asymptotic evolution of a blob, or equivalently the decay case and the continuous injection case. Because of the specific structure of the chaotic saddle and its manifolds, worst-mixed parts of the short-time (in the decay case) or continuous patterns are found in the holes of the asymptotic decay pattern. In the butterfly case, we have proposed a geometric method that allows to determine a chart of elements that will escape the mixing region. We have also studied in the 1-D model how the respective measure of each set – the fattened unstable manifold, and its complementary set where large high-variance strips can nest – evolves when the measurement scale, or the initial scale of the pattern are changed.

7.2.3 Characterization of mixing efficiency

Beyond the study of mixing processes, we have also asked how mixing can be characterized, the underlying goal being to compare the efficiency of different mixing devices. Throughout this manuscript, we have concentrated on the first moments of the concentration field, that is its mean (which is not conserved in open flows, in particular for decay experiments) and above all, its variance which measures directly the inhomogeneity of the concentration field.

In open flows, we have used the intensity of segregation $I(\phi^2)$, which evaluates the rate of the downstream variance with respect to the initial upstream variance, for a continuous injection of inhomogeneity. As mentioned above, we have shown for the 1-D map that the intensity of segregation is correlated with the variance of the decay pattern, and that $1 - I(\phi)^2$, i.e. the amount of variance lost in the mixer, scales as a power-law with the measurement scale, or the typical length scale of the upstream pattern.

We have also insisted on the importance of characterizing the distribution of length scales in the case of a continuous injection. We have underlined that open-flow mixing is a very "unfair" process, as some elements leave the mixer very rapidly and do not experience much stretching, while other parts are compressed up to the Batchelor scale – this wide range of stretching histories cannot be avoided. We have suggested that a local analysis such as wavelets analysis might be necessary to measure the spatial distribution of inhomogeneity in a relevant fashion.

7.3 A few take-home messages

7.3.1 Can you read the speed of mixing ?

We have studied several quantitative characterizations of mixing in this thesis, and we have evidenced different evolutions of the concentration variance, depending on the phase portrait of the flow. Yet, precise measures of the concentration field are not always available when testing a mixing device, and less refined measures might be necessary. To this respect, it is important to note that some low-hanging fruits can be picked directly from our understanding of mixing mechanisms. Some important information about the mixing scenario at play are readily available in the pictures of dye patterns, and the speed of mixing may sometimes be deciphered directly from the images.

For instance, in the case of a closed-flow mixer in the figure-eight class, the cusped shape of the pattern betrays the presence of a parabolic point on the wall. The distance of the filamentary pattern to the wall, if mea-

sured at two different times, provides an estimation of the strength of the parabolic point (which we have called a), that is the rate at which the pattern converges to the wall. The knowledge of a gives the width of the reinjected white filaments, and therefore the speed of mixing, as we derived in chapter 4. Conversely, in the case of a mixing region of limited extent, and with a smooth boundary, we might expect homogenization dynamics to be exponential if no elliptical islands are visible. However, elliptical islands allow us to reconstruct a braid formed with the islands and the rods, that provides directly a lower bound on the stretching rate of a material line...

This "image-reading" method applies to open flows as well: for example, pictures of the decay pattern at long times may be simply binarized in order to count the area of the holes, where large high-variance large filaments will be nested in the case of a continuous injection of inhomogeneity. The measure of this area provides a good first-order measure of mixing efficiency.

7.3.2 Specficities of open-flow mixing

One could naively expect close similarities between open-flow mixing and finite-time closed-flow mixing. Yet, homogenization mechanisms in both systems are very different, as mixing in open flows is limited by elements that spend much less time than the average residence time inside the mixing region. Evaluating the mixing efficiency of an open-flow system must therefore take into account the fraction of fluid that escapes quickly, and measures of the stretching experienced by fluid particles that spend a long time inside the mixing region, such as the Lyapunov exponent of the flow, are not directly related to the efficiency of a mixer. We have suggested instead to count the fraction of holes in the asymptotic decay pattern, which should provide a satisfying approximation of the efficiency of mixing (measured e.g. by the intensity of segregation) when the fraction of holes is significant.

7.3.3 The importance of solid walls

The role of fixed solid walls cannot be disregarded when designing an industrial mixer. For closed flows in the figure-eight class, we have suggested that "scraping the bowl" as close as possible can reduce the limiting effect of the walls. On the other hand, the central part of a mixer in the epitrochoid class is mixed exponentially fast. If one can afford to discard the annular regular region, such mixers might be a good choice.

We do not yet understand completely the influence of walls on mixing efficiency in open flows. In the butterfly case, high variance elements escape

freely along the layers of free trajectories on both sides of the channel, which is disastrous for mixing – except if one is interested only in the central part of the pattern, which is very well mixed. This could be the case for some applications. In the breaststroke case, parabolic points on the walls store for long times poorly stretched fluid. This is in any case non-optimal, as fluid particles spend a long time in the mixer without being stretched. We yet have to understand the effect of such parabolic points on e.g the intensity of segregation.

7.4 Perspectives - outlook on future work

Future research could proceed in different directions. First, we advocate that the topological description of mixing processes should be developed further, in order to derive a minimal characterization of mixers, in terms of a limited set of braiding orbits. Understanding the role of bulk parabolic points, in particular, seems of prime importance to us.

Second, the departure from the strange eigenmode observed in some breaststroke experiments needs further clarification, as we have not yet understood quantitatively the effect of the wall parabolic points.

Regarding mixing measures, our experimental pictures could be analyzed to test the mixing measures introduced for the 1-D map. This study should start with the more ideal butterfly case, where one could measure the fractal dimension of the decay pattern, compare the variance of the decay and the – artificially obtained – continuous patterns, and observe their evolution with the coarse-graining scale. For the breaststroke case, one should first investigate if the decay pattern shows some departure from multifractality due to the injection of darker filaments from the walls, or not. Either the same mixing criteria, or modified measures could then be performed on breaststroke concentration fields. Measures of the spatial distribution of the concentration field, such as wavelets analysis, should also be adapted to 2-D flows and tested on our experimental pictures.

Finally, the characterization of 3-D flows clearly lags behind the understanding of 2-D flows. It is our hope that some mechanisms evidenced here, such as the importance of no-slip walls, could be adapted to 3-D flows. This will be the subject of future research.

Bibliography

[1] R. L. Adler, *Symbolic dynamics and Markov partitions*, Bull., new ser., Am. Math. Soc., 35 (1998), pp. 1–56.

[2] A. Adrover, M. Giona, F. Muzzio, S. Cerbelli, and M. Alvarez, *Analytic expression for the short-time rate of growth of the intermaterial contact perimeter in two-dimensional chaotic flows and Hamiltonian systems*, Phys. Rev. E, 58 (1998), p. 447.

[3] K. T. Alligood, T. D. Sauer, and J. A. Yorke, *Chaos: An Introduction to Dynamical Systems*, Springer, 1997.

[4] M. M. Alvarez, F. J. Muzzio, S. Cerbelli, A. Adrover, and M. Giona, *Self-similar spatiotemporal structure of intermaterial boundaries in chaotic flows*, Phys. Rev. Lett., 81 (1998), pp. 3395–3398.

[5] T. Antonsen, Z. F. Fan, and E. Ott, k *spectrum of passive scalars in Lagrangian chaotic fluid flows*, Phys. Rev. Lett., 75 (1995), p. 1751.

[6] T. Antonsen and E. Ott, *Multifractal power spectra of passive scalars convected by chaotic fluid flows*, Phys. Rev. A, 44 (1991), p. 851.

[7] ——, *The role of chaotic orbits in the determination of power spectra of passive scalars*, Phys. Fluids, 8 (1996), p. 3094.

[8] H. Aref, *Stirring by chaotic advection*, J. Fluid Mech., 143 (1984), pp. 1–21.

[9] ——, *The development of chaotic advection*, Phys. Fluids, 14 (2002), pp. 1315–1325.

[10] H. Aref and H. Balachandar, *Chaotic advection in a Stokes flow*, Phys. Fluids, 29 (1986), pp. 3515–3521.

[11] P. Arratia and J. Gollub, *Statistics of stretching fields in experimental fluid flows exhibiting chaotic advection*, J. Stat. Phys., 121 (2005), p. 805.

[12] G. Ascanio, M. Brito-Bazán, E. B.-D. L. Fuente, P. Carreau, and P. A. Tanguy, *Unconventional configuration studies to improve mixing times in stirred tanks*, The Canadian Journal of Chemical Engineering, 80 (2002), pp. 558–565.

[13] D. Auerbach, P. Cvitanović, J.-P. Eckmann, G. Gunaratne, and I. Procaccia, *Exploring chaotic motion through periodic orbits*, Phys. Rev. Lett., 58 (1987), p. 2387.

[14] G. L. Baker and J. P. Gollub, *Chaotic Dynamics- An Introduction*, Cambridge University Press, Cambridge, U.K., 1996.

[15] E. Balkovsky and A. Fouxon, *Universal long-time properties of Lagrangian statistics in the Batchelor regime and their application to the passive scalar problem*, Phys. Rev. E, 60 (1999), p. 4164.

[16] D. Beigie, A. Leonard, and S. Wiggins, *A global study of enhanced stretching and diffusion in chaotic tangles*, Phys. Fluids, 3 (1991), p. 1039.

[17] P. L. Boyland, *Topological methods in surface dynamics*, Topology Appl., 58 (1994), p. 223.

[18] P. L. Boyland, H. Aref, and M. A. Stremler, *Topological fluid mechanics of stirring*, J. Fluid Mech., 403 (2000), pp. 277–304.

[19] C. Castelain, A. Mokrani, Y. L. Guer, and H. Peerhossaini, *Experimental study of chaotic advection regime in a twisted duct flow*, European Journal of Mechanics - B/Fluids, 20 (2001), pp. 205–232.

[20] A. Celani, A. Lanotte, A. Mazzino, and M. Vergassola, *Fronts in passive scalar turbulence*, Phys. Fluids, 13 (2001), p. 1768.

[21] S. Cerbelli, J. M. Zalc, and F. J. Muzzio, *The evolution of material field lines curvature in deterministic chaotic flows*, Chem. Eng. Sci., 55 (1998), p. 363.

[22] J. Chaiken, R. Chevray, M. Tabor, and Q. M. Tan, *Experimental study of Lagrangian turbulence in a Stokes flow*, Proc. Roy. Soc. Lond., 408 (1986), pp. 165–174.

[23] M. Chertkov, G. Falkovich, I. Kolokolov, and V. Lebedev, *Statistics of a passive scalar advected by a large-scale two-dimensional velocity field: Analytic solution*, Phys. Rev. E, 51 (1995), p. 5609.

[24] M. Chertkov and V. Lebedev, *Boundary effects on chaotic advection-diffusion chemical reactions*, Phys. Rev. Lett., 90 (2003), p. 134501.

[25] ——, *Decay of scalar turbulence revisited*, Phys. Rev. Lett., 90 (2003), p. 034501.

[26] W. L. Chien, H. Rising, and J. M. Ottino, *Laminar mixing and chaotic mixing in several cavity flows*, J. Fluid Mech., 170 (1986), pp. 419–451.

[27] P. Cvitanović, *Invariant measurements of strange sets in terms of cycles*, Phys. Rev. Lett., 61 (1988), p. 2729.

[28] D. D'Alessandro, M. Dahleh, and I. Mezíc, *Control of mixing in fluid flow: A maximum entropy approach*, IEEE Transactions on automatic control, 44 (1999), p. 1852.

[29] P. Danckwerts, *The definition and measurement of some characteristics of mixtures*, Appl. Sci. Res., A3 (1952), p. 279.

[30] ——, *Continuous flow systems-distribution of residence times*, Chem. Eng. Sci., 2 (1953), pp. 1–13.

[31] B. Eckhardt, *Irregular scattering*, Physica D, 33 (1988), p. 89.

[32] R. S. Ellis, *Entropy, Large Deviations, and Statistical Mechanics*, Springer-Verlag, New York, 1985.

[33] G. Falkovich, K. Gawedzki, and M. Vergassola, *Particles and fields in fluid turbulence*, Rev. Mod. Phys., 73 (2001), p. 913.

[34] M. Farge, *Wavelet transforms and their applications to turbulence*, Annu. Rev. Fluid Mech., 24 (1992), pp. 395–457.

[35] J. D. Farmer, E. Ott, and J. A. Yorke, *The dimension of chaotic attractors*, Physica D, 7 (1983), pp. 153–180.

[36] D. R. Fereday and P. H. Haynes, *Scalar decay in two-dimensional chaotic advection and batchelor-regime turbulence*, Phys. Fluids, 16 (2004), p. 4359.

[37] D. R. Fereday, P. H. Haynes, A. Wonhas, and J. C. Vassilicos, *Scalar variance decay in chaotic advection and Batchelor-regime turbulence*, Phys. Rev. E, 65 (2002), p. 035301.

[38] M. Finn, S. Cox, and H. Byrne, *Topological chaos in inviscid and viscous mixers*, J. Fluid Mech., 493 (2003), pp. 345–361.

[39] ——, *Mixing measures for a two-dimensional chaotic Stokes flow*, Journal of Engineering Mathematics, 48 (2004), pp. 129–155.

[40] M. D. Finn and S. M. Cox, *Stokes flow in a mixer with changing geometry*, Journal of Engineering Mathematics, 41 (2001), pp. 75–99.

[41] J. G. Franjione, C.-W. Leong, and J. M. Ottino, *Symmetries within chaos: A route to effective mixing*, Phys. of Fluids A, 1 (1989), pp. 1772–1783.

[42] A. D. Gilbert, *Advected fields in maps — iii. passive scalar decay in baker's maps*, Dynamical Systems, 21 (2006), p. 25.

[43] E. Gouillart, N.Kuncio, O. Dauchot, B.Dubrulle, S. Roux, and J.-L. Thiffeault, *Walls inhibit chaotic mixing*, Phys. Rev. Lett., (2007).

[44] E. Gouillart, J.-L. Thiffeault, and M. D. Finn, *Topological mixing with ghosts rods*, Phys. Rev. E, 73 (2006), p. 036311.

[45] C. Grebogi, E. Ott, and J. A. Yorke, *Crises, sudden changes in chaotic attractors, and transient chaos*, Physica D, 7 (1983), p. 181.

[46] G. Haller, *Exact theory of unsteady separation for two-dimensional flows*, J. Fluid Mech., 512 (2004), p. 257.

[47] T. C. Halsey, M. H. Jensen, L. P. Kadanoff, I. Procaccia, and B. I. Shraiman, *Fractal measures and their singularities: The characterization of strange sets*, Phys. Rev. A, 33 (1986), p. 1141.

[48] P. H. Haynes and J. Vanneste, *What controls the decay of passive scalars in smooth flows?*, Phys. Fluids, 17 (2005), p. 097103.

[49] M. Horner, G. Metcalfe, S. Wiggins, and J. M. Ottino, *Transport enhancement mechanisms in open cavities*, J. Fluid Mech., 452 (2002), p. 199.

[50] S. C. Jana, G. Metcalfe, and J. M. Ottino, *Experimental and computational studies of mixing in complex stokes flows: the vortex mixing flow and multicellular cavity flows*, J. Fluid Mech., 269 (1994), pp. 199–246.

[51] G. Jeffery, *The rotation of two circular cylinders in a viscous fluid*, Proc. R. Soc. Lond. A, 101 (1922), pp. 169–174.

[52] M.-C. Jullien, P. Castiglione, and P. Tabeling, *Experimental observation of batchelor dispersion of passive tracers*, Phys. Rev. Lett., 85 (2000), p. 3636.

[53] C. Jung, T. Tél, and E. Ziemniak, *Application of scattering chaos to particle transport in a hydrodynamical flow*, Chaos, 3 (1993), p. 555.

[54] H. Kantz and P. Grassberger, *Repellers, semi-attractors, and long-lived chaotic transients*, Physica D, 17 (1985), p. 75.

[55] J. Kaplan and J. A. Yorke, in Lecture Notes in Mathematics, H. O. Peitgen and H. O. Walther, eds., vol. 730, Springer-Verlag, Berlin, 1978, p. 228.

[56] A. Katok and B. Hasselblatt, *Introduction to the Modern Theory of Dynamical Systems*, Cambridge University Press, 1995.

[57] R. Kraichnan, *Models of intermittency in hydrodynamic turbulence*, Phys. Rev. Lett., 65 (1990), p. 575.

[58] Y.-C. Lai, M. Ding, C. Grebogi, and R. Blümel, *Algebraic decay and fluctuations of the decay exponent in hamiltonian systems*, Phys. Rev. A, 46 (1992), p. 4661.

[59] V. V. Lebedev and K. S. Turitsyn, *Passive scalar evolution in peripheral region*, Phys. Rev. E, 69 (2004), p. 036301.

[60] J.-P. Leclerc, S. Claudel, H.-G. Lintz, O. Potier, and B. Antoine, *Theoretical interpretation of residence-time distribution measurements in industrial processes*, Oil & Gas Science and Technology - Rev. IFP, 55 (2000), pp. 159–169.

[61] C. W. Leong and J. M. Ottino, *Experiments on mixing due to chaotic advection in a cavity*, J. Fluid Mech., 209 (1989), pp. 463–499.

[62] K.-W. Lin and J.-T. Yang, *Chaotic mixing of fluids in a planar serpentine channel*, International Journal of heat and mass transfer, 50 (2007), pp. 1269–1277.

[63] M. Liu and F. J. Muzzio, *The curvature of material lines in chaotic cavity flows*, Phys. Fluids, 8 (1996), p. 75.

[64] W. Liu and G. Haller, *Strange eigenmodes and decay of variance in the mixing of diffusive tracers*, Physica D, 188 (2004), pp. 1–39.

[65] C. López, E. Hernández-Garcia, O. Piro, A. Vulpiani, and E. Zambianchi, *Population dynamics advected by chaotic flows: A discrete-time map approach*, Chaos, 11 (2001), p. 397.

[66] E. N. Lorenz, *Deterministic nonperiodic flow*, J. Atmos. Sci., 20 (1963), p. 130.

[67] P. Manneville, *Instabilities, Chaos And Turbulence- An Introduction to Nonlinear Dynamics and Complex Systems*, Imperial College Press, 2004.

[68] G. Mathew, I. Mezić, and L. Petzold, *A multiscale measure for mixing*, Physica D, 211 (2005), pp. 23–46.

[69] V. Meleshko and H. Aref, *A blinking rotlet model for chaotic advection*, Phys. Fluids, 8 (1996), pp. 3215–3217.

[70] P. Meunier and E. Villermaux, *How vortices mix*, J. Fluid Mech., 476 (2003), p. 213.

[71] L. M. Milne-Thomson, *Theoretical Hydrodynamics*, Macmillan, New York, 1968.

[72] J.-O. Moussafir, *On computing the entropy of braids*.

[73] F. J. Muzzio, M. M. Alvarez, S. Cerbelli, M. Giona, and A. Adrover, *The intermaterial area density generated by tme- and spatially periodic 2d chaotic flows*, Chem. Eng. Sci., 55 (2000), pp. 1497–1508.

[74] F. J. Muzzio, C. Meneveau, P. D. Swanson, and J. M. Ottino, *Scaling and multifractal properties of mixing in chaotic flows*, Phys. Fluids A, 4 (1992), p. 1439.

[75] F. J. Muzzio, P. D. Swanson, and J. M. Ottino, *The statistics of stretching and stirring in chaotic flows*, Phys. Fluids A, 3 (1991), pp. 5350–5360.

[76] Z. Neufeld and T. Tél, *Advection in chaotically time-dependent open flows*, Phys. Rev. E, 57 (1998), p. 2832.

[77] C. R. Nugent, W. M. Quarles, and T. H. Solomon, *Experimental studies of pattern formation in a reaction-advection-diffusion system*, Phys. Rev. Lett., 93 (2004), p. 218301.

[78] V. I. Oseledec, *A multiplicative ergodic theorem: Lyapunov characteristic numbers for dynamical systems*, Trans. Mosc. Math. Soc., 19 (1968), pp. 197–231.

[79] E. Ott, *Chaos in Dynamical Systems*, Cambridge University Press, Cambridge, U.K., second ed., 2002.

[80] E. Ott and T. M. Antonsen, *Fractal measures of passively convected vector fields and scalar gradients in chaotic fluid flows*, Phys. Rev. A, 39 (1989), p. 3660.

[81] E. Ott and T. Tél, *Chaotic scattering: An introduction*, Chaos, 3 (1993), p. 417.

[82] J. M. Ottino, *The Kinematics of Mixing: Stretching, Chaos, and Transport*, Cambridge University Press, Cambridge, U.K., 1989.

[83] J. M. Ottino, F. J. Muzzio, M. Tjahjadi, J. G. Franjione, S. Jana, and H. A. Kusch, *Chaos, symmetry, and self-similarity: Exploiting order and disorder in mixing processes*, Science, 257 (1992), pp. 754–760.

[84] E. L. Paul, V. Atiemo-Obeng, and S. M. Kresta, eds., *Handbook of Industrial Mixing: Science and Practice*, Wiley, 2003.

[85] A. Péntek, G. Károlyi, I. Scheuring, T. Tél, Z. Toroczkai, J. Kadtke, and C. Grebogi, *Fractality, chaos and reactions in imperfectly mixed open hydrodynamical flows*, Physica A, 274 (1999), p. 120.

[86] A. Péntek, T. Tél, and Z. Toroczkai, *Chaotic advection in the velocity field of leapfrogging vortex pairs*, J. Phys. A, 28 (1995), p. 2191.

[87] A. Péntek, Z. Toroczkai, T. Tél, C. Grebogi, and J. Yorke, *Fractal boundaries in open hydrodynamical flows: Signatures of chaotic saddles*, Phys. Rev. E, 51 (1995), pp. 4076–4089.

[88] R. T. Pierrehumbert, *Tracer microstructure in the large-eddy dominated regime.*, Chaos Solitons Fractals, 4 (1994), pp. 1091–1110.

[89] A. Pikovsky and O. Popovych, *Persistent patterns in deterministic mixing flows*, Europhys. Lett., 61 (2003), p. 625.

[90] O. V. Popovych, A. Pikovsky, and B. Eckhardt, *Abnormal mixing of passive scalars in chaotic flows*, Phys. Rev. E, 75 (2007), p. 036308.

[91] C. Pozrikidis, *Boundary Integral and Singularity Methods for Linearized Viscous Flow*, Cambridge University Press, 1992.

[92] A. Pumir, B. Shraiman, and E. D. Siggia, *Exponential tails and random advection*, Phys. Rev. Lett., 66 (1991), p. 2984.

[93] A. Renyi, *Probability Theory*, North-Holland Pub., Amsterdam, 1970.

[94] V. Rom-Kedar, A. Leonard, and S. Wiggins, *An analytical study of transport, mixing and chaos in an unsteady vortical flow*, J. Fluid Mech., 214 (1990), p. 347.

[95] D. Rothstein, E. Henry, and J. P. Gollub, *Persistent patterns in transient chaotic fluid mixing*, Nature (London), 401 (1999), p. 770.

[96] H. Salman and P. H. Haynes, *A numerical study of passive scalar evolution in peripheral regions*, Phys. Fluids, 19 (2007), p. 067101.

[97] I. Scheuring, G. Károlyi, Z. Toroczkai, T. Tél, and A. Péntek, *Competing populations in flows with chaotic mixing*, Theor. Popul. Biol., 63 (2003), p. 77.

[98] J. Schneider and T. Tél, *Extracting flow structures from tracer data*, Ocean Dynamics, 53 (2003), pp. 64–72.

[99] J. Schumacher and K. R. Sreenivasan, *Statistics and geometry of passive scalars in turbulence*, Phys. Fluids, 17 (2005), p. 125107.

[100] T. Shaw, J.-L. Thiffeault, and C. Doering, *Stirring up trouble: Multi-scale mixing measures for steady scalar sources*, Physica D, 231 (2007), pp. 143–164.

[101] Y. A. Sinai and V. Yakhot, *Limiting probability distributions of a passive scalar in a random velocity field*, Phys. Rev. Lett., 63 (1989), p. 1962.

[102] T. H. Solomon and J. P. Gollub, *Sheared boundary layers in turbulent Rayleigh-Bénard convection*, Phys. Rev. Lett., 64 (1990), p. 2382.

[103] T. H. Solomon, E. R. Weeks, and H. L. Swinney, *Observation of anomalous diffusion and Lévy flights in a two-dimensional rotating flow*, Phys. Rev. Lett., 71 (1993), p. 3975.

[104] J. C. Sommerer, H.-C. Ku, and H. E. Gilreath, *Experimental evidence for chaotic scattering in a fluid wake*, Phys. Rev. Lett., 77 (1996), p. 5055.

[105] A. D. Stroock, S. K. W. Dertinger, A. Adjari, I. Mezić, H. A. Stone, and G. M. Whitesides, *Chaotic mixer for microchannels*, Science, 295 (2002), p. 647.

[106] R. Sturman, J. Ottino, and S. Wiggins, *The Mathematical Foundations of Mixing: The Linked Twist Map as a Paradigm in Applications, Micro to Macro, Fluids to Solids*, Cambridge University Press, Cambridge, U.K., 2006.

[107] J. Sukhatme and R. T. Pierrehumbert, *Decay of passive scalars under the action of single scale smooth velocity fields in bounded two-dimensional domains: From non-self-similar probability distribution functions to self-similar eigenmodes*, Phys. Rev. E, 66 (2002), p. 056302.

[108] P. D. Swanson and J. M. Ottino, *A comparative computational and experimental study of chaotic mixing of viscous fluids*, J. Fluid Mech., 213 (1990), pp. 227–249.

[109] T. Tél, in Directions in Chaos, H. B. Lin, ed., vol. 3, World Scientific, Singapore, 1990, p. 149.

[110] T. Tél, A. de Moura, C. Grebogi, and G. Károlyi, *Chemical and biological activity in open flows: A dynamical system approach*, Physics Reports, 413 (2005), p. 91.

[111] T. Tél, G. Károlyi, A. Péntek, I. Scheuring, Z. Toroczkai, C. Grebogi, and J. Kadtke, *Chaotic advection, diffusion, and reactions in open flows*, Chaos, 10 (2000), p. 89.

[112] J.-L. Thiffeault, *The strange eigenmode in lagrangian coordinates*, Chaos, 14 (2004).

[113] ——, *Stretching and curvature along material lines in chaotic flows*, Physica D, 198 (2004).

[114] ——, *Measuring topological chaos*, Phys. Rev. Lett., 94 (2005), p. 084502.

[115] ——, *Scalar decay in chaotic mixing*, in Transport in Geophysical Flows: Ten Years After. Proceedings of the Gran Combin Summer School, Valle d'Aosta, Italy, 14-24 June 2004, Springer Verlag, in press.

[116] J.-L. Thiffeault and S. Childress, *Chaotic mixing in a torus map*, Chaos, 13 (2003), p. 502.

[117] J.-L. Thiffeault, E. Gouillart, and M. D. Finn, *The size of ghost rods*, in Proceedings of the Workshop on Analysis and Control of Mixing with Applications to Micro and Macro Flow Processes, CISM, Udine, Italy, 27 June - 1 July 2005, Springer Verlag, 2006, in press.

[118] W. Thurston, *On the geometry and dynamics of diffeomorphisms of surfaces*, Bull. Am. Math. Soc., 19 (1988), p. 417.

[119] Z. Toroczkai, G. Károlyi, A. Péntek, T. Tél, and C. Grebogi, *Advection of active particles in open chaotic flows*, Phys. Rev. Lett., 80 (1998), pp. 500–503.

[120] V. Toussaint and P. Carriére, *Diffusive cut-off scale of fractal surfaces in chaotic mixing*, International Journal of Bifurcations and Chaos, 9 (1999), pp. 443–454.

[121] V. Toussaint, P. Carrière, and F. Raynal, *A numerical Eulerian approach to mixing by chaotic advection*, Phys. Fluids, 7 (1995), p. 2587.

[122] V. Toussaint, P. Carrière, J. Scott, and J.-N. Gence, *Spectral decay of passive scalar in chaotic mixing*, Phys. Fluids, 12 (2000), p. 2834.

[123] C. L. Tucker, *Principles of mixing measurement*, in Mixing in Polymer Processing, Marcel Dekker Inc., 1991, pp. 101–127.

[124] A. Venaille and J. Sommeria, *A dynamical equation for the distribution of a scalar advected by turbulence*, Phys. Fluids, 19 (2007), p. 028101.

[125] E. Villermaux and J. Duplat, *Mixing as an aggregation process*, Phys. Rev. Lett., 91 (2003), p. 184501.

[126] E. Villermaux and J.-P. Hulin, *Chaos lagrangien et mélange de fluides visqueux*, Eur. J. Phys., 11 (1990), p. 179.

[127] G. Voth, T. Saint, G. Dobler, and J. Gollub, *Mixing rates and symmetry breaking in two-dimensional chaotic flow*, Phys. Fluids, 15 (2003), p. 2560.

[128] G. A. Voth, G. Haller, and J. P. Gollub, *Experimental measurements of stretching fields in fluid mixing*, Phys. Rev. Lett., 88 (2002), p. 254501.

[129] W. Wang, I. Manas-Zloczower, and M. Kaufman, *Entropic characterization of distributive mixing in polymer processing equipment*, AIChE J., 49 (2003), p. 1637.

[130] S. Wiggins and J. Ottino, *Foundations of chaotic mixing*, Phil. Trans. R. Soc. Lond. A, 362 (2004), pp. 937–970.

[131] A. Wonhas and J. C. Vassilicos, *Mixing in fully chaotic flows*, Phys. Rev. E, 66 (2002), p. 051205.

[132] J. Zalc, E. S. Szalai, M. Alvarez, and F. J. Muzzio, *Using cfd to understand chaotic mixing in laminar stirred tanks*, AIChE J., 48 (2002), p. 2124.

[133] E. H.-G. Zoltán Neufeld, Cristóbal López and O. Piro, *Excitable media in open and closed chaotic flows*, Phys. Rev. E, 66 (2002), p. 066208.

Index